ASME
SETTING THE STANDARD
1880 — 2005

Transactions of the ASME, Journal of Heat Transfer (ISSN 0022-1481) is published monthly by The American Society of Mechanical Engineers, Three Park Avenue, New York, NY 10016. Periodicals postage paid at New York, NY and additional mailing offices. POSTMASTER: Send address changes to Transactions of the ASME, Journal of Heat Transfer, c/o THE AMERICAN SOCIETY OF MECHANICAL ENGINEERS, 22 Law Drive, Box 2300, Fairfield, NJ 07007-2300. **CHANGES OF ADDRESS** must be received at Society headquarters seven weeks before they are to be effective. Please send old label and new address.

Journal of Heat Transfer

Published Monthly by ASME

VOLUME 127 • NUMBER 7 • JULY 2005

669 **Editor's Farewell Note**
Vijay K. Dhir

RESEARCH PAPERS

Conduction

670 **Solution of Transient Temperature Field for Thermographic NDT Under Joule Effect Heating**
Zhuo Qiu Li, Xiong Zhang, and Jiang Tao Zhang

Evaporation, Boiling, and Condensation

675 **Boiling Performance of Single-Layered Enhanced Structures**
Camil-Daniel Ghiu and Yogendra K. Joshi

684 **Additive Adsorption and Interfacial Characteristics of Nucleate Pool Boiling in Aqueous Surfactant Solutions**
Juntao Zhang and Raj M. Manglik

Forced Convection

692 **Discrete Green's Function Measurements in Internal Flows**
Charles Booten and John K. Eaton

699 **Heat Transfer Studies in the Flow Over Shallow Cavities**
Paulo S. B. Zdanski, M. A. Ortega, and Nide G. C. R. Fico, Jr.

Micro/Nanoscale Heat Transfer

713 **Comparison of Different Phonon Transport Models for Predicting Heat Conduction in Silicon-on-Insulator Transistors**
Sreekant V. J. Narumanchi, Jayathi Y. Murthy, and Cristina H. Amon

724 **Damage-Free Low Temperature Pulsed Laser Printing of Gold Nanoinks On Polymers**
Jaewon Chung, Seunghwan Ko, Costas P. Grigoropoulos, Nicole R. Bieri, Cedric Dockendorf, and Dimos Poulikakos

Natural and Mixed Convection

733 **Laminar Natural Convection Heat Transfer From a Vertical Baffled Plate Subjected to a Periodic Oscillation**
Xinrong Zhang, Shigenao Maruyama, and Hiroshi Yamaguchi

Radiative Heat Transfer

740 **Narrow-Band Based Multiscale Full-Spectrum *k*-Distribution Method for Radiative Transfer in Inhomogeneous Gas Mixtures**
Liangyu Wang and Michael F. Modest

Heat Exchangers

749 **Stability Behavior of a Natural Circulation Loop With End Heat Exchangers**
N. M. Rao, B. Maiti, and P. K. Das

Electronic Cooling

760 **Optimized Heat Transfer for High Power Electronic Cooling Using Arrays of Microjets**
Matteo Fabbri and Vijay K. Dhir

770 **Fluid Flow and Thermal Characteristics of a Microchannel Heat Sink Subject to an Impinging Air Jet**
Seok Pil Jang and Sung Jin Kim

(**Contents continued on inside back cover**)

This journal is printed on acid-free paper, which exceeds the ANSI Z39.48-1992 specification for permanence of paper and library materials. ♾™
♻ 85% recycled content, including 10% post-consumer fibers.

(**Contents continued**)

Journal of Heat Transfer **Volume 127, Number 7** **JULY 2005**

TECHNICAL BRIEFS

780 Effects of Backfill on Heat Transfer From a Buried Pipe
C. C. Ngo and F. C. Lai

785 Fluid Flow Around and Heat Transfer From an Infinite Circular Cylinder
W. A. Khan, J. R. Culham, and M. M. Yovanovich

791 Study on the Imaginary Temperature of Open Boundary Wall in Cylindrical Medium by Partition Allocation Method
H. Qi, L. M. Ruan, and L. H. Liu

The ASME Journal of Heat Transfer is abstracted and indexed in the following:

Applied Science and Technology Index, Chemical Abstracts, Chemical Engineering and Biotechnology Abstracts (Electronic equivalent of Process and Chemical Engineering), Civil Engineering Abstracts, Compendex (The electronic equivalent of Engineering Index), Corrosion Abstracts, Current Contents, E & P Health, Safety, and Environment, Ei EncompassLit, Engineered Materials Abstracts, Engineering Index, Enviroline (The electronic equivalent of Environment Abstracts), Environment Abstracts, Environmental Engineering Abstracts, Environmental Science and Pollution Management, Fluidex, Fuel and Energy Abstracts, Index to Scientific Reviews, INSPEC, International Building Services Abstracts, Mechanical & Transportation Engineering Abstracts, Mechanical Engineering Abstracts, METADEX (The electronic equivalent of Metals Abstracts and Alloys Index), Petroleum Abstracts, Process and Chemical Engineering, Referativnyi Zhurnal, Science Citation Index, SciSearch (The electronic equivalent of Science Citation Index), Theoretical Chemical Engineering

Journal of Heat Transfer

Editor's Note

Editor's Farewell Note

Serving as Editor for the Journal of Heat Transfer (JHT) from 2000 to 2005 has been rewarding as well as challenging. Increasing the submission base of JHT and insuring that papers are reviewed in a timely manner has been a goal of mine from the start. Achieving this goal has only been possible through the support and diligence of JHT's Board of Editors, and it has been a great pleasure to work with a group so dedicated to the well being of this journal and the technical community.

The frequency of the journal has increased from quarterly to bi-monthly (although efforts in this direction were made by the previous Editor, Jack Howell) in February 2001, and now since January 1, 2005, it is published monthly. The impact factor has also improved significantly and stood at 1.252 in the 2003 JCR Science Edition.

During my term JHT has published three special issues covering the areas of micro/nanoscale heat and mass transfer, electronics cooling, and gas turbine heat transfer. There are also two special issues currently in the works: one on fuel cells and one on boiling and interfacial phenomena. Besides presenting outstanding archival material on a particular area of heat transfer, special issues help to increase readership because they invite readers from industry as well as academia, especially students.

I am indebted to my assistant, Jenell Rae, for her dedicated service to the Journal and her support of the Associate Editors. She interacted well with the authors, reviewers, and ASME staff. I am grateful to the contributions of the Executive Committee of the Heat Transfer Division (HTD) of ASME for supporting my visions and goals for the Journal throughout my term. I am equally grateful for the support and guidance of ASME's capable staff: Philip DiVietro, Colin McAteer, Cynthia Clark, and Beth Darchi.

On July 1, 2005, the Journal will be handed over to Dr. Yogesh Jaluria. Dr. Jaluria is an eminent figure in the heat transfer community, and as the past Chair of the Heat Transfer Division, I am confident that he will uphold the excellent reputation of the Journal.

Best wishes to all,

Vijay K. Dhir
Editor
2000–2005

Solution of Transient Temperature Field for Thermographic NDT Under Joule Effect Heating

Zhuo Qiu Li

Xiong Zhang

Jiang Tao Zhang

School of Science,
Wuhan University of Technology,
430070, Wuhan, China

Conducting infrared thermographic nondestructive testing (NDT) by the internal heat generated by Joule effect of components is a new heating approach for flaw detection. Due to the combination of electric field and thermal field, the irregular geometric boundary and the complicated internal heat source distribution, the theoretical solution of transient temperature field is very difficult. Nowadays numerical solution by FEM and FDM is mainly applied. By adopting certain assumptions, this paper presents a method to obtain the approximate temperature field by using Green's function, and gives the solution of a two-dimensional rectangular field including a circular flaw. By contrast, the result tallies with the FEM results well. [DOI: 10.1115/1.1924625]

1 Introduction

During the past several years, infrared thermography has evolved into a powerful investigative tool of nondestructive test. In fact, it has proved its ability to satisfy a lot of requirements in a wide range of fields. The existence of temperature difference is an essential requirement for infrared NDT. If the structure does not glow itself, to conduct inspection, we must apply heat flux on the surface of it. The temperature difference is formed on the surface during the diffusion of the heat flux, due to the difference of thermal resistance between defects and sound places. Nowadays, different heating techniques are being applied: pulse laser heating, heating unit method, etc. With the development of infrared thermography detection, adopting a new heating method that is fast, convenient, and automatic becomes one of the most important directions.

Conducting infrared thermographic NDT by the internal heat generated by the Joule effect of components is a new heating approach adopted recently for flaw detection. It aims at components made by conducting materials. By applying a voltage at the two ends of the specimen, the current density around the flaw distributes unevenly, and so does the Joule heat. Due to the uneven Joule heat, temperature differences come into being, and then can be inspected and identified by an infrared camera. This method is mainly used for aircraft metal components in the beginning, and it is now also used for other conducting components; carbon fiber reinforced concrete, for instance [1,2]. The experimental setup is shown in Fig. 1 and a representative result is given in Fig. 2.

The defect in the middle of the component in Fig. 2 can be identified clearly. By technical treatment, the quantitative information of flaws can be derived. One of the recent trends in the development of thermographic NDT is the use of transient temperature data [3]. The purpose of this paper is not to seek the quantitative evaluations of defects but to give an approximate method to derive the temperature distribution. Due to the combination of electric field and thermal field—the irregular geometric boundary and the complicated internal heat distribution—the theoretical solution of transient temperature field of this problem is very difficult. Nowadays, numerical solution by the finite element method (FEM) and finite difference method (FDM) is mainly applied. By adopting certain assumptions, this paper presents a method to obtain the approximate temperature field by using Green's function, and gives the solution of a two-dimensional rectangular field including a circular flaw (or three-dimensional field involve an infinitely long cylindrical flaw). By contrast, the results tally with the FEM results well.

2 Simplification of the Model

Take the two-dimensional rectangular field including a circular flaw, for example. We introduce the simplification of the thermal model.

Sound component should generate Joule heat homogeneously under the action of uniform electric field. Because of the existence of flaw, the distribution of heat generation surrounding the flaw changes in the defective component, which results in the surface temperature discrepancy on which we depend to conduct the infrared inspection. Since the flaw is small by contrast with the component, the disturbance of the thermal field caused by the flaw is local. In addition, the Joule heat surrounding the circular flaw distributes symmetrically, as does the temperature. Consequently, we can assume the boundary condition is adiabatic in the symmetrical axes of the flaw. The simplified model is shown in Fig. 3. We take the boundary condition on the surrounding surface as a convective condition, which denotes the adiabatic condition when we assume the convection coefficient is equal to zero. The voltage added to the component is V.

As shown in Fig. 3, we assume the material of the flaw is the same material as other parts of the component in the process of heat conduction. But when considering the heat generation, we think that the Joule heat generation of the component is distributed the same as before. That is to say, considering the heat generation, we deem the component is defective, but in the process of conduction we deem the component is sound. The influence of this assumption to the whole model stems from the discrepancy of conductivity between these two materials in the part of the flaw. Since the flaw is small relative to the component and the boundary that abuts on the flaw is adiabatic, the influence is diminutive and limited. When the size of the flaw increases, the error caused by this assumption will accordingly be enhanced.

Generally, when we conduct experiments, the environmental temperature and the initial temperature of the specimens are constant T_0. If we ignore the existence of flaw, the heat conduction equation and the initial-boundary conditions listed as follows:

$$\frac{\partial^2 T}{\partial x^2} + \frac{\partial^2 T}{\partial y^2} + \frac{1}{k} g(x,y,t) = \frac{1}{\alpha} \frac{\partial T}{t}$$

Contributed by the Heat Transfer Division for publication in the JOURNAL OF HEAT TRANSFER. Manuscript received February 24, 2004. Final manuscript received January 6, 2005. Review conducted by: Ashley F. Emery.

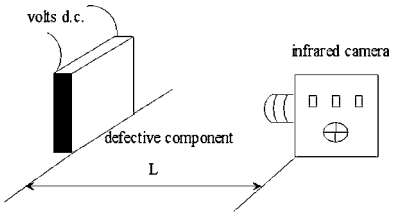

Fig. 1 Experimental set-up

$$\frac{\partial T}{\partial x}=0 \quad x=0 \qquad \frac{\partial T}{\partial x}+H_1(T-T_0)=0 \quad x=a$$

$$\frac{\partial T}{\partial y}=0 \quad y=0 \qquad \frac{\partial T}{\partial y}+H_2(T-T_0)=0 \quad y=b$$

$$T=T_0 \quad t=0 \tag{1}$$

where $H_1=h_1/k$, $H_2=h_2/k$, $T=T(x,y,t)$ is the temperature distribution, h_1 and h_2 are the heat exchange coefficient ($W/m^2\,°C$); k, the thermal conductivity of the material ($W/m\,°C$); $g(x,y,t)$ is the internal heat generation function.

3 Green's Functions and Their Interpretation

Green's functions (GF) are powerful mathematical tools suitable for obtaining solutions of linear heat conduction problems [4–6]. There are two possible interpretations of GF. First, they can be regarded as a temperature response at a point r at time t caused by an instantaneous energy generation at a point r' at time τ. Thus, theoretically, in order to obtain the temperature response in time, it is sufficient to integrate the GF over all points and times at which energy is generated. Alternatively, a GF is the temperature response at a point r in time t due to the initial temperature rise at a point r'. Then, the temperature distribution is obtained as an integral of a GF evaluated at initial time over the whole analysis domain. Particular forms of GFs depend only on the structure geometry and the applied boundary conditions. Therefore, the same GF can be used then for solving all the problems, whatever temperature distribution it results from. Namely, for linear problems the overall temperature rise can be computed as the sum of the individual temperature rises caused by all the contributing factors, such as the initial temperature distribution, the internal energy generation or the nonhomogeneous boundary conditions, as shown in Eq. (5).

As for initial-boundary value problem for heat conduction ($\mathbf{r}$ denotes 1, 2 or 3 dimensions):

$$\nabla^2 T(\mathbf{r},t)+\frac{1}{k}g(r,t)=\frac{1}{\alpha}\frac{\partial T(\mathbf{r},t)}{\partial t} \quad \text{in domain } R \quad t>0 \tag{2}$$

$$k_i\frac{\partial T(\mathbf{r},t)}{\partial n_i}+h_iT(\mathbf{r},t)=f_i(\mathbf{r},t) \quad \text{on boundary } S_i \quad t>0 \tag{3}$$

$$T(\mathbf{r},t)=F(\mathbf{r}) \quad \text{in domain } R \quad t=0 \tag{4}$$

h_i is the heat exchange coefficient ($W/m^2\,°C$); k_i is the thermal conductivity of the material ($W/m\,°C$); α is thermal diffusivity (m^2/s).

The temperature can be stated in the form of integrals with the method of Green's functions. If Green's function $G(\mathbf{r},t|\mathbf{r}',\tau)$ is known, then the temperature that satisfies Eq. (2) is given by [7]

$$\begin{aligned}T(\mathbf{r},t)=&\int_R G(\mathbf{r},t|\mathbf{r}',\tau)|_{\tau=0}F(\mathbf{r}')dv'\\&+\frac{\alpha}{k}\int_{\tau=0}^{t}d\tau\int_R G(\mathbf{r},t|\mathbf{r}',\tau)g(\mathbf{r}',\tau)dv'\\&+\int_{\tau=0}^{t}d\tau\sum_{i=1}^{S}\int_{S_i}G(\mathbf{r},t|\mathbf{r}',\tau)|_{r'=r_i}\cdot\frac{1}{k}f_i(\mathbf{r},\tau)dS_i\end{aligned} \tag{5}$$

The GFs can be derived using different methods, such as the method of images, the Laplace transform method or the Fourier method of separation of variables. All these methods lead to solutions in different forms of mathematically equivalent expressions. From the computational point of view, the main difference between the methods is the series convergence, which in turn determines the simulation time. Usually, the first two methods yield series, which are rapidly convergent for low Fourier numbers and the Fourier method produces series, which are better convergent for large Fourier numbers. The dimensionless Fourier number F_0 can be found from the following formula: $F_0=\alpha t/l^2$. The symbol l in the denominator denotes any distance for which the speed of the heat diffusion is assessed, in particular it could be the dimension of a structure. More information on GFs and methods of obtaining them can be found in Refs. [8–11].

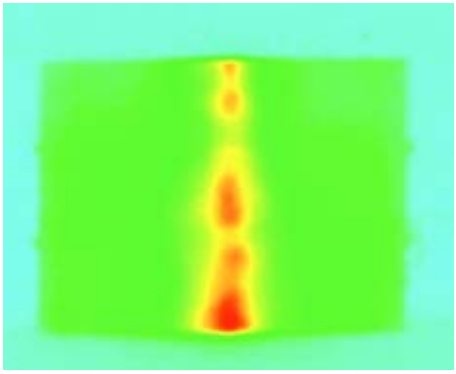

Fig. 2 Representative result

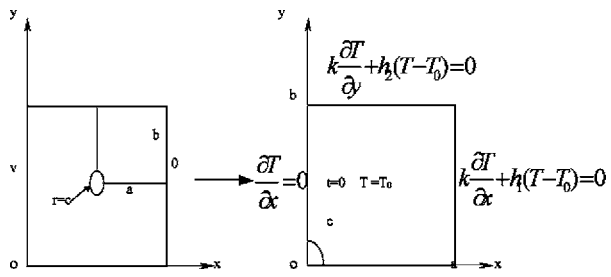

Fig. 3 Simplification of the model

4 Heat Equation Solution and Flaw Simulation

Defining $U=T-T_0$ in Eq. (1), we can derive the homogeneous initial and boundary conditions,

$$\frac{\partial^2 U}{\partial x^2}+\frac{\partial^2 U}{\partial y^2}+\frac{1}{k}g(x,y,t)=\frac{1}{\alpha}\frac{\partial U}{t}$$

$$\frac{\partial U}{\partial x}=0 \quad x=0 \qquad \frac{\partial U}{\partial x}+H_1U=0 \quad x=a$$

$$\frac{\partial U}{\partial y}=0 \quad y=0 \qquad \frac{\partial U}{\partial y}+H_2U=0 \quad y=b$$

$$U=0 \quad t=0$$

$$U=U(x,y,t)=T(x,y,t)-T_0 \tag{6}$$

Then we obtain the Green's function by method of separation of variables [7,12] as follows:

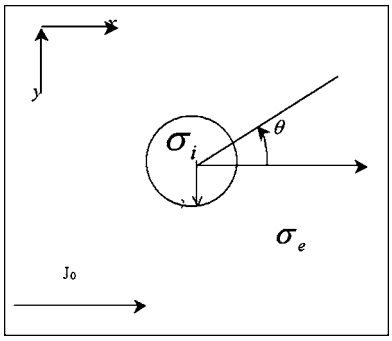

Fig. 4 Schematic of coordinate system

$$G(x,y,t|x',y',\tau) = 4\sum_{m=1}^{\infty}\sum_{n=1}^{\infty} e^{-\alpha(\beta_m+\gamma_n)(t-\tau)} \times \frac{\beta_m^2+H_1^2}{a(\beta_m^2+H_1^2)+H_1}\frac{\gamma_n^2+H_2^2}{b(\gamma_n^2+H_2^2)+H_2} \cdot \cos\beta_m x \cos\gamma_n y \cos\beta_m x' \cos\gamma_n y' \quad (7)$$

where β_m, γ_n are the positive solution of equations:

$$\beta_m \tan\beta_m a = H_1 \text{ and } \gamma_n \tan\gamma_n b = H_2$$

Because the flaw is small and Joule heat degenerates rapidly along the distance, we can deal with the problem as a circular flaw in an infinite medium. The dimensions a and b are critical in this assumption. With the size of flaw increases, the error caused by this assumption will accordingly be enhanced. But the error analysis shows that if the ratio of c to the less of a and b is less than 0.5, the accuracy is always satisfying. Figure 4 shows the coordinate system.

The electric field intensity inside and outside the flaw are distributed as follows [13]:

$$E_i = \frac{2}{\sigma_i+\sigma_e}J_0\vec{\mathbf{x}} \quad (r<c) \quad (8)$$

$$E_e = \left[\frac{\sigma_i-\sigma_e}{\sigma_i+\sigma_e}\left(\frac{c}{r}\right)^2+1\right]J_0\cos\theta/\sigma_e\vec{\mathbf{r}} + \left[\frac{\sigma_i-\sigma_e}{\sigma_i+\sigma_e}\left(\frac{c}{r}\right)^2-1\right]J_0\sin\theta/\sigma_e\vec{\theta} \quad (r>c) \quad (9)$$

where c is the radius of the flaw, J_0 is current density, σ_i is the electrical conductivity of the flaw, σ_e is the electrical conductivity outside the flaw, E_i is the electric field intensity inside the flaw, E_e is the electric field intensity outside flaw.

Accordingly, the Joule heat generated inside and outside the flaw:

$$g_i(r,\theta,t) = \frac{4\sigma_i}{(\sigma_i+\sigma_e)^2}J_0^2 \quad (r<c) \quad (10)$$

$$g_e(r,\theta,t) = \left[1+\left(\frac{\sigma_i-\sigma_e}{\sigma_i+\sigma_e}\right)^2\left(\frac{c}{r}\right)^4+2\frac{\sigma_i-\sigma_e}{\sigma_i+\sigma_e}\left(\frac{c}{r}\right)^2\cos 2\theta\right]J_0^2/\sigma_e \quad (r>c) \quad (11)$$

Change the polar coordinate into Cartesian coordinate:

$$g_i(x,y,t) = \frac{4\sigma_i}{(\sigma_i+\sigma_e)^2}J_0^2 \quad (r<c) \quad (12)$$

$$g_e(x,y,t) = \frac{J_0^2}{\sigma_e}\left(1+\frac{\eta^2c^4-2\eta c^2(x^2-y^2)}{(x^2+y^2)^2}\right) \quad (r>c) \quad (13)$$

where

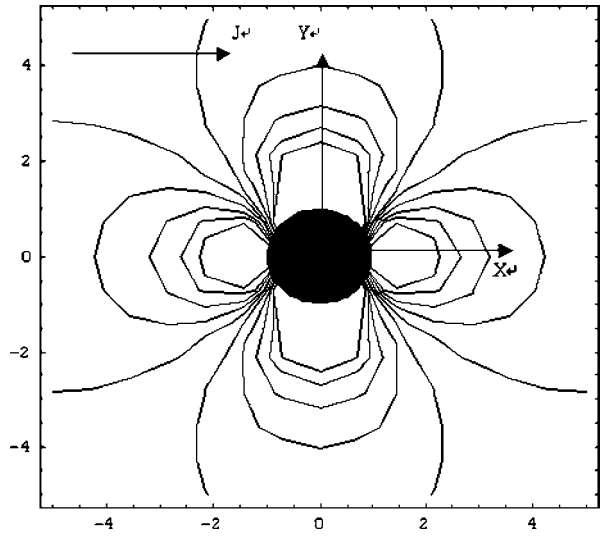

Fig. 5 Joule heat distribution

$$\eta = \frac{\sigma_i-\sigma_e}{\sigma_i+\sigma_e}$$

The Joule heat distribution of a plate with a circular cavum is shown in Fig. 5 to prove that Joule heat degenerates rapidly with the distance to the flaw increasing. We can see that the Joule heat disturbance caused by the flaw weakens very quickly. In place that 5 times the radius away from the flaw, the Joule heat almost resumes completely (the ratio of heat generation resume to 1). Joule heat along axis x is shown in Fig. 6 and Joule heat along axis y is shown in Fig. 7.

Since the Joule heat expressions inside and outside the flaw are different, the whole domain must be divided into two parts in computation. It is evident that the region outside the flaw must be divided into two parts for the integral. So we divide the whole region into three parts altogether as Fig. 8. According to Eqs. (5)–(7), (12), and (13), we obtain the solution of the temperature field by integrating separately.

$$T(x,y,t) = T_0 + 4\sum_{m=1}^{\infty}\sum_{n=1}^{\infty} e^{-\alpha(\beta_m+\gamma_n)(t-\tau)} \times \frac{\beta_m^2+H_1^2}{a(\beta_m^2+H_1^2)+H_1}\frac{\gamma_n^2+H_2^2}{b(\gamma_n^2+H_2^2)+H_2} \cdot \cos\beta_m x \cos\gamma_n y \left(\int_{x'=c}^{a}\int_{y'=0}^{b} g_e(x',y',\tau)\right.$$

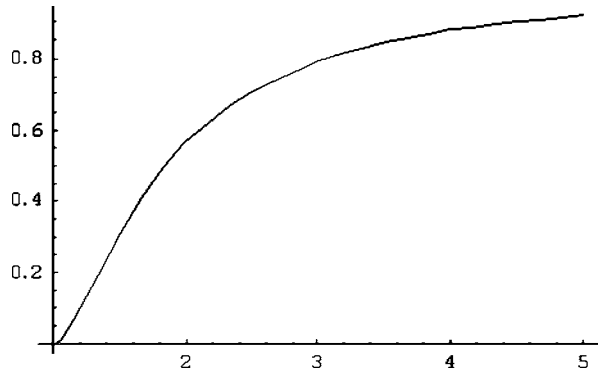

Fig. 6 Joule heat along axis *x*

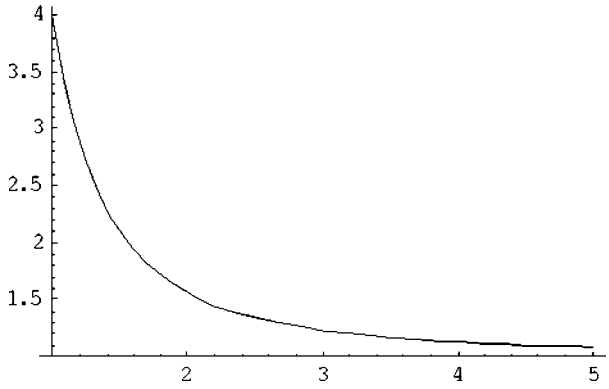

Fig. 7 Joule heat along axis *y*

$$\cdot \cos \beta_m x' \cos \gamma_n y' dy' dx'$$
$$+ \int_{x'=0}^{c} \int_{y'=\sqrt{c^2-x'^2}}^{b} g_e(x', y', \tau) \cdot \cos \beta_m x' \cos \gamma_n y' dy' dx'$$
$$+ \int_{x'=0}^{c} \int_{y'=0}^{\sqrt{c^2-x'^2}} g_i(x', y', \tau) \cdot \cos \beta_m x' \cos \gamma_n y' dy' dx' \Bigg) \tag{14}$$

After acquiring the transient temperature field, we can get the temperature of any point in the domain at any time point, including the surface temperature field.

5 Solution and Analysis

Taking the material CFRC, for example, the flaw here is a cavum, which means σ_e is equal to zero. Other parameters are listed in Table 1.

Calculate the integration in Eq. (14) by numerical integration of the GaussKronrod method. By taking the top 36 terms of the series, that is to say, setting m and n from one to six, we draw the contours of temperature at 10 min in Fig. 9(*a*). The FEM solution is shown in Fig. 9(*b*).

The two temperature fields tally well in Fig. 9 in almost the whole region except the region close to the flaw. Since we are most concerned with surface temperature distribution, surface temperature distributive curves are drawn in Fig. 10. Results show that the difference of the two results is about 1%. The FEM results

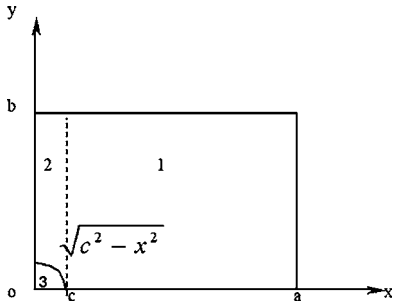

Fig. 8 Dividing the region into three parts

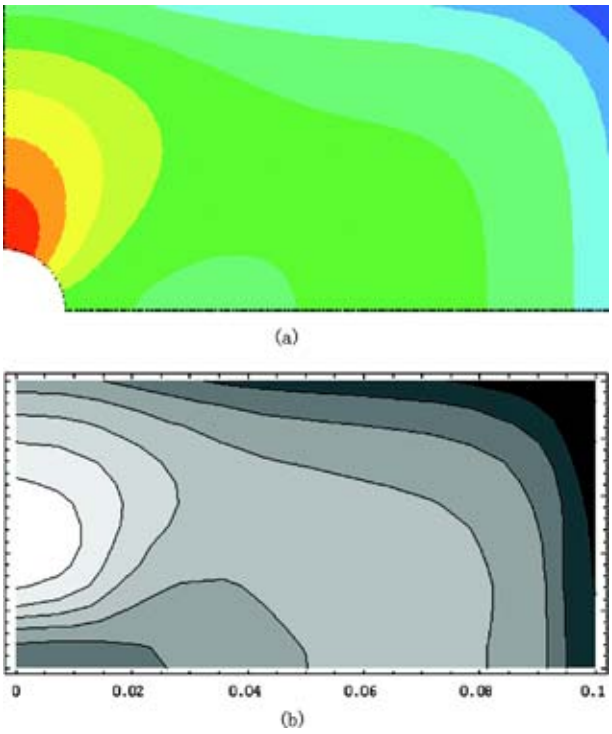

Fig. 9 (*a*) Solution of FEM; (*b*) solution of the analytical expression

are derived by adopting the thermal-electric coupled-field element. The error is caused by both two assumptions adopted in Secs. 2 and 4.

As we have stated that with the size of the flaw increases, the error caused by the two assumptions will be enhanced. The influence of the assumption is associated with the relative sizes of the flaw and the plate. The study shows that the main factor that decides the accuracy is the ratio of c to the lesser of a and b. Figure 11 shows the difference when the radius is 20 mm. The biggest error is a percentage of 2.6, which exists in location $x = 0$. Further analysis shows that when the ratio of c to b goes to 0.5, the error is 5.1%. It is evident that when the ratio is less than 0.5, the error will be less than 5.1%. On different conditions, when we change the material, the initial temperature or the boundary condition, the error will differ. But in most cases, the accuracy is satisfying. Especially when the size of the flaw decreases, the error caused by the two assumptions will surely diminish.

6 Conclusions

By adopting the simplified model and computation method of this paper, we can obtain the approximate analytical solution of the temperature field of components with one symmetrical and relatively small flaw during infrared inspection by internal joule heat. Compared with FEM results, results given by this analytical solution tally well and give good precision. Furthermore, a similar analysis can be performed for the three-dimensional problem, but the whole region should be divided into four parts and the integration will be more complicated. In addition, what should be paid

Table 1 Parameters

Thermal conductivity	(σ_e)Electric conductivity	a	b	Radius of the circular flaw c	Voltage	Environmental temperature
1.25W/m·K	0.75 Ω·m	100mm	50mm	10mm	25V	20℃

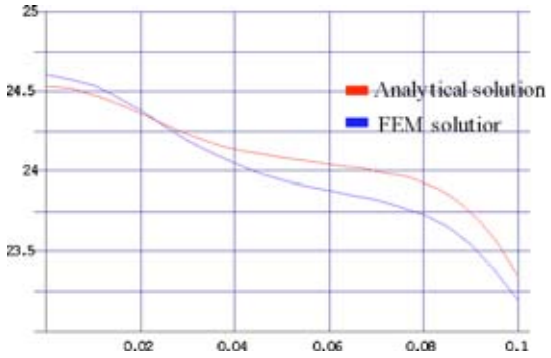

Fig. 10 Contrast curve of surface temperature ($c=10$ mm)

more attention to is the mathematic expressions of Green's function. For different expressions there is different series convergence, and we should choose an expression with better convergence.

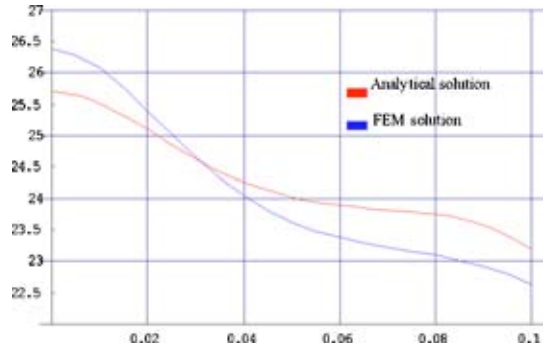

Fig. 11 Contrast curve of surface temperature ($c=20$ mm)

Acknowledgment

This work was supported by the National Nature and Science Fund, serial number 50238040.

References

[1] Huang, Li, Zhuoqiu, Li, Xianhui, Song, and Hongbing, Qian, 2003, "Infrared Thermographic Inspection for the Crack in Carbon Fiber Reinforced Concrete," Exp. Mech., **18**, pp. 403–408.
[2] Sakagami, Takahide, and Ogura, Keiji, 1994, "Thermographic NDT Based on Transient Temperature Field Under Joule Effect Heating," Proc. SPIE, **2245**, pp. 120–130.
[3] Sakagami, Takahide, and Kubo, Shiro, 2002, "Applications of Pulse Heating Thermography and Lock-In Thermography to Quantitative Nondestructive Evaluations," Infrared Phys. Technol., **43**, pp. 211–218.
[4] Cole, Kevin D., and Yen, David H. Y., 2001, "Green's Functions, Temperature and Heat Flux in the Rectangle," Int. J. Heat Mass Transfer, **44**, pp. 3883–3894.
[5] Efstathios, Zhi-Gangfeng, and Mirchaelides, E., 1997, "The Use of Modified Green's Functions in Unsteady Heat Transfer," Int. J. Heat Mass Transfer, **40**, pp. 2997–3002.
[6] Melnikov, Y. A., 2000, "An Alternative Construction of Green's Functions for the Two-Dimensional Heat Equation," Eng. Anal. Boundary Elem., **24**, pp. 467–475.
[7] Ozisik, M. N., and Changming, Yu, 1984, *Heat Conduction*, Advanced Education Press.
[8] Carslaw, H. S., and Jaeger, J. S., 1947, *Conduction of Heat in Solids*, Clarendon Press, Oxford.
[9] Beck, J. V., Cole, K. D., Haji-Sheikh, A., and Litkouhi, B., 1992, *Heat Conduction Using Green's Functions*, Hemisphere, Washington, D.C.
[10] Stakgold, I., 1979, *Green's Functions and Boundary Value Problems*, Wiley–Interscience, New York.
[11] Beck, J. V., 1984, "Green's Function Solution for Transient Heat Conduction Problems," Int. J. Heat Mass Transfer, **27**, pp. 1235–1244.
[12] Qiangsheng, Yang, and Baorong, Pu, 2001, *Advanced Heat Conduction*, Shanghai Communication University Press.
[13] Kunmiao, Xu, 1979, *Method of Mathematical Physics*, The People's Education Press.

Boiling Performance of Single-Layered Enhanced Structures

Camil-Daniel Ghiu

Yogendra K. Joshi
e-mail: yogendra.joshi@me.gatech.edu

G. W. Woodruff School of Mechanical Engineering,
Georgia Institute of Technology,
Atlanta, Georgia 30332

A study of pool boiling at atmospheric pressure from single-layered enhanced structures was conducted for a dielectric fluorocarbon liquid (PF 5060). The parameters investigated in this study were: (a) Heat flux (1–45 W/cm^2)*; (b) width of the microchannels* (65–105 μm)*; and (c) microchannel pitch* (0.2–0.7 mm)*. The boiling performance of the enhanced structures was found to increase with the increase in channel width and decrease in channel pitch. A simple single line curve fit is provided as a practical way of predicting the data over the entire nucleate boiling regime. The exponent n in the single line power curve fit was found to be between 1 and 2. The modes of boiling from an enhanced structure proposed by previous researchers were unable to explain the boiling curves obtained in this study. The present data are explained in light of the contribution from the top finned surface of the enhanced structure.* [DOI: 10.1115/1.1924568]

Keywords: Boiling, Electronics, Enhancement, Experimental, Heat Transfer, Microstructures

1 Introduction

An established way of improving the heat transfer in nucleate boiling is by employing enhanced structures. Two types of such structures exist: Porous coatings and re-entrant grooves. A number of investigations on porous coatings have been carried out ([1–3]). The latter category of structures, the focus of the present paper, has special surface microgeometry (small features), which promotes high performance nucleate boiling. The heat transfer coefficients achieved with these structures are much greater than those obtained with smooth surfaces. (Thome [1], Webb [2]).

Several researchers have investigated the boiling phenomena pertaining to re-entrant grooved enhanced structures. Nakayama et al. [4] developed flat boiling enhancement structures simulating the Hitachi Thermoexcel-E commercial surface [5]. These structures consisted of interconnected internal cavities (tunnels) communicating with the external liquid pool through small openings (pores). Water, R-11, and liquid nitrogen constituted the working fluids. This type of enhanced structure proved to be highly efficient in transferring heat especially for small wall superheats (in the range of 0.5–5 K). The surface structure having a pore diameter of around 0.1 mm achieved the best heat transfer performance for all fluids.

Arshad and Thome [6] studied structures similar to ones of Nakayama et al. [4]. Their structures had rectangular, triangular, and circular cross-section subsurface channels connected with the liquid pool through pores of diameters 0.18 and 0.25 mm. The working fluid was water and the range of investigated heat fluxes 1–20 W/cm^2. The structure having pores of 0.25 mm diameter showed as much as seven times improvement in performance over the smooth surface of Nakayama et al. [4].

Chien and Webb [7] employed refrigerants R-11 and R-123 for heat fluxes in the range of 0.1–8 W/cm^2. By soldering a thin copper foil (50 μm) around a 19.1 mm diameter horizontal integral-fin tube they obtained a structure similar to Nakayama et al. [4]. Round pores of 0.12, 0.18, 0.23, and 0.28 mm diameter were provided on the cover foil by piercing. The heat transfer coefficient was found to strongly depend on pore size at a given heat flux. For heat fluxes less than 3.5 W/cm^2 the optimum pore diameter was 0.23 mm. For higher heat fluxes the structure with the largest diameter pores (0.28 mm) showed the best performance.

Electronics cooling applications place specific requirements on boiling from enhanced structures. First of all, the temperature of the electronic component to be cooled must be held below a certain value (typically 85°C for conventional silicon electronics), based on performance and reliability considerations. Second, only dielectric fluids are suitable for direct contact with electronics, and these fluids have poor thermal transport properties. In addition, the heat source surface area is small, which leads to high heat fluxes. Another limitation comes from the small space available around the heat generating chip.

The above-mentioned studies did not specifically address the unique issues identified above. The working fluids were not suitable for use in electronic systems, except R-11, which has since been phased out due to environmental concerns. Additionally, the enhanced structure employed had discrete pores through which it communicated with the liquid pool. This particular configuration could not assure the high heat flux dissipation needed in electronics cooling. The critical heat flux was found to be 17 W/cm^2 in boiling FC 72 under atmospheric pressure [8]. This is well below heat fluxes of interest in electronics cooling, typically 40 W/cm^2 or higher. To address these issues, Nakayama et al. [8] developed enhanced multilayer structures especially for use in electronics cooling. By placing a five-layer stack on top of a 5 mm long cylindrical stud, a heat flux of 110 W/cm^2 was dissipated at a surface superheat of 35 K in pool boiling with FC-72 as the working fluid.

Anderson and Mudawar [9] tested three categories of surfaces (smooth, drilled, and low-profile structures) placed vertically in a stagnant pool of FC-72 maintained at atmospheric pressure. It was found that low-profile surface geometries resulted in significant enhancement of nucleate boiling. The CHF was 34.6 W/cm^2 for microfin structures and 51.1 W/cm^2 for microstud surfaces.

Mudawar and Anderson [10] subsequently constructed and evaluated a structure with multiple levels of enhancement. Low profile microstructures were machined on the lateral surface of a single extended cylindrical stud. Additionally, microscopic surface characteristics were obtained by blasting the surface with an air–

Contributed by the Heat Transfer Division for publication in the JOURNAL OF HEAT TRANSFER. Manuscript received May 4, 2004. Final manuscript received February 2, 2005. Review conducted by: Jacob N. Chung.

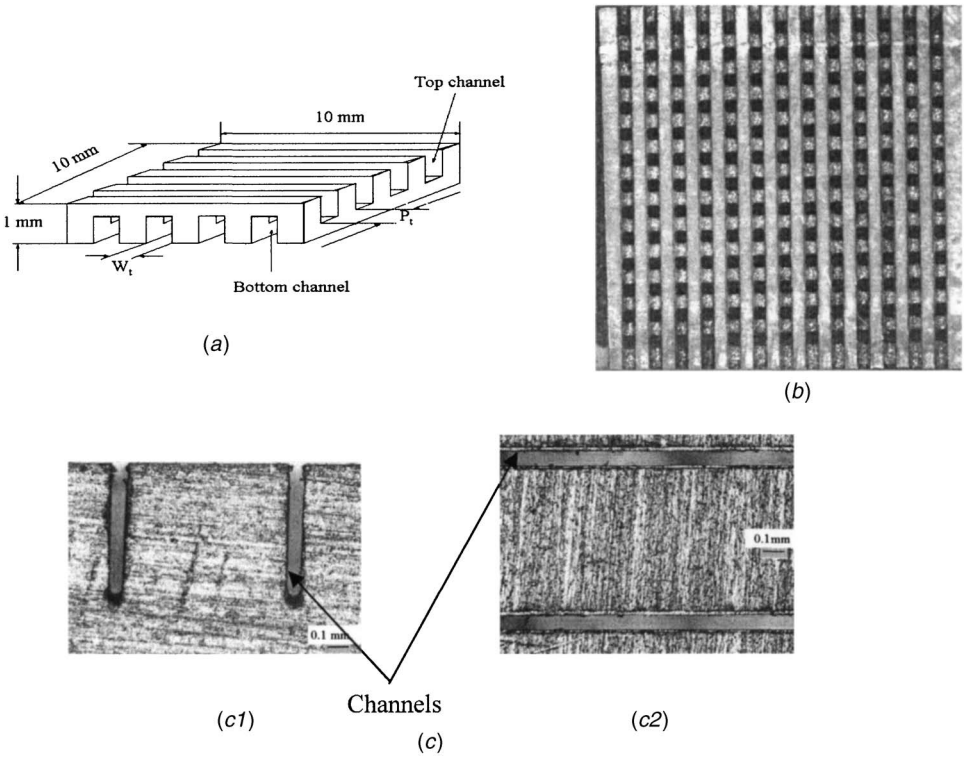

Fig. 1 Enhanced structures used in this study. (a) Sketch illustrating microchannels on the top and bottom faces. (b) Pore formation at the intersection of microchannels. Top view of structure C-0.360-0.7 is shown. (c) Magnified (50 *X*) pictures of the structure C-0.065-0.7. (c1) Lateral view. (c2) Top view.

water–silica slurry prior to testing. A CHF value of 105.4 W/cm^2 at a wall superheat of 90 K was obtained with saturated FC-72.

Ramaswamy [11] and Ramaswamy et al. [12] employed the type of enhanced structures proposed by Nakayama et al. [6] in a compact (50 mm$\times$50 mm$\times$40 mm) evaporator chamber of a thermosyphon loop. They investigated 0.5 mm thick silicon structures having channel widths in the range 0.090–0.320 mm and channel pitches between 0.5 and 2.1 mm. For a constant channel pitch, the heat dissipation increased with increase in the pore size, particularly at low to intermediate wall superheats (4–12 K). The single-layered silicon structures performed similarly for a wall superheat beyond 30 K. This effect was explained in light of the "dried-up" mode of boiling in a tunnel proposed by Nakayama et al. [13]. The effect of channel pitch on heat transfer performance was found to be more significant. The heat dissipation increased significantly through reduction in pitch at all superheats.

The reduction in electronic chip sizes (going down to a few square millimeters in certain applications) places a space constraint on the micro-geometric enhancement features to be provided on the cooling device. There is virtually no information on the effectiveness of enhanced structures in the range of small channel width (65–105 μm) and channel pitch (0.2–0.7 mm). While the small channel width and pitch allow an increase in pore density, it is unclear whether such an increase results in a commensurate increase in the overall heat removal capability of the structure. Therefore, the objective of this study is to investigate the effect of reduction in these geometrical dimensions on the heat transfer performance. The enhanced structure employed is similar to one proposed by Nakayama et al. [8]. Predictive correlations for the nucleate boiling regime are explored for the proper design and employment of the enhanced structures.

2 Enhanced Structures

The Hitachi Thermoexcel surface [5] has been developed and proved successful in enhancing nucleate boiling heat transfer at low heat fluxes. In order to ensure a similar good performance at the high heat fluxes encountered in electronics applications, the original Hitachi design was modified by providing rectangular fins on the external surface by Nakayama et al. [8]. The present study utilizes the same structure geometry, but with significantly smaller feature sizes than previously studied.

A schematic diagram and optical micrographs of the enhanced structures are presented in Fig. 1. The single layer structures were fabricated in copper, had an overall size of 10 mm$\times$10 mm and were 1 mm thick. Their geometrical parameters are summarized in Table 1. The structure identification code employed indicates the constitutive material (copper) followed by the channel width and channel pitch. Structures C-0.065-0.7, C-0.085-0.7, and C-0.105-0.7 were produced by employing an automated dicing saw. The cutting element consisted of nickel blades (having diamond particles embedded at the periphery) rotating at 30 000 rpm. A row of parallel microchannels was cut on the bottom surface. The top surface also had parallel microchannels aligned 90 deg to those on the bottom surface [Fig. 1(*a*)]. Since the depth of the microchannels (0.6 mm) exceeds half the thickness of the structure, an array of pores resulted at the intersections [Fig. 1(*b*)]. Wire electro-discharge machining was used to fabricate the structures C-0.360-0.7 and C-0.470-0.7.

The external surfaces of the structure were mirror-polished with fine sand paper. The roughness of the top surface was 0.15 μm [root-mean square (rms)] as measured with a profilometer. The roughness of the internal surfaces (produced by the blades in the

Table 1 Geometrical parameters of the enhanced structures

Structure identification	Channel width W_t (mm)	Channel pitch P_t (mm)	Channel depth H_t (mm)	Ratio wetted/projected areas (A_w/A)
C-0.065-0.20	0.065	0.20	0.6	8.05
C-0.065-0.35	0.065	0.35	0.6	5.21
C-0.065-0.50	0.065	0.50	0.6	4.08
C-0.065-0.70	0.065	0.70	0.6	3.26
C-0.085-0.70	0.085	0.70	0.6	3.26
C-0.105-0.35	0.105	0.35	0.6	5.12
C-0.105-0.50	0.105	0.50	0.6	4.06
C-0.105-0.70	0.105	0.70	0.6	3.26
C-0.360-0.70	0.360	0.70	0.6	3.12
C-0.470-0.70	0.470	0.70	0.6	2.97

cutting process) could not be determined exactly. Visual observation indicates that the surfaces are fairly smooth.

The effects of channel width (W_t) and channel pitch (P_t) were studied because of their significant impact on the boiling phenomena. In general, wider channels tended to be flooded with liquid at low heat fluxes, so the heat transfer performance was improved at higher heat fluxes. On the other hand, narrow channels could be choked with vapor at high heat fluxes, a fact that deteriorated the heat transfer performance. Due to the small sizes involved in electronic chips, channels around 100 μm wide are of significant practical interest.

3 Experimental Setup

The single-layered structures were included in a thermosyphon loop consisting of an evaporator chamber, connecting tubes, and a condenser (Fig. 2). The condenser is placed at a higher elevation than the evaporator to allow liquid return by gravity. The transparent evaporator chamber is made of Plexiglas and has inner dimensions of 40 mm $\times$ 40 mm $\times$ 30 mm. Four auxiliary foil heaters were placed on the inside lateral walls of the evaporator chamber to maintain the liquid pool at saturation temperature. A dielectric, inert liquid (PF 5060) was used as the working fluid. Its thermophysical properties closely match FC 72 and are available in [14].

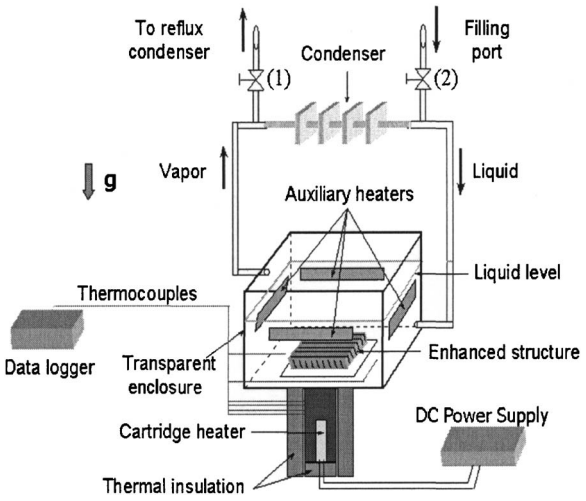

Fig. 2 Schematic of the thermosyphon loop

The liquid level in the evaporator chamber was maintained at 20 mm above the top surface of the structure under un-powered conditions. The system pressure was set at 1 atm in all the experiments by keeping the valve (1) open and value (2) closed. In an actual implementation, a thermosyphon loop will be hermetically sealed with the system operating pressure set by the level of heat input (for constant cooling conditions at the condenser). Ramaswamy et al. [15] found that the performance of a thermosyphon similar to the one employed in the present study does not depend on the internal pressure once the saturated boiling regime is reached ($q'' > 9$ W/cm^2). Therefore, by maintaining the system open to atmosphere a close simulation of the real case was reached, along with experimental convenience. The dissolved gas content (by volume) was measured with a Seaton-Wilson AD-4000 Aire-ometer. The content before charging the system (from the bottle) was 50%, decreasing to 40% after one hour of vigorous boiling and going up to 46% after cooling down (at the beginning of the run).

A plate fin condenser (11 fins) was employed to close the loop. A reflux condenser was placed at a higher elevation in order to trap any escaping vapor. The structures were attached to the heating surface using 63Sn 37Pb solder alloy. The thickness of the solder layer was $\sim$50 μm. The thin solder layer provided a strong mechanical bond with a low thermal contact resistance. An Omega cartridge heater embedded in a copper rod with square cross section (9 mm $\times$ 9 mm) was used to provide heat to the structure. To firmly fit the heater into the rod, a high temperature, high thermal conductivity paste (Omegatherm® "201," $k_{\text{eff}} = 2.31$ W/m K) was employed. In order to minimize the heat losses, the copper rod was peripherally surrounded with a glass sheath. Thermal insulation and plexiglass provided additional insulation. At the end of the rod four copper-constantan sheathed thermocouples (0.127 mm diameter) were embedded, starting from 4 mm below the enhanced structure. The thermocouples were used to calculate the surface temperature (by extrapolation) and the heat flux at the base of the enhanced structure, assuming one-dimensional heat conduction. The temperature of the liquid pool was monitored using two copper-constantan thermocouples (0.128 mm diameter). All temperatures were measured using an automated data acquisition system.

A regulated dc power supply (0–100 V, 0–0.5 A) was used to provide power to the cartridge heater. The auxiliary heaters were supplied with power from a dedicated power supply. A precision resistor (1 $\Omega \pm 0.01$ Ω) connected in series with the power supply served to measure the current. The voltage drops across the heater and the precision resistor were also measured.

4 Experimental Procedure

The working fluid was maintained at saturation (~56°C at 1 atm) throughout the experiments. For heat inputs $Q>5$ W (heat flux 4.8 W/cm^2) through the copper rod saturated conditions existed. For lower heat inputs the auxiliary heaters were employed in conjunction with the main heater to maintain saturation conditions throughout the run. Due to its unusually high air solubility, the use of PF 5060 for electronics cooling requires careful deaeration to ensure predictable thermal performance. Therefore, a degassing operation preceded every run. The system was kept open to the atmosphere, while an electrical power input of ~11 W was applied via the cartridge heater. The liquid was boiled vigorously for about one hour, and then allowed to cool down until it reached room temperature. This procedure ensured that the dissolved gas concentration was around 46% (by volume) at the beginning of every run. Bhavnani et al. [16] found that the dissolved gas content did not decrease below a certain level (39% in their case) even after several days of degassing.

The electrical power to the cartridge heater was provided in incremented or decremented steps. The power steps were 0.5 W until 2 W, 2 W until 10 and 5 W until the highest heat flux tested. The experiments were performed for power inputs resulting in a maximum temperature at the base of the enhanced structure of 85°C. It should be noted that the highest heat fluxes reported in the present paper do not represent critical heat flux values, but maximum values for which the wall temperature stays below 85°C. This has been done in light of the possible application of this study to electronics cooling. For these applications the maximum surface temperature is typically limited to 85°C. In experiments performed with decreasing heat flux, the first heat flux level was established by trial and error. Initially, the highest power input that resulted in a steady wall temperature was imposed. The surface temperature was above 85°C at this condition. The corresponding heat fluxes were 5%–10% higher than the highest values presented in this study. It is believed that the critical heat flux will be reached in this region, as also reported in [9,10]. These authors have measured both critical heat flux and heat flux at 85°C for structured surfaces in dielectric liquids. The six temperatures were monitored continuously, with readings taken after steady state was reached. After reaching steady state, temperatures were recorded for 35 min and mean values were calculated. These values were subsequently used to calculate the surface temperature and the heat input. The electrical power input was calculated by multiplying the voltage drop across the heater with the line current. The heat loss (defined as the difference between the electrical power input and the heat input) was always within 10%. The heat flux was calculated based on the surface projected area (10 mm $\times$10 mm). The experiments were performed for power inputs resulting in a maximum temperature at the base of the enhanced structure of 85°C.

5 Measurements and Uncertainty Analysis

The thermocouples and the data acquisition system were calibrated against a precision mercury thermometer at ice point to an uncertainty of 0.1 K. The precision resistor employed for current measurement was accurate to 1%. The voltage measurement uncertainty was specified by the instrument manufacturer as being 0.045% of the reading. The uncertainty in the channel width (5 μm) was due to the uneven width with the depth. The resulting maximum uncertainty in the heat flux was ±14.5% (with over 90% of the data within ±10%). The uncertainty in the wall superheat values was ±0.15 K.

Usually, after an experimental run, the structure was kept immersed under a nonboiling condition overnight. Under these conditions, the performance degraded in time due, perhaps, to variation in surface finish. The decrease in the performance was more pronounced at low heat fluxes. At the same (imposed) heat flux the day-to-day variations of the temperature measured below the surface (T_1) were within +1°C.

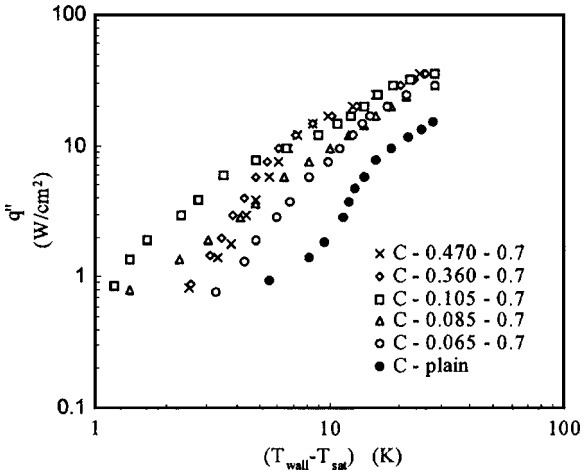

Fig. 3 Boiling curves at saturation for various channel widths

6 Influence of Channel Width on Thermal Performance

For this set of experiments the channel pitch was maintained constant at 0.7 mm. The enhancement of boiling due to the structured surfaces is obvious from the boiling curves shown in Fig. 3. The curves were obtained with decreasing heat flux, the fluid being at saturation point throughout the run. It is evident that the enhanced structures are highly efficient in promoting boiling heat transfer, especially in the low heat fluxes range ($q''<8$ W/cm^2). The superheat required to transfer a certain heat flux is reduced to nearly one fifth, at best (structure C-0.105-0.7, $q''=2$ W/cm^2). Since the wetted area is increased by only a factor of 3.26 (at most), this enhancement cannot be attributed to the increase in wetted surface area alone. The highest attained heat flux was 34.8 W/cm^2 for structure C-0.105-0.7, as opposed to 15.4 W/cm^2 for the C-plain structure.

In general, the performance improves with increase in channel width. This effect diminishes for heat fluxes exceeding 15 W/cm^2. Table 2 summarizes this enhancement. The improvement is presented relative to the plain structure for heat fluxes less than 15 W/cm^2. For 15 W/cm$^2<q''<29$ W/cm^2 the reference is structure C-0.065-0.7. Since the maximum heat flux applied to the structure C-0.065-0.7 is $q''=29$ W/cm^2, data for $q''>29$ W/cm^2 were not included in Table 2. It is noted that structures C-0.065-0.7 and C-0.085-0.7 perform similarly within the heat flux range 10–29 W/cm^2, within experimental uncertainty. The same observation can be made about structures C-0.360-0.7 and C-0.470-0.7 for heat fluxes 12 W/cm$^2<q''<35$ W/cm^2.

Three distinct regions can be delineated from Fig. 3: For low heat fluxes $q''=1-10$ W/cm^2 the structure C-0.105-0.7 displays the best performance. For intermediate heat fluxes $q''=10-25$ W/cm^2 the structures C-0.360-0.7 and C-0.470-0.7 show better heat transfer characteristics. For high heat fluxes $q''=25-35$ W/cm^2 the structures perform similarly. Two observations can be made from the data shown in Fig. 3. First, no decrease in performance was present in the high heat flux region. For their porous structures, Nakayama et al. [13] noted a decrease in performance for heat fluxes larger than 15 W/cm^2, the boiling curves of the porous structures converged towards the boiling curve of the plain surface. This decrease in performance was attributed to the "dried-up" mode of boiling. It was hypothesized that the structure will revert towards the plain surface behavior once the tunnel space is filled with vapor. For the present struc-

Table 2 Relative enhancement (percentage) in heat dissipation compared to a plain surface for the enhanced structures with P_t=0.7 mm

q'' (W/cm^2)	C-0.065-0.7	C-0.085-0.7	C-0.105-0.7	C-0.360-0.7	C-0.470-0.7
2	96	206	513	188	151
4	80	143	343	188	153
6	71	115	311	194	157
8	62	91	224	195	161
10	69	81	180	200	184
15	93	85	141	214	218
20			25	38	43
25			33	33	34
29			49	38	42

tures no such trend was noticed. It must be noted that the construction of the present structures lets the top finned face open to the liquid pool [see Fig. 1(*a*)]. This feature is believed to be the reason for the superior heat transfer performance over the entire range of heat fluxes.

Second, the performance of the enhanced structures does not deteriorate even for the largest channel tested (0.47 mm), over the entire range of heat fluxes tested. In the low heat flux region (q'' <10 W/cm^2) the flooded mode may take place for larger channel widths, decreasing the heat transfer coefficient. A change in slope occurs at around 10 W/cm^2 indicating a change in the boiling mode. The superior performance in the intermediate and high heat flux regions is believed to be due again to the presence of fins on the external surface. The fins provide separation of the vapor columns emerging from adjacent channels. This delays the formation of the vapor blanket above the structure and pushes the onset of film boiling toward higher heat fluxes.

Although performing better than the plain structure, the enhanced structure with the narrowest channels (C-0.065-0.7) displays the least amount of enhancement over the entire range of tested heat fluxes. This behavior is linked to the geometry in the following way. The small channel width results in inadequate communication between the bottom and top channels, as well as between the top channels and the surrounding liquid pool.

Figure 4 compares the performance of enhanced structures with that of the plain structure when the heat flux is computed based on the total wetted area. It is clear from this figure that the enhancement is not a result of the increased surface area. However, in the high heat flux region, the effective enhancement is reduced as the data come closer together.

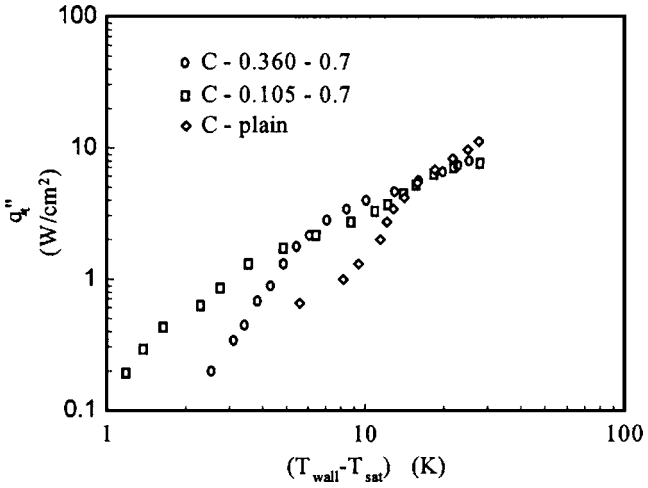

Fig. 4 Boiling curves based on total surface area

Very few data are available for the structured surface-coolant combination employed in this study. Ramaswamy et al. [12] studied the same type of enhanced structure with the same working fluid. However, the majority of their data were taken with structures made of silicon and having a 0.5 mm overall thickness. Their copper structures had larger channel widths (see Table 3) due to limitations of their fabrication methods. The data of Nakayama et al. [8] are for a similar but larger channel width structure and a different coolant (R-11), whereas the data of Nakayama et al. [4] and Chien and Webb [7] refer to structures similar to the Hitachi Thermoexcel-E.

The geometrical parameters of the structures used in prior related studies are summarized in Table 3. From Fig. 5 it can be seen that the structure C-0.105-0.5 exhibits good performance over a wide range of heat fluxes. As pointed out by Nakayama et al. [8], the working fluid influences the heat transfer performance of the enhanced structures greatly. In general, the refrigerants (h_{fg}=147 kJ/kg for R-113) tend to produce better heat transfer performance than the fluorocarbons (h_{fg}=88 kJ/kg for PF 5060). This can explain the superior performance exhibited by the porous surface [4] in the low heat flux range. Another factor is believed to be the higher channel width (0.2 and 0.25 mm). The structure C-0.200-0.5 (Ramaswamy et al. [12]) displays the best heat transfer performance for heat fluxes in excess of 11 W/cm^2. The highest attainable heat flux was 61.2 W/cm^2 at a wall superheat of 31°C. In addition to the larger channel width, the data in [12] were obtained using a slightly different heater assembly ([11]) resulting in higher conductive heat spreading.

Table 3 Geometrical parameters of the structures presented in Fig. 5

Authors	Nakayama et al. (1980) [4]	Nakayama et al. (1984) [8]	Chien and Webb (1998) [7]	Ramaswamy et al.(2003) [12]
Fluid	R-11	R-11	R-11	FC-72
W_t (mm)	0.25	0.25	0.4	0.2, 0.27
P_t (mm)	0.55	0.55	0.73	0.5, 0.63
H_t (mm)	0.4	0.55	0.5	0.55
d_p (mm)	0.1	0.25	0.12	0.2,0.27
P_p (mm)	0.7	0.55	0.75	0.5, 0.63

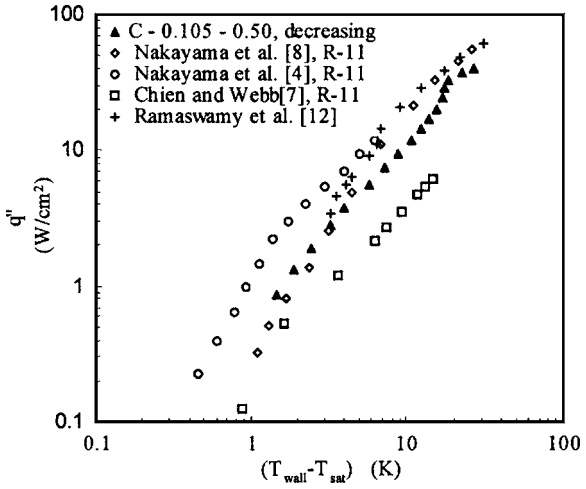

Fig. 5 Boiling performance of structure C-0.105-0.5 compared with existing data

7 Channel Pitch Effect

The effect of varying the channel pitch was investigated for two channel widths: 65 and 105 μm. The ranges investigated were 0.2–0.7 mm for the 65 μm wide channel and 0.35–0.7 mm for the 105 μm wide channel. By reducing the pitch, the area of the structure wetted by the liquid increases up to a maximum of ~8 times of that of the plain surface. Therefore, the heat transfer performance is expected to increase over the entire range of heat fluxes.

The boiling curves for the channel width of 65 μm are presented in Fig. 6. The structure C-0.065-0.2 exhibits the best heat transfer performance up to 28 W/cm^2. Beyond that, the slope of the boiling curves changes, signaling deteriorating performance for all the structures tested. The maximum heat flux of 34 W/cm^2 at a wall superheat of 28.3 K was attained with structure C-0.065-0.35. The improvement showed by the structure C-0.065-0.5 over structure C-0.065-0.7 is only marginal up to a heat flux of ~17 W/cm^2. For $q'' > 17$ W/cm^2 the improvement is significant. The enhancement is summarized in Table 4.

A deviation from the expected behavior occurs in the case of 0.105 mm channel width. The results are presented in Fig. 7. In the low heat flux region ($1 < q'' < 12$ W/cm^2) the best performance is shown by the structure with the largest channel pitch (C-0.105-0.7). A second region ($12 < q'' < 25$ W/cm^2) is characterized by a similar performance for the structures C-0.105-0.5 and C-0.105-0.7, with a slightly higher boiling curve for the structure C-0.105-0.35. Finally, the last region ($q'' > 25$ W/cm^2) exhibits a clear differentiation between the structures, with the expected hierarchy in performance (the smaller the channel pitch, the better the performance). The boiling curve for structure C-0.105-0.35 presents an almost vertical portion (for $25 < q'' < 35$ W/cm^2). The maximum heat flux dissipated was 43 W/cm^2 at a wall superheat of 24.4°C.

Ramaswamy et al. [12] found that, in general, a smaller channel pitch resulted in a better heat transfer performance. The exception was constituted by the structure with a 1.4 mm channel pitch. For a wall superheat of around 15 K this structure dissipated less heat than a structure with a 2.1 mm channel pitch. The authors attributed this phenomenon to a difference in surface areas participating in boiling. For the 2.1 mm channel pitch structure the entire channel network contributed to boiling, whereas for the 1.4 mm channel pitch structure just the pores were active.

Table 4 Heat transfer enhancement (percentage) relative to the structure C-0.065-0.7

q'' (W/cm^2)	C-0.065-0.2	C-0.065-0.35	C-0.065-0.5
5	166	64	7
10	97	58	9
15	78	25	4.5
20	74	35	19.4
25	77	46	33
29	89	63	42

8 Hysteresis Effect

Nakayama et al. [8] reported that the hysteresis shown by the porous and microfinned surfaces is more pronounced than for the plain surfaces. The hysteresis effect induced by the enhanced structures employed in this study is presented in Figs. 8 and 9. Similar to the plain structure, the boiling curve for structure C-0.065-0.7 (Fig. 8) presents insignificant hysteresis. The intermediate channel size structure (C-0.085-0.7) exhibits a more pronounced hysteresis (from the boiling incipience up to ~15 W/cm^2). Structure C-0.105-0.7 shows significant hysteresis at the boiling incipience. After this initial region the two curves almost coincide.

A peculiar phenomenon is observed for structures C-0.105-0.5 and C-0.105-0.35. As illustrated in Fig. 9 for structure C-0.105-0.35, the boiling curves show the expected hysteresis behavior at

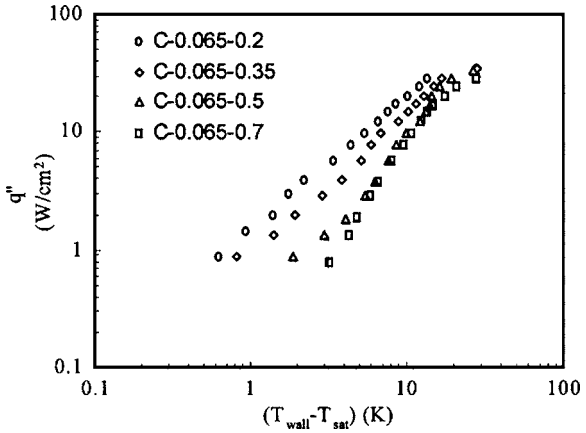

Fig. 6 Effect of channel pitch on boiling heat transfer (W_t =65 μm)

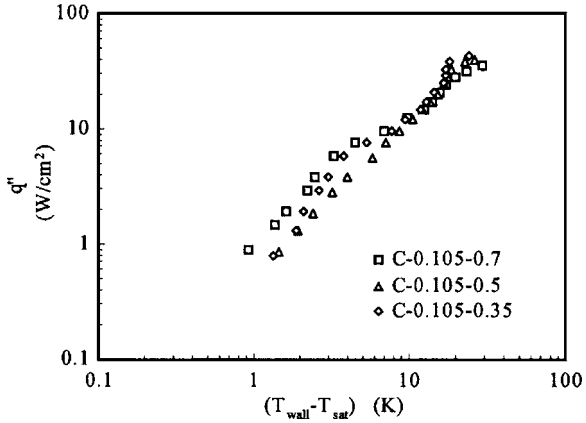

Fig. 7 Effect of channel pitch on boiling heat transfer (W_t =105 μm)

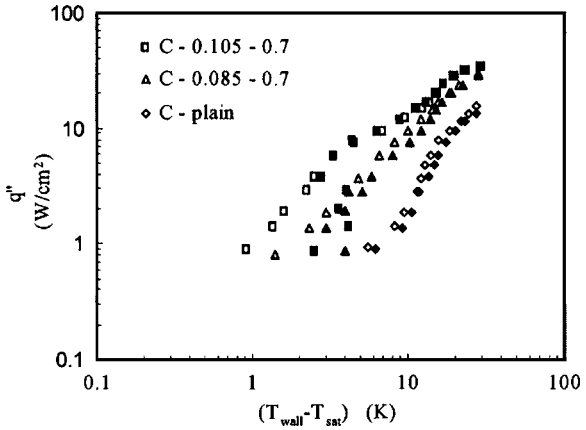

Fig. 8 Hysteresis of boiling curves for different channel widths. The solid symbols correspond to increasing heat fluxes and open symbols to decreasing heat fluxes

boiling incipience: The boiling curves taken with increasing heat flux are to the right of those constructed with decreasing heat flux. However, a "reverse" hysteresis was present in the heat fluxes range 4–20 W/cm^2 (well into the established boiling region of the nucleate boiling curve). This is true for all the structures but is particularly noticeable for C-0.105-0.5 and C-0.105-0.35. For heat fluxes beyond 20 W/cm^2 this effect diminishes. Arshad and Thome [6] reported a similar behavior of the boiling curves for water. The structures employed in their study had rectangular, triangular, and circular cross-section subsurface channels connected with the liquid pool through pores of diameters 0.18 and 0.25 mm. Kovalev et al. [17] reported the same phenomenon for porous coatings. They hypothesized that a vapor layer forms at the base of the porous structure at high heat fluxes that insulates the base and deteriorates the heat transfer. If the heat flux is not raised above this threshold level then there is no hysteresis. It is believed this explanation for porous coatings may apply for the present structures as well.

9 Correlation of Boiling Data

As noted by previous researchers, any attempt to establish a physics based predictive correlation of heat transfer data for enhanced structures should begin with the identification of the heat transfer modes operating inside the structure. While physics based models for specific sub-regimes have been developed [4,11], they do not apply to the large range of superheats encountered in applications.

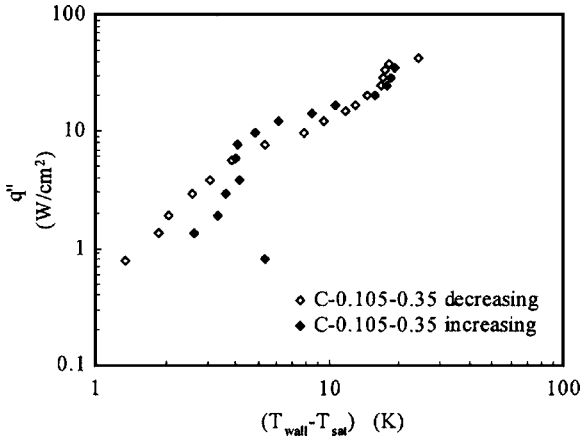

Fig. 9 Hysteresis effect for structure C-0.105-0.35

Table 5 Coefficient *C* and exponent *n* for the enhanced structures with $W_t<100$ μm

Structure identification	C	n	Heat flux range (W/cm^2)
C-plain	0.1098	1.2387	$0.9 < q'' < 2.1$
	5×10^{-5}	4.461	$2.1 < q'' < 4.8$
	0.0126	2.3189	$4.8 < q'' < 8.5$
	0.3285	1.1589	$8.5 < q'' < 15.4$
C-0.065-0.70	0.0716	2.0449	$0.7 < q'' < 14.6$
	1.2685	0.9503	$14.6 < q'' < 28.9$
C-0.065-0.50	0.477	0.9687	$0.9 < q'' < 2$
	0.1144	1.9052	$2 < q'' < 24.6$
	5.0063	0.5769	$24.6 < q'' < 33$
C-0.065-0.35	0.9061	1.1950	$0.9 < q'' < 28.6$
	10.514	0.3544	$28.6 < q'' < 34.2$
C-0.065-0.20	0.4885	1.1162	$0.9 < q'' < 28.4$
	15.064	0.2412	$28.4 < q'' < 33.8$
C-0.085-0.70	0.4823	1.2865	$0.8 < q'' < 23$
	2.4411	0.7453	$23 < q'' < 29.4$

If a correlation of the usual simplified form:

$$q'' = C \cdot (\Delta T)^n \tag{1}$$

is sought, the coefficient C ($W/cm^2 \cdot K^{-n}$) and the exponent n should depend on the working fluid, structure geometry (channel width and pitch), as well as the level of heat flux (boiling mode from the structure).

In the present study, a multiline power-law curve fit of the data (155 experimental points) is performed to approximate the boiling curves of the enhanced structures. The results are presented in Tables 5 and 6. Table 7 provides more approximate single line fits to the data for each of the structures tested, in addition to the piecewise linear fits in Tables 5 and 6. The present curve fits are intended to provide empirical relations to represent thermal performance over the entire nucleate boiling regime.

9.1 Structures With 65 μm$< W_t <$105 μm. The boiling curves can be approximated by linear segments for the tested range of heat fluxes. In general, two segments suffice for the linearization of the boiling curves. Close to the highest heat flux a decrease in the slope of the boiling curves can be detected. This signals the proximity of the critical heat flux. The decrease in channel pitch P_t for the structures with $W_t=65$ μm results in increased thermal performance (see Fig. 6). This is reflected in the values of C and n (Table 7). While the coefficient C increases from 0.1173 to 1.5844, the exponent n follows the opposite trend: it decreases from 1.7787 to 1.0476.

9.2 Structures With 105 μm$< W_t <$470 μm. The values of C and n for the structures with larger channel widths tested (105, 360, and 470 μm) are summarized in Tables 6 and 7. For structures with $W_t=105$ μm, multiple linear segments have to be used. Particularly noticeable is the presence of a steep portion before the decline in the heat transfer coefficient. The slope of this curve increases with the increase in the channel pitch, reaching a value

Table 6 Coefficient C and exponent n for the enhanced structures with 105 μm $< W_t <$ 470 μm

Structure identification	C	n	Heat flux range (W/cm^2)
C-0.105-0.70	0.9746	1.4506	$0.9 < q'' < 6$
	2.6231	0.6801	$6 < q'' < 15$
	0.0931	1.9645	$15 < q'' < 25$
	7.0747	0.4736	$25 < q'' < 34.9$
C-0.105-0.50	0.4901	1.5132	$0.8 < q'' < 3$
	0.6765	1.2254	$3 < q'' < 20$
	0.0006	3.7456	$20 < q'' < 33$
	6.9838	0.5324	$33 < q'' < 39.6$
C-0.105-0.35	0.4517	1.4506	$0.8 < q'' < 6$
	2.7993	0.6002	$6 < q'' < 10$
	0.6956	1.2558	$10 < q'' < 25$
	2×10^{-12}	10.647	$25 < q'' < 34$
	11.831	0.4035	$34 < q'' < 43$
C-0.360-0.70	0.0561	2.907	$0.9 < q'' < 10$
	2.6151	0.7995	$10 < q'' < 35.25$
C-0.470-0.70	0.163	1.7854	$0.8 < q'' < 2$
	0.0381	2.9145	$2 < q'' < 14$
	2.8393	0.7786	$14 < q'' < 34.9$

Table 7 Coefficient C and exponent n for the enhanced structures over the entire nucleate boiling regime

Structure identification	C	n	Heat flux range (W/cm^2)
C-plain	0.0293	1.9366	$0.9 < q'' < 15.4$
C-0.065-0.20	1.5844	1.0476	$0.9 < q'' < 33.8$
C-0.065-0.35	0.9486	1.1566	$0.9 < q'' < 34.2$
C-0.065-0.50	0.2532	1.5593	$0.9 < q'' < 33$
C-0.065-0.70	0.1173	1.7787	$0.7 < q'' < 28.9$
C-0.085-0.70	0.5006	1.2608	$0.8 < q'' < 29.4$
C-0.105-0.35	0.7335	1.2878	$0.8 < q'' < 43$
C-0.105-0.50	0.5583	1.3303	$0.8 < q'' < 39.6$
C-0.105-0.70	1.2493	1.0284	$0.9 < q'' < 34.9$
C-0.360-0.70	0.4168	1.4835	$0.9 < q'' < 35.3$
C-0.470-0.70	0.2969	1.6163	$0.8 < q'' < 34.9$

of 10.647 for a 0.35 mm pitch. No clear trend can be detected for the values of C and n (see Table 7). At the high end of the tested channel widths (W_t=360 μm and W_t=470 μm) the boiling curves become linear again, although with a different slope.

9.3 Discussion. Nakayama et al. [13] hypothesized the presence of three modes of boiling from a subsurface channel. The modes were coined "flooded" (for the large channel sizes at low heat fluxes), "suction-evaporation" and "dried-up" (likely to be present at high heat fluxes on a surface with small pores). The authors assumed that the different boiling modes inside the channels should reflect on the shape of the boiling curves. From their boiling curves, Nakayama et al. [13] noticed that the exponent n decreases with increase in the diameter of the pores. They also found that, for a constant pore diameter, n decreases as the population density increases. It was concluded that on a surface having small pores or reduced density of pores, the mechanism of heat transfer approaches the one existent in plain surface boiling. As the dried-up mode prevails, the exponent n approaches that for the plain surface. On the other hand, smaller values of n indicate the predominance of heat transfer inherent to the structured surfaces. Also of interest is the relative invariance of n with the system pressure.

The boiling curves obtained for structures with small channel widths (W_t=65 μm and W_t=85 μm) and different channel pitches, do not display a significant variation in shape across the nucleate boiling regime. Therefore, the possible modes of boiling are not reflected in the shape of the boiling curves. The "dried-up" boiling mode, expected to occur at high heat fluxes, is not present. As the channel pitch decreases, the exponent n decreases as well, similar to the findings of Nakayama et al. [13].

On the other hand, the shape of the boiling curves in the case of larger channel widths (W_t=105 μm, W_t=360 μm, and W_t=470 μm) indicates the presence of different boiling regimes from the structures. As for the "flooded" mode, the data obtained in the present study do not indicate a sharp decline in heat transfer performance even for the largest channel width tested (W_t=470 μm) and for $q'' < 2$ W/cm^2.

The above differences between the findings of this study and the hypotheses of Nakayama et al. [13] can be explained in light of the differences between the enhanced structures employed in the two studies. The structures employed in this study have an array of microfins on the outside surface, bounding the pores. The morphology of the structures permits the communication with the surrounding liquid pool through continuous channels rather than discrete pores. This is probably the reason why the "dried-up" mode does not seem to occur. This feature of the present surface is believed to be responsible for the superior performance of the structure in the high heat fluxes region, making it suitable for employing in electronics cooling.

10 Conclusions

The following conclusions can be drawn from the present study:

1. The enhanced structures employed in this study show superior heat transfer performance in comparison with the plain surface. This type of enhanced structures is highly efficient in promoting boiling heat transfer, especially in the low heat fluxes range (q''=1–8 W/cm^2). The superheat required to transfer a certain heat flux is reduced to nearly one-fifth, at best.

2. In general, the performance of the enhanced structure increases with the increase of the channel width. This effect is more pronounced in the low to intermediate heat fluxes range (1–10 W/cm^2). At higher heat flux levels (more than 15 W/cm^2) this effect diminishes, ultimately disappearing.

3. The channel pitch has a large influence on the boiling performance of the enhanced structures. For the 65 μm channel

width, the pitch reduction improves the performance at all heat fluxes (except the highest). For the 105 μm channel width, the improvement is significant only beyond $q'' \sim 25$ W/cm^2.

4. The best thermal performance is obtained with structure C-0.065-0.2 for $q'' < 30$ W/cm^2 and with structure C-0.105-0.35 for $q'' > 30$ W/cm^2.

5. A simple multiline curve fit along with a more approximate single line curve fit is provided as an empirical predictive correlation for the enhanced structures.

6. The modes of boiling from an enhanced structure proposed by Nakayama et al. [13] were unable to explain the boiling curves obtained in this study. The present data are explained in light of the contribution from the top finned surface of the enhanced structure.

Acknowledgments

This study was supported by Semiconductor Research Corporation contract 649.001 and Defense Advanced Research Projects Agency HERETIC Program under contract N00164-99-C-0039. The authors want to acknowledge Professor Sushil Bhavnani from Auburn University for facilitating the air concentration measurement.

Nomenclature

A = total external area of the structure (projected) (m^2)
A_w = structure wetted area (m^2)
C = coefficient in Eq. (1) ($W/\text{cm}^2 \cdot K^{-n}$)
d_p = pore diameter (m)
g = acceleration due to gravity (m/s^2)
h_{fg} = latent heat of vaporization (kJ/kg)
H_t = channel depth (m)
n = exponent of ΔT_w in Eq. (1)
P_p = pore pitch (m)
P_t = channel pitch (m)
q'' = heat flux based on projected surface area (W/cm^2)
q''_t = heat flux based on total surface area (W/cm^2)
Q = heat dissipation (W)
T_{sat} = saturation temperature of liquid, PF 5060 (K)
T_{wall} = temperature at base of enhanced structure (K)
W_t = channel width (m)
ΔT_w = wall superheat (K)

References

[1] Thome, J. R., 1990, *Enhanced Boiling Heat Transfer*, Hemisphere, New York.
[2] Webb, R. L., 1994, *Principles of Enhanced Heat Transfer*, Wiley, New York.
[3] O'Connor, J. P., and You, S. M., 1995, "A Painting Technique to Enhance Pool Boiling Heat Transfer in Saturated FC-72," ASME J. Heat Transfer, **117**, pp. 387–393.
[4] Nakayama, W., Daikoku, T., Kuwahara, H., and Nakajima, T., 1980, "Dynamic Model of Enhanced Boiling Heat Transfer on Porous Surfaces, Part I: Experimental Investigation," ASME J. Heat Transfer, **102**, pp. 445–450.
[5] Fujie, K., Nakayama, W., Kuwahara, H., and Kakizaki, K., 1977, "Heat Transfer Wall for Boiling Liquids," U.S. Patent 4,060,125.
[6] Arshad, J., and Thome, J. R., 1983, "Enhanced Boiling Surfaces: Heat Transfer Mechanism and Mixture Boiling," *Proceedings of ASME-JSME Thermal Engineering Joint Conference*, 1, pp. 191–197.
[7] Chien, L-H., and Webb, R. L., 1998, "A Parametric Study of Nucleate Boiling on Structured Surfaces, Part II: Effect of Pore Diameter and Pore Pitch," ASME J. Heat Transfer, **120**, pp. 1049–1054.
[8] Nakayama, W., Nakajima, T., and Hirasawa, S., 1984, "Heat Sink Studs Having Enhanced Boiling Surfaces For Cooling of Microelectronic Components," ASME Paper No. 84-WA/HT-89.
[9] Anderson, T. M., and Mudawar, I., 1989, "Microelectronic Cooling by Enhanced Pool Boiling of a Dielectric Fluorocarbon Liquid," ASME J. Heat Transfer, **111**, pp. 752–759.
[10] Mudawar, I., and Anderson, T. M., 1993, "Optimization of Enhanced Surfaces for High Flux Chip Cooling by Pool Boiling," ASME J. Electron. Packag., **115**, pp. 89–100.
[11] Ramaswamy, C., 1999, "A Compact Two-Phase Thermosyphon Employing Microfabricated Boiling Enhancement Structures," Ph.D. dissertation, University of Maryland at College Park, MD.
[12] Ramaswamy, C., Joshi, Y., Nakayama, W., and Johnson, W. B., 2003, "Effects of Varying Geometrical Parameters on Boiling From Microfabricated Enhanced Structures," ASME J. Heat Transfer, **125**, pp. 103–109.
[13] Nakayama, W., Daikoku, T., and Nakajima, T., 1982, "Effects of Pore Diameters and System Pressure on Saturated Pool Nucleate Boiling Heat Transfer from Porous Surfaces," ASME J. Heat Transfer, **104**, pp. 286–291.
[14] 3M Company, 1995, Specialty Fluids Newsletter, Vol. 1, No. 1.
[15] Ramaswamy, C., Joshi, Y., Nakayama, W., and Johnson, W. B., 1998, "Combined Effects of Sub-Cooling and Operating Pressure on the Performance of a Two-Chamber Thermosyphon," *Proceedings of the 6th Intersociety Conference on Thermal and Thermomechanical Phenomena in Electronic Systems*, pp. 349–355.
[16] Bhavnani, S., Fournelle, G., and Jaeger, R. C., 2000, "Immersion-Cooled Heat Sinks for Electronics: Insight from High-Speed Photography," *Proceedings of the 7th Intersociety Conference on Thermal and Thermomechanical Phenomena in Electronic Systems*, Vol. 2, pp. 310–311.
[17] Kovalev, S. A., Solov'yev, S. L., and Ovodkov, O. A., 1987, "Liquid Boiling on Porous Surfaces," Heat Transfer-Sov. Res., **19**(3), pp. 109–120.

Additive Adsorption and Interfacial Characteristics of Nucleate Pool Boiling in Aqueous Surfactant Solutions

Juntao Zhang

Raj M. Manglik[1]
ASME Fellow
e-mail: Raj.Manglik@uc.edu

Thermal-Fluids and Thermal Processing Laboratory,
Department of Mechanical, Industrial and Nuclear Engineering,
University of Cincinnati,
Cincinnati, OH 45221-0072

Interfacial phenomena and ebullient dynamics in saturated nucleate pool boiling of aqueous solutions of three surfactants that have different molecular weight and ionic nature are experimentally investigated. The additive molecular mobility at interfaces manifests in a dynamic surface tension behavior (surfactant adsorption–desorption at the liquid–vapor interface), and varying surface wetting (contact angle) with concentration (surfactant physisorption at the solid–liquid interface). This tends to change, enhance, and control the boiling behavior significantly, and an optimum heat transfer enhancement is obtained in solutions at or near the critical micelle concentration (CMC) of the surfactant. Furthermore, wettability (contact angle) is observed to be a function of the molecular makeup of the reagent, and shows distinct regions of change along the adsorption isotherm that are associated with the aggregation mode of adsorbed ions at the solid–water interface. This distinguishably alters the ebullience from not only that in pure water, but also between pre- and post-CMC solutions. Increased wetting tends to suppress nucleation and bubble growth, thereby weakening the boiling process.
[DOI: 10.1115/1.1924626]

Introduction

Surfactants have a unique long-chain molecular structure composed of a hydrophilic head and a hydrophobic tail. Based on the nature of the hydrophilic part of the molecule, which is ionizable, polar, and polarizable, surfactants are generally categorized as anionics, nonionics, cationics, and zwitterionics [1]. They all have a natural tendency to adsorb at surfaces and interfaces when added in low concentrations in water. With nucleate phase-change and ebullience in their aqueous solutions, or an association colloid system [solutions where molecules of surface-active agents are associated together to form small aggregates (micelles) in water, and the aggregates tend to adopt an ordered structure [2]], the reagent molecular dynamics affects the two interfaces illustrated in Fig. 1 as follows:

(1) Surfactant adsorption–desorption at the vapor–liquid interface alters the surface tension, which decreases continually with increasing concentrations until the critical micelle concentration (CMC) [concentration at which micelles (colloid-sized clusters or aggregates of monomers) start to form] is reached. This surface tension relaxation is a diffusion-rate dependent process, which typically depends on the type of surfactant, its diffusion-adsorption kinetics, micellar dynamics, ethoxylation, and bulk concentration levels [3].
(2) The physisorption of surfactant molecules at the solid–liquid interface changes the surface wetting behavior. With increasing concentration, the resulting adsorption isotherm and surface state can be divided into four regimes [4]: (a) low-concentration adsorption as individual ions; (adsorption takes place with polar heads of the surfactant ions oriented toward the surface that yields a hydrophobic surface with most surfactants except for high molecular weight ones, whose bulky polar head would occupy a larger surface area.) (b) sharp increase in the adsorption density due to self-association of adsorbed surfactant ions and the formation of hemimicelles; (c) adsorption as reverse hemimicelles, with their polar heads oriented both toward the surface and liquid, to render the surface increasingly hydrophilic; and (d) as the CMC is approached, the adsorption becomes independent of the bulk concentration, and the surfactant molecules form a bilayer on the surface to make it strongly hydrophilic.

Furthermore, and as also pointed out by Hoffmann and Rehage [5], dilute solutions of both ionic and nonionic surfactants usually behave as Newtonian liquids, and their viscosity is always close to that of the solvent (The measured shear-rate and temperature-dependent viscosity in this study, though not presented here, showed insignificant change from that for water [6].)

Small amounts of surfactant additives in water tend to change and enhance the boiling heat transfer of the solution by modifying nucleation and the concomitant bubble dynamics. The importance of enhanced nucleate boiling heat transfer has been widely recognized [7–9], and a recent review of studies on enhanced pool boiling in aqueous surfactant solutions has been provided by Wasekar and Manglik [10] with a more complete chronological listing of the available literature given by Zhang and Manglik [11]. For boiling in pure liquids, a variety of different parameters and mechanisms have been proposed to describe the complex behavior [12,13]. The potential mechanisms that affect nucleate boiling in aqueous surfactant solutions have been outlined as a conjugate problem involving the heater, liquid pool, and their interface by Zhang and Manglik [14]. Besides the effects of heater geometry, its surface characteristics and wall heat flux level, the bulk concentration of surfactant and its chemistry (ionic nature and molecular weight), dynamic surface tension, surface wetting and nucleation cavity distribution, marangoni convection, surfactant adsorption and desorption, and foaming are considered to have a significant influence [11,15,16]. Also, the bubble dynamics (inception and gestation → growth → departure), with reduced de-

[1]Author to whom all correspondence should be addressed.

Contributed by the Heat Transfer Division for publication in the JOURNAL OF HEAT TRANSFER. Manuscript received May 4, 2004; Final manuscript received January 10, 2005. Review conducted by: Jacob Chung.

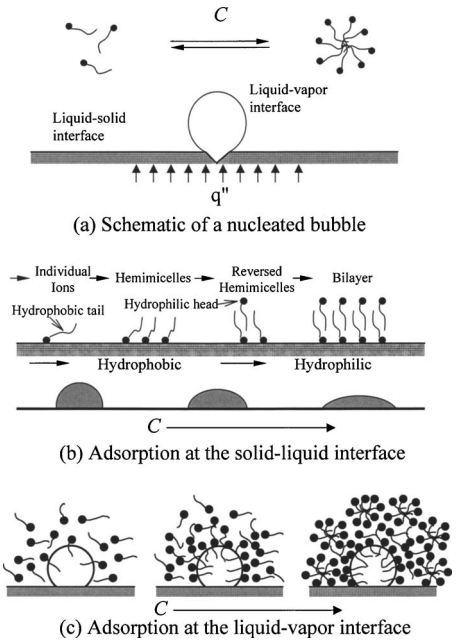

Fig. 1 Schematic of interfacial phenomena in aqueous surfactant solutions (not to scale)

parture diameters, increased frequencies, and decreased coalescence, is substantially altered [14–18]. A direct correlation of the heat transfer with suitable descriptive parameters for these effects, however, is difficult because of the complex nature of the problem. A few recent attempts have been made [14,17,18] to correlate the nucleate boiling heat transfer for aqueous surfactant solutions, but the adopted methodologies have significant limitations, and their general applicability is not established.

Wen and Wang [19] modified the pure-fluid Mikic–Rohsenow [21] correlation with limited available contact angle and surface tension data to represent their own boiling data. However, equilibrium surface tension at room temperature, rather than the dynamic effects, and that too without stipulating the level of concentration has been used in their analysis. Because a single concentration value seems to be the implicit guiding factor in its applicability, a generalization of the correlation is circumscribed. Sher and Hetsroni [20] considered a surfactant diffusion mechanism for both the liquid–vapor and solid–liquid surface tensions, and proposed a model based on the Rohsenow [22] correlation. Acceptable agreement with their own data for pre-CMC solutions is shown, and that too for only one surfactant (Habon G). No data for post-CMC solutions were presented, and it was speculated that the diffusion and adsorption mechanisms might be altered in such a case. It should be noted, however, that at low concentrations the adsorption process is generally in the monolayer region, which will not lend to drastic wetting changes on the heater surface [4,14]; wettability is essentially governed by the concentration of a particular reagent and its adsorption process at the solid–liquid interface. Furthermore, nucleate boiling heat transfer is also influenced by variations in the surfactant chemistry. Wasekar and Manglik [16] considered the effect of surfactant molecular weight and ionic nature on the pool boiling performance of water, and pointed out that dynamic surface tension is perhaps a critical predictor of the ebullient phase-change behavior. However, rather simplistically, the value of σ at a fixed bubble frequency or surface age τ was adopted to represent the dynamic surface tension effects.

This study explores the role of surfactant adsorption and interfacial phenomena, manifest in a dynamic surface tension relaxation due to the dynamic adsorption–desorption process at the liquid–vapor interface, and the surface wettability changes due to surfactant physisorption at the solid–liquid interface, on nucleate boiling heat transfer. Aqueous solutions with concentrations $C \leqslant$ CMC and $C >$ CMC of three surfactants are considered, namely, sodium dodecyl sulfate (SDS, anionic, $M=288.3$), cetyltrimethyl ammonium bromide (CTAB, cationic, $M=364.5$), and octylphenoxy plyethoxy ethanol (Triton X-305, nonionic, $M=1526$). They have different molecular weights and ionic nature, and their chemical composition and relevant physico-chemical properties are listed in Table 1. To characterize their vapor–liquid and solid–liquid interfacial behaviors, variations with concentration in both the dynamic and equilibrium surface tension of their solutions as well as those in the contact angle (measure of surface wetting) are recorded. Pool boiling curves ($q''_w \propto \Delta T_{sat}$) for incipience to fully-developed nucleate boiling regimes are presented, along with a photographic documentation of the ebullient activity on a cylindrical heater surface. An extended discussion of these results highlights the influences of the additive chemistry, pre- and postmicellar bulk concentration, wall heat flux, surface wettability, and dynamic surface tension relaxation.

Pool Boling Experiment Setup

The pool boiling experiments were carried out at atmospheric-pressure saturated conditions in the apparatus shown schematically in Fig. 2(*a*). The inner glass tank, which contains the surfactant solution pool and the cylindrical heater, is encased in an outer glass tank that has circulating mineral oil fed from a constant-temperature recirculating bath (not shown in figure) to maintain the test pool at its saturation temperature. A water-cooled reflux condenser, along with a second coiled-tube water-cooled con-

Table 1 Physico-chemical properties of surfactants

Surfactant (Chemical Name)	SDS (Sodium dodecyl sulfate)	CTAB (Cetyltrimethyl ammonium bromide)	Triton X-305 (Octylphenoxy plyethoxy ethanol)
Chemical formula	$C_{12}H_{25}SO_4Na$	$C_{19}H_{42}BrN$	$C_{14}H_{21}(OCH_2CH_2)_{30}OH$
Ionic nature	Anionic	Cationic	Nonionic
EO group[a]	0	0	30
Appearance	White powder	White powder	Clear liquid
Molecular weight	288.3	364.5	1526 (average)
Manufacturer	Fisher	Sigma-Aldrich	Union Carbide
Purity	≥ 99%	≈ 99%	–
Melting point	> 206°C	> 230°C	–
Solubility (20°C)	150mg/mL	10 % (w/v)	–
Specific Gravity	0.4	–	1.095
Viscosity (cp)[b] (pure liquid)	–	–	470 (25°C)

[a] Ethoxy or ethylene oxide group
[b] Brookfield viscometer

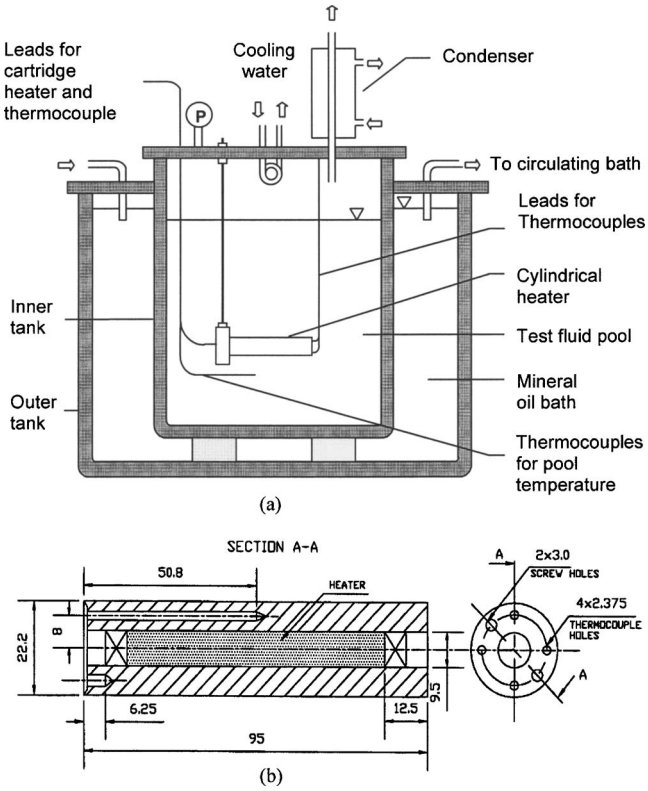

Fig. 2 Schematic of experimental facility: (a) pool boiling apparatus, and (b) cross-sectional view of cylindrical heater assembly

denser, helps condense the generated vapor and maintain an atmospheric-pressure pool. A pressure gage (±0.0025 bar precision) is mounted on top of the boiling vessel to monitor the pressure in the pool throughout the experiments. The heating test section, shown in Fig. 2(*b*), consists of a horizontal, gold plated, hollow copper cylinder of 22.2 mm outer diameter; the 0.0127 mm thick gold plating mitigates any surface degradation and oxidation from chemicals in the test fluids. A 240 V, 1500 W cartridge heater, with insulated lead wires, is press-fitted in the hollow cylinder with conductive grease to fill any remaining air gaps and provide good heat transfer to the inside of the tube. The cartridge heater is centrally located inside the copper tube, and the gaps at each end are filled with silicone rubber to prevent water contact.

The heater-wall and pool-bulk temperature measurements were recorded using copper-constantan precision (±0.5°C) thermocouples, interfaced with a computerized data acquisition system with an in-built ice junction and calibration curve. A variac-controlled ac power supply, a current shunt (0.15 Ω with 1% accuracy), and two high-precision digital multimeters (for current and voltage measurements) provided the controls and measurements of the input electric power. At each incremental value of power input or heat load, the dissipated wall heat flux q''_w and the wall superheat ΔT_w were computed from the measured values of V, I, the four wall thermocouple readings ($T_{i,r}$), and saturation temperature of the pool from the following set of equations:

$$q''_w = (VI/A) \tag{1}$$

$$T_w = \frac{1}{4}\sum_{i=1}^{4} [T_{i,r} - (q''_w r_o/k)\ln(r_o/r)] \tag{2}$$

$$\Delta T_w = (T_w - T_{\text{sat}}) \tag{3}$$

The maximum experimental uncertainties in q''_w and ΔT_w, based on a propagation of error analysis [23], were ±1.44% and ±0.5%, respectively. Details of the experimental procedure, uncertainty analysis, and the extended validation of test measurements with boiling data for water are given by [24].

Surface Tension and Contact Angle Measurement

Surface tension measurements were made by the maximum bubble pressure method using a twin orifice computerized surface tensiometer (SensaDyne QC6000, CSC Scientific Company). Dry air at 3.4 bar is slowly bubbled through a parallel set of small and large glass orifice probes of 0.5 and 4.0 mm diameter, respectively, which are immersed in the test fluid pool in a small beaker to produce a differential pressure signal proportional to the fluid surface tension. The temperature of the test fluid is measured using a well-calibrated thermistor (±0.1°C precision, 0–150°C) attached to the orifice probes. The aqueous solution container is immersed in a constant temperature bath in order to control and maintain its desired temperature. The time interval between the newly formed interface and the point of bubble break-off is referred to as "surface age," and it gives the measure of bubble growth time that corresponds to the dynamic surface tension value at a given operating bubble frequency. Thus, by altering the air–bubble frequencies through the probes, both static or equilibrium and dynamic surface tension can be measured. Detailed descriptions of the solution preparation, instrument calibration, and validation procedures, along with measurement uncertainties can be found in Refs. [3,6]. The maximum uncertainties in the measurement of concentration, temperature, and surface tension were found to be ±0.4% for powder form additives, ±5% for additives in liquid form, and ±0.5% and ±0.7%, respectively. The liquid–solid contact angle was measured by the sessile drop method, using a Kernco GI contact angle meter and wettability analyzer. The measurement uncertainty in this case is estimated to be a maximum of ±1.4%.

Photographic Observations

The growth of nucleating vapor bubbles and their motion near the cylindrical heater surface were recorded by a PULNiX TMC-7 high-speed color CCD camera with shutter speeds of up to 0.1 μs. The CCD camera is interfaced with a PC through a FLASHBUS MV Pro image capture kit that has high-speed PCI-based bus-mastering capabilities (up to 132 Mbytes/s). It delivers consecutive frames of video in real time into the system memory while keeping the CPU free to operate on other applications. Furthermore a FUJI 12.5–75 mm microlens was used on the CCD camera to facilitate high quality close-up photography.

Results and Discussion

The variations in equilibrium surface tension σ with concentration C for the three different surfactant solutions at bulk temperatures of 23°C and 80°C are graphed in Fig. 3. In both cases, σ is seen to decrease with increasing surfactant concentration to asymptotically attain a minimum constant value beyond CMC. The CMCs for the three surfactants at 23°C (obtained from the lower asymptotic inflection point on the equilibrium adsorption isotherm) are ~2500 wppm for SDS, ~400 wppm for CTAB, and ~2000 wppm for Triton X-305. For aqueous CTAB solutions, the σ–C data compare quite well with the Razafindralambo et al. [24] results at 20°C, and so does the CMC value of 392.5 wppm at 25°C reported by Holmberg et al. [1]. It may be noted though that the process of micelle formation generally takes place over a range of concentrations [26]. The 80°C results show further overall reductions in σ, which are essentially due to increased surfactant diffusivity with increased temperature [1]. These σ isotherms can be nominally considered as atypical of the additive

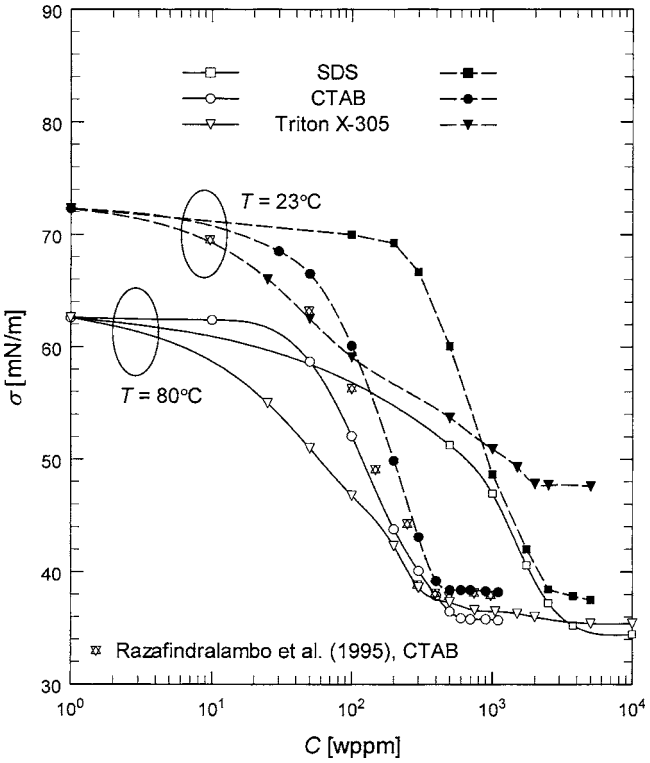

Fig. 3 Equilibrium surface tension measurements for aqueous surfactant solutions at 23°C and 80°C

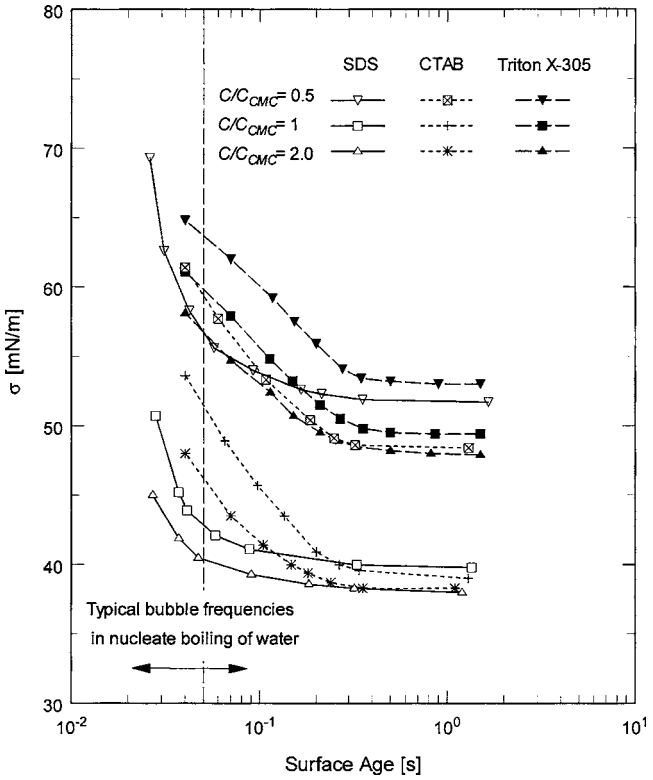

Fig. 4 Dynamic surface tension measurements for aqueous surfactant solutions

adsorption–desorption kinetics during atmospheric-pressure boiling of aqueous surfactant solutions, (while 80°C is the upper limit for QC-6000 surface tensiometer, the surface tension data at real boiling temperature can be obtained by extrapolation of surface tension data with temperature, which typically has a linear relationship [6]) and the equilibrium value at CMC represents the maximum possible surface tension reduction for the solutions at 80°C. From the measurements in Fig. 3, CMCs at 80°C are found to be ~2700 wppm for SDS, ~450 wppm for CTAB, and ~650 wppm for Triton X-305.

When a new surface is created in a surfactant solution, a finite time is required for the reagent adsorption to reach an equilibrium state between the surface concentration and bulk concentration. This time-dependent surfactant adsorption at the vapor-liquid interface of a bubble gives rise to the dynamic surface tension (DST) behavior, which, however, eventually reduces to the equilibrium condition after a long time period [1,3,26]. In boiling applications, the formation and departure of bubbles is also a highly dynamic process, where the vapor–liquid interface has a small surface age; typically in the range of 0–100 ms [27]. The dynamic surface tension relaxation rather than the equilibrium or static surface tension, therefore, becomes the more critical determinant. The variation of σ with surface age depicted in Fig. 4 clearly illustrates this. The time-dependent surface tension relaxation process is primarily related to surfactant molecular mobility (molecular weight). A lower molecular weight surfactant diffuses faster than its higher molecular weight counterpart, and this is seen in the faster σ relaxation of SDS solutions in comparison with that for CTAB or Triton X-305 solutions in Fig. 4.

In most surfactant solutions, the time scale to reach the equilibrium value (total relaxation) at the newly-created interface is of the same order as that of bubble formation and departure in nucleate boiling (0–100 ms). When a bubble starts to form at a nucleating site, the initial surface tension is or close to that of solvent [unlike a pure liquid, the surface tension, or more aptly the *interfacial tension* of an aqueous surfactant solution is an interface-related property and not an inherent bulk liquid property. It is dependent upon the bubble life time or its surface age, which is directly reflected in the dynamic surface tension measurement (Fig. 4)] and it then reduces continually with time τ as more and more surfactant molecules move to the interface during the adsorption process. At the same time, desorption may also occur till an equilibrium condition is reached and surface tension becomes constant. This time-dependent adsorption/desorption process around a nucleating, growing, and departing bubble is schematically illustrated in Fig. 5(*a*), and is reflected in the measured dynamic surface tension behavior seen in Fig. 4. The effects of dynamic surface tension on bubble formation and departure are more clearly demonstrated in Fig. 5(*b*), where results of a controlled adiabatic single-bubble experiment are presented. Photographic images of a near-departure air bubble, captured by a high-speed (2000 frames/s) camera under identical operating conditions, are presented. Constant-pressure bubbling activity in the following three liquids was recorded: water (pure liquid, $\sigma_{eq}=72.3$), 2500 wppm SDS solution (surfactant solution, $\sigma_{eq}=37.5$ at CMC), and *N*,*N*-dimenthyl formamide or DMF (pure liquid, $\sigma_{eq}=37.1$). The bubble surface age was controlled at ~100 ms, which is of the same order as the time scales for the dynamic adsorption/desorption process in aqueous surfactant solutions and ebullience in nucleate boiling. Dynamic σ effects are self-evident in Fig. 5(*b*), where a larger bubble is seen in aqueous SDS solution when compared to that in a pure liquid (DMF) that has the same equilibrium σ value (~37 mN/m). This is essentially due to the time-dependent surfactant adsorption/desorption process at the liquid–vapor interface.

The change in surface wettability (measured by the contact angle) with concentration for the three surfactants is graphed in Fig. 6. Ionic surfactants undergo a different adsorption process than that for nonionic surfactants due to the latter's lack of charge. The adsorption isotherms for ionics (SDS and CTAB) correlate well with the physisorption characterization schematically illus-

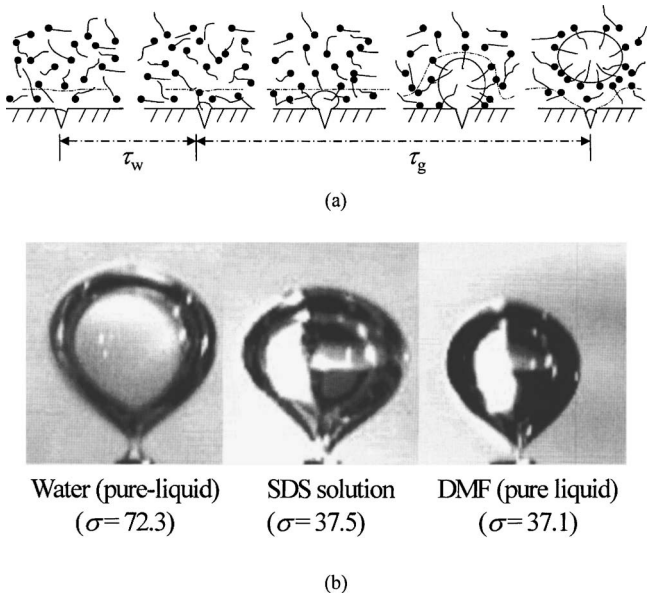

Fig. 5 (a) Schematic of surfactant transport process during a bubble formation and departure (not to scale); (b) Dynamic surface tension effect on bubble dynamics (evolution of predeparture shape and size)

trated in Fig. 1. The contact angle reaches a lower plateau around the CMC where bilayers start to form on the surface. Wettability of nonionic surfactants in aqueous solutions, on the other hand, shows that the contact angle data attains a constant value much below CMC. Direct interactions of their polar chain are generally weak in nonionics, and it is possible for them to build and rebuild adsorption layers below CMC [28]. The reduced contact angle trough at lower concentrations ($C<$CMC) can also be attributed to the absence of any electrical repulsion that could oppose molecular aggregation unlike that associated with ionic surfactants [29]. Furthermore, the continuous decrease in contact angle for nonionic Triton X-305 solutions prior to reaching a constant value is brought about by the presence of 30 ethoxy or ethylene oxide

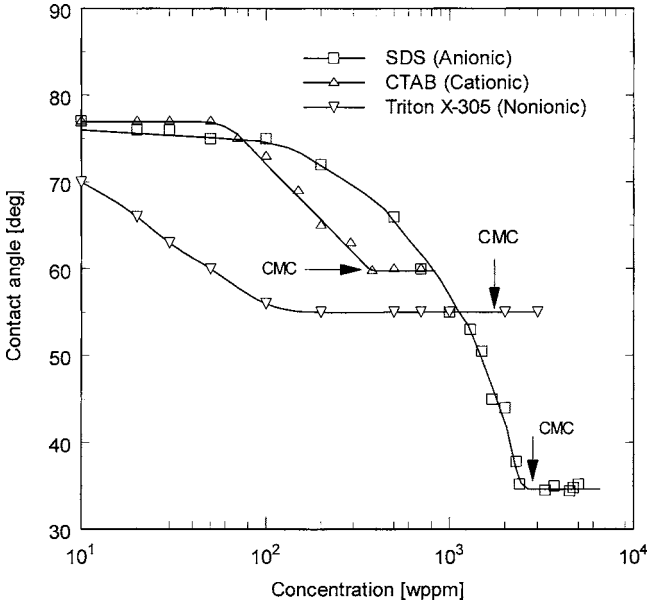

Fig. 6 Measured contact angle θ for aqueous surfactant solutions

(EO) groups in the surfactant molecular chain. The number of EO groups increases the overall size of the polar head, and controls the hydrophilic/hydrophobic balance on the surfactant molecule [1].

The pool boiling data for different concentration aqueous solutions of SDS, CTAB, and Triton X-305, are presented in Fig. 7. In general, with the addition of a surfactant to water, considerable boiling heat transfer enhancement is obtained with increasing concentration, as represented by the characteristic leftward shift in the boiling curve relative to that for distilled water. The optimum enhancement is seen to be obtained with solutions at or near CMC, when the additives are characterized by micellar formations [16]. But with $C>$CMC, the enhancement decreases and the heat transfer even deteriorates below that in distilled water with very high concentration solutions, particularly at low heat fluxes. The boiling behavior was further observed to generally have an early onset of nucleate boiling (ONB), except in solutions with surfactant concentrations higher than CMC when there was a delay in incipience. In fact, a thermal hysteresis is seen in the latter case that is characteristic of high wettability [13,30]. A much larger temperature overshoot is evident in SDS solutions with very high concentrations ($C\gg$CMC) than that in corresponding Triton X-305 and CTAB solutions, and in that order. This correlates very well with the surface wettability measurement in Fig. 6, which shows that $\theta_{SDS}<\theta_{\text{Triton X-305}}<\theta_{CTAB}$ when $C>$CMC.

Figure 8 provides some insights on the role of dynamic surface tension on the heat transfer enhancement in surfactant solutions. Here the normalized optimum pool boiling heat transfer coefficient data for SDS (2500 wppm), CTAB (400 wppm), and Triton X-305 (700 wppm) solutions are graphed. While their respective concentration is different, the equilibrium surface tension value of their aqueous solutions at 80°C is about the same ($\sim$37 mN/m) in each case. In the measured range of heat fluxes, the heat transfer enhancement is seen to be in the order of SDS$>$CTAB $>$Triton X-305, which is in the reverse order of their respective molecular weights. Within the range of typical time transients for bubble formation, growth, and departure in nucleate boiling of water, the faster diffusion of lower molecular weight surfactants (higher mobility) leads to a larger number of surfactant molecules approaching the growing bubble interface. This promotes a faster surface tension relaxation, as represented by the gradient ($d\sigma/d\tau$), [the dynamic surface tension gradient ($d\sigma/d\tau$) is at a nominal surface age of 50 ms, which is representative of bubble frequencies typically encountered in nucleate boiling of water] which then increases the bubble growth and departure frequencies to yield a better heat transfer performance. Thus, in this dynamic ebullient (small surface age bubble interface) and additive adsorption–desorption process, a measure of the dynamic surface tension is clearly the more appropriate scaling property instead of the equilibrium surface tension value. This contention is supported by the results in Figs. 4 and 8, which show that the heat transfer performance correlates well with dynamic surface tension relaxation for the three surfactants of different molecular weight.

It may be noted that the boiling heat transfer performance of aqueous surfactant solutions is governed by a rather complex combined effects of both the dynamic surface tension and contact angle changes. However, the degree of their respective impact on the heat transfer coefficient h can be quite different. In boiling of pure liquids, it has been shown that whereas h is related to surface tension as $h\propto(1/\sigma^3)$ [22], the contact angle θ affects the active nucleation site density N_a and its influence on h can be expressed as $h\propto N_a\propto(1-\cos\theta)$ [31]. These functional relationships suggest an apparently more significant and higher order impact of the dynamic surface tension, compared to that of surface wetting on boiling in aqueous surfactant solutions. This in essence explains the heat transfer enhancement with increasing interfacial tension relaxation or dynamic σ effects (Triton$\rightarrow$CTAB$\rightarrow$SDS) seen in Fig. 8 for the three surfactant solutions; the corresponding de-

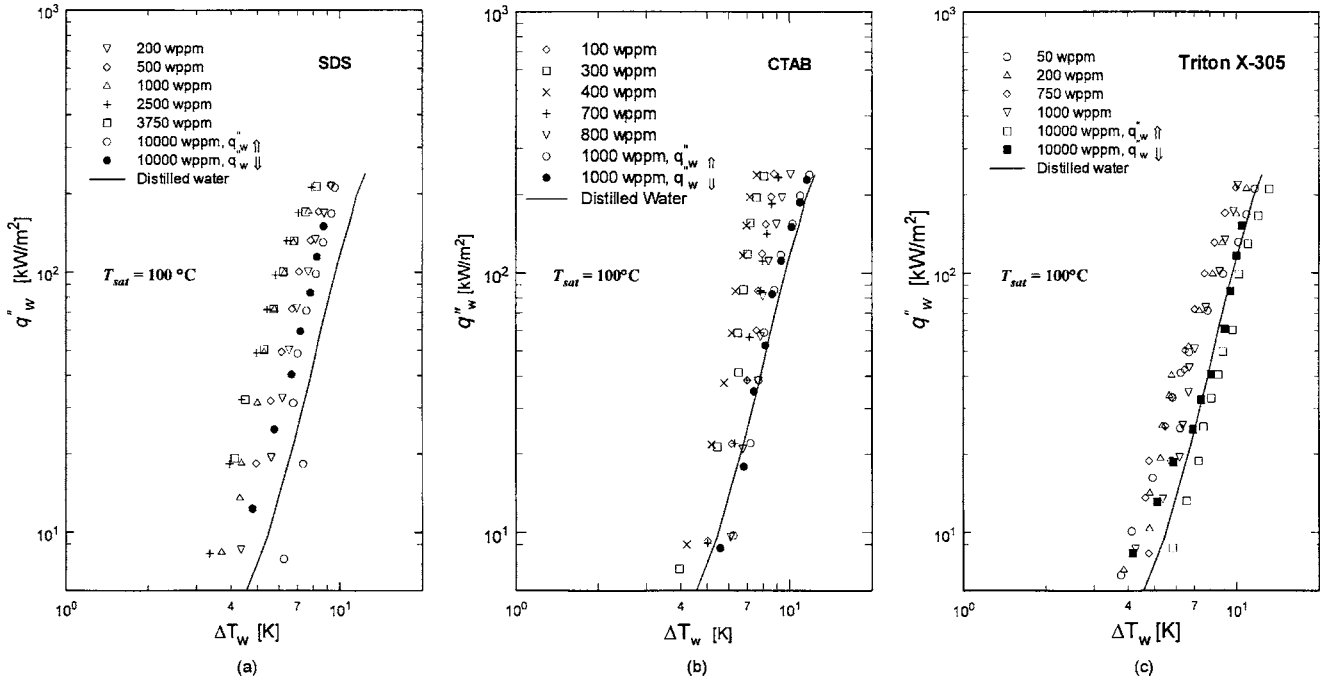

Fig. 7 Nucleate pool boiling data for aqueous solutions of (a) SDS, (b) CTAB, and (c) Triton X-305

crease in θ or wetting at the respective bulk concentrations would suggest a different order of enhancement (SDS→Triton →CTAB).

Nucleate boiling in aqueous surfactant solutions is a complex conjugate process [14], and it depends on a variety of factors. However, the primary heat transfer is by evaporation and its efficiency is directly related to nucleation site density and bubble dynamics, and phenomenological insights can be obtained from a visual observation of the ebullience. This is seen from the photographs in Fig. 9, which represent the boiling behavior in water, and SDS, CTAB and Triton X-305 solutions of three different concentrations ($C/C_{CMC}=0.5$, 1, and 2) at heat fluxes of $q''_w = 20$ kW/m^2 and 50 kW/m^2. In comparison to that in water, boiling in SDS and CTAB solutions is more vigorous and characterized by clusters of smaller-sized, more regularly shaped bubbles that originate at the underside of the cylindrical heater. These bubbles then slide along the heater surface at departure, thereby knocking off much smaller bubbles growing on the top surface of the heater. This process was observed to increase with heat flux and lend to the consequent higher bubble departure frequency. Also, because of the considerable reduction in σ for SDS and CTAB solutions, much smaller-sized bubbles are nucleated in a cluster of active nucleation sites, especially at lower heat fluxes. They have a significantly higher bubble departure frequency, with virtually no coalescence of either the neighboring or sliding bubbles that come in contact with others around the heater's periphery when $C<$CMC. However, when $C\geqslant$CMC, some foaming patches begin to occur, the liquid only coverage area of the heater surface increases, and slightly larger bubbles are formed. All of this is indicative of a surface wetting condition change, which is more evident in SDS solutions. This surface-wetting induced change in ebullience again correlates well with the contact angle measurements in Fig. 6, which clearly shows a stronger adsorption of SDS than that of CTAB. Boiling in Triton X-305, on the other hand, shows much smaller-sized bubbles in pre-CMC solutions, and considerably fewer and larger-sized bubbles are formed with increasing concentrations. This presents a contrastingly different behavior from not only that of water but also that of SDS and CTAB, and is perhaps due to the continuous decrease in contact angle with increasing concentration as seen in Fig. 6. The bulky polar head of the Triton X-305 molecule, which reduces surface tension slower than SDS and CTAB, may perhaps also play a role here.

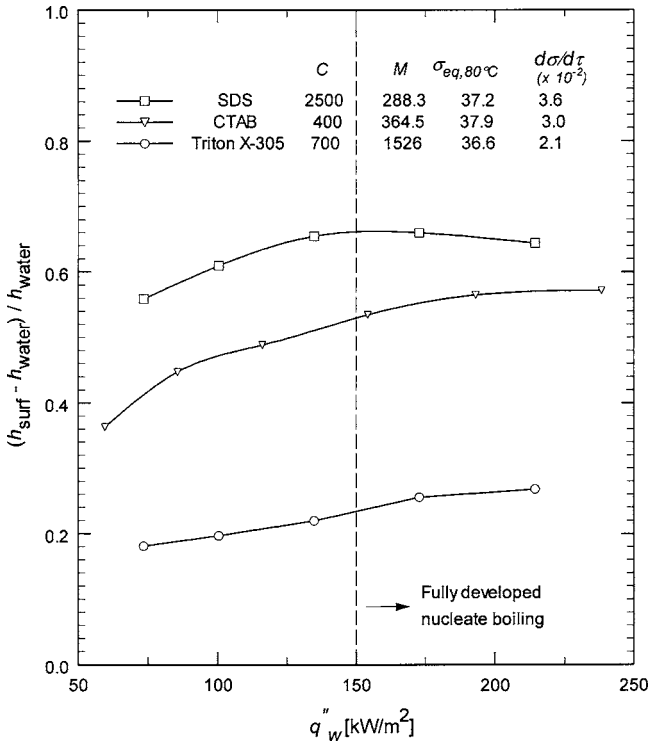

Fig. 8 Effects of surfactant molecular weight and dynamic surface tension on the optimum heat transfer coefficient enhancement

The observed ebullience and boiling heat transfer data cannot be explained by the reduced dynamic surface tension alone. If this were so, then smallest-sized bubbles would be seen in $C\geqslant$CMC solutions, where the surface tension reaches the lowest possible

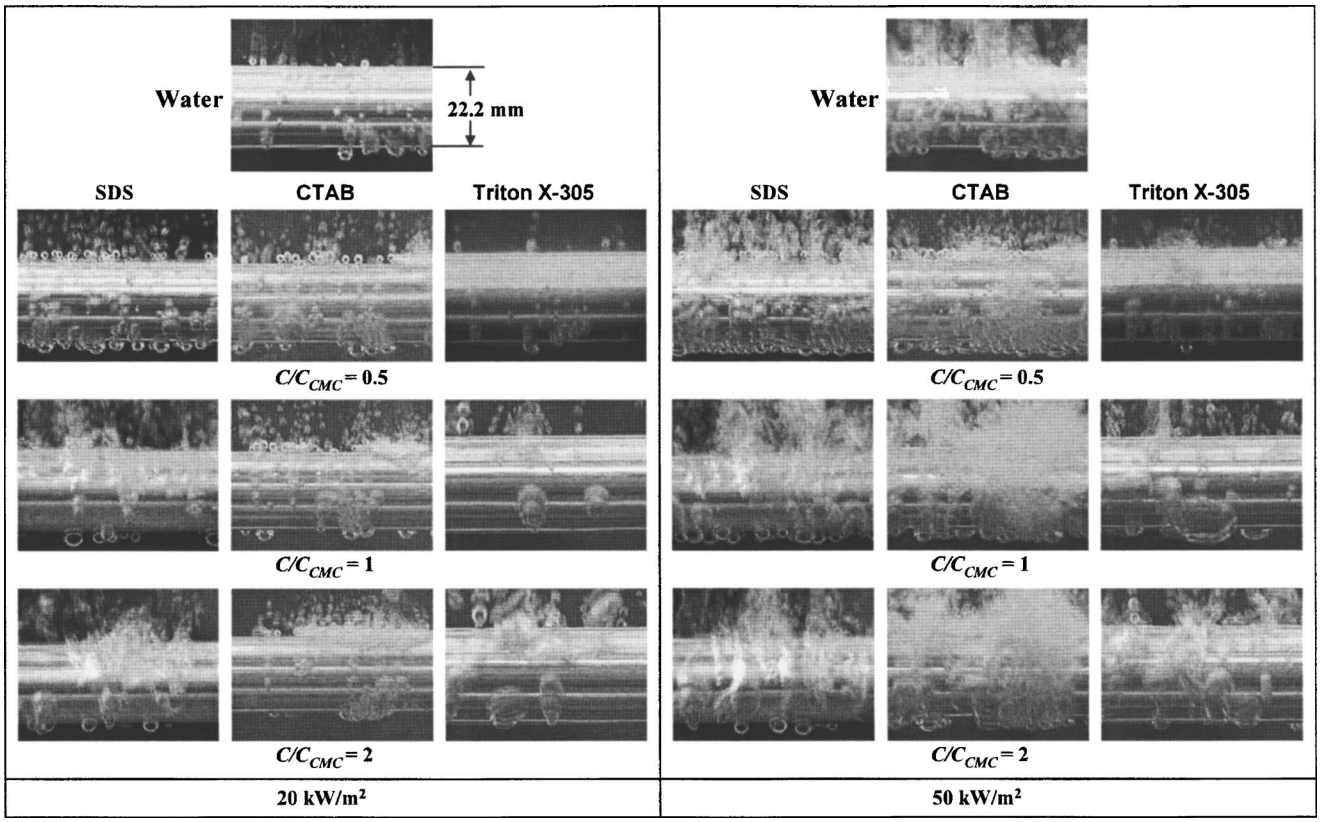

Fig. 9 Boiling behavior for distilled water, and aqueous SDS, CTAB, and Triton X-305 solutions of different concentrations at q''_w=20 kW/m² and 50 kW/m²

value. Instead, because of the adsorption of surfactant molecules and their different orientations in the adsorption layer (Fig. 1), the heater surface wettability increases with increasing concentration and larger nucleation cavities get flooded. Fewer bubbles are thus nucleated, and they tend to have relatively larger departure diameters, which is typical of wetting liquid ebullience [30]. These variations in the observed ebullience at the heater surface (Fig. 9) along with the measured contact angle data (Fig. 6) that reflect the wettability changes with concentration, are thus clearly seen to scale and correspond very well with the surfactant adsorption characterization schematically illustrated in Fig. 1.

Conclusions

With the addition of small amounts of surfactants, the saturated nucleate pool boiling of water on a cylindrical heater is altered significantly. The heat transfer is enhanced in solutions with $C \leqslant$ CMC, but decreases when $C >$ CMC. [The critical micelle concentration or CMC is a significantly important characteristic of surfactants, as it demarcates the transitions in both the liquid–vapor and solid–liquid interfacial phenomena. At CMC, the surface tension of a given surfactant solution reaches the lowest possible value, and is a manifestation of the additive adsorption at the liquid-vapor interface. Post-CMC, surfactant molecules tend to form bilayers (or other micellar layers) on the solid surface to make it strongly hydrophilic.] In general, besides the heat flux (or wall superheat) levels, the relative extent of performance change is seen to be governed by the surfactant interfacial phenomena at both the liquid–vapor and solid–liquid interfaces. These in turn are determined by several additive physico-chemistry-based factors, and their rather complex inter-relationships are characterized in Fig. 10.

Interfacial properties at the liquid–vapor (dynamic and equilibrium surface tensions) and solid–liquid (surface wetting or contact angle) interfaces characterize the adsorption behaviors of additives in their aqueous solutions. Surfactants lower the surface tension of water considerably, and their adsorption–desorption process at the liquid–vapor interface is time-dependent. This manifests in a dynamic surface tension behavior, which eventually reduces to an equilibrium value after a long time span. Also, the surfactant physisorption process tends to follow a characteristic adsorption isotherm at the solid–liquid interface, and the consequent changes in surface wetting conditions, as measured by the contact angle, correlate well with the adsorption characterization.

The measured heat transfer data in saturated nucleate pool boiling of aqueous surfactant solutions, and the photographically recorded ebullient behavior are also found to correlate well with the measured interfacial properties. The boiling performance can fun-

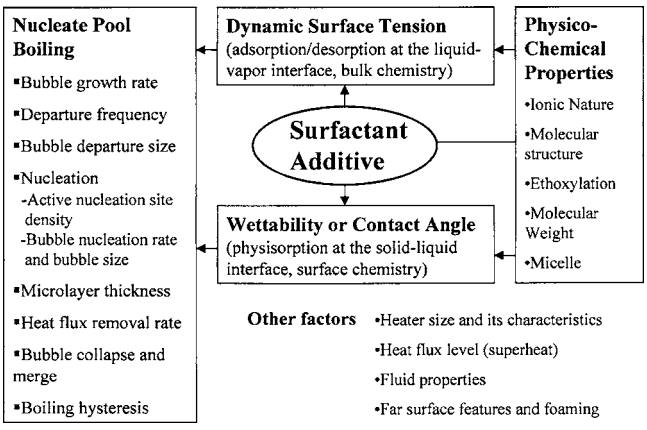

Fig. 10 Characterization of nucleate pool boiling and its determinants in aqueous surfactant solutions

damentally be characterized on the basis of dynamic surface tension relaxation and change in surface wettability (contact angle). Reflecting the highly dynamic, small-surface-age-interface nature of nucleate boiling in surfactant solutions, a measure of dynamic surface tension rather than the equilibrium value is seen to be an effective scaling property for the heat transfer data. The faster diffusion of lower molecular weight surfactants tends to reduce the surface tension faster in a short period of time, which results in the better heat transfer performance of their solutions. Furthermore, besides the dynamic surface tension relaxation, the altered wettability of heater surface due to the interfacial physisorption of surfactant molecules at the solid–liquid interface is shown to be another critical parameter in predicting the enhanced nucleate pool-boiling behavior.

Acknowledgments

This study was supported in part by the National Science Foundation (Grant No. CTS-9502128), Ohio Board of Regents, and University Research Council. Satish Vishnubhatla and S. Sethu Raghavan provided technical assistance in acquiring some interfacial data. Also, the valuable suggestions of Professor Douglas W. Fuerstenau, University of California, Berkeley, are gratefully acknowledged.

Nomenclature

A = heater surface area ($=2\pi r_o L$) (m^2)
C = concentration (wppm)
h = boiling heat transfer coefficient ($kW/m^2\,K$)
I = current (A)
k = thermal conductivity of heater material (kW/mK)
L = length of heated cylinder (m)
M = molecular weight (kg/kmol)
N_a = Active nucleate sites (m^{-2})
q''_w = wall heat flux (W/m^2 or kW/m^2)
r = radius of wall thermocouple location (m)
r_o = cylindrical heater radius (m)
T = temperature (°C, or K)
ΔT_w = wall superheat (K)
V = voltage (V)

Greek Symbols

θ = contact angle (deg)
σ = surface tension (mN/m)
τ = surface age (s)

Subscripts

eq = equilibrium condition
o = outer surface
r = radial location
sat = saturation
surf = pertaining to aqueous surfactant solution
w = at heater wall
water = pertaining to pure water

References

[1] Holmberg, K., Jönsson, B., Kronberg, B., and Lindman, B., 2003, *Surfactants and Polymers in Aqueous Solution*, 2nd ed., Wiley, New York.
[2] Hunter, R. J., 2001, *Foundations of Colloid Science*, 2nd ed., Oxford University Press, Oxford.
[3] Manglik, R. M., Wasekar, V. M., and Zhang, J., 2001, "Dynamic and Equilibrium Surface Tension of Aqueous Surfactant and Polymeric Solutions," Exp. Therm. Fluid Sci., **25**, pp. 55–64.
[4] Fuerstenau, D. W., 2002, "Equilibrium and Nonequilibrium Phenomena Associated with the Adsorption of Ionic Surfactants at Solid–Water Interfaces," J. Colloid Interface Sci., **256**, pp. 79–90.
[5] Hoffmann, H., and Rehage, H., 1986, "Rheology of Surfactant Solutions," in *Surfactant Solutions—New Methods of Investigation*, Zana, R., ed., Marcel Dekker, New York, Vol. 22, pp. 209–239.
[6] Manglik, R. M., Bahl, M., Vishnubhatla, S., and Zhang, J., 2003, "Interfacial and Rheological Characterization of Aqueous Surfactant Solutions," Thermal-Fluids and Thermal Processing Laboratory Report No. TFTPL-9, University of Cincinnati, Cincinnati, OH.
[7] Thome, J. R., 1990, *Enhanced Boiling Heat Transfer*, Hemisphere, New York.
[8] Bergles, A. E., 1997, "Enhancement of Pool Boiling," Int. J. Refrig., **20**(8), pp. 545–551.
[9] Manglik, R. M., 2003, "Heat Transfer Enhancement," in *Heat Transfer Handbook*, A. Bejan and A. D. Kraus, eds., Wiley, New York, Chap. 14.
[10] Wasekar, V. M., and Manglik, R. M., 1999, "A Review of Enhanced Heat Transfer in Nucleate Pool Boiling of Aqueous Surfactant and Polymeric Solutions," J. Enhanced Heat Transfer, **6**(2–4), pp. 135–150.
[11] Zhang, J., and Manglik, R. M., 2004, "Experimental and Computational Study of Nucleate Pool Boiling Heat Transfer in Aqueous Surfactant and Polymer Solutions," Thermal-Fluids and Thermal Processing Laboratory Report No. TFTPL-10, University of Cincinnati, Cincinnati, OH.
[12] Nelson, R. A., Kenning, D. B. R., and Shoji, M., 1996, "Nonlinear Dynamics in Boiling Phenomena," Japan Heat Transfer Society Journal, **35**(136), pp. 22–34.
[13] Dhir, V. K., 1998, "Boiling Heat Transfer," Annu. Rev. Fluid Mech., **30**, pp. 365–401.
[14] Zhang, J., and Manglik, R. M., 2004, "Effect of Ethoxylation and Molecular Weight of Cationic Surfactants on Nucleate Boiling in Aqueous Solutions," J. Heat Transfer, **126**(1), pp. 34–42.
[15] Wasekar, V. M., and Manglik, R. M., 2000, "Pool Boiling Heat Transfer in Aqueous Solutions of an Anionic Surfactant," J. Heat Transfer, **122**(4), pp. 708–715.
[16] Wasekar, V. M., and Manglik, R. M., 2002, "The Influence of Additive Molecular Weight and Ionic Nature on the Pool Boiling Performance of Aqueous Surfactant Solutions," Int. J. Heat Mass Transfer, **45**(3), pp. 483–493.
[17] Hetsroni, G., Zakin, J. L., Lin, Z., Mosyak, A., Pancallo, E. A., and Rozenblit, R., 2001, "The Effect of Surfactants on Bubble Growth, Wall Thermal Patterns and Heat Transfer in Pool Boiling," Int. J. Heat Mass Transfer, **44**, pp. 485–497.
[18] Zhang, J., and Manglik, R. M., 2003, "Visualization of Ebullient Dynamics in Aqueous Surfactant Solutions," J. Heat Transfer, **125**(4), p. 547.
[19] Wen, D. S., and Wang, B. X., 2002, "Effect of Surface Wettability on Nucleate Pool Boiling Heat Transfer for Surfactant Solutions," Int. J. Heat Mass Transfer, **45**, pp. 1739–1747.
[20] Sher, I., and Hetsroni, G., 2002, "An Analytical Model for Nucleate Pool Boiling with Surfactant Additives," Int. J. Multiphase Flow, **28**, pp. 699–706.
[21] Mikic, B. B., and Rohsenow, W. M., 1969, "A New Correlation of Pool-Boiling Data Including Effect of Heating Surface Characteristics," J. Heat Transfer, **9**, pp. 245–250.
[22] Rohsenow, W. M., 1952, "A Method of Correlating Heat Transfer Data for Surface Boiling of Liquids," Trans. ASME, **74**, pp. 969–976.
[23] Moffatt, R. J., 1988, "Describing the Uncertainties in Experimental Results," Exp. Therm. Fluid Sci., **1**(1), pp. 3–17.
[24] Wasekar, V. M., and Manglik, R. M., 2001, "Nucleate Pool Boiling Heat Transfer in Aqueous Surfactant Solutions," Thermal-Fluids and Thermal Processing Laboratory Report No. TFTPL-4, University of Cincinnati, Cincinnati, OH.
[25] Razafindralambo, H., Blecker, C., Delhaye, S., and Paquot, M., 1995, "Application of the Quasi-Static Mode of the Drop Volume Technique to the Determination of Fundamental Surfactant Properties," J. Colloid Interface Sci., **174**, pp. 373–377.
[26] Rosen, M. J., 1989, *Surfactants and Interfacial Phenomena*, 2nd ed., Wiley, New York.
[27] Prosperetti, A., and Plesset, M., 1978, "Vapor-Bubble Growth in a Superheated Liquid," J. Fluid Mech., **85**(2), pp. 340–368.
[28] Levitz, P. E., 2002, "Adsorption of Non Ionic Surfactants at the Solid/Water Interface," Colloids Surf., A, **205**, pp. 31–38.
[29] Miller, C. A., and Neogi, P., 1985, *Interfacial Phenomena: Equilibrium and Dynamic Effects*, Marcel Dekker, New York, Chap. 4.
[30] Kenning, D. B. R., 1999, "What Do We Really Know about Nucleate Boiling," in *IMechE Trans: 6th UK National Heat Transfer Conference*, Edinburgh, 15–16 September, pp. 143–167.
[31] Basu N., Warrier G. R., and Dhir V. K., 2002, "Onset of Nucleate Boiling and Active Nucleation Site Density During Subcooled Flow Boiling," J. Heat Transfer, **124**(4), pp. 717–728.

Discrete Green's Function Measurements in Internal Flows

Charles Booten
e-mail: booten@stanford.edu
Department of Mechanical Engineering,
Stanford University,
Stanford, CA 94305-3030

John K. Eaton
e-mail: eaton@vk.stanford.edu
Department of Mechanical Engineering,
Stanford University,
Stanford, CA 94305-3030

The discrete Green's function (DGF) for convective heat transfer was measured in a fully developed, turbulent pipe flow to test a new technique for simple heat transfer measurement. The 10×10 *inverse DGF,* G^{-1}*, was measured with an element length of approximately one pipe diameter and Reynolds numbers from 30,000 to 100,000 and compared to numerical predictions using a parabolic flow solver called STANTUBE. The advantages of using the DGF method over traditional heat transfer coefficients in predicting the thermal response for flows with nonuniform thermal boundary conditions are also demonstrated.* [DOI: 10.1115/1.1924567]

Keywords: Forced Convection, Heat Transfer, Internal, Measurement Techniques, Turbulent

Introduction

Inaccurate knowledge of internal heat transfer rates is a major factor in the uncertainty of turbine-blade life-span prediction, resulting in more conservative, and less efficient, internal cooling passage designs. The convective heat transfer inside these blades is generally characterized using a heat transfer coefficient, h, that varies with geometry, flow parameters, fluid properties, and thermal boundary conditions. The most common thermal boundary conditions that are applied when measuring h for internal flows are constant wall temperature and constant heat flux. Most practical situations, however, have more complex boundary conditions. As an example, consider a modern turbine blade which is cooled by rows of film cooling holes. The metal temperature varies periodically along each of these rows; therefore, applying an h measured for uniform wall temperature or heat flux would yield incorrect internal heat transfer rates.

To accurately describe steady-state heat transfer, a heat transfer coefficient that is valid for a variety of thermal boundary conditions (for a given geometry and hydrodynamic conditions) is necessary. It is well known that, if the energy equation is linear, superposition can be used to calculate heat transfer rates for arbitrary thermal boundary conditions in simple geometries such as flat plates and round tubes [1–3]. A summary of the development of superposition techniques in convective heat transfer is presented in [4]. More recently this idea has been extended to the use of a Green's function approach for studying laminar and slug pipe flow [5] and a discrete Green's function approach (actually a discretized Green's function solution as explained below) to characterizing heat transfer for external flows [4,6]. Mukerji [7] showed that it can be easier to measure the DGF than h in complex external flows where it is difficult to achieve constant wall temperature or heat flux. To measure the DGF, the experimenter need only apply heating over small patches of the surface of interest and measure the temperature response. The present work is motivated by the desire to obtain DGF-type measurements in complex internal flows such as the serpentine cooling passages in turbine blades. It is very difficult experimentally to obtain uniform heat flux or wall temperature in such a complex geometry. Transient measurement techniques [8] may be used, but the resulting measurements are difficult to compare to steady-state calculations since the thermal boundary conditions are indeterminate. Therefore, there may be a significant advantage to developing DGF techniques for internal flows.

The specific objectives of the present work are to develop a DGF measurement technique applicable to internal flows and to document its performance in fully developed turbulent pipe flow over a range of Reynolds numbers. The measurements are verified using semianalytical and numerical calculations. The measured DGF for turbulent pipe flows is useful for pipe flow heat transfer calculations, and the results indicate the utility of the DGF technique for complex internal flow measurements.

Formulation of the Discrete Green's Function

The heat transfer characteristics of pipe flow can be represented mathematically through the use of a Green's function. For the case of an applied, constant heat flux from $x=0$ to Δx the temperature rise is

$$\Delta T(r,\Delta x)=\int_0^R\int_0^{\Delta x} I(r,r^*;x-x^*)\dot{q}''\delta(R-r^*)dx^*2\pi r^*dr^*. \quad (1)$$

In Eq. (1), I is the impulse, or Green's function, and is used instead of the customary G to prevent confusion with the DGF as presented in this paper. Equation (1) can be integrated to find the wall temperature rise in terms of the heat transfer into the flow over a given distance Δx, $\dot{q}$, and another function,

$$\Delta T(R,\Delta x)=\frac{\dot{q}}{\Delta x}\int_0^{\Delta x} I(r^*,r^*;x-x^*)dx^*. \quad (2)$$

Equation (2) shows that the DGF is in fact a discretized Green's function solution.[1] In order for Eq. (2) to be useful there must be knowledge of I. In fully developed pipe flow I is a known quantity, however, in more complex flows it is not. Instead the integral in Eq. (2) can be calculated by knowing ΔT and $\dot{q}$. These two quantities cannot be measured with infinite resolution; hence I cannot be determined from measured data but only approximated in discrete intervals. This method is referred to as the discrete Green's function, DGF, method.

The DGF is essentially a heat transfer coefficient which provides a relationship between the wall temperature and heat flow. The formulation represents the surface as a set of N discrete elements each of which has an average, steady-state temperature rise above a suitable reference and a heat transfer rate to the flow. The

Contributed by the Heat Transfer Division for publication in the JOURNAL OF HEAT TRANSFER. Manuscript received May 4, 2004. Final manuscript received February 2, 2005. Review conducted by: Jay Khodadadi.

[1]This interpretation was suggested by a reviewer.

DGF is an $N \times N$ matrix, G with units of W/K, which relates the vector of heat transfer rates, $\dot{\mathbf{q}}$, to the steady-state wall temperature rise vector, $\Delta\mathbf{T}$, as

$$\dot{\mathbf{q}} = G\Delta\mathbf{T}. \tag{3}$$

Equation (3) shows that the DGF relates the heat transfer from a given element to the wall surface temperature rise on every element. Thermal boundary condition effects are accounted for directly in the formulation through $\Delta\mathbf{T}$.

The DGF technique was developed for external flows where T_∞ is the appropriate reference temperature. Typical formulations of h for internal flows use the mixed mean temperature [9]. In this study the fixed inlet temperature is used as a reference as is common for developing pipe flow problems [10,11]. The $\Delta\mathbf{T}$ in Eq. (3) is therefore defined as

$$\Delta\mathbf{T} = \mathbf{T}_{\text{wall}} - T_{\text{entrance}}. \tag{4}$$

In most instances it is easier to measure the inverse DGF (IDGF) which is defined by

$$\Delta\mathbf{T} = G^{-1}\dot{\mathbf{q}}. \tag{5}$$

G^{-1} is also an $N \times N$ matrix with units of K/W, but it is important to note that since the DGF is calculated for finite element sizes, G^{-1} is not a direct inversion of G; this is discussed in more detail later.

Simplifications can be made in the case of hydrodynamically fully developed pipe flow with equally sized elements by realizing that all columns of G (and G^{-1}) have identical entries except they are aligned along the main diagonal instead of along the rows. This is true because a step in the thermal boundary condition at any point in the pipe produces an identical heat transfer response downstream of the step. A further simplification is that G and G^{-1} are lower triangular matrices. The DGF, G_{pipe}, then takes the form

$$G_{\text{pipe}} = \begin{bmatrix} g_1 & 0 & 0 & 0 \\ g_2 & g_1 & 0 & 0 \\ \vdots & \vdots & \ddots & 0 \\ g_n & g_{n-1} & \cdots & g_1 \end{bmatrix}. \tag{6}$$

Having a lower triangular G or G^{-1} physically means that a heated element in the wall boundary condition has no upstream effect, which is not necessarily true in geometries with separation and recirculation. In these cases, G will then have nonzero entries above the main diagonal and can potentially have columns whose entries do not match along the diagonals. Both of these effects complicate the determination of G and G^{-1}, but the present measurement technique is still applicable. Extra nonzero terms can be determined by iteration and in practice a single iteration is often sufficient. Nonmatching columns require that the same experiment be repeated at different locations to determine columns independently. If the entries in different columns are similar then interpolation can be used as a substitute for measuring every column.

A column in G_{pipe} can be determined by heating a single element to a known ΔT while cooling all other elements to maintain them at T_{entrance} and measuring the heat transfer from each element. The column vector $\mathbf{g}$ is then

$$g(i) = \frac{\dot{q}(i)}{\Delta T}. \tag{7}$$

The process to obtain G_{pipe}^{-1} is conceptually similar but much simpler experimentally. In this case, one needs the distribution of wall temperature associated with an applied steady-state spatial pulse of wall heat transfer over a single element, while maintaining all other elements adiabatic

$$g^{-1}(i) = \frac{\Delta T(i)}{\dot{q}}. \tag{8}$$

The form of G_{pipe}^{-1} is identical to the lower triangular form of G_{pipe} given in Eq. (6).

For geometries where an analytical DGF can be calculated (i.e., flat plates and round tubes), the approach is to first conceptually discretize the geometry into elements. The elements need not be the same length; however, there are certain simplifications mentioned above that arise if they are. Choosing the appropriate element size is important as it determines the resolution of the applied thermal boundary conditions and the thermal response. The next step in calculating G is to determine the total wall heat transfer, $\dot{q}_i$, for each element for a steady-state spatial pulse in wall temperature between $x^+=0$ and $x^+=\Delta x^+$, where x^+ is the dimensionless axial coordinate defined as $x^+ \equiv 2x/(\text{DRePr})$. One way to calculate $\dot{q}_i$ is by superimposing the wall heat transfer rate for a step change in wall temperature at $x^+=0$ with the solution arising from a negative step in temperature (of identical magnitude) at Δx^+. The elements of G are then calculated by substituting the resulting $\dot{\mathbf{q}}$ into Eq. (7). The process for calculating the elements of G^{-1} is analogous to that for G, except that the wall temperature is calculated for a spatial pulse in heat flux and substituted into Eq. (8). Semianalytical solutions for turbulent pipe flow are presented in [1], but for small step sizes ($\Delta x^+ \leqslant 4.5\text{e}-5$) the accuracy of the eigenvalues and eigenfunctions is not sufficient for calculating the DGF. More accurate eigenvalues and eigenfunctions for the present comparisons were calculated based on the method in [13–15].

Numerical Comparison

The IDGF was calculated using STANTUBE as a check on the semianalytical method of calculating G_{pipe}^{-1}. STANTUBE is a modification of a boundary layer code (STAN5) developed at Stanford University [12] that uses a finite-difference method for solving the boundary layer momentum and energy equations for laminar or turbulent flows over or inside a round tube. A fully developed inlet velocity profile is prescribed using the 1/7th power law profile with either a mixing-length or k-ε model (results are essentially identical) and either fixed or variable fluid properties based on the local temperature. The axial grid spacing was equal to 0.015 times the pipe diameter, and the radial grid spacing was such that the outside element had a $y^+=0.1$ with a total of 30 elements within the log layer and viscous sublayer. The comparison between the semianalytical and numerical methods in Fig. 1 shows excellent agreement. The element length corresponds to approximately one pipe diameter (37.85 mm) with Re = 60,000. The difference is mainly in the first off diagonal element where for this case the maximum deviation is 3%.

Nonlinearity in the energy equation manifests itself in two ways: Variable properties and natural convection. The DGF method is only strictly applicable when neither of these effects are present; however, tests were conducted with STANTUBE that suggest the method can be utilized in pipe flow even with large temperature variations in the fluid. The nonlinear STANTUBE simulations consider only the variable properties. Steady-state spatial temperature pulses of 1000°C and 10°C were used to produce a G_{pipe} with elements agreeing within 7%. This is an important result as it demonstrates that the DGF method is very versatile and that the experimentally measured DGF and IDGF are useful even in situations with extremely large temperature gradients relative to those for which they were measured.

Converting Between G and G^{-1}

It is generally much easier to measure G^{-1} than G because of the difficulty of maintaining sharp temperature steps as a thermal boundary condition. The G^{-1} matrix can then be inverted to give an estimate of G, G_{est}. However, G^{-1} is the inverse of G, and vice

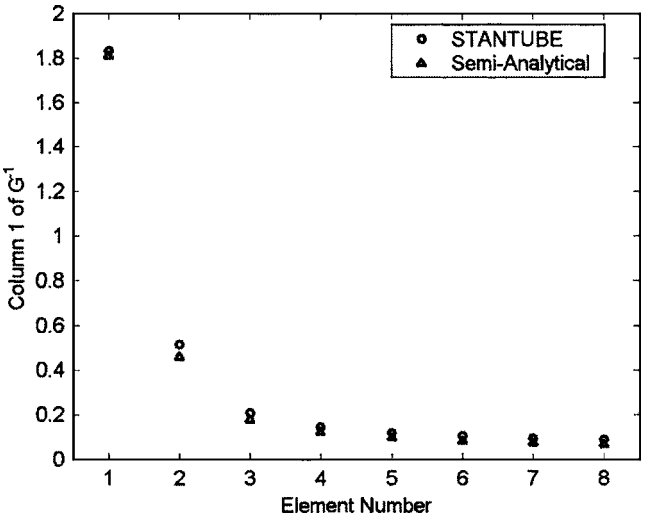

Fig. 1 Semianalytical G^{-1} compared to STANTUBE G^{-1} for heat flux of 1500 W/m^2, Re=60,000

versa, only with infinite resolution. To assess the accuracy of this inversion approach to estimating G at typical measurement resolution, the semianalytical IDGF was inverted and compared to the semianalytical DGF. Figure 2 shows the difference between the two for $\Delta x^+ = 4.6e-5$ and Re=60,000. This Δx^+ corresponds to an element length of approximately one pipe diameter. The differences between elements are within the experimental uncertainty as listed in Table 1, except for the second element. This inversion

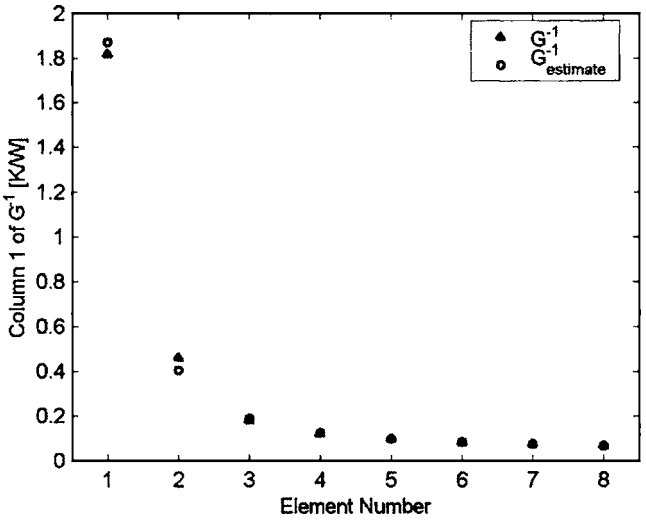

Fig. 2 Comparing G^{-1} and the inverse of G, Re=60,000

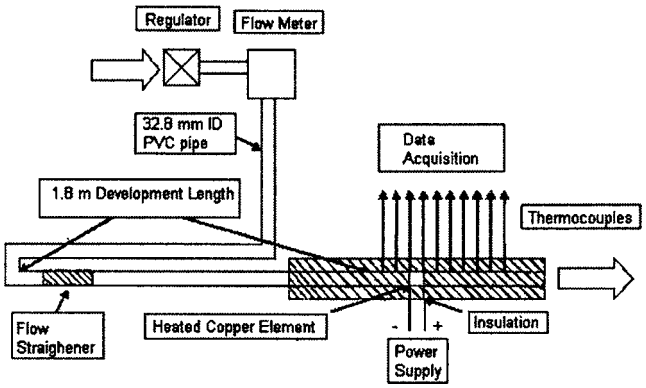

Fig. 3 Schematic of experiment

error has been documented before in [3]. However, the inversion errors between G and G_{est} grow significantly as Δx^+ increases. At Re=60,000 the difference on the main diagonal element exceeds 7% for $\Delta x^+ > 3.7e-3$ compared to 2.9% for $\Delta x^+ = 4.6e-5$ as in the case of Fig. 2.

Experimental Apparatus

The IDGF was measured in a hydrodynamically fully developed flow in a 32.8 mm ID round tube. An electrically heated annular copper element approximately 1 pipe diameter long was integrated smoothly between two sections of PVC plastic pipe. Pipe wall temperatures were measured along the length of the test section using thermocouples embedded in the pipe wall such that they are flush with the inner pipe surface.

The apparatus consists of a compressed air supply, a Meriam 50MH10-4T laminar flow meter, a 1.8 meter long development tube, and the test section as shown schematically in Fig. 3. The development tube was bored to the precise diameter of the test section (±0.05 mm) and honed to a surface roughness of 16 microinches. The long development length (63 pipe diameters) and precision bored tube insured hydrodynamically fully developed pipe flow at the inlet to the test section. The velocity profile at the entrance to the test section was measured using a pitot probe and is shown in Fig. 4.

The test section shown in Fig. 5 consisted of 267 mm long sections of PVC pipe upstream and downstream of the heated element. The PVC pipe was bored to a 32.8 mm±0.05 mm ID from the nominal ID of 31.8 mm to ensure the tubes were round. The heated element was a 31.8 mm long annulus with a 32.8 mm ID and 2.54 mm wall thickness. The ends of the copper annulus were chamfered as shown in Fig. 5 to minimize the contact area and thus thermal conduction between the copper and the PVC pipe sections. The step size between the ID of the copper element and the PVC pipes either upstream or downstream was maintained within ≈0.15 mm by alignment fingers on the PVC pipes. The

Table 1 % uncertainty contribution of quantities to the overall root-sum-square uncertainty for the first column of G^{-1}_{pipe} for Re=60,000

DGF Element	Power Input	T_{TC}	k_{PVC}	$t_{insulation}$	ε	$k_{insulation}$	RSS
1	0.54	3.14	0.07	0.04	0.21	0.05	3.20
2	0.53	9.29	0.05	0.07	0.15	0.08	9.32
3	0.53	25.94	0.10	0.06	0.22	0.07	25.95
4	0.53	38.52	0.05	0.05	0.09	0.06	38.52
5	0.53	51.16	0.04	0.05	0.02	0.06	51.17
6	0.53	60.21	0.02	0.05	0.02	0.06	60.21
7	0.53	63.75	0.01	0.05	0.02	0.06	63.75
8	0.53	70.03	0.01	0.05	0.02	0.06	70.03
9	0.53	75.27	0.00	0.05	0.03	0.06	75.27
10	0.53	74.99	0	0	0	0	74.99

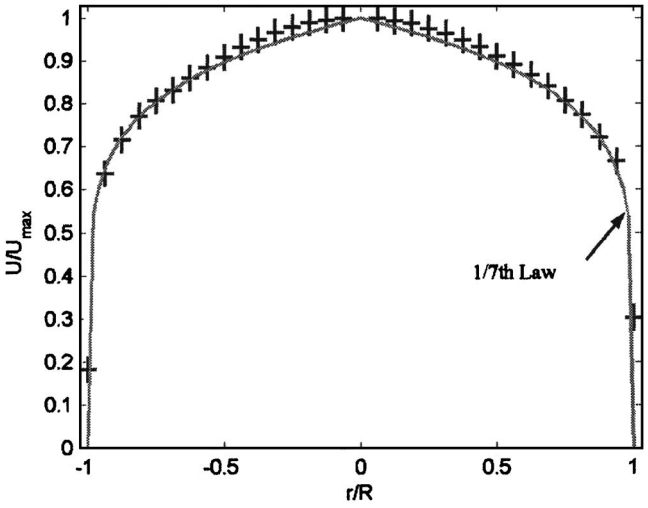

Fig. 4 Velocity profile at upstream end of heated element with uncertainty indicated by symbol size

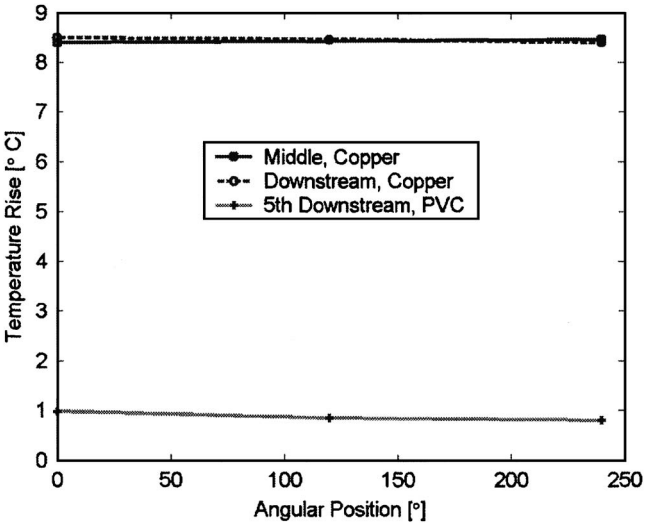

Fig. 6 Circumferential temp distribution on copper and PVC pipe, Re=60,000

test section was put into compression and the joints sealed with RTV to insure no leakage at the butt joints to the copper section.

The PVC and copper sections were instrumented with 19 thermocouples aligned axially throughout the length of the copper and downstream PVC pipe. The upstream PVC pipe had a reference thermocouple for measuring the inlet temperature 230 mm upstream of the copper element. In addition, two thermocouples were placed in the tube wall directly upstream of the copper to evaluate heat conduction upstream. The thermocouples were mounted flush with the inner surface of the pipe through 1 mm diameter holes. The holes were drilled through the walls and the thermocouples were held in place using high thermal conductivity (1 W/mK) epoxy. There were three sets of thermocouples evenly distributed circumferentially on the copper and at one axial location on the downstream PVC pipe, to check that the temperature distribution was axisymmetric. Figure 6 confirms that the temperature rise at each section is essentially uniform. The maximum circumferential temperature difference is 0.11°C, which is approximately half of the uncertainty of the thermocouple measurements (±0.22°C) used to determine the overall uncertainty in the DGF. All sections of PVC pipe were well insulated with 50 mm of polyethylene foam (thermal conductivity 0.04 W/mK) to approximate an adiabatic boundary condition and 20 mm of the same insulation was used on the upstream development pipe.

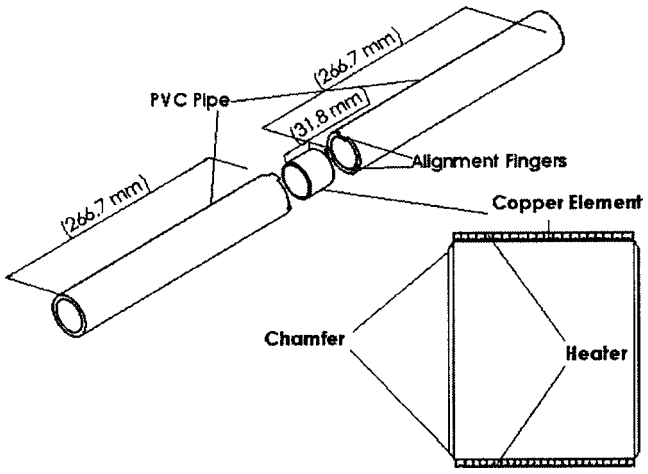

Fig. 5 Test section exploded view

The copper element was wrapped in a 0.3 mm thick MINCO HK5333 thermofoil heater as shown in Fig. 5. It is able to supply up to 10 W of power in a circumferentially uniform manner to the flow. The outside of the heater was covered in 1 mm thick rhoacell foam (thermal conductivity 0.031 W/mK) which was then covered in 51 mm of polyethylene pipe insulation. It should be noted that even though the imposed boundary conditions are on the heat flux (as required when measuring G^{-1}) the flow actually is exposed to a constant temperature boundary condition over the OFHC copper element, while the PVC pipes are both approximately adiabatic throughout their length. This mix of boundary conditions is not strictly consistent with measuring G^{-1}, but is much more convenient experimentally than providing a uniform heat flux over a length of pipe.

Experimental Results

Tests were performed for $30{,}000 \leqslant \mathrm{Re} \leqslant 100{,}000$. Before the tests, air was run through the pipe until it was isothermal (±0.05°C) then the power supply was turned on to supply between 5 and 10 W to the thermofoil heater, depending on the Reynolds number. Temperatures were monitored until a new steady state was reached, at which point 1000 voltage samples were acquired from each thermocouple.

Figure 7 shows the temperature distribution for a typical test case measured at a Reynolds number of 60,000 and with a nominal heat input of 7.9 W. Also shown are the raw experimental temperatures averaged over elements, $\Delta \mathbf{T}_{\text{uncorrected}}$. These data are the basis for determining G^{-1}_{pipe} experimentally. To estimate conduction effects the experimental wall temperature distribution for each Reynolds number is used as a boundary condition at the pipe wall and the conduction through the pipe and insulation is modeled using FLUENT. A two-dimensional axisymmetric mesh was used with the coupled implicit double-precision solver. The up and downstream ends of the model, corresponding to the ends of the experimental test section, were treated as adiabatic and the outside surface of the insulation was modeled as being at ambient temperature. Using a specified $h=5$ W/m^2 K on the outer insulation surface resulted in negligible differences in heat transfer rates.

Only conduction losses from the copper element were corrected using FLUENT for several reasons. Heat gains on the adjacent downstream element are corrected using a different method discussed below. The magnitudes of the losses on other elements are much smaller than on the copper element. Therefore, not only are

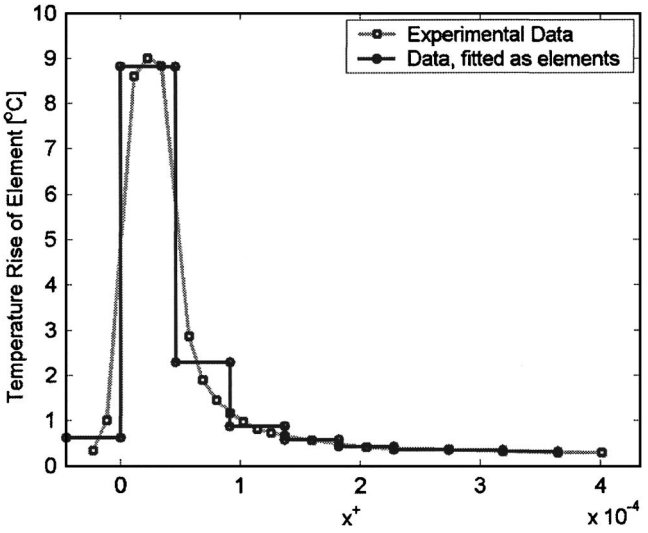

Fig. 7 Experimental temperature rise distribution Re=60,000

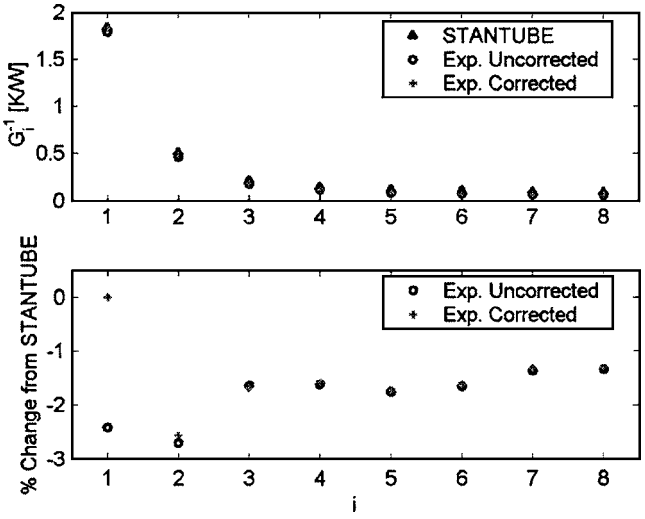

Fig. 8 Comparing elements of G^{-1} for Re=60,000

the effects of these losses less important than on the copper but the relative accuracy with which they can be predicted is reduced. In more complex geometries the downstream elements may not be measured at all, therefore, it is more important to see the effects of neglecting the temperature rises on these elements completely rather than correct them.

$G^{-1}_{\text{corrected}}$ is the IDGF determined by using the nominal power input into the copper element, the heat losses calculated in FLUENT, and the experimental temperature distribution. The nominal power input and $\Delta\mathbf{T}_{\text{uncorrected}}$ are used to create a $G^{-1}_{\text{uncorrected}}$ through Eq. (8) (the temperature rise upstream of the copper is neglected in $\Delta\mathbf{T}_{\text{uncorrected}}$). $G^{-1}_{\text{uncorrected}}$ is then used to estimate the correction to $\Delta\mathbf{T}_{\text{uncorrected}}$ needed to account for heating of the first element downstream of the copper by conduction. The new temperature rise on this element is

$$\Delta T_{\text{corrected}}(2) = \Delta T_{\text{uncorrected}}(2) - g^{-1}_{\text{uncorrected}}(1)\dot{q}_{\text{loss,down}}. \quad (9)$$

Where $\dot{q}_{\text{loss,down}}$ is the heat loss conducted from the copper to the first downstream element. This process can be repeated for all elements where conduction losses are calculated, however, it only has a significant effect on the element adjacent to the copper.

The calculated heat losses from the copper are then subtracted from the nominal heat input into the copper to create a corrected applied heat flow, $\dot{\mathbf{q}}_{\text{corrected}}$. This heat flow vector is further modified to account for radiation loss from the copper element (the emissivity of the PVC is estimated to be 0.8 [16]). The new temperature rise vector, $\Delta\mathbf{T}_{\text{corrected}}$, is used in conjunction with $\dot{\mathbf{q}}_{\text{corrected}}$ to calculate $G^{-1}_{\text{corrected}}$ via Eq. (8).

Figure 8 shows the uncorrected, corrected and STANTUBE values of G^{-1}_{pipe} and the percentage differences between them. The main error in the uncorrected version is on the copper element and is adequately adjusted using the correction analysis described above. The correction to the first downstream element does not significantly change the accuracy. However, demonstrating the feasibility of making this correction could be important in other geometries. The downstream elements agree within 3% of the magnitude of the semianalytical main diagonal element for all conditions measured. This accuracy, combined with their small magnitudes justifies using the uncorrected values.

The accuracy of the corrected IDGF varies somewhat with Reynolds number. Figure 9 shows the percentage error in the elements of $G^{-1}_{\text{corrected}}$ normalized by the value of the main diagonal element of G^{-1}_{STANTUBE} for all Reynolds numbers investigated here. It should be noted that this is a different normalization than is used for the percent uncertainties listed in Table 1. In Fig. 9 values are normalized by the value of the main diagonal element, which is the best measure of how an error will affect heat transfer predictions. The maximum error between $G^{-1}_{\text{corrected}}$ and G^{-1}_{STANTUBE} is less than 3%, which is less than the experimental uncertainty and suggests that the measurement techniques applied here are sufficiently accurate.

The following example illustrates the advantage of using the DGF over conventional correlations for h. The case considered is fully developed pipe flow with a sinusoidal variation in axial wall temperature at a Reynolds number of 60,000. Figure 10 shows the heat flux calculation using a correlation from [1] (similar to the Dittus–Boelter correlation), and an accurate calculation of the heat flux using a semianalytical DGF with a step size of 3.18 mm. The correlation prediction has large systematic errors, underestimating the heat transfer in regions where the wall temperature is rising and overestimating it elsewhere. The third set of points on Fig. 10 uses a reduced DGF (RDGF) calculated using $G^{-1}_{\text{corrected,reduced}}$. The RGDF is a truncated version of G_c^{-1} where g_i is assumed to be zero for $i>5$. It is difficult to measure the DGF for $i>5$, and the values are known to be small. This truncation will cause errors in the heat transfer prediction for simple boundary conditions such as constant wall temperature. However, for more complex bound-

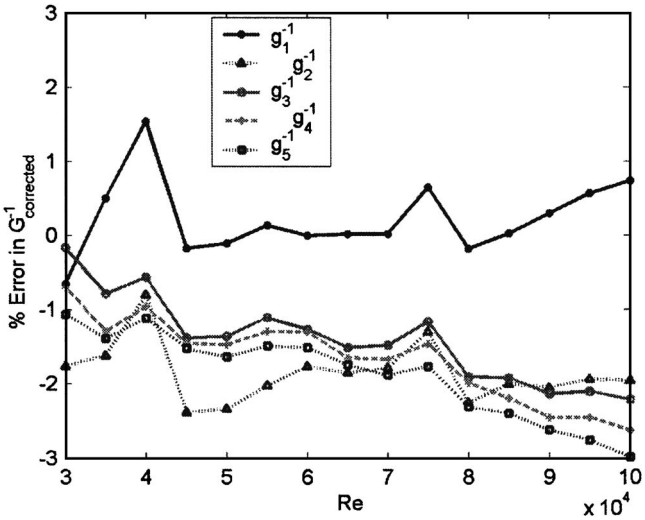

Fig. 9 Error in $G^{-1}_{\text{corrected}}$ normalized by main diagonal element vs Reynolds number

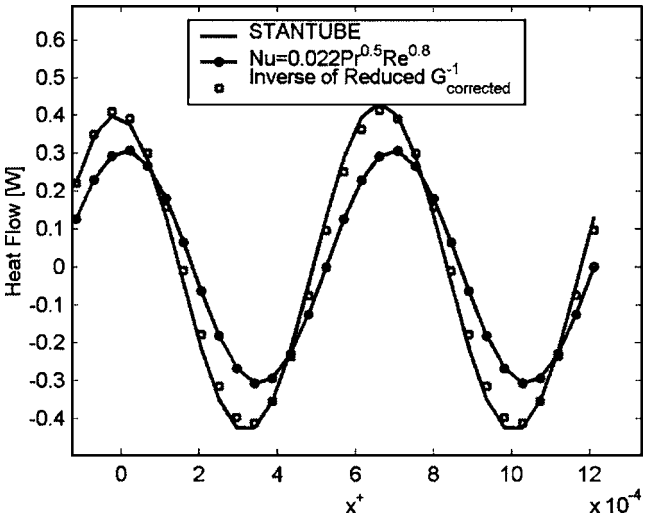

Fig. 10 Experimental and STANTUBE DGF compared to standard correlation for "*h*" for sinusoidal boundary conditions, Re=60,000

ary conditions where the wall temperature varies, the small errors tend to cancel. This is well illustrated by Fig. 10 which shows good agreement between the actual heat transfer rate and the rate calculated by the RDGF.

Uncertainty Analysis

Uncertainties in experimental results were calculated using the single-sample uncertainty analysis put forth by Kline and McClintock [17] and Moffat [18]. There are six major sources of experimental uncertainty in the calculation of the DGF: Thermocouple resolution, thermal conductivity of the PVC pipe and of the insulation, thickness of the thermal insulation around the pipe, the power applied to the heated copper element and the emissivity of the PVC pipe. It should be noted that uncertainty in the actual mass flow rate, and hence Reynolds number, does not directly affect the formulation of the DGF. Therefore, this uncertainty is accounted for by performing simulations using STANTUBE over the range of uncertainty in the Reynolds number.

The effect these uncertainties have on the values of the elements in the DGF is listed in Table 1 for Re=60,000. The trends are similar for all Reynolds numbers measured with the temperature uncertainty being the dominant effect.

The purpose of this paper is to introduce the DGF method for use in complex geometries encountered in engineering application; therefore, some discussion on the uncertainties that might be encountered is warranted. A major source of uncertainty could arise from estimating conduction losses. In this simple, axisymmetric geometry, a finite element code can be used to predict conduction losses. In more complex geometries the thermal boundary conditions are more difficult to define and the heat losses can come into contact with the flow at many locations, making corrections more uncertain. As an example consider rectangular cross-section serpentine cooling passages. The conduction is highly three-dimensional and heat losses can come back into the flow from upstream, downstream or on the sides of any heated element making heat loss corrections much more difficult and essentially necessitating the use of finite element codes for predicting heat losses. Embedded thermocouples away from the surface of the flow can be used to aid in the boundary condition specification in the heat loss models. In serpentine passage models there can also be significant pressure drop in the passages at Reynolds numbers similar to the highest of those in this paper such that variable properties could be present. The high levels of turbulence can also lead to lower temperature recovery factors such that the adiabatic wall temperatures vary spatially and differ significantly from the stagnation temperature. These effects can be difficult to quantify accurately.

Conclusions

This investigation has presented a discrete Green's function (DGF) approach for predicting heat transfer characteristics in internal flows, specifically fully developed pipe flows, that is valid for arbitrary thermal boundary conditions. Previous investigations have used the DGF method only for external flows. This new application of the DGF method provides a useful advantage over traditional heat transfer coefficients that are only valid for a single thermal boundary condition but are commonly used with other boundary conditions for a lack of a convenient alternative.

The Inverse discrete Green's function (IDGF) is measured experimentally and compared to analytical and numerical results. For moderate element sizes the IDGF results show excellent agreement with the numerical results generated using STANTUBE and with the semianalytical results. The experimental method employed here can be extended for use in more complex internal flows such as gas turbine blade internal cooling passages. This is advantageous for multiple reasons. Analytical and numerical solutions are not always available, or accurate, in complex geometries and any experimentally derived heat transfer coefficients will generally only be available for the simplest boundary conditions because of the experimental difficulties involved in measuring them. These cooling passages operate with very nonuniform thermal boundary conditions and large temperature gradients, making typical *h* formulations very inaccurate. The DGF technique is particularly well suited for this type of application, even when the temperature gradients are large enough to cause significant nonlinearity in the energy equation.

The flexibility to be applied to situations involving complex thermal boundary conditions and still yield accurate results is the greatest advantage the DGF has over traditionally calculated heat transfer coefficients.

Acknowledgment

The authors would like to thank Professor William Kays for his assistance and guidance with STANTUBE as well as the Department of Defense for support through the National Defense Science and Engineering Graduate (NDSEG) Fellowship and General Electric Aircraft Engines (GEAE) for financial support under the University Strategic Alliance program.

Nomenclature

D = Pipe inner diameter [m]
g_i = Element in row i column 1 of G [W/K]
g_i^{-1} = Element in row i column 1 of G^{-1} [K/W]
G = DGF matrix [W/K]
G^{-1} = Inverse DGF matrix [K/W]
G_{est} = Estimated DGF matrix, $(G^{-1})^{-1}$ [W/K]
h = Heat transfer coefficient, [W/m^2 K]
i = Index corresponding to row of G, G^{-1}
k = Thermal conductivity of fluid [W/mK]
Pr = Prandtl number, 0.707 for air
$\dot{q}''$ = Heat flux [W/m^2]
$\dot{q}$ = Heat flow [W]
r^+ = Dimensionless radial coordinate,[r/R]
R = Pipe radius [m]
Re = Reynolds number based on pipe diameter, D
ΔT = Wall temperature rise, see Eq. (4) [K]
x^+ = Dimensionless axial coordinate, $=2x/(\text{DRePr})$
y^+ = Dimensionless distance, normal to surface

References

[1] Kays, W. M., and Crawford, M. E., 1993, *Convective Heat and Mass Transfer*, McGraw-Hill, New York, Chaps. 9 and 14.

[2] Siegel, R., Sparrow, E. M., and Hallman, T. M., 1958, "Steady Laminar Heat Transfer in a Circular Tube with Prescribed Wall Heat Flux," Appl. Sci. Res., Sect. A, **7**(A), pp 386–392.

[3] Sleicher, C. A., and Tribus, M., 1957, "Heat Transfer in a Pipe with Turbulent Flow and Arbitrary Wall-Temperature Distribution" Trans. ASME, **79**, pp. 789–797.

[4] Batchelder, K., and Eaton, J. K., 2001, "Practical Experience with the Discrete Green's Function Approach to Convective Heat Transfer," ASME J. Heat Transfer, **123**, pp. 70–76.

[5] Vick, B., Beale, J. H., and Frankel, J. I., 1987, "Integral Equation Solution for Internal Flow Subjected to a Variable Heat Transfer Coefficient," ASME J. Heat Transfer, **109**(4), pp. 856–860.

[6] Hacker, J. M., and Eaton, J. K., 1997, "Measurements of Heat Transfer in a Separated and Reattaching Flow with Spatially Varying Thermal Boundary Conditions," Int. J. Heat Fluid Flow, **18**(1), pp 131–141.

[7] Mukerji, D., 2002, "Spatially-Resolved Measurements of Heat Transfer in Turbomachinery Applications" Thermosciences Division Report, TSD–145, Mechanical Engineering Department, Stanford University, Stanford, CA.

[8] Wang, Z., Ireland, P. T., Kohler, S. T., and Chew, J. W., 1998, "Heat Transfer Measurements to a Gas Turbine Cooling Passage with Inclined Ribs," ASME J. Turbomach., **120**, pp. 63–69.

[9] Mills, A. F., 1995, *Heat and Mass Transfer*, Irwin, Chicago, IL.

[10] Hsu, C., 1968, "Exact Solution to Entry-Region Laminar Heat Transfer with Axial Conduction and the Boundary Condition of the Third Kind" Chem. Eng. Sci., **23**, pp. 457–468.

[11] Notter, R. H., and Sleicher, C. H., 1971, "A Solution to the Turbulent Graetz Problem by Matched Asymptotic Expansions-II The Case of Uniform Wall Heat Flux" Chem. Eng. Sci., **26**, pp. 559–565.

[12] Crawford, M. E., and Kays, W. M., 1976, NASA CR–2742.

[13] Notter, R. H., and Sleicher, C. A., 1972, "A Solution to the Turbulent Graetz Problem—III Fully Developed and Entry Region Heat Transfer Rates" Chem. Eng. Sci., **27**, pp. 2073–2093.

[14] Notter, R. H., 1969, "Two Problems in Turbulence: A. A Theoretical and Empirical Study of the Limiting Form of the Eddy Diffusivity Near a Wall. B. Matched Asymptotic Expansions Applied to the Turbulent Graetz Problem" Ph.D. Thesis, University of Washington, Seattle, WA.

[15] Notter, R. H., and Sleicher, C. H., 1971, "The Eddy Diffusivity in the Turbulent Boundary Layer Near a Wall" Chem. Eng. Sci., **26**, pp. 161–171.

[16] Siegel, R., and Howell, J. R., 2002, *Thermal Radiation Heat Transfer*, Taylor & Francis, New York, App. B, C.

[17] Kline, S. J., and McClintock, F. A., (1953), "Describing Uncertainties in Single-Sample Experiments" Mech. Eng. (Am. Soc. Mech. Eng.), pp. 53–57.

[18] Moffat, R. J., (1988), "Describing the Uncertainties in Experimental Results" Exp. Therm. Fluid Sci., **1**, no. 1, pp. 3–17.

Heat Transfer Studies in the Flow Over Shallow Cavities

Paulo S. B. Zdanski
Department of Mechanical Engineering,
State University of Santa Catarina,
89223-000 Joinville, SC, Brazil

M. A. Ortega

Nide G. C. R. Fico, Jr.

Department of Aeronautical Engineering, Instituto Tecnológico de Aeronáutica, ITA 12228-900, S. J. dos Campos, SP, Brazil

Fluid flows along a shallow cavity. A numerical study was conducted to investigate the effects of heating the floor of the cavity. In order to draw a broader perspective, a parametric analysis was carried out, and the influences of the following parameters were investigated: (i) cavity aspect ratio, (ii) turbulence level of the oncoming flow, and (iii) Reynolds number. A finite-difference computer code was used to integrate the incompressible Reynolds-averaged Navier–Stokes equations. The code, recently developed by the authors, is of the pressure-based type, the grid is collocated, and artificial smoothing terms are added to control eventual odd–even decoupling and nonlinear instabilities. The parametric study revealed and helped to clarify many important physical aspects. Among them, the so called "vortexes encapsulation," a desirable effect, because the capsule works well as a kind of fluidic thermal insulator. Another important point is related to the role played by the turbulent diffusion in the heat transfer mechanism.
[DOI: 10.1115/1.1924630]

1 Introduction

Flow over cavities is encountered in many engineering applications. Solar energy collectors, combustion chambers, and environmental problems are some examples. The inspiration for this research work is the flat plate solar energy collector equipped with wind barriers. Gomes [1] has shown experimentally that the efficiency of heat absorption improves accordingly, if we introduce vertical wind fences along the perimeter of the collector (Fig. 1). The fluid-dynamical details of the problem were investigated by the present authors in previous works [2,3]. In general, the flow over solar collectors—imagined mounted on the roof of a building—is three-dimensional in character. Besides, the angle of attack between the wind direction and the plane of the collector can take any value, from zero up to 90 deg. In order to start with a tractable problem, we have made the following simplifying assumptions: (i) the flow is two-dimensional, (ii) the angle of attack of the wind is equal to zero, and (iii) stretches of horizontal walls are mounted at the entrance and exit so as to flush the top of the barriers. With these simplifications we end up with a shallow cavity (Fig. 2).

The flow inside cavities is characterized by the appearance of large recirculation regions [4]. Most of the works reported in the literature refer to two-dimensional cavities for which the ratio of length to height (aspect ratio) is small. Richards et al. [5] have studied experimentally the turbulent heat transfer inside cavities with small aspect ratios (less than one). They showed that the heat transfer rate is sensitive to the aspect ratio, but little affected by the boundary layer thickness at the separation point. Aung [6] reports on experimental laminar heat transfer data for cavities with aspect ratios from one to four. Besides, this author compares cavity and flat plate results, at the same conditions. The conclusion is that the heat transfer rate is more intense in the flat plate than in the cavity. Matos et al. [7] presented turbulent heat transfer results for two-dimensional cavities, but data for the free cavity is restricted to the presentation of a pressure distribution along the floor. More recently, Zdanski et al. [2,3] have reported numerical results for both laminar and turbulent flows over cavities of high aspect ratio. The results showed that, for some range of certain investigated parameters (Reynolds number, entrance turbulence level and aspect ratio), the mean external flow does not touch the floor of the cavity. This condition may be attained either when only one rotating cell covers all the cavity floor or when two cells are present but are, say, "encapsulated" [3].

The main objective of this work is to extend the analysis to cavities of large aspect ratios including heat transfer effects. We consider now heating of the cavity floor. As before, a parametric study was conducted. This has confirmed the beneficial effect of vortex encapsulation, a phenomenon that was inferred in former woks [2,3]. Besides, the results have also revealed that the maximum heat transfer rate at the cavity floor occurs at the position of maximum turbulent diffusion on layers adjacent to the floor.

The numerical scheme adopted to solve the system of equations was developed by the authors [4]. Central difference schemes are used to discretize both convective and diffusive terms in a collocated mesh. To control eventual odd–even decoupling and nonlinear instabilities, artificial viscosity terms are added to the equations. The magnitude of these terms is controlled by the user, in such a way that their influence upon the final results is practically eliminated. Turbulence is predicted by means of two-equation $\kappa-\varepsilon$ modeling methods [8,9].

It is important to have in mind that ours here is essentially an engineering approach, and, therefore, the interest is focused on the steady mean flow. We are aware that the dynamics inside the cavity is extremely important (and complicated), and that the instantaneous flow play a very important role. In order to learn about this and compare results in the future, we are working the same problem with our group's DNS/LES capability. But, the emphasis of this paper is on the engineering aspect of the problem.

2 Mathematical Model

2.1 Governing Equations. The flow is mathematically modeled by the continuity, momentum and energy equations. The incompressible, Reynolds-averaged form of these equations, in Cartesian coordinates and indicial notation, is

$$\frac{\partial U_j}{\partial x_j} = 0, \tag{1}$$

$$\frac{\partial(\rho U_i)}{\partial t} + \frac{\partial(\rho U_j U_i)}{\partial x_j} = -\frac{\partial p}{\partial x_i} + \frac{\partial}{\partial x_j}(2\mu S_{ij} - \rho\overline{u_i' u_j'}), \tag{2}$$

$$\frac{\partial(\rho c_p T)}{\partial t} + \frac{\partial(\rho c_p U_i T)}{\partial x_i} = \frac{\partial}{\partial x_i}\left[\kappa\frac{\partial T}{\partial x_i} - \rho c_p \overline{u_i' T'}\right], \tag{3}$$

where S_{ij}, the mean strain rate, is given by

Contributed by the Heat Transfer Division for publication in the JOURNAL OF HEAT TRANSFER. Manuscript received February 5, 2004. Final manuscript received December 20, 2004. Review conducted by: Karen Thole.

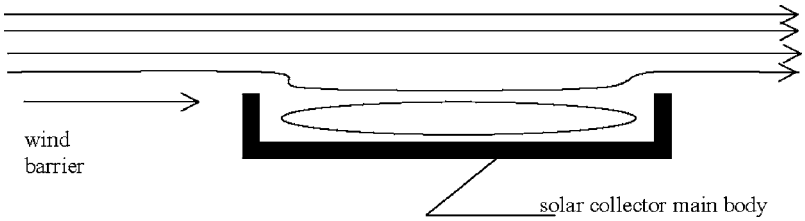

Fig. 1 Sketch of the flow over a solar collector with wind barriers

$$S_{ij} = \frac{1}{2}\left(\frac{\partial u_i}{\partial x_j} + \frac{\partial u_j}{\partial x_i}\right). \quad (4)$$

The symbols that appear in the equations above are standard, so there is no need to redefine them here (see also the Nomenclature). The bar on top of fluctuating correlation terms are indicative of mean values, and parameters with no bars are, evidently, mean values of corresponding properties. The set of Eqs. (1)–(3), are usually known in the literature as the Reynolds-Averaged Navier–Stokes (RANS) equations. Within the framework of an eddy viscosity concept, and adopting the traditional Boussinesq approximation, the Reynolds stresses and turbulent heat fluxes are approximated by

$$-\rho\overline{u_i' u_j'} = \mu_T\left(\frac{\partial U_i}{\partial x_j} + \frac{\partial U_j}{\partial x_i}\right) - \frac{2}{3}\delta_{ij}\rho k, \quad (5)$$

$$-\rho c_p\overline{u_i' T'} = \kappa_T\frac{\partial T}{\partial x_i}, \quad (6)$$

where μ_T and κ_T are turbulent viscosity and turbulent thermal conductivity, respectively. Values of κ_T are obtained by introducing the turbulent Prandtl number, Pr_t. The usual practice indicates $\mathrm{Pr}_t = 0.9$. In this work, values of μ_T and κ_T are obtained after the solution of a two-equation $k-\varepsilon$ turbulence model. k here stands for the turbulent kinetic energy (per unit mass), while ε indicates the turbulent kinetic energy dissipation (also per unit mass). We have employed two different types of models: a standard high-Reynolds number version [8] and a specialized low-Reynolds number version due to Hwang and Lin [9]. Because we have not introduced any novelty in the models, and in order to spare space, we shall not present those equations here. The interested reader should consult the corresponding literature.

2.2 Numerical Procedure. Discretization, in a collocated mesh, is done using central-difference expressions both for diffusion and convection terms. Smoothing by artificial dissipation is adopted in order to control odd–even decoupling and nonlinear instabilities. The equations, written in conservation-law form, are solved implicitly. Approximate factorization [10] is introduced to reduce the computational effort. The principle of mass conservation, i.e., free divergence of the velocity field, is enforced by solving a Poisson equation for pressure. In contrast to other traditional pressure-correction methods, convergence of the present scheme is assured without resorting to any kind of relaxation parameters. For further details the reader can consult Zdanski et al. [4].

2.3 Boundary Conditions. At the inlet plane (Fig. 2) distributions of velocity, temperature, turbulent kinetic energy, and turbulent dissipation rate are specified. The pressure at the entrance plane was extrapolated from internal cells. At the exit frontier parabolic conditions were established for all variables. At the upper boundary, coupling with the free stream flow is used. At solid walls the condition of no-slip was enforced, and the shear stress and heat flux are obtained from the law of the wall together with the standard high-Reynolds $k-\varepsilon$ model. The values of pressure and turbulent kinetic energy at the wall are obtained by a zero-order extrapolation from the values at the first node. Values of the turbulent dissipation at the first node away from the wall are not obtained by solving the complete ε equation, but, rather, they result from a balance between production and dissipation [11]. For the simulations with the low-Reynolds number model, the values of the turbulent kinetic energy and the modified dissipation rate [9], $\tilde{\varepsilon}$, at the wall, are assumed to be zero.

3 Results and Discussion

3.1 Verification and Validation of the Numerical Code. For the purposes of verification and validation of the numerical code an assortment of several cases were run. Many of these have already been published [3] and will not be treated here. We shall

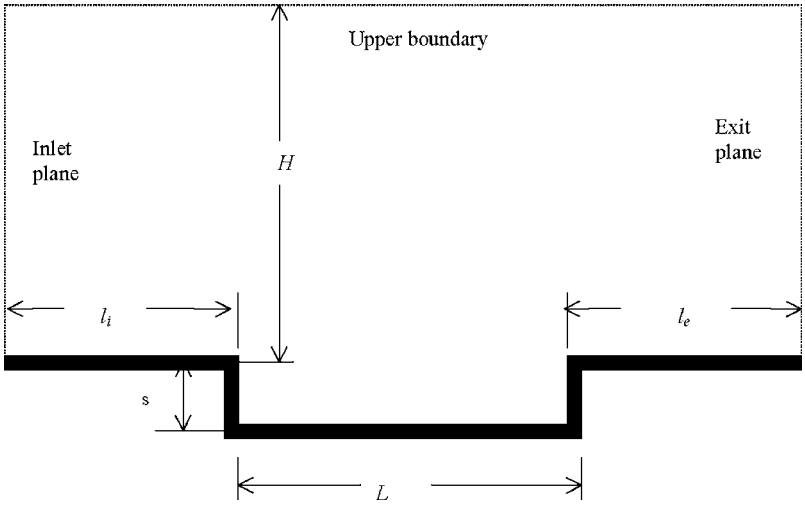

Fig. 2 Cavity geometry with the main dimensions

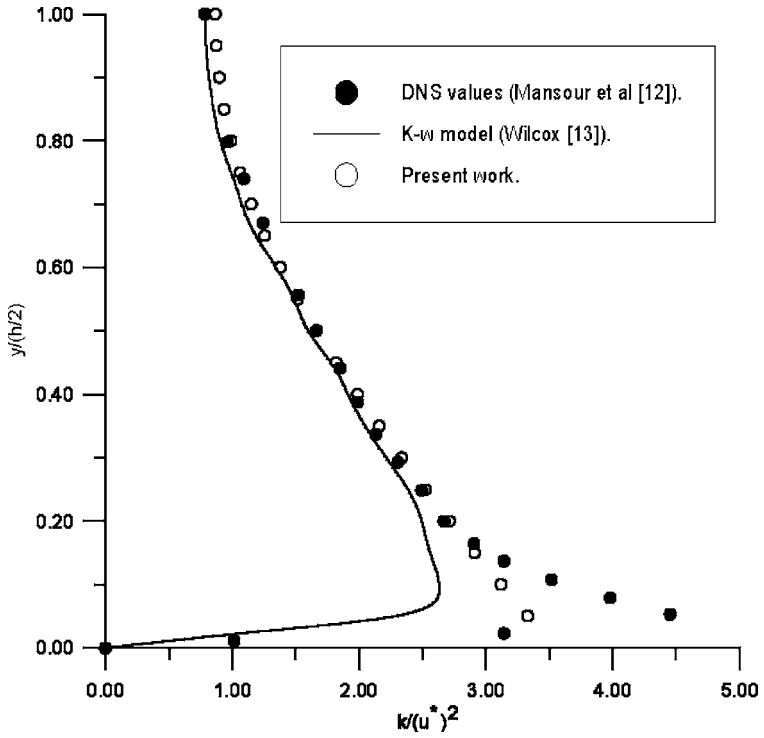

Fig. 3 Cross-sectional profiles of turbulent kinetic energy for the two-dimensional duct

concentrate only on those cases that involve heat transfer. Specifically, we present results for the turbulent flow in a two-dimensional duct, first with a constant cross section and then with a sudden expansion. The overall agreement with literature data was in general very good.

3.1.1 The Turbulent Two-Dimensional Duct. The turbulent flow with heat transfer in a two-dimensional duct was simulated. The height of the duct is h, and its length is $60h$. The computational mesh is uniform with 201×31 grid points in the streamwise and cross-sectional directions, respectively. Boundary conditions at the inlet plane: uniform velocity and temperature profiles, with the Reynolds number, based on the height of the channel, equal to 13750. For this test, the following values were adopted: $u_i=18.5$ m/s, $k_i=0.02(u_i)^2/2.0$, where u_i and k_i are, respectively, mean velocity and mean turbulent kinetic energy (considered also uniform) at the inlet section. At the exit plane, parabolic nonreflexive conditions are specified for all variables, except for pressure, whose variation is considered linear. At the walls, a constant heat flux is imposed, $q_w=270$ W/m^2. The turbulence model used in this simulation is the standard high-Reynolds number $k-\varepsilon$. The first computational grid point lies in the turbulent region, i.e., $y^+=30$, and the gap between the first point and the wall is bridged by the wall functions.

Figure 3 presents nondimensional turbulent kinetic energy profiles, $k^+=k/(u^*)^2$, at the exit section of the channel. The present high-Reynolds number solution is compared with DNS data of Mansour et al. [12] and RANS computations by Wilcox [13]. The overall agreement is good, except in the near wall region. The standard $k-\varepsilon$ model underpredicts the maximum value in the buffer zone, because the first computational point falls already in the fully turbulent region. The nondimensional velocity and temperature profiles are plotted in Figs. 4 and 5. The velocity profile, $u^+=u/u^*$, is compared with the universal log-law, while the temperature profile, $T^+=(T_w-T)/T^*$, is checked against analytical correlations [14]. In the above expressions u^* is the friction velocity, T^* is the characteristic temperature, and T_w is the local wall temperature. The overall agreement is quite satisfactory for all ranges of y^+.

For this case, a grid-independence study was conducted, and the solutions for three different grid resolutions appear in Fig. 6. As the reader can observe, the code behaved very well under this test and the results are basically grid independent.

The turbulent flow with heat transfer in a two-dimensional duct was also simulated with the low-Reynolds number $k-\varepsilon$ model of Hwang and Lin [9]. In this test the computational domain has a height of $h/2$ (half channel) and the length is $60h$. The grid is stretched, with points clustering at the near wall region, having a total of 201×31 points in the streamwise and cross-sectional directions, respectively. The first point close to the wall is placed at $y^+=1$, a position inside the viscous sublayer. Constant velocity and temperature profiles were enforced at the entrance, i.e., $u_i=7$ m/s and $T_i=300$ K. The Reynolds number based on the height of the channel is $\mathrm{Re}_s=6500$. At the wall, we assumed no-slip condition for the velocity and a constant heat flux, $q_w=270$ W/m^2. At the exit section parabolic conditions were employed for all variables (excepting the pressure). For the turbulent quantities (k and $\tilde{\varepsilon}$) the following boundary conditions were specified: at the entrance section, uniform profiles; at the walls, the two variables vanish. The turbulence model uses a modified variable, $\tilde{\varepsilon}$, for the turbulent dissipation [9]. This variable is defined in such way that its value at the wall is zero.

Figure 7 shows normalized turbulent kinetic energy profiles (k^+) at the exit section of the channel. Agreement with literature data is good, especially at the near wall region. Profiles of non dimensional turbulent dissipation rate, $\varepsilon^+=\nu\varepsilon/(u^*)^4$, are presented in Fig. 8. Here, agreement is quite good along all the range of y^+. It is worth noting that the turbulence model of Hwang and Lin [9] predicts a maximum value for ε^+ exactly at the wall. This behavior agrees with DNS data [12], but contrasts the experimental evidence [15]. This seems to be an open question, and the correct

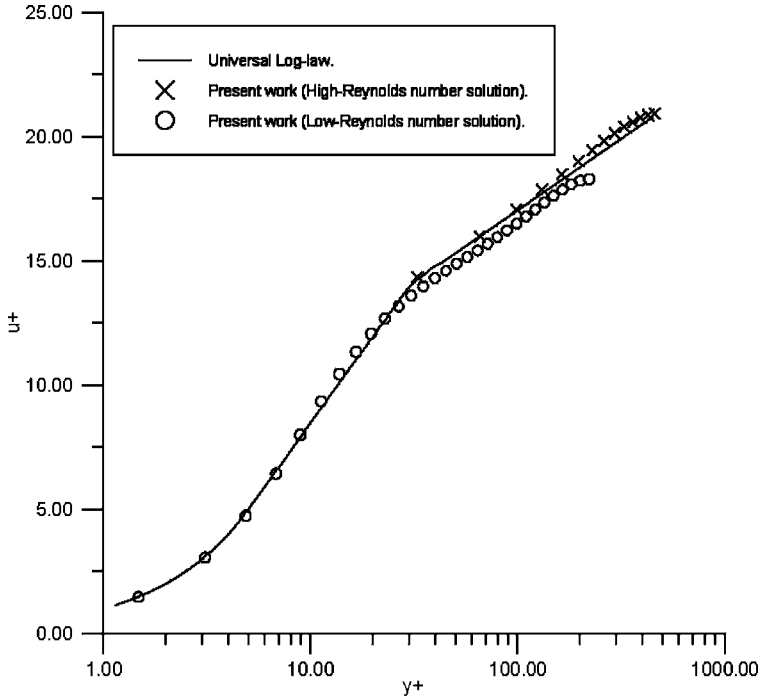

Fig. 4 Comparison of normalized velocity profile with the universal log law

behavior of ε near the wall is under discussion. Normalized velocity and temperature profiles are shown on Figs. 4 and 5. Once again the results of the present work compared well with analytical data.

3.1.2 The Two-Dimensional Duct with a Sudden Expansion. This case is commonly used in the validation of codes whose scope is basically the calculation of flows with large recirculation regions. Besides, there is a great number of literature references, both numerical and experimental. The overall geometry is depicted in Fig. 9. The dimensions of the computational domain are: $l=3s$, $L=20s$, $h=4s$, and $H=5s$. This geometry was simulated with both high- and low-Reynolds number turbulence models. The computational mesh, for the high-Reynolds number model, has the following distribution: 31×31 grid points in the entrance region and 121×71 in the region downstream of the step. The grid is stretched with points clustering next to the walls and in the region of the expansion. The Reynolds number based on the step height is $\mathrm{Re}_s=28\,000$. At the inlet plane, a turbulent mean velocity profile is adopted, i.e., $u_i=u_\infty(y/\delta)^{1/7.05}$, where $u_\infty=11.3$ m/s and $\delta=1.1$ s. The temperature, $T_i=300$ K, is considered uniform along the inlet section. At the horizontal wall downstream of the step a constant heat flux, $q_w=270$ W/m^2, was imposed. At the exit section parabolic boundary conditions are applied to all variables. Let us also point out that the Cartesian coordinates x and y are measured from the lower step corner.

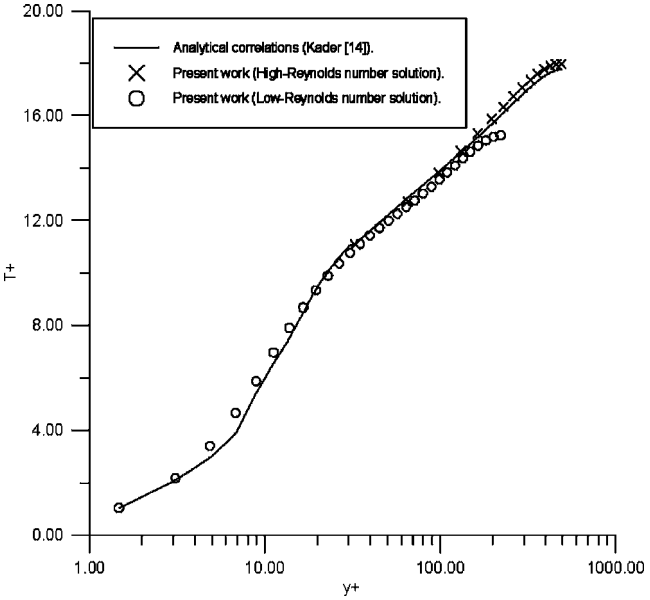

Fig. 5 Comparison of normalized temperature profile with analytical data

First, we discuss the high-Reynolds number case. The calculated reattachment length is $(x_r/s)=5.9$. Experimental data due to Vogel and Eaton [16] shows that $(x_r/s)=6.65$. Keeping in mind the well-known fact that the standard high-Reynolds number $\kappa-\varepsilon$ model underestimates the reattachment length [11,17], the result can be considered as good. In Fig. 10 the friction coefficient, c_f, at the horizontal wall downstream of the step, is compared with experimental data (Vogel and Eaton [16]). The Stanton number, $\mathrm{St}=h/\rho c_p u_\infty$, is defined in terms of the local convection coefficient, $h=q_w/(T_w-T_i)$. One can observe in Fig. 11 that our solution is overestimating the amount of heat transfer at the recirculation region $(x/h<7)$. This is due to two different reasons, both related to the high-Reynolds number turbulence model. The first is connected to the fact that, as we mentioned earlier, this type of $k-\varepsilon$ model underpredicts the reattachment length. In the present instance our solution gives $x_r/s=5.9$, while the experimental value corresponds to $x_r/s=6.65$. But the peak of heat transfer is located slightly to the left of x_r [16]. This explains why ours and the experimental peak are not in phase. The second point is connected to the value of the turbulent Prandtl number, Pr_t. In our simulations we have used $\mathrm{Pr}_t=0.9$, a value usually encountered in the literature. What happens is that, in general, $\mathrm{Pr}_t=0.9$ contributes to overpredicted values of heat fluxes [18].

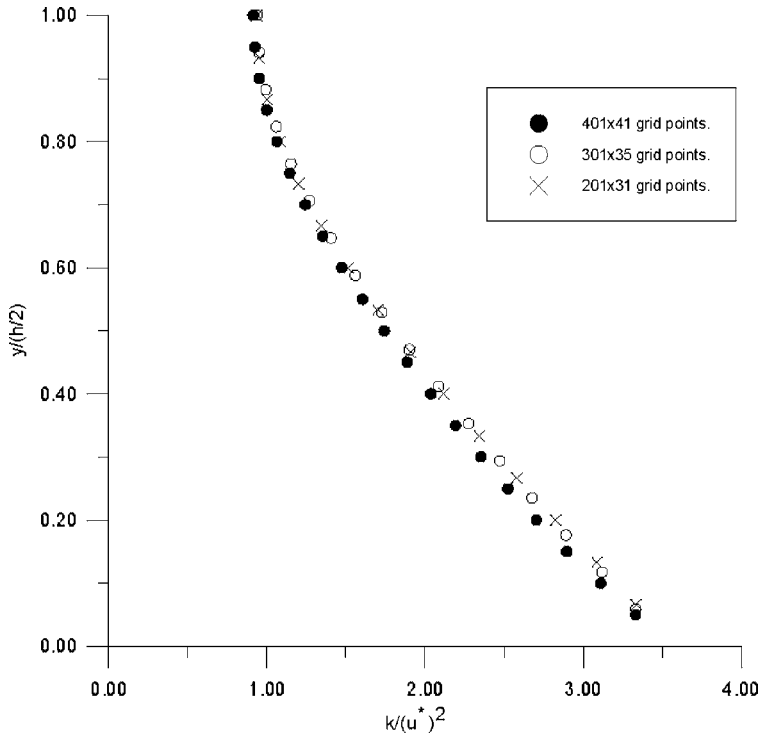

Fig. 6 Cross-sectional profiles of turbulent kinetic energy: Grid refinement study

The sudden expansion geometry was also simulated with the low-Reynolds number $k-\varepsilon$ model of Hwang and Lin [9]. For this case the computational mesh has 31×31 and 171×91 grid points in the regions before and after the step, respectively. Boundary conditions are the same as those for the high-Reynolds number simulations, with the exception of the vanishing values of the turbulent quantities at the wall. The reattachment length computed with the low-Reynolds $k-\varepsilon$ model is $(x_r/s)=6.4$, a value that is in close agreement with the experimental data ($(x_r/s)=6.65$). Figures 10 and 11 present friction coefficient and Stanton number distributions, respectively, along the floor downstream of the step. Again, comparisons are made with the experimental data of Vogel and Eaton [16]. As can be observed, our results are in good agreement with the experimental data.

The two-dimensional duct with a sudden expansion was taken as a fundamental reference for the cavity flow exploration that were to come, especially in the choosing of the turbulence model. Figure 11 indicates that the gain in accuracy resulting from the use of the low-Reynolds number model, when compared to the high-Reynolds number model, is not so expressive (in terms of the heat

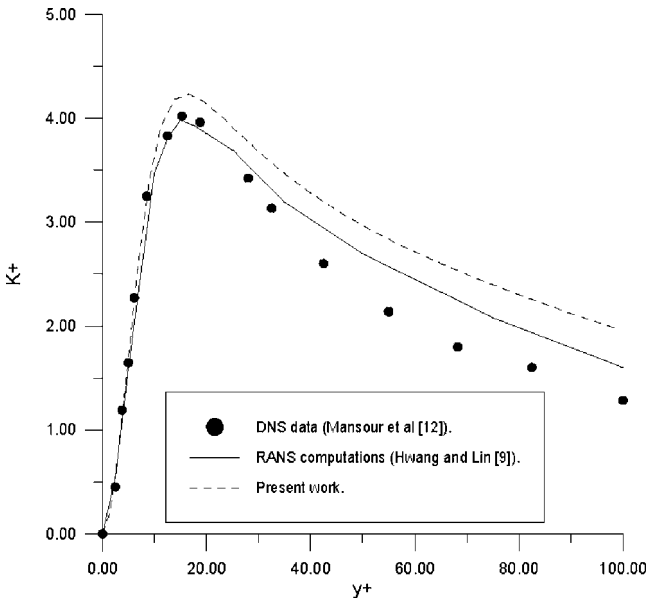

Fig. 7 Two-dimensional duct: Cross-sectional profiles of normalized turbulent kinetic energy

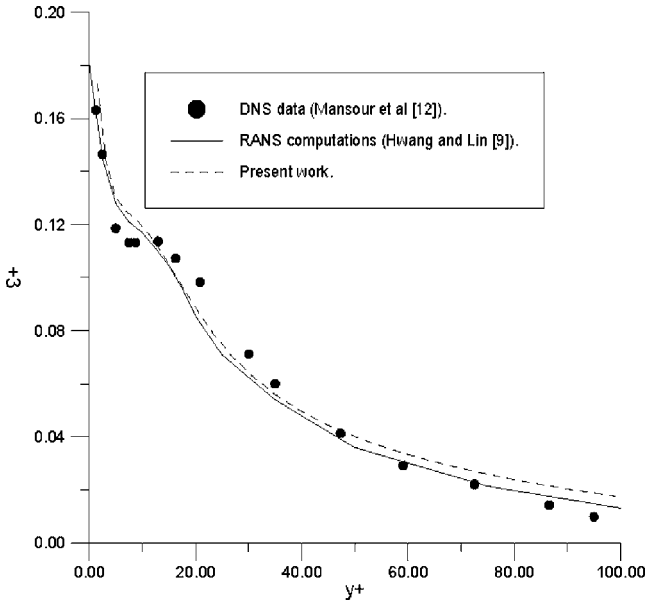

Fig. 8 Two-dimensional duct: Cross-sectional profiles of normalized turbulent kinetic energy dissipation

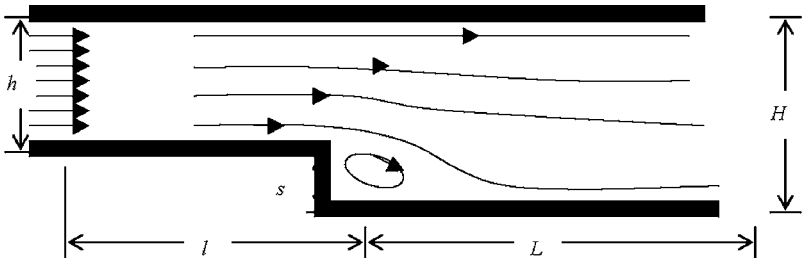

Fig. 9 Two-dimensional channel with a sudden expansion

transfer at the wall), and this is most so in the region of the recirculating bubble. Therefore, for the extensive parametric studies, we have, usually, used the high-Reynolds number model. This has spared a great amount of computing time. Anyhow, some of the most important cases were also calculated using the low-Reynolds model what has enriched the comparison of cases.

By observing the results presented above, which span all the main aspects of the cases to be tackled in the sequel, the reader can appreciate the good overall agreement between our solutions and former published data. This fact corroborates the validation of the computational code—now in terms of heat transfer predictions—as a valid numerical tool.

3.2 Numerical Accuracy Analysis. The degree of accuracy of a numerical scheme, just like the uncertainties in an experimental work, is essential for the credibility of the obtained results. The spatial accuracy of a numerical method can be obtained comparing solutions, with different grid resolutions, to an analytical case [19]. This procedure was adopted in this work. The following expression is used to estimate the error at each grid point:

$$e(h) = \sqrt{(\text{analytical value-numerical value})^2}. \tag{7}$$

Having obtained h_1 and h_2, the errors for two grid resolutions, the order of the scheme follows from the expression [20]

$$\text{ord} = \left(\log\left[\frac{e(h_1)}{e(h_2)} \right] \Big/ \log\left[\frac{h_1}{h_2} \right] \right). \tag{8}$$

The laminar flow in a two-dimensional duct was used as the reference case for this study. The fully developed parabolic profile was compared to the numerical solution obtained with the present code. The results of this comparison are presented in Table 1. As can be observed, the order of the scheme has a value around 1.64 (taken as the arithmetic mean along the section). The numerical code uses central difference formulas for the space discretization [4], what corresponds, nominally, to order two. In reality, the study shows that the scheme is a little less accurate, with order 1.64.

3.3 Computational Grid for the Cavity Studies. A typical computational grid for the cavity simulations is shown in Fig. 12. Points clustering is applied close to solid walls and to the horizontal plane connecting the two corners, that is, where the strongest gradients are expected to appear. In spite of the parabolic character of the boundary conditions at the exit boundary, numerical experiments showed that, a minimum value of $l_e = 6s$ (Fig. 2), was necessary in order to avoid spurious interference on the numerical solution. As indicated in Fig. 2, H is the height of the computational domain above the horizontal basic plane. For the

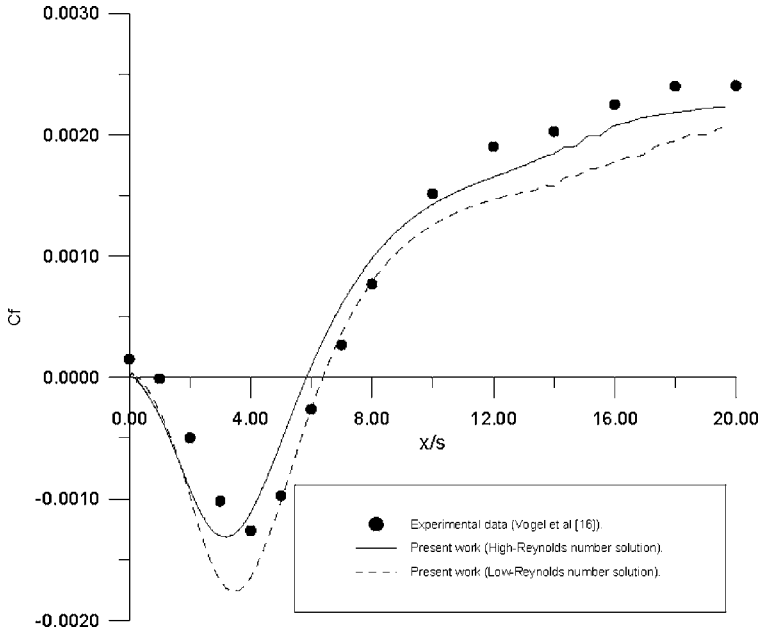

Fig. 10 Friction coefficient distribution along the horizontal wall downstream of the step

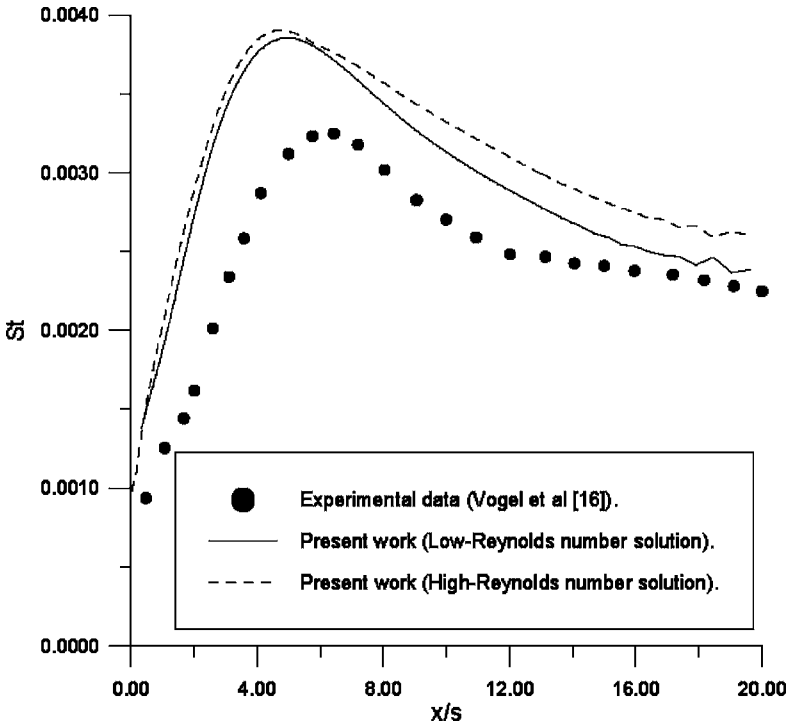

Fig. 11 Stanton number distributions along the horizontal wall downstream of the step: Comparison of high- and low-Reynolds number solutions

simulations performed in this work a minimum value of $H=3s$ was sufficient. Any grid specifics for different situations will be indicated in the text.

3.4 Turbulent Heat Transfer in Shallow Cavities. Most flows of interest are turbulent. To the author's knowledge very little work has been done on turbulent flows over high aspect ratio cavities. Therefore, careful attention will be devoted to this type of flow. At first we shall discuss the case of the "reference cavity," for which an assortment of results will be presented. After this, a parametric study will be conducted. For the reference cavity, and for the sake of a thorough and complete comparison, both turbulent models, high and low, were used. As mentioned earlier, the parametric study was conducted relying essentially on the high-Reynolds number $k-\varepsilon$ model.

3.4.1 Reference Cavity. The aspect ratio of the typical cavity is equal to 8. This figure comes out from the work of Gomes [1] as the value that corresponds to the minimum heat loss. The depth was taken as equal to 4.0 cm and the entrance velocity equal to 8 m/s, what corresponds to $Re_s=21{,}255$. The oncoming turbulent kinetic energy is assumed as 4% of the mean free-stream kinetic energy. The temperature at the entrance section is uniform, i.e., $T_i=300$ K. The same value was enforced at solid walls, except at the floor of the cavity, where we have adopted $T_w=350$ K. The calculation domain is such that $l_i=3s$, $l_e=6s$, and $H=3s$ (Fig. 2). The grid is not uniform along the domain. For the high-Reynolds

Table 1 Results of the numerical accuracy study

Analytical solution (u/u_i)	141x41 grid points (u/u_i)	Error (h_1)	141x81 grid points (u/u_i)	Error (h_2)	Order of the scheme
0.285	0.2679	0.0171	0.280	0.005	1.77
0.54	0.5116	0.0284	0.5315	0.0085	1.74
0.765	0.7287	0.0363	0.7539	0.0111	1.71
0.96	0.9170	0.043	0.9468	0.0132	1.70
1.125	1.0780	0.047	1.1099	0.0151	1.64
1.26	1.210	0.05	1.2437	0.0163	1.61
1.44	1.3830	0.057	1.420	0.02	1.51
1.5	1.4430	0.057	1.4785	0.0215	1.41

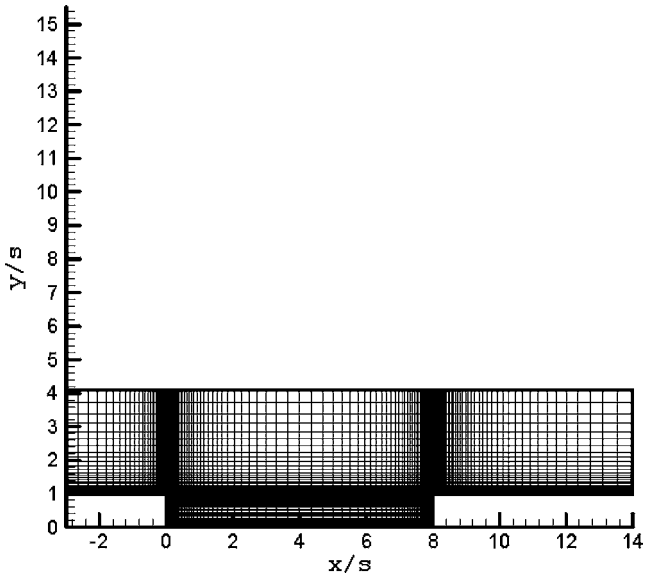

Fig. 12 Typical computational grid with points clustering

number model simulation, the total number of nodes is 31×31 upstream of the first corner, 81×71 in the region of the cavity, and 51×31 downstream of the second corner. In the case of the low-Reynolds number model solution, the number of grid points used is 31×31, 103×91, and 51×31 in the regions referred above, respectively. The maximum stretching factor was equal to 9%.

Figure 13(*a*) shows the topology of the flow inside the cavity obtained with the high-Reynolds number $k-\varepsilon$ turbulence model. Two structures are formed, a big one resulting from the main separation at the upstream corner and a small one in front of the downstream vertical wall. The external stream does not reattach and the flow is reversed along all the floor of the cavity—this is an important point, and more about it will be discussed later. The streamlines map for the mean flow in the case of the low-Reynolds number simulation is showed in Fig. 13(*b*). As one can observe there is only slight differences between the two solutions.

The pressure variation in an incompressible flow field is in general quite small. One can observe in Fig. 14 the C_p distribution along the cavity floor. There is a region for which the pressure coefficient is negative, and this corresponds to the center of the great recirculating bubble. The region of high pressure corresponds to stagnation conditions in front of the downstream vertical wall. Values of C_p plotted in Fig. 14 are referred to a mean value of pressure at the entrance section. Again there is good agreement between high- and low-Reynolds number solutions.

Figure 15 shows transversal mean temperature profiles for some stations inside the cavity, i.e., $x/s=1.0,3.0,5.0,7.0$. As can be observed, close to the upstream step, $x/s=1.0$ and $x/s=3.0$, a high temperature level is maintained from the floor up to $y/s=1$. This is a consequence of the insulating effect due to the presence of the large recirculating structure that is formed at this region. As the distance increases, $x/s=5.0$ and 7.0, the temperature level drops accordingly. For the later positions, the external flow penetrates further inside the cavity and the convection mechanism becomes more intense. The agreement between the high- and low-Reynolds number solutions, for the temperature distribution, is quite satisfactory.

The heat flux at the cavity floor is plotted in Fig. 16(*a*). As can be seen, a low heat transfer rate occurs in the region of the large bubble, and the distribution passes by a maximum around $x/s=5$. A difference exists between the high- and low-Reynolds number solutions, in spite that the qualitative trend is basically the same. This difference is related to the way by which the wall heat rate is predicted. The high-Reynolds number model uses the law of the wall (Arpaci and Larsen [21], p. 445), while the low-Reynolds number model permits the calculation of the temperature gradient at the wall, after the solution of the entire temperature field is obtained.

To better understand the heat flux behavior at the cavity floor, we have computed the turbulent correlation $\overline{u'T'}$ at a region close to the wall. This correlation represents the heat flux due to turbulent fluctuations, and is plotted in Fig. 16(*b*). As can be observed, the distribution of $\overline{u'T'}$ at a plane parallel and close to the wall $(y/s=0.1)$ is very similar to the heat flux distribution at the wall itself $(y/s=0)$. Besides, the peaks of these two quantities are in phase. This is strong evidence that the maximum value of the heat flux at the cavity floor occurs at the position where the turbulent diffusion close to the wall is also a maximum. What is certainly happening is that, due also to the low velocities at this position, the main mechanism of wall heat "pumping" is the turbulent diffusion.

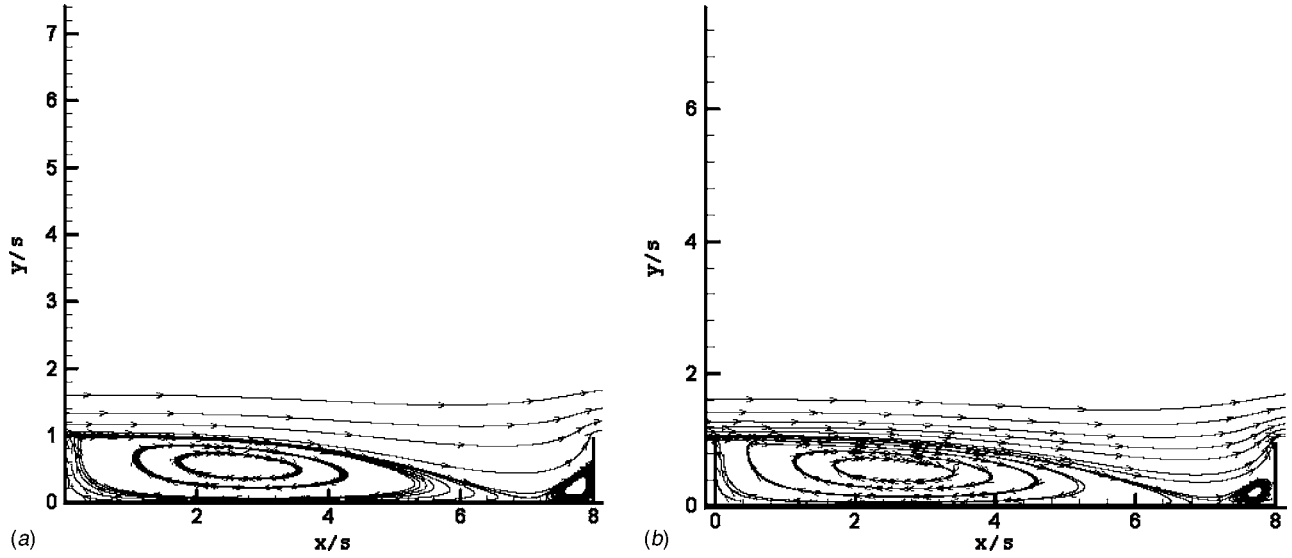

Fig. 13 Streamlines for the typical cavity, AR=8. (a) High-Reynolds number turbulence model solution; (b) Low-Reynolds number turbulence model solution.

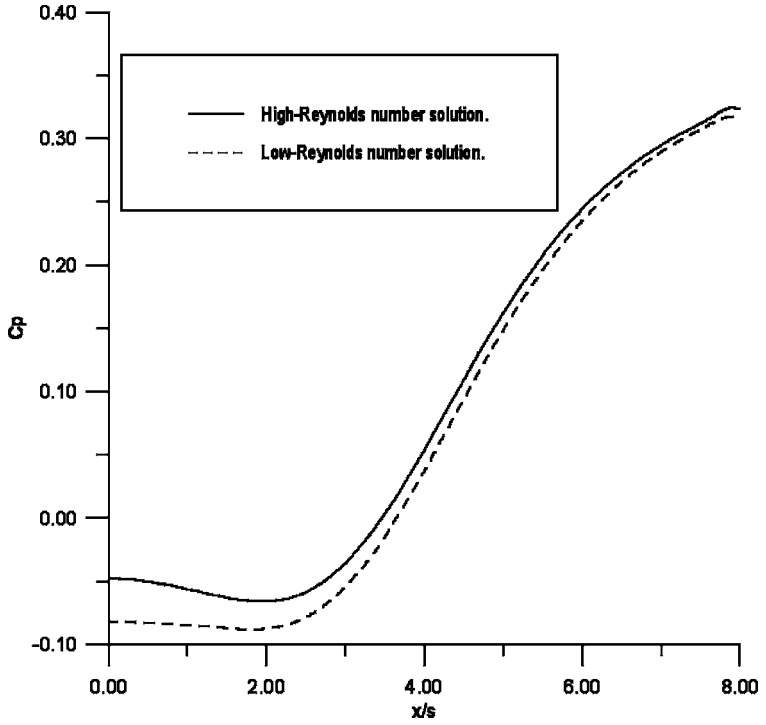

Fig. 14 Distribution of pressure coefficient along the cavity floor (AR =8)

We pass now to a parametric study of the flow over the cavity. The following influences will be investigated: (i) Aspect ratio, (ii) Entrance level of turbulence, and (iii) Reynolds number, Re_s. In the discussions to follow we shall concentrate mainly on the heat transfer at the cavity floor, because our main objective here is to understand the conditions for minimum convective activities along the floor of the cavity.

3.4.2 Influence of the Aspect Ratio. We have considered cavities with aspect ratios equal to 6, 8, 10, and 12. All the other parameters defining the flow, including the Reynolds number and the level of turbulence of the incoming stream, were considered equal to the values of the reference case (Sec. 3.4). Figure 17 gives the streamline map for AR=6. There is only one recirculating bubble inside the cavity. The distribution of the heat flux at the wall is shown in Fig. 21(*a*). Again, there is a peak of heat transfer, now between $x/s \approx 4$ and $x/s \approx 5$. And also again, this position is basically coincident with the peak of the turbulent correlation $\overline{u'T'}$ [see Fig. 21(*b*)].

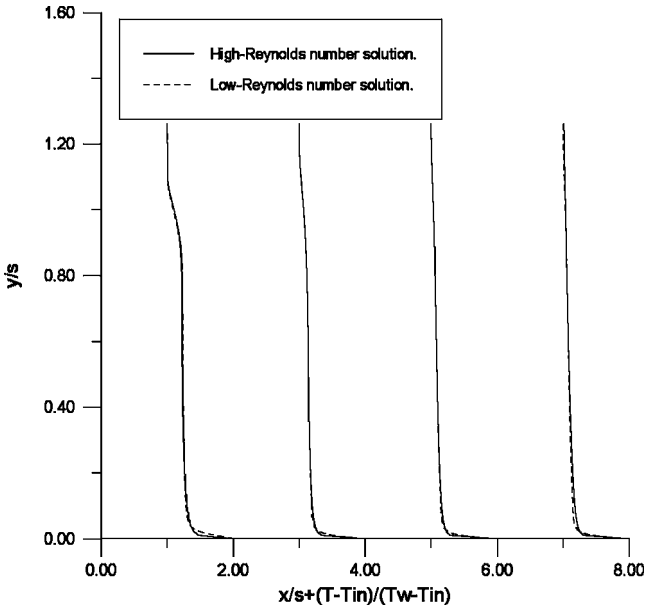

Fig. 15 Cross-sectional mean temperature profiles: $x/s=1.0$, $x/s=3.0$, $x/s=5.0$, and $x/s=7.0$

For AR=8 there is already two bubbles inside the cavity (Fig. 13), and the same two bubbles pattern is also found for aspect ratios equal to 10 and 12 (Figs. 18 and 19). For AR equal to 6 and 8 the velocity is reversed all along the floor of the cavity and there is no reattachment point. For AR equal to 10 and 12 the external flow reattaches at the cavity floor. This is corroborated by Figs. 20(*a*) and 20(*b*) where the distribution of the horizontal component of the velocity (at the first node close to the wall) along the floor of the cavity is shown. Hence, for a value of AR between 8 and 10, there is an important change in the physics inside the cavity: the outside flow starts to get in touch with the floor. Observation of Figs. 17 and 13 will reveal that the bubbles, one for AR=6 and two for AR=8 are, say, "encapsulated" by an enveloping streamline along all the space of the cavity. This "capsule" serves the purpose of a thermal insulating mechanism, because the convective action due to the external flow is isolated from the floor of the cavity. This situation will change considerably when the capsule is ruptured, what can be seen to have happened for AR=10. In this case the external flow "touches" the cavity floor and convective effects will certainly increase. This result has a fundamental impact upon the heat transfer rates. Figure 21(*a*) shows the heat flux along the horizontal wall of the cavity. Again, we can observe the existence of a peak in the distribution. The maximum heat rate, as had happened already for AR=6 and 8, occurs at the position where the turbulent diffusion of heat is more intense. This can be observed by inspecting Figs. 21(*a*) and 21(*b*). Besides, for these two aspect ratios (AR=10 and 12) the external flow reattaches and the convection mechanism is more intense [see Figs. 21(*a*) and 21(*b*)].

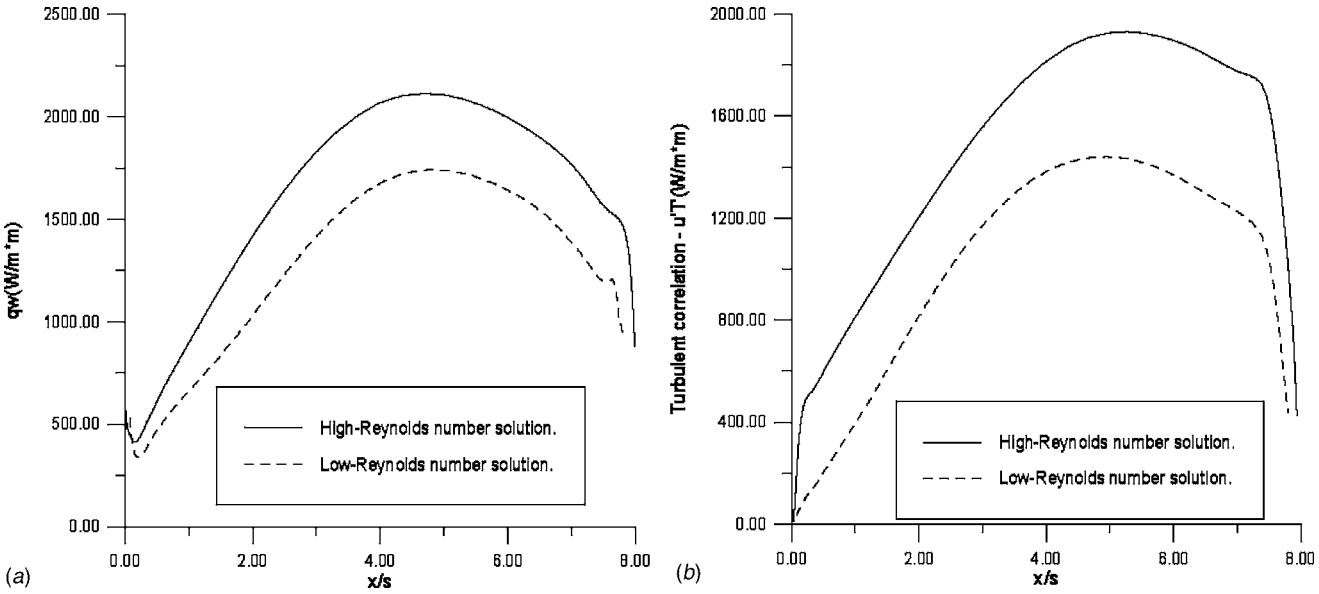

Fig. 16 (a) Heat transfer rate distribution along the cavity floor; (b) Heat flux due to turbulent fluctuations at a plane parallel to the wall and such that $y/s=0.1$

Figures 21(*a*) and 21(*b*) show all these results together for comparison purposes. Some very important conclusions can be drawn from these representations. The most obvious is that the overall heat transfer augments with the aspect ratio. This, evidently, is happening, because as the aspect ratio increases, the possibility of exchanging heat with the external flow increases accordingly. This increase is even more amplified when the external flow reattaches—Fig. 21(*a*) shows this clearly. Another very important, yet more subtle, conclusion, can be drawn from Fig. 21(*b*). The reader should observe that the peak of $\overline{u'T'}$ for AR=6 is much lower, but, most importantly, it has lost phase in relation to the other peaks. On the other hand, for AR=8, 10, and 12, not only the peaks have almost the same value but they are in phase. What happened? For AR=6 the cavity is working, say, like a true cavity, in the sense that there is only one recirculating structure inside of it. For AR=8, 10, and 12, we have two structures. What aspect of the entire situation decides if there will be one or two bubbles? We believe that this will happen when L, the length of the cavity floor (Fig. 2), grows greater than the reattachment length, that for this case is around 6*s*. After that, the great bubble will not change remarkably, and, in fact, the cavity starts to function as a sequence of steps, backward first and than forward. In other words, augmenting the aspect ratio will not produce any great modifications in the large bubble. Because the great structure is the one that largely commands the turbulence production process—especially through the shear layer that runs along its roof—this probably explains why the amount of turbulent heat diffusion for AR=8, 10, and 12 is almost the same, and also, why the peaks of $\overline{u'T'}$ are in phase.

3.4.3 Influence of the Entrance Level of Turbulence. All the basic parameters are assumed to be equal to those that were used in the study of the reference cavity (for which, AR=8). Now, the oncoming turbulence level was made to vary and the values of the turbulent kinetic energy investigated corresponded to 4% and 10% of the mean entrance kinetic energy. In both cases there were two bubbles inside the cavity. Figures 22(*a*) and 22(*b*) show the details of the flow field topology in the region between the two bubbles.

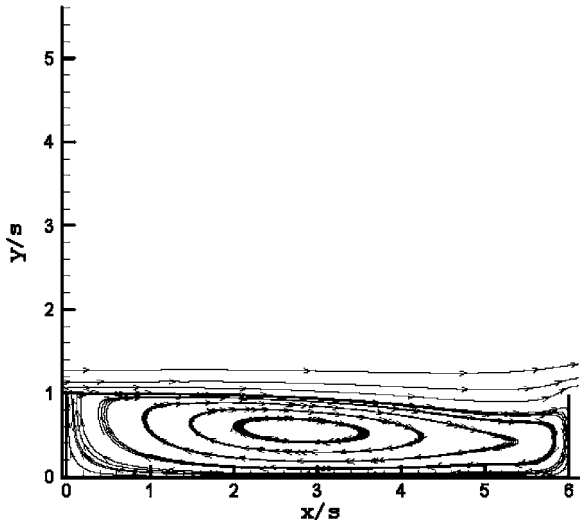

Fig. 17 Streamlines for the cavity with aspect ratio AR=6

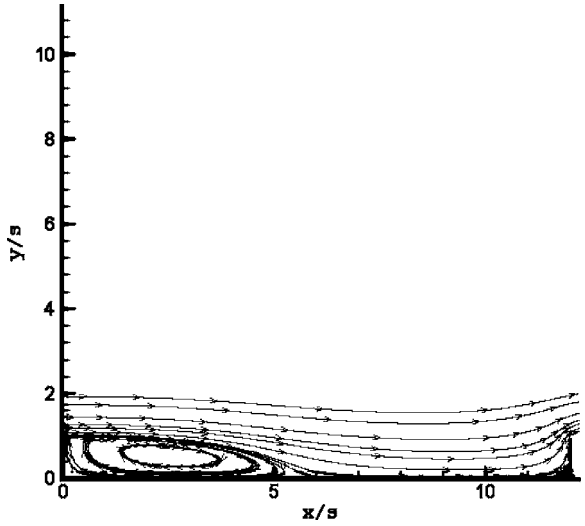

Fig. 18 Streamlines for the cavity with aspect ratio AR=12

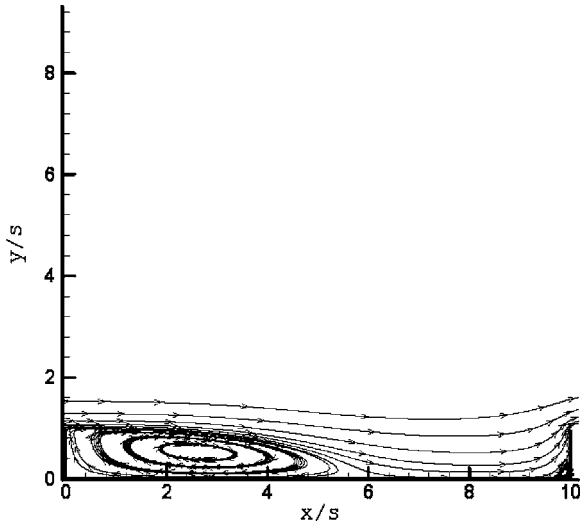

Fig. 19 Streamlines for the cavity with aspect ratio AR=10

We verified that the same phenomenon of vortexes encapsulation appears also here [3]. The heat flux distribution at the wall is plotted in Fig. 23(*a*). Once again, we observe a region of low heat loss, near the upstream step, where the great structure is positioned. The heat transfer increases at the cavity floor when a higher level of turbulence is introduced. This growth of the heat transfer rate occurs mainly for the region $x/s \leqslant 6$, and is due to the intensification of the convection and diffusion mechanisms. The convection heat loss increases because the external flow reattaches at the cavity floor for a higher level of turbulence (10%) at the entrance. The reattachment is a result of the shortening of the great bubble as the level of incoming turbulence increases [2,3]. Besides, the diffusion mechanism also increases in this region [see Fig. 23(*b*)]. This is an answer to the rise in the "turbulence feeding"—from 4% to 10%. Another very important aspect that can be observed in Fig. 23(*b*) is that the heat flux at the wall on the region near the downstream step is not affected by increasing the turbulence level at the entrance. This is an indication that the behaviour here is dominated by local conditions. The maximum of

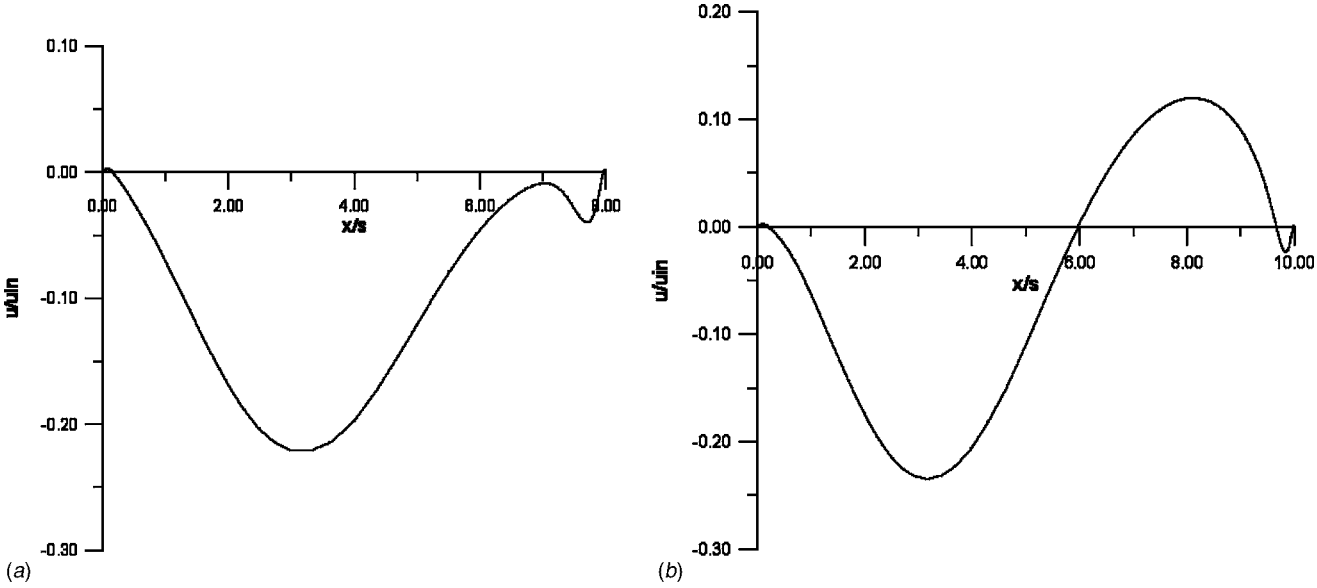

Fig. 20 Horizontal velocity component at the first computational node: (a) AR=8; (b) AR=10

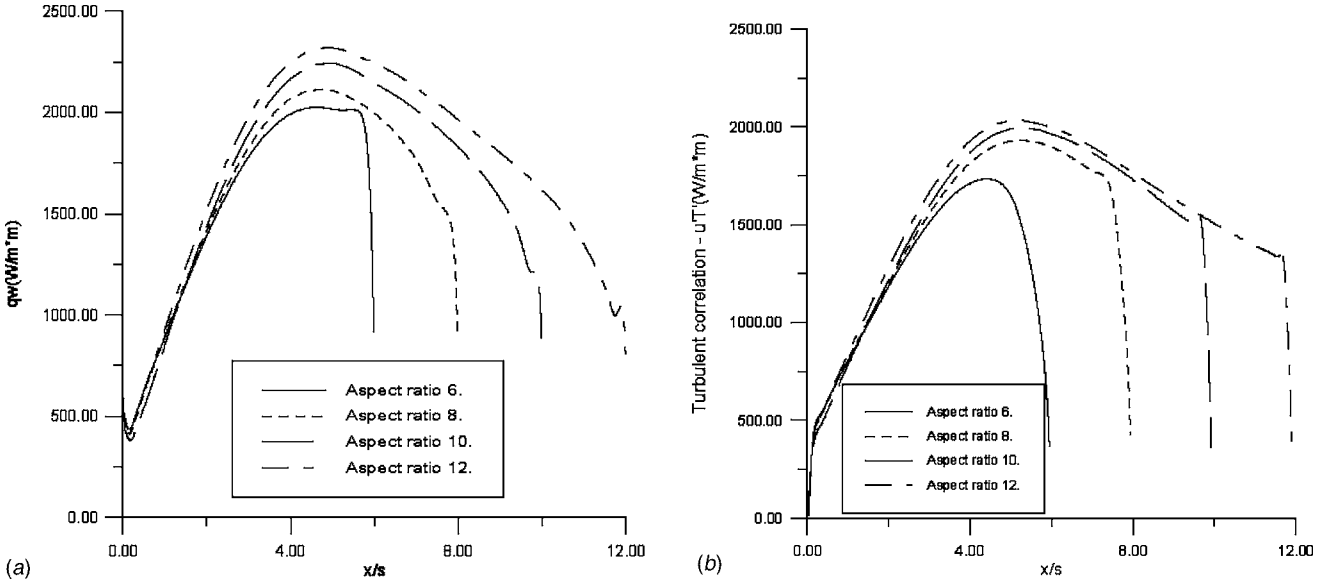

Fig. 21 Turbulent flow in a shallow cavity: aspect ratio influence. (a) Heat flux at the wall ($y/s=0$); (b) Heat flux due to turbulent fluctuations at a plane $y/s=0.1$.

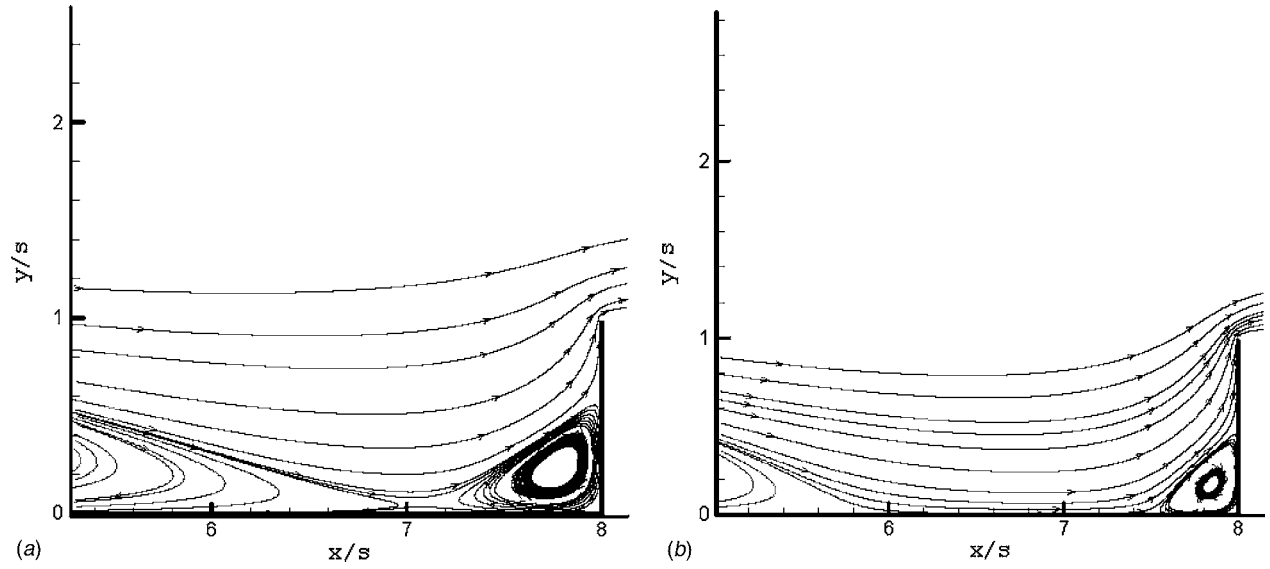

Fig. 22 Streamlines for the cavity with aspect ratio AR=8: (a) Turbulence level, 4%, (b) Turbulence level, 10%

turbulence production in the domain occurs exactly at the exit corner [3], and this maximum value is practically unaffected by the level of incoming turbulence. Therefore, heat transfer conditions at this region are practically unchanged.

3.4.4 Influence of the Reynolds Number. As for the other two studies the reference here is the cavity with AR=8. The variation of the Reynolds number was a consequence of the variation of the entrance velocity. Values of u_i equal to 5 m/s, 8 m/s, and 12 m/s, corresponded to values of Re_s equal to 13,285, 21,255, and 31,880, respectively. For all these values of the Reynolds number, the two bubbles pattern was established inside the cavity. The streamlines of the mean flows for these three cases are represented, respectively, in Figs. 24(*a*), 22(*a*), and 24(*b*). Inspection of the figures suggests one more time the existence of two regimes. For lower values of Re_s vortices encapsulation occurs, while for higher values the "capsule" is ruptured and the external flow reattaches. Figure 25(*a*) shows the heat flux distributions at the cavity floor. We can see that the heat loss increases all along the cavity floor for higher velocities at the inlet plane. This is due to the enhancement of the same two combined mechanisms: turbulent diffusion and external convection. Convection increases as a result of increasing the external velocity, what ultimately induces reattachment. Diffusion enhancement can be observed by the turbulent heat flux distribution at the near wall region [see Fig. 25(*b*)]. The important aspect here is that, by increasing the Reynolds number, the heat transfer increases uniformly. The same behavior is observed for the turbulent heat flux distribution. This is so, because, for higher inlet velocities, the mechanism of turbulence production increases accordingly in the two corners of the cavity. Thus, the heat flux at the wall and the turbulent heat diffusion at the near wall region augment all along the cavity floor.

4 Concluding Remarks

Investigation of the basic heat transfer mechanisms in the turbulent flow over shallow cavities was presented. The parametric

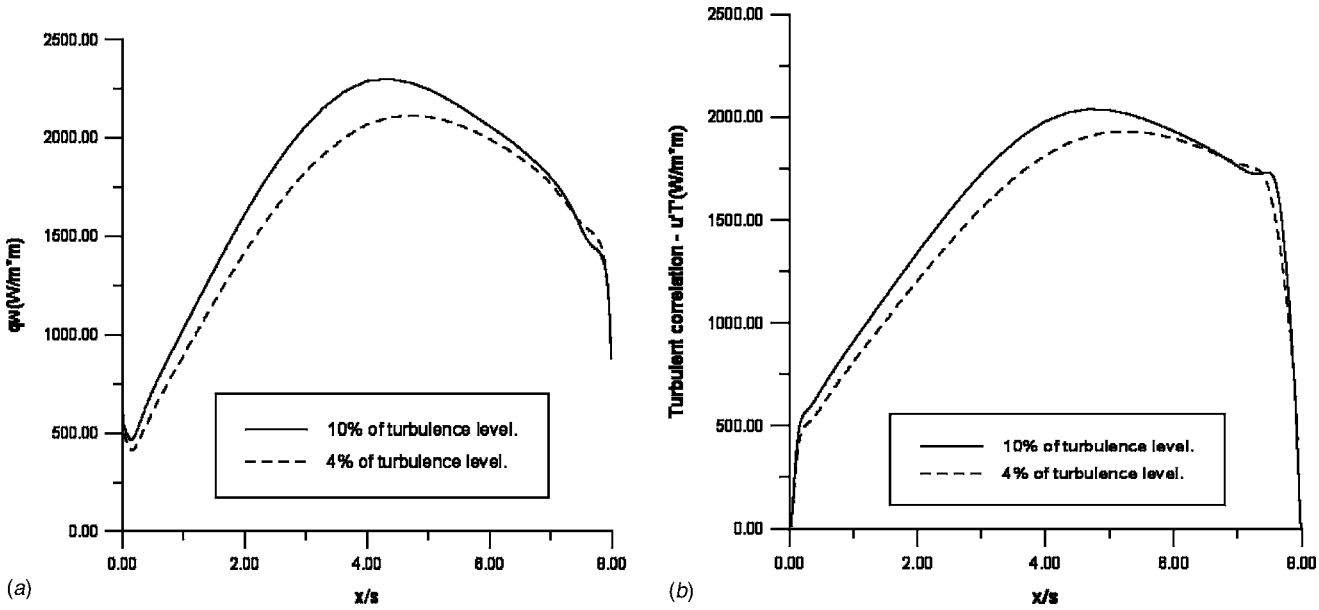

Fig. 23 Turbulent flow in a cavity with AR=8. Influence of the entrance turbulent level: (a) Heat flux at the wall ($y/s=0$); (b) Turbulent heat flux at a plane $y/s=0.1$.

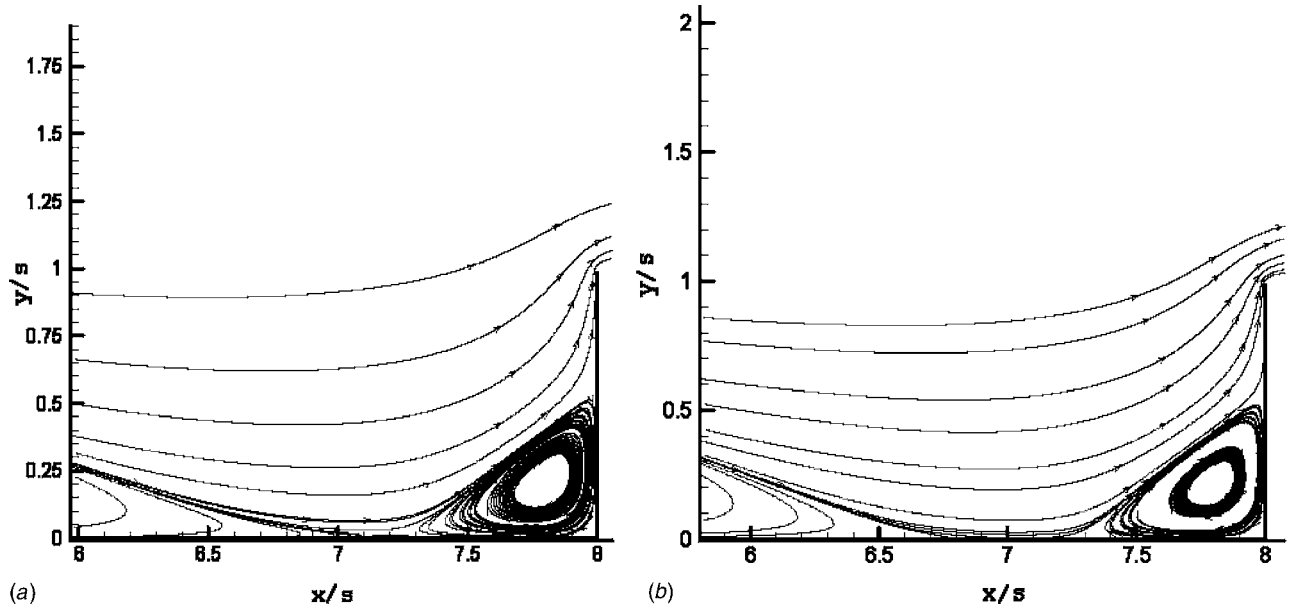

Fig. 24 Streamlines for the cavity with aspect ratio AR=8: (a) Re_s=13,285; (b) Re_s=31,880

studies revealed and helped to clarify important trends of the heat transfer rates at the floor of the cavity. The most important conclusions can be summarized as follows:

(a) *Interaction Between the External Flow and the Cavity Floor:* In a former work by the same authors [3], it was introduced the idea of vortexes encapsulation, and, at that time, it was inferred that once this mechanism is installed inside the cavity, the heat loss by convection would be greatly reduced. This result has been completely confirmed by the present heat transfer studies [Figs. 21(*a*) and 21(*b*)].

(b) *Turbulent Diffusion:* Not only the importance of this mechanism (what, in a certain way, is obvious) is shown, but its strong connection with the overall process of heat transfer gets demonstrated, where there is a peak of heat transfer at the wall of the cavity, there is also a peak of turbulent diffusion close to the wall. Besides, most of the heat that comes from the wall is "pumped" by turbulent diffusion. The reader can appreciate this by inspecting the many pair of figures that compare heat flux and turbulent diffusion at the wall. As an example, for AR=10, the peak values of these quantities are 2250 W/m^2 and 2000 W/m^2, respectively, and the diffusion represents 89% of the total flux. Hence, turbulent diffusion seems to be instrumental for the mechanism of heat transfer at the floor of the cavity.

(c) *Heat Transfer at the Upstream Step Region:* It is well known, from backward-facing step flows studies, that this region is strongly influenced by the conditions of the boundary layer that separates at the upstream corner. The parametric study has shown that the same situation is en-

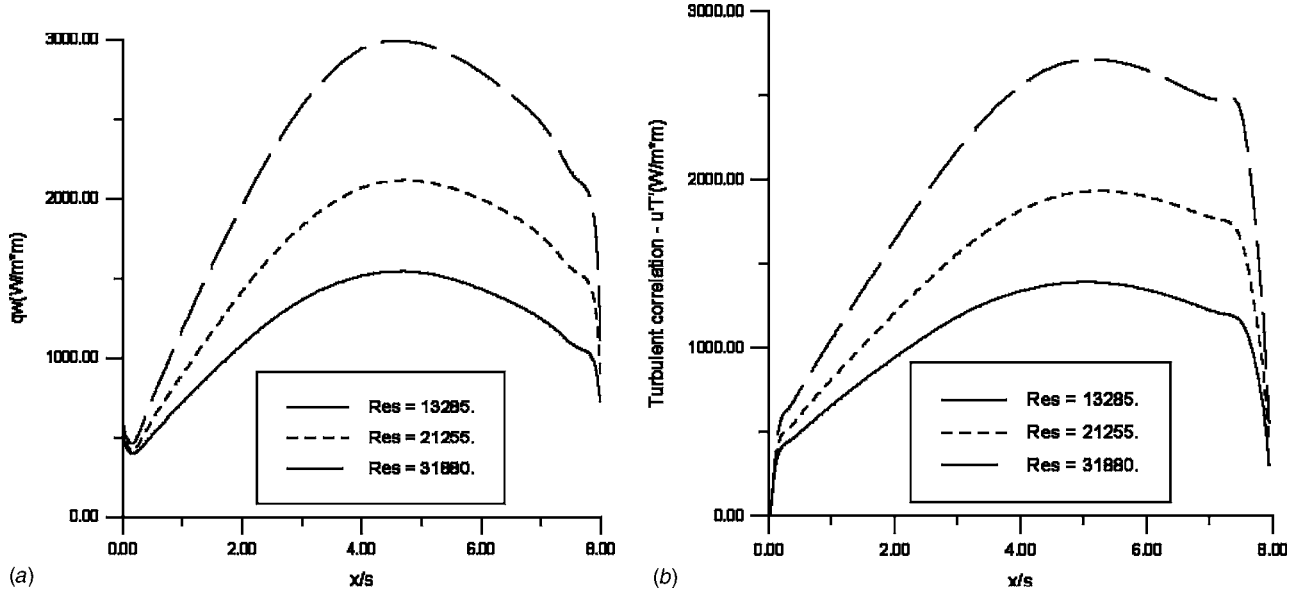

Fig. 25 Turbulent flow in a cavity with AR=8. Influence of the Reynolds number: (a) Heat flux at the wall (y/s=0); (b) Turbulent heat flux at a plane y/s=0.1.

countered in cavities. When conditions at the entrance of the domain, i.e., turbulence level or velocity, varied, the heat flux at the wall in this region was affected.

(d) *Heat Transfer at the Downstream Step Region:* The parametric studies demonstrated that this region is basically unaffected by the level of turbulence at the entrance plane. This is a consequence of the local production of turbulence, a maximum in the whole domain. This basically dictates the local heat transfer scenario.

Acknowledgments

This work was supported by the Brazilian agency, CNPq, National Council of Scientific and Technological Development, through Grant No. 141387/2001-7.

References

[1] Gomes, D. G., 1998, "Optimization of Flat Plate Solar Collectors," Master thesis dissertation, TIA—Technological Institute of Aeronautics, São José dos Campos, SP, Brazil (in Portuguese).

[2] Zdanski, P. S. B., Ortega, M. A. and Fico Jr., N. G. C. R., 2002, "Convection Effects in Flows over Cavities of High Aspect Ratios," AIAA Paper 2002-3301.

[3] Zdanski, P. S. B., Ortega, M. A., Fico Jr., N. G. C. R., 2003, "Numerical Study of the Flow Over Shallow Cavities," Int. J. Comput. Fluid Dyn., **32**, pp. 953–974.

[4] Zdanski, P. S. B., Ortega, M. A., and Fico Jr., N. G. C. R., 2003, "A Novel Algorithm for the Incompressible Navier-Stokes Equations," AIAA Paper 2003-0434.

[5] Richards, R. F., Young, M. F., and Haiad, J. C., 1987, "Turbulent Forced Convection Heat Transfer from a Bottom Heated Open Surface Cavity," Int. J. Heat Mass Transfer, **30**, pp. 2281–2287.

[6] Aung, W., 1983, "An Interferometric Investigation of Separated Forced Convection in Laminar Flow Past Cavities," ASME J. Heat Transfer, **105**, pp. 505–512.

[7] Matos, A., Pinho, F. A. A., and Silveira-Neto, A. S., 1999, "Large-Eddy Simulation of Turbulent Flow Over a Two-Dimensional Cavity with Temperature Fluctuations," Int. J. Heat Mass Transfer, **42**, pp. 49–59.

[8] Launder, B. E., and Spalding, D. B., 1974, "The Numerical Computation of Turbulent Flows," Comput. Methods Appl. Mech. Eng., **3**, pp. 269–289.

[9] Hwang, C. B., and Lin, C. A., 1998, "Improved Low-Reynolds-Number $k-\tilde{\varepsilon}$ Model Based on Direct Numerical Simulation Data," AIAA J., **36**, pp. 38–43.

[10] Beam, R. M., and Warming, R. F., 1978, "An Implicit Factored Scheme for the Compressible Navier-Stokes Equations," AIAA J., **16**, pp. 393–401.

[11] Mansour, N. M., Kim, J., and Moin, P., 1983, "Computation of Turbulent Flows Over a Backward-Facing Step," Nasa Technical Memorandum, 85851.

[12] Mansour, N. M., Kim, J., and Moin, P., 1988, "Reynolds Stress and Dissipation Rate Budgets in Turbulent Channel Flow," J. Fluid Mech., **194**, pp. 15–44.

[13] Wilcox, D. C., 1998, *Turbulence Modeling for CFD*, 2nd ed., DCW Industries, La Canãda, CA.

[14] Kader, B. A., 1981, "Temperature and Concentration Profiles in Fully Turbulent Boundary Layers," Int. J. Heat Mass Transfer, **24**, pp. 1541–1544.

[15] Patel, V. C., Rodi, W., and Scheurer, G., 1985, "Turbulence Models for Near-Wall and Low Reynolds Number Flows," AIAA J., **23**, pp. 1308–1319.

[16] Vogel, J. C., and Eaton, J. K., 1985, "Combined Heat Transfer and Fluid Dynamics Measurements Downstream of a Backward-Facing Step," ASME J. Heat Transfer, **107**, pp. 922–929.

[17] Silveira-Neto, A., Grand, D., Métais, O., and Lesieur, M., 1993, "Numerical Investigation of the Coherent Vortices in Turbulence Behind a Backward-Facing Step," J. Fluid Mech., **256**, pp. 1–25.

[18] Abe, K., Nagano, Y., and Kondoh, T. A., 1995, "A New Turbulence Model for Predicting Fluid Flow and Heat Transfer in Separating and Reattaching Flows," Int. J. Heat Mass Transfer, **38**, pp. 1467–1481.

[19] Rizzi, A., and Vos, J., 1998, "Towards Establishing Credibility in Computational Fluid Dynamics Simulations," AIAA J., **36**, pp. 668–675.

[20] Strickwerda, J. C., 1989, *Finite Difference Schemes and Partial Differential Equations*, Wadsworth, New York.

[21] Arpaci, V. S., and Larsen, P. S., 1984, *Convection Heat Transfer*, Prentice–Hall, New Jersey.

Comparison of Different Phonon Transport Models for Predicting Heat Conduction in Silicon-on-Insulator Transistors

Sreekant V. J. Narumanchi[1]
Institute for Complex Engineered Systems and
Department of Mechanical Engineering,
Carnegie Mellon University,
5000 Forbes Ave,
Pittsburgh, PA 15213

Jayathi Y. Murthy
e-mail: jmurthy@ecn.purdue.edu.
School of Mechanical Engineering,
Purdue University,
585 Purdue Mall, W. Lafayette, IN 47907

Cristina H. Amon
Institute for Complex Engineered Systems and
Department of Mechanical Engineering,
Carnegie Mellon University,
5000 Forbes Ave,
Pittsburgh, PA 15213

The problem of self-heating in microelectronic devices has begun to emerge as a bottleneck to device performance. Published models for phonon transport in microelectronics have used a gray Boltzmann transport equation (BTE) and do not account adequately for phonon dispersion or polarization. In this study, the problem of a hot spot in a submicron silicon-on-insulator transistor is addressed. A model based on the BTE incorporating full phonon dispersion effects is used. A structured finite volume approach is used to solve the BTE. The results from the full phonon dispersion model are compared to those obtained using a Fourier diffusion model. Comparisons are also made to previously published BTE models employing gray and semi-gray approximations. Significant differences are found in the maximum hot spot temperature predicted by the different models. Fourier diffusion underpredicts the hot spot temperature by as much as 350% with respect to predictions from the full phonon dispersion model. For the full phonon dispersion model, the longitudinal acoustic modes are found to carry a majority of the energy flux. The importance of accounting for phonon dispersion and polarization effects is clearly demonstrated. [DOI: 10.1115/1.1924571]

Keywords: Computations, BTE, Finite Volume Method, SOI Transistors, Phonons, Phonon Dispersion, Phonon Polarization, Micro/Nano Scale Heat Conduction, Hot Spot

Introduction

During the last two decades, aggressive scaling trends have exacerbated self-heating problems in microelectronic devices. These problems are particularly severe in emerging device designs employing silicon-on-insulator (SOI) technology or new generations of low-k dielectrics. In SOI, for example, the silicon device layer is fabricated on the buried oxide layer, which is made from low-conducting SiO_2. Electron-phonon scattering in the channel region causes heat release that must be transported to the exterior for dissipation. However, transport is severely impeded by the low thermal conductivity of SiO_2. In addition, microscale thermal transport phenomena such as phonon confinement, phonon boundary scattering and nonequilibrium in the silicon device layer, may also serve to exacerbate local heating and seriously degrade device performance. As channel dimensions, currently at 180 nm, fall to less than 70 nm over the next few years, it is becoming increasingly important to understand the role played by microscale thermal phenomena in device heat transfer.

It is now well known that conventional Fourier analysis leads to erroneous results when the mean free path of the energy carriers is comparable to or larger than the characteristic length scales of the domain. Fourier analysis is also questionable when the time scale under consideration is smaller than the relaxation time of the energy carriers [1,2]. Typically, when the system length scale is comparable to the carrier mean free path, but larger than the carrier wavelength, and phase coherence effects are unimportant [3,4], the Boltzmann transport equation in the relaxation time approximation [5] can be employed to describe phonon transport. Phonons, which are quantized lattice vibrations [6,7], are the predominant energy carriers in semiconductors like silicon at and above room temperature.

The problem of Joule heating in submicron transistors has been addressed in the literature at various levels of approximation. Two-dimensional (2D) simulations of concurrent electrical and thermal transport in semiconductor devices (GaAs metal-semiconductor field effect transistors and Si metal-oxide-semiconductor field effect transistors) have been reported [8–11]. The approach is to consider hydrodynamic equations for electron transport, as well as energy transport equations for electrons and the different phonon polarizations. The equations are derived by taking moments of the Boltzmann equations, and are therefore lower-order approximations. The analysis is semigray because frequency-dependent relaxation times and phonon group velocities are not considered. Also, an important simplifying assumption in these studies is that heat propagation by acoustic phonons is assumed to be diffusive.

Thermal predictions in submicron SOI transistors have been reported [12–17], by employing the two-fluid model [18,19] to solve the phonon Boltzmann transport equation (BTE). In this approach the phonons are divided into propagating and reservoir modes. The propagating mode is responsible for energy transport, while the reservoir mode functions purely capacitatively. Energy exchange between the branches is restricted to interactions between the reservoir and propagating mode. However, this model is a primarily gray model in the sense that only a single phonon relaxation time and velocity are used. The unsteady hot spot problem with a gray assumption has been recently studied [20,21].

The purpose of this study is to examine the problem of a hot spot in a SOI transistor by using different phonon transport models and to compare their predictions. The primary focus is the full phonon dispersion model presented recently by the authors [22]. This model accounts for transverse and longitudinal acoustic phonons as well as optical phonons. The interactions among the

[1]Current address: National Renewable Energy Laboratory Golden, CO 80601

Contributed by the Heat Transfer Division for publication in the JOURNAL OF HEAT TRANSFER. Manuscript received August 11, 2003; final manuscript received March 1, 2005; review conducted by Gang Chen.

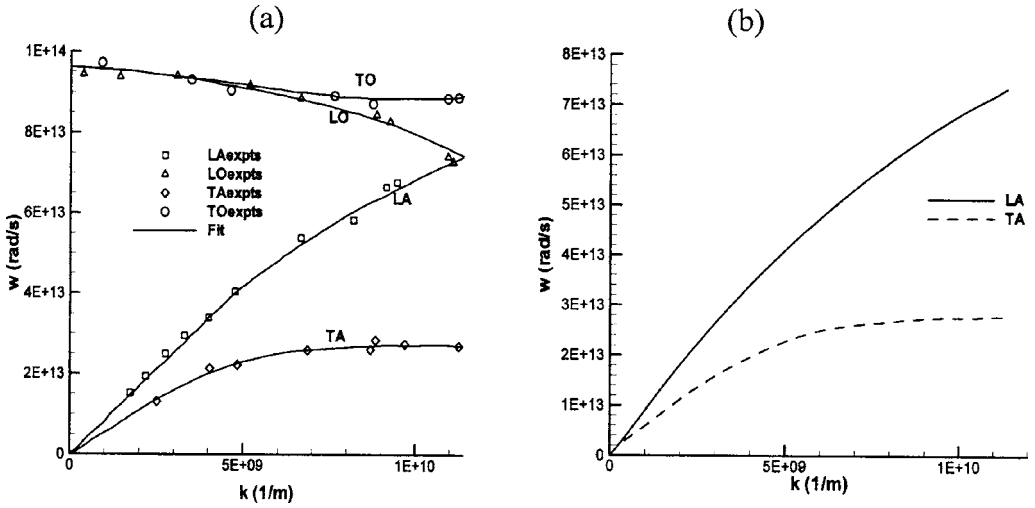

Fig. 1 (a) Experimental dispersion curve in the [001] direction in silicon at 300 K [27]; (b) spline curve fit to the LA and TA branches

different phonon branches and frequencies are described by frequency-dependent relaxation times. The relaxation times are obtained by perturbation theory techniques [23–26].

The results are compared to those obtained from conventional Fourier analysis, and also to those obtained from semi-gray [12–17] and gray approaches to solving the BTE. In all cases, the heat source size, location, and strength are assumed prescribed *a priori*. The full phonon dispersion model reveals the specific phonon groups involved in energy transport and points to the limitations of simpler gray and semi-gray models.

Full Phonon Dispersion Model Based on Boltzmann Transport Equation (BTE)

The complete details of the model have been presented in[22]. Important features are presented below for completeness. The model is based on the solution to the BTE in the relaxation time approximation

$$\frac{\partial f_w}{\partial t} + \mathbf{v}_w \cdot \nabla f_w = \frac{f_w^0 - f_w}{\tau_w} + \left(\frac{\partial f}{\partial t}\right)_{\text{e-ph}}$$

$$f_w^0 = \frac{1}{(e^{\hbar w/k_B T} - 1)} \tag{1}$$

where w is the frequency, f_w is the frequency dependent distribution function of phonons, $\mathbf{v}_w$ is the group velocity vector of the phonons, f_w^0 is the equilibrium Bose-Einstein distribution function, k_B is Boltzmann's constant, τ_w is the frequency dependent relaxation time of phonons and $(\partial f/\partial t)_{\text{e-ph}}$ is the scattering term describing electron-phonon scattering. Defining the following quantities:

$$e_w'''(\mathbf{r},\hat{s},w) = \hbar w f_w D(w);\ e_w'' = \int_{\Delta w_i} e_w''' dw.$$

$$e_w = \int_{4\pi} e_w'' d\Omega;\ e_w^0 = \frac{1}{4\pi}\int_{4\pi} e_w'' d\Omega = \frac{1}{4\pi} e_w \tag{2}$$

where e_w''' is the volumetric energy density per unit frequency per unit solid angle (Js/m^3 sr rad), e_w'' is the volumetric energy density per unit solid angle (J/m^3 sr) for a given frequency band, $\mathbf{r}$ is the position vector, and $\hat{s}$ is the unit direction vector. The quantity e_w is the volumetric energy density (J/m^3) in the band and e_w^0 is the associated angular average, as shown in Eq. (2). The term $\hbar$ is the reduced Planck constant, and $D(w)$ is the phonon density of states. The frequency integration is done over a discrete frequency band Δw_i.

The bulk phonon dispersion curves for silicon at 300 K are shown in Fig. 1 for the [001] direction [27]. Assuming isotropy, these dispersion curves are used in all directions. In the [001] symmetry direction, silicon has three acoustic branches and three optical branches. Of the three acoustic branches, one is longitudinal and two are degenerate transverse branches. Similarly, there is one longitudinal optical phonon branch and two degenerate transverse optical phonon branches. In the proposed model, only one frequency band is used for the optical phonon branch, while there are N_{LA} and N_{TA} bands in the longitudinal acoustic (LA) and transverse acoustic (TA) branches, respectively. The experimental dispersion curves for the LA and TA branches are fit by cubic splines and all relevant dispersion curve information (e.g., phonon group velocity, density of states) is extracted from these fits.

The optical mode for silicon has negligible group velocity and therefore the ballistic term in Eq. (1) is absent. The BTE for the optical mode can be written as

$$\frac{\partial e_o}{\partial t} = \sum_{j=1}^{N\text{bands}-1} \left(\int_{T_{\text{ref}}}^{T_{\text{oj}}} C_o dT - e_o\right)\gamma_{\text{oj}} + q_{\text{vol}} \tag{3}$$

where $e_o = \int_{T_{\text{ref}}}^{T_o} C_o dT$, $\gamma_{\text{oj}} = \overline{(1/\tau_{\text{oj}})} = 1/\Delta w_o \int_{\Delta w_o} 1/\tau_{\text{oj}} dw$ is the band-averaged inverse relaxation time for the interaction between the optical phonons and the jth band of an acoustic branch, and C_o is the optical mode specific heat. The *interaction temperature* T_{oj} is defined below in Eq. (8). The term q_{vol} is the volumetric heat generation. In microelectronics applications, it would represent the transfer of energy from the energetic electrons to the optical phonons. It is argued [16] that the electron-phonon interaction can be represented as a heat source term for the phonon BTE since the relaxation time for electron-phonon interaction is about two orders of magnitude smaller than the relaxation time for phonon-phonon scattering. The same approach is adopted in the present study.

The BTE for the ith frequency band of the acoustic branches (valid for both LA and TA) in the direction $\hat{s}$ (Fig. 2) is written as

$$\frac{\partial e_i''}{\partial t} + \nabla \cdot (v_i \hat{s} e_i'') = (e_i^0 - e_i'')\gamma_{ii} + \sum_{\substack{j=1 \\ j\neq 1}}^{N\text{bands}} \left\{\left(\frac{1}{4\pi}\int_{T_{\text{ref}}}^{T_{ij}} C_i dT - e_i''\right)\gamma_{ij}\right\} \tag{4}$$

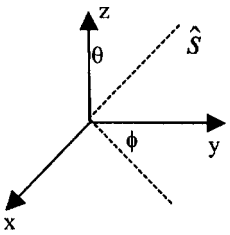

Fig. 2 Coordinates axes and representative phonon direction $\hat{s}$

$$\nu_i = \frac{1}{\Delta w_i}\int_{\Delta w_i} \nu_w dw;\ C_i = \int_{\Delta w_i} C_{wi} dw,$$

$$e_i'' = \int_{\Delta w_i} \hbar w f_w D(w) dw;\ \gamma_{ii} = \overline{(1/\tau_{ii})} = \frac{1}{\Delta w_i}\int_{\Delta w_i} \frac{1}{\tau_{ii}} dw,$$

$$\gamma_{ij} = \overline{(1/\tau_{ii})} = \frac{1}{\Delta w_i}\int_{\Delta w_i} \frac{1}{\tau_{ij}} dw \tag{5}$$

where ν_i is the band-averaged group velocity, C_{wi} is the specific heat per unit frequency in band i, C_i is the band-integrated specific heat, e_i'' the band-integrated energy density per unit solid angle, γ_{ii} is the band-averaged inverse relaxation time for interaction of band i with itself, and γ_{ij} is the band-averaged inverse relaxation time for interaction of band i with band j. The first term on the right hand side (RHS) of Eq. (4) depicts scattering within a given frequency band, but across directions (elastic scattering). Physically, processes such as impurity scattering may be described by such a term. The second term on the RHS depicts the scattering from the ith band of the acoustic band considered to all other bands in all branches except to itself. T_{ij} is an *interaction* temperature between the two bands i and j. In order to satisfy energy conservation, the scattering terms on the RHS of the BTE equation must cancel out when summed over all bands. This requirement leads to

$$T_{ij} = T_{ji};\ \text{and}\ \int_{\Delta w_i} \frac{1}{\tau_{ij}} dw = \int_{\Delta w_i} \frac{1}{\tau_{ji}} dw \tag{6}$$

where i is any frequency band in a given phonon branch and j is any other band, in the same or different branch, with which energy is being exchanged.

The equilibrium energy density is defined as

$$e_i^0 = \frac{1}{4\pi}\int_{4\pi} e_i'' d\Omega = \frac{1}{4\pi}\int_{T_{\text{ref}}}^{T_i} C_i dT = \frac{e_i}{4\pi} \tag{7}$$

where T_i is the temperature associated with the ith band of the branch considered.

In order for energy conservation to be satisfied [22], the following condition is also satisfied:

$$\int_{T_{\text{ref}}}^{T_{ij}} \left(\frac{C_i}{\Delta w_i} + \frac{C_j}{\Delta w_j}\right) dT = \int_{T_{\text{ref}}}^{T_i} \frac{C_i}{\Delta w_i} dT + \int_{T_{\text{ref}}}^{T_j} \frac{C_j}{\Delta w_j} dT \tag{8}$$

This is satisfied for all i and j band combinations (with $i \neq j$) including the optical phonon band. Equation (8) serves as the definition of the interaction temperature T_{ij}. An overall lattice temperature T_L may be defined as follows: [22]

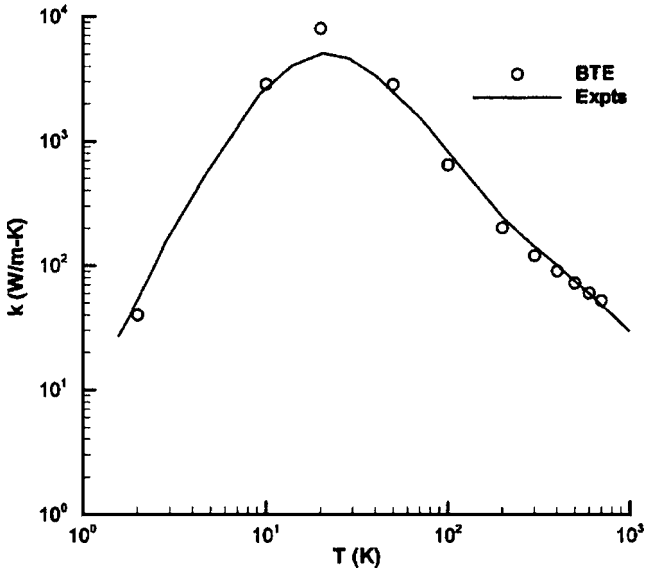

Fig. 3 Bulk thermal conductivity of silicon. Experimental data from Holland [27]

$$e_{\text{total}} = \int_{T_{\text{ref}}}^{T_L} C dT = \int_{T_{\text{ref}}}^{T_o} C_o dT + \sum_{i=1}^{N\text{bands}-1} \left(\int_{T_{\text{ref}}}^{T_i} C_i dT\right) \tag{9}$$

where C is the total specific heat of the solid, and e_{total} is the total energy density.

The details of the relaxation time as well as specific heat computations can be found in Ref. [22]. It has been shown that the model satisfies energy conservation. The model has been validated against known solutions from the radiative transport literature. It has also been validated in the acoustically thick limit by comparisons to solutions to the parabolic diffusion equation. The bulk thermal conductivity of silicon at different temperatures is also recovered [22]. The experimental thermal conductivity of doped and undoped silicon thin films is matched satisfactorily. In the sections below, thermal conductivity results for bulk silicon as well as undoped and doped silicon thin films are presented.

Bulk Silicon Thermal Conductivity. In this section, the aim is to predict the variation of bulk thermal conductivity of silicon with temperature. Since a pure sample of single crystal silicon is considered, isotope scattering [23–25] is the only form of impurity scattering considered. Umpklapp processes are the only three-phonon processes considered. The details of the relaxation time treatment have been described [22]. For the thermal conductivity computations, 150 spatial cells are used; the angular resolution in the octant is 8×8. The number of frequency bands is $6 \times 6 \times 1$ (6 in the LA branch, 6 in the TA branch and 1 band in the optical mode). The boundary scattering treatment is similar to that presented by Holland [27]. The relaxation time due to boundary scattering is incorporated as $1/\tau_b = \nu/LF$, where $\nu = 6400\ \text{ms}^{-1}$, $L = 0.716$ cm, $F = 0.8$ [27]. Boundary scattering is incorporated by adding the term $(e_i^0 - e_i''/\tau_b)$ on the RHS of Eq. (4). If boundary scattering were to be modeled more rigorously, a three-dimensional simulation of the bulk silicon sample would be required. Such an approach would be intensive computationally. Hence, as an approximation, boundary scattering is incorporated as a volumetric scattering term. The thermal conductivity is extracted by computing the total phonon energy flux at the boundary, and is presented in Fig. 3 for a wide range of temperatures. A reasonable match is found with experimental data [27]. The relaxation times for three-phonon processes are strictly appropriate only for temperatures >300 K ($T > 0.5T_{\text{Debye}}$ for silicon [24]), since U processes are the only three-phonon processes considered.

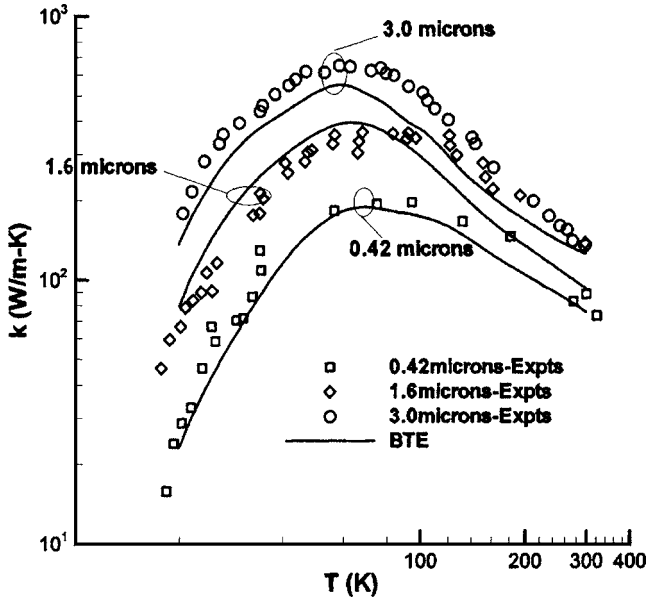

Fig. 4 Undoped silicon thin film in-plane thermal conductivity. Experimental data are from Asheghi et al. [29] (for the 0.42 and 1.6 μm films), and from Asheghi et al. [30] (for the 3.0 μm film)

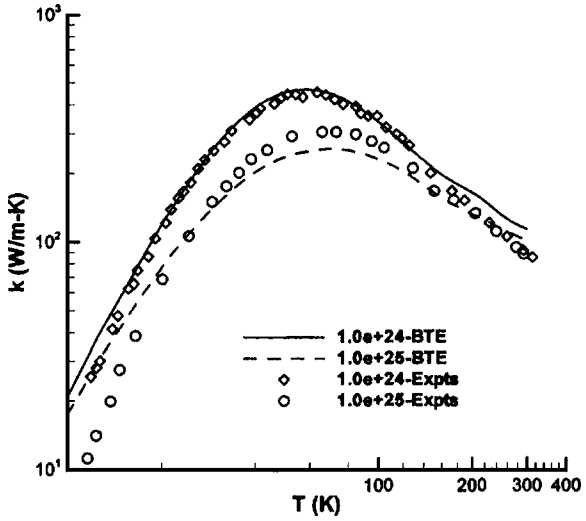

Fig. 5 Doped 3.0 μm silicon thin film in-plane thermal conductivity. Experimental data are from Asheghi et al. [30]

Nevertheless, the computations are seen to match low-temperature data quite well. This is because, at low temperatures, the thermal conductivity is dominated by isotope and boundary scattering processes.

Undoped Silicon Thin Films. In the literature, in-plane experimental thermal conductivity data for undoped silicon thin films have been reported [28–30]. Here an attempt will be made to match these experimental data. For thermal conductivity simulations, a two-dimensional (2D) domain is considered. The top and bottom boundary of the domain are considered reflecting. The degree of specularity is given by a factor p; $p=1.0$ indicates a completely specular interface, while $p=0$ indicates a completely diffuse interface. A small temperature difference is maintained across the side boundaries, which are maintained at constant temperature. Thermal conductivity is again extracted by computing the phonon energy flux across the boundaries. For the BTE simulations, 100 cells are used in the in-plane direction. The angular discretization is 8×8 in the octant, while the frequency discretization is $6\times6\times1$. Figure 4 shows the thermal conductivity data for three different films of thicknesses 0.42, 1.6, and 3.0 μm, along with the predictions from the numerical solution to the full phonon dispersion BTE model. The experimental data for the 0.42 and 1.6 μm film are taken from Ref. [29], while the 3.0 μm film data come from Ref. [30]. A specularity parameter of $p=0.4$ appears to give a reasonable match between the BTE results and the experimental data for all three films over a range of temperatures. Mazumder and Majumdar [31] have used a p value of 0.6 to obtain a match between their numerical results and experimental data for the undoped 3.0-μm-thick silicon film.

Doped Silicon Thin Films. We now attempt to match the experimental thermal conductivity data of boron-doped 3.0-μm-thick silicon films [30]. We follow the same simplified approach for the additional dopant impurity scattering as Mazumder and Majumdar [31]. The numerical mesh is the same as for the case of undoped thin films. The expression for impurity scattering involves a constant which is determined empirically to give the best fit with experimental data [31]. The value of the constant we use is 50. This value differs from that used in Ref. [31] because the differences in other relaxation times used here. The corresponding results are shown in Fig. 5. We show results for two different dopant (boron) concentrations—1.0e+24 and 1.0e+25 atoms/m^3. Given the very approximate form of the relaxation time expression for dopant impurity scattering, the match between experimental data and the BTE results over a wide range of temperatures is fair.

The above results give some degree of confidence in the full phonon dispersion model and also the numerical code in which it is implemented. Hence, we now study the problem of self-heating a silicon-on-insulator (SOI) transistor.

Silicon-on-Insulator (SOI) Transistor. A 2D domain approximating the device and buried oxide layers in an SOI transistor is shown in Fig. 6. The domain is similar to that studied in Ref. [16]. A thin silicon device layer resides on top of a thicker insulating SiO_2 layer. The left hand side (LHS), right hand side (RHS) and the bottom boundary are all maintained at 300 K and serve as heat sinks, while the top silicon boundary is diffusely reflecting (adiabatic). The shaded region in Fig. 6 represents the channel region of the transistor, where most of the electron-phonon scattering, and consequently the heat generation, occurs. The heated region (100 nm$\times$10 nm), has a volumetric heat generation of 6.0×10^{17} W/m^3, for a total heat generation per unit depth of 600 W/m. The entire heat generation is assumed to occur via electron-optical phonon interaction and is incorporated via the term q_{vol} in Eq. (3).

A discussion of the imposed boundary conditions is in order. Typically, the device and buried oxide layers are fabricated on a silicon wafer several hundred microns thick, with multiple devices being present in close proximity in the device layer. The electronic

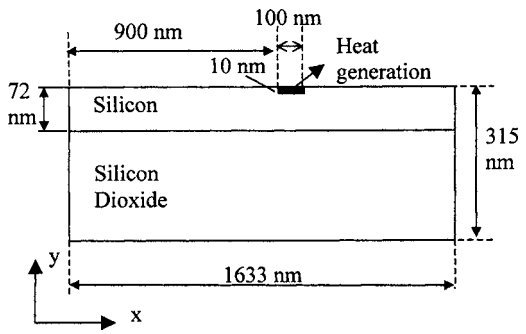

Fig. 6 Two-dimensional computational domain of the silicon-on-insulator transistor

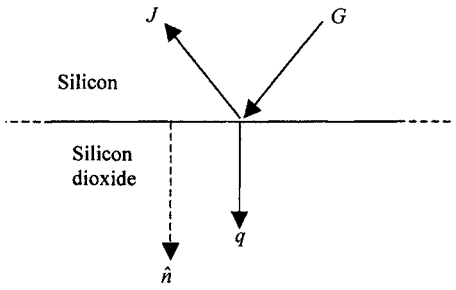

Fig. 7 Energy balance at the silicon/silicon dioxide interface

package is cooled using a heat sink attached to the bottom of the chip package, and heat transfer through the bottom of the domain is the primary path for cooling. Therefore, it is justified to treat the silicon layer top boundary as adiabatic. The present treatment imposes a uniform temperature on the lateral and bottom boundaries in order to isolate a single device from the rest of the structure. Since both the BTE and Fourier models considered here are linear in e_i'', the specific value of boundary temperature is not important. The boundary temperature of 300 K is therefore to be construed as a reference temperature. The actual temperature on these boundaries is a function of the package and heat sink resistance, and depends on the details of the package structure, the type of heat sink used as well as the external flow conditions. However, the temperature differences predicted in this study with respect to the boundary temperature are independent of the specific value of boundary temperature chosen.

Modeling the Si/SiO_2 Interface. In the silicon region, the BTE [Eqs. (1)–(9)] is solved and in the SiO_2 region, the heat diffusion equation is solved

$$\nabla \cdot (K \nabla T) = 0 \tag{10}$$

The thermal conductivity of SiO_2 is 1.38 W/m K [28]. For simplicity the material properties (specific heat, thermal conductivity and relaxation times) of Si and SiO_2 are evaluated at 300 K. The flux passing into SiO_2 (Fig. 7) may be written as [13,16]

$$q = G - J, \tag{11}$$

$$G = \sum_i \left(\int_{\forall \hat{s}\cdot\hat{n}>0} v_i e_i'' \hat{s}\cdot\hat{n} d\Omega \right) \tag{12}$$

$$J = \sum_i \left(\rho_i \int_{\forall \hat{s}\cdot\hat{n}>0} v_i e_i'' \hat{s}\cdot\hat{n} d\Omega \right) + \sum_i \left(\varepsilon_i \int_{\forall \hat{s}\cdot\hat{n}<0} v_i e_{\text{wall},i}^0 \hat{s}\cdot\hat{n} d\Omega \right) \tag{13}$$

$$\varepsilon_i = \alpha_i = 1 - \rho_i \tag{14}$$

$$e_{\text{wall},i}^0 = \frac{1}{4\pi} \int_{T_{\text{ref}}}^{T_{\text{interface}}} C_i dT = \frac{1}{4\pi} C_i (T_{\text{interface}} - T_{\text{ref}}) \tag{15}$$

where G is the net irradiation of the Si/SiO_2 interface from the silicon side, J is the radiosity of the interface facing the silicon, ρ_i is the band-wise reflectivity and α_i is the band-wise transmissivity, ε_i is the emissivity of spectral band i, and the summation is over all frequency bands in the acoustic branches. Part of the phonon flux incident on the interface from the silicon side is reflected and part of it is transmitted. Also, the interface at temperature $T_{\text{interface}}$ emits a phonon flux into the silicon region and this is incorporated via the second term in Eq. (13). The diffuse mismatch model is used to compute α_i [32]. Unlike Ref. [16], the Debye approximation is not invoked for silicon to compute α_i. The most general form for the transmission probability is given as [32]

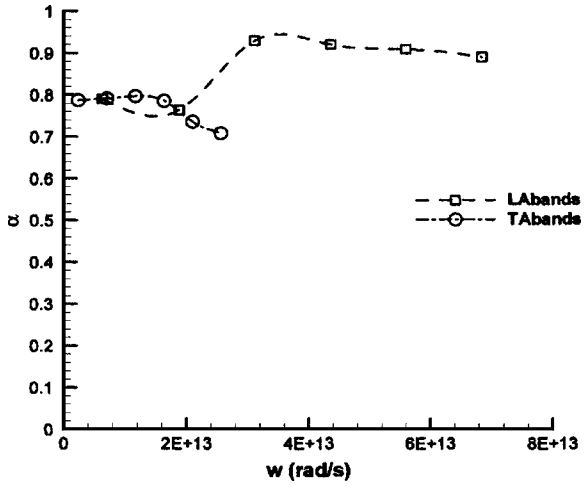

Fig. 8 Transmission coefficient in silicon as a function of frequency, 6×6×1 frequency bands

$$\alpha_i(w) = \frac{\sum_j v_{3-i,j} D_{3-i,j}(w,T)}{\sum_{i,j} v_{i,j} D_{i,j}(w,T)} \tag{16}$$

where ν is the phonon group velocity, D is the phonon density of states, i refers to the side with respect to the interface (1 being silicon, 2 being silicon dioxide), and j refers to the polarizations. Based on arguments presented in Ref. [32], α_i is a function of frequency only and is independent of polarization. Equation (16) can be further simplified to give

$$\alpha_i(w) = \frac{\dfrac{3w^2}{2\pi^2 v_{\text{SiO}_2}^2}}{v_{\text{Si,LA}} D(w)_{\text{Si,LA}} + v_{\text{Si,TA}} D(w)_{\text{Si,TA}} + \dfrac{3w^2}{2\pi^2 v_{\text{SiO2}}^2}} \tag{17}$$

where ν_{SiO_2}=4100 m/s [16], quantities with subscripts LA and TA refer to the appropriate branches, and the Debye approximation is made for SiO_2. The group velocities and density of states for the two branches in silicon are obtained from curve fits to the dispersion curves (Fig. 1). The α-w plot is presented in Fig. 8. It was found that the results are not very sensitive to the actual value of α in the range of 0.2–1.0, consistent with results in Ref. [16]. This aspect will be elaborated on in a later section. At the interface, energy balance dictates that

$$q = -K\frac{\partial T}{\partial y} = G - J \tag{18}$$

The energy density leaving the Si/SiO_2 interface and entering the silicon domain in direction $\hat{s}$ may be written as (Fig. 7) [13,16]

$$e_i''(\hat{s}) = \frac{(1-p)}{\pi}\left(\rho_i \int_{\hat{s}\cdot\hat{n}>0} e_i'' \hat{s}\cdot\hat{n} d\Omega \right) + \rho_i p e_i''(\hat{s} - 2(\hat{s}\cdot\hat{n})\hat{n}) + \varepsilon_i e_{\text{wall},i}^0 \tag{19}$$

where p is the specularity parameter of the interface (zero for fully diffuse and unity for fully specular surface). Equation (19) is obtained from the assumption that the reflection of phonons is partially specular and partially diffuse. In addition, the interface emits energy. It is assumed that $\alpha_i=\varepsilon_i=(1-\rho_i)$ [16,32]. In this study, it is assumed that the Si/SiO_2 interface as well as the top surface of the silicon layer is fully diffuse.

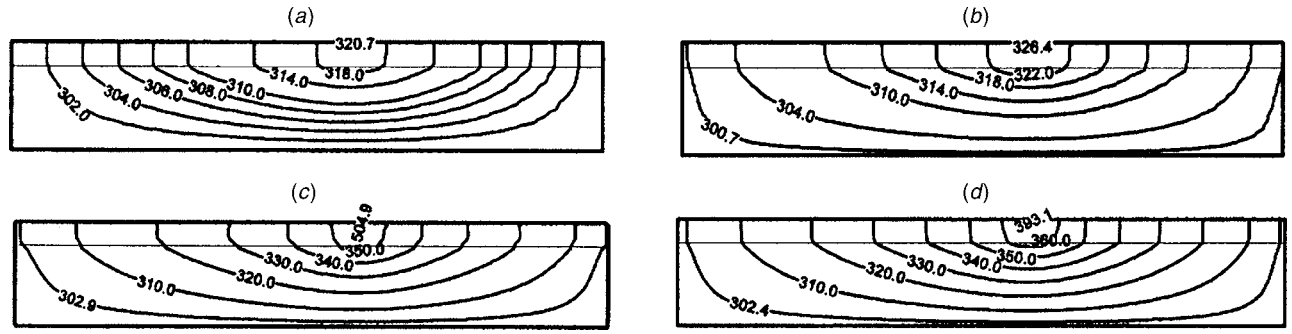

Fig. 9 Total lattice temperature contours in the domain using: (a) Fourier diffusion, (b) gray model, (c) semi-gray model, (d) full dispersion model

Fourier Model

The Fourier model solves the following equation in the domain:

$$\nabla \cdot (K \nabla T) + q = 0 \tag{20}$$

Here, the heat generation q is assumed to be 6.0×10^{17} W/m^3 in the heated region in Fig. 6, but zero elsewhere. The value of K is 142.3 and 1.38 W/m K for silicon and silicon dioxide, respectively. Continuity of heat flux is assumed at the Si/SiO_2 interface. Constant temperature boundary conditions with $T=300$ K are imposed on the lateral and bottom boundaries of the domain, while an adiabatic condition is imposed on the top boundary.

Gray Model

In this approach, all phonons are assumed to have the same group velocity and relax to equilibrium with the same relaxation time τ. The BTE is solved in the silicon region (Fig. 6), while the diffusion equation [Eq. (10)] is solved in the SiO_2 region. The main BTE equations are

$$\frac{\partial e''}{\partial t} + \nabla \cdot (v \hat{s} e'') = \frac{e^0 - e''}{\tau} + q_{\text{vol}} \tag{21}$$

$$e^0 = \frac{1}{4\pi} \int_{4\pi} e'' d\Omega = \frac{1}{4\pi} C (T_L - T_{\text{ref}}) \tag{22}$$

where e'' is the energy density/unit solid angle, e^0 is the equilibrium energy density, C is the total specific heat, and T_L is the lattice temperature. The value of ν for silicon is chosen to be 6400 m/s [27], while C is 1.66×10^6 J/m^3 K at 300 K [33]. The relaxation time of $\tau=6.28$ ps is obtained from the relation $K = 1/3 C \nu^2 \tau$, where $K=142.3$ W/m K for silicon. Hence, in the acoustically thick limit, this model is expected to yield results similar to the solutions from the diffusion equation. For SiO_2, a thermal conductivity of 1.38 W/m K is used as before. At the interface, $\alpha=0.71$ is obtained from Eq. (16) by assuming Debye density of states for silicon, with $\nu=6400$ m/s as the group velocity. Again, the lateral and bottom boundaries are assumed to be at 300 K. The top boundary is assumed diffusely reflecting.

Semi-Gray Model

The next modeling approach is a semi-gray model proposed in literature [13,16]. In this approach the phonons are divided into propagating and reservoir modes. Propagating mode phonons are responsible for transporting energy while the reservoir mode phonons are purely capacitative. Longitudinal acoustic phonons are considered to be the propagating mode, while the transverse acoustic and optical phonons are lumped together in the reservoir mode. Heat generation is incorporated via a source term for the reservoir mode BTE. The BTE is solved in the silicon region (Fig. 6). The main equations are [13,16]

$$\frac{\partial e_p''}{\partial t} + \nabla \cdot (v_p \hat{s} e_p'') = \frac{\frac{1}{4\pi} C_P (T_L - T_{\text{ref}}) - e_p''}{\tau} \tag{23}$$

$$C_R \frac{\partial (T_R - T_{\text{ref}})}{\partial t} = \frac{C_R (T_L - T_{\text{ref}}) - C_R (T_R - T_{\text{ref}})}{\tau} + q_{\text{vol}} \tag{24}$$

$$C_P (T_P - T_{\text{ref}}) = \int_{4\pi} e_p'' d\Omega \tag{25}$$

$$T_L = \frac{C_R T_R + C_P T_P}{(C_R + C_P)} \tag{26}$$

where T_L is the lattice temperature, T_P is the propagating mode phonon temperature, T_R is the reservoir mode phonon temperature, C_P and C_R are the propagating and reservoir mode specific heats, respectively, τ is the relaxation time, ν_P is the propagating mode group velocity, e_p'' is the propagating mode energy density per unit solid angle (J/m^3 sr). T_L is the overall lattice temperature, and is to be interpreted as an average of the propagating and reservoir mode temperatures as expressed in Eq. (26). The value of C_P is 0.32×10^6 J/m^3 K, C_R is 1.34×10^6 J/m^3 K, τ is 74.2 ps, ν_P is 4240 m/s [13,16]. It is worth discussing the rationale of choosing these values. The propagating and reservoir mode specific heats are obtained by evaluating their contributions based on the phonon dispersion curve (Fig. 1). The details of the method for computing these specific heats are given in Ref. [22]. The phonon velocity of 4240 m/s corresponds approximately to the group velocity of the higher frequency longitudinal acoustic phonons, which, following Ref. [16], are assumed to be the main energy carriers. The relaxation time is chosen so as to recover the bulk thermal conductivity of silicon (142.3 W/m K) in the acoustically thick limit using $K = 1/3 C_P \nu^2 \tau$. Hence, in the acoustically thick limit, this model will yield results similar to those from the diffusion equation [Eq. (10)]. The Fourier diffusion equation is solved in the SiO_2 region. At the interface between the two regions, a gray treatment similar to Eqs. (11)–(15) is used, with a value of $\alpha=0.52$ [16], obtained from a simplified version of Eq. (16). Again, the lateral and bottom boundaries are assumed to be at 300 K. The top boundary is assumed diffusely reflecting.

Numerical Method

The finite volume method [34–36] is employed to solve the 2D BTE. The spatial domain is discretized into rectangular control volumes, and the angular domain at any spatial point is discretized into non-overlapping control angles. The centroid of each control angle is denoted by the direction vector $\hat{s}$ (Fig. 2). Each octant is divided into $N_\theta \times N_\phi$ control angles. The details of the discretization procedure are described in Refs. [21,35,36]. The third-order accurate SMART scheme [37,38] is used to treat the ballistic term.

Each discrete angular direction in every frequency band results in a linear set of algebraic equations, which are solved using the tridiagonal matrix algorithm [34]. The directions themselves are solved sequentially using Picard iteration. The diffusion equation [Eq. (10)] is also solved by a structured finite volume approach [34]. Procedures for computing conjugate heat transfer are those described in Ref. [34].

Results

Comparison of Temperature Predictions.

Fourier Model. Computations of the temperature field are first done using the Fourier model described previously and are shown in Fig. 9(*a*). The number of spatial cells used is 100×30 (100 in the x direction, 30 in the y direction). This spatial mesh yields mesh-independent results to well within 1%. The peak temperature rise is 320.7 K in the hot spot region. An approximate estimate of hot spot temperature rise with respect to the boundary temperature can be made from fin theory using

$$\Delta T \sim \frac{q}{2\sqrt{2\frac{d}{D}k_{\mathrm{SiO_2}}k_{\mathrm{Si}}}}$$

and predicts a hot spot temperature of 331.5 K. Here d is the thickness of the silicon layer and D the thickness of the oxide layer. The temperature profile in the silicon region is nearly isothermal in the y direction.

Gray Model. Figure 9(*b*) shows the total lattice temperature contours computed using the gray BTE model. The number of spatial cells used in the entire domain is 100×30. The angular resolution in the octant is 8×8. These yield mesh independent results to within 1%. The maximum temperature is 326.4 K. This value is somewhat higher than the peak temperature obtained using the Fourier solution (320.7 K). Ballistic phonon and boundary scattering effects present in the gray model are responsible for this departure from the Fourier solution.

Semi-Gray Model. For the BTE solution, the angular discretization in the octant is 8×8 and 100×30 spatial cells are used. These yield mesh independent results to well within 1%. Figure 9(*c*) shows the contour plot of overall lattice temperature in the domain. The peak temperature is 504.9 K—drastically different from either the Fourier or the gray predictions. This high temperature is a direct result of the long relaxation time (74.2 ps) for energy scattering from the reservoir to the propagating mode, which creates an energy bottleneck in the reservoir mode. Qualitatively, the pattern of the contours is similar to those for the Fourier and gray predictions.

Full Phonon Dispersion Model. Computations are performed using six frequency bands in the LA branch, six in the TA branch, and one band to represent the optical phonon branch. The frequency range for the LA branch is from 0 to 7.46×10^{13} rad/s (Fig. 1), which is the frequency at the edge of the first Brillouin zone. This range is divided into six equal frequency bands. The frequency range for the TA branch is from 0 to 2.786×10^{13} rad/s (Fig. 1), and this range is also divided into six equal frequency bands. The optical mode is assumed to be at a frequency 9.0×10^{13} rad/s with a bandwidth of 1.5×10^{13} rad/s.

The angular resolution in the octant is 8×8 and 100×52 spatial cells are used. The results are mesh independent (frequency, angular resolution, and spatial cells) to within 4%. Figure 9(*d*) shows the total lattice temperature contours in the domain. The peak temperature is 393.1 K in the hot spot, which is significantly different from predictions using the other models. It is also significantly lower than the prediction of the semi-gray model. The effective relaxation time for the energy transfer from the optical to the acoustic modes is 7.2 ps. This is significantly smaller than the value of 74.2 ps from the semi-gray model and allows energy to be scattered to the acoustic modes without a bottleneck being created. Also, even though the effective relaxation time for the full dispersion model (7.2 ps) is comparable to the relaxation time for the gray model (6.28 ps), the results are very different. This is because the phonon group velocities in the two models are different, with the full dispersion model transporting high-frequency phonons at lower velocities than the gray model.

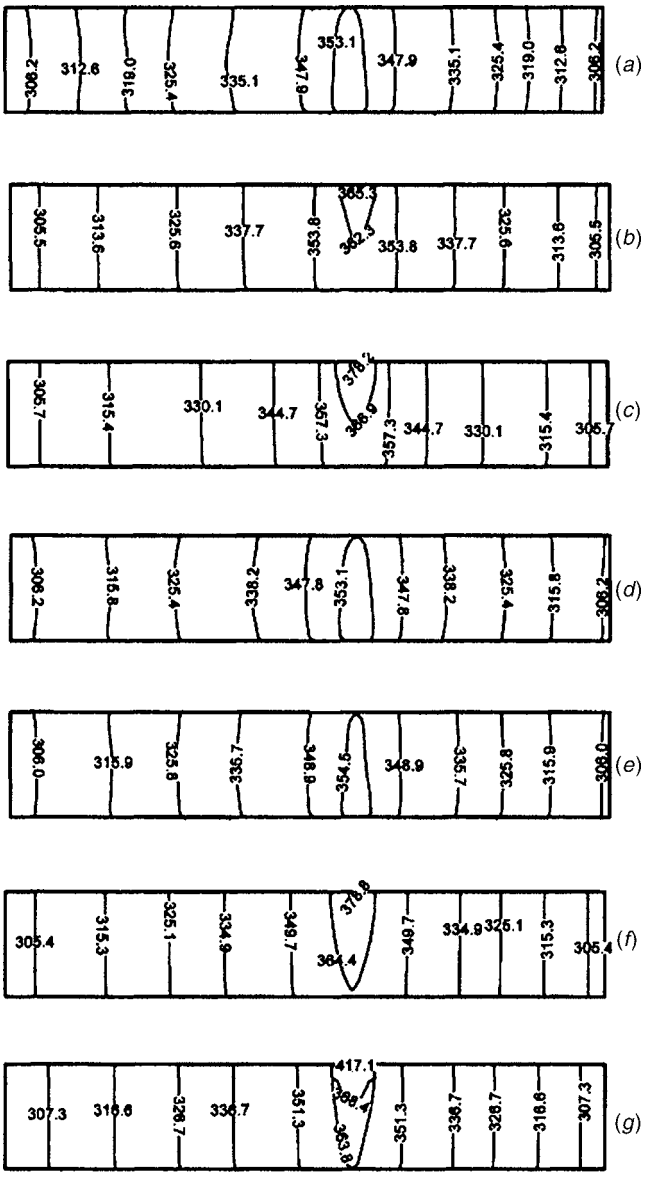

Fig. 10 Temperature contours in the silicon layer for the different frequency bands in the phonon branches: (a) LA band 1, (b) LA band 3, (c) LA band 6, (d) TA band 1, (e) TA band 3, (f) TA band 6, (g) optical band

The individual band temperatures in the silicon layer are shown in Fig. 10. Temperature contours for three bands for the LA branch, three in the TA branch and the optical mode are shown in the figure. For the LA and TA branch, higher band number corresponds to higher frequency. For the LA and TA branches, number 6 corresponds to the band with highest frequency, while number 1 corresponds to the lowest frequency. Figures 10(*a*)–10(*f*) indicate that the maximum LA and TA phonon temperature in the hot spot are in the range of 353–378 K for the different bands. Also noticeable is the fact that the higher frequency bands for both LA and TA branches are associated with higher temperatures. Higher

Table 1 Energy transfer rates at the silicon layer boundaries in each frequency band—Left hand boundary (LHB), right hand boundary (RHB), and interface

	LHB (%)		RHB (%)		Interface (%)		All Boundaries	
Band	LA	TA	LA	TA	LA	TA	LA	TA
1	0.13	0.04	0.19	0.06	-0.31	-0.10	0.01	0
2	0.61	0.26	0.97	0.41	0.20	-0.62	1.78	0.05
3	1.44	0.59	2.30	0.91	2.52	-1.22	6.26	0.28
4	2.49	1.06	3.97	1.68	6.68	0.95	13.14	3.69
5	4.08	1.61	6.49	2.55	12.60	4.49	23.17	8.65
6	4.38	2.77	6.94	4.31	18.02	6.53	29.34	13.61
Branch totals	13.14	6.32	20.86	9.93	39.71	10.0	73.71	26.25
Overall		19.46		30.79		49.71		99.96

frequency phonons are associated with lower group velocity (Fig. 1). Also, higher frequency bands are associated with smaller relaxation times. These two factors combine and result in the higher frequency phonons getting "hotter." Furthermore, as seen in Table 1 (discussed below), energy from the hot spot is deposited disproportionately in the high-frequency LA and TA bands. Figure 10(*g*) shows the optical mode temperature. The optical mode is the "hottest" with the maximum temperature in the hot spot of 417.1 K. Optical phonons are associated with zero group velocity and lose energy only via interactions with acoustic phonons. The extent of the optical phonon temperature rise is dependent on how quickly the energy is transferred to the acoustic modes. The maximum lattice temperature in the hot spot [393.1 K from Fig. 10(*d*)] is an average of these acoustic and optical mode temperatures.

Band-wise energy transfer rates at the boundaries of the silicon layer are shown in Table 1. The boundaries considered are the left side, right side and the Si/SiO_2 interface of the silicon layer. The values presented in Table 1 represent the net energy transfer rates per unit depth (W/m) crossing the respective boundaries. Heat transfer rates are deemed positive when leaving the silicon layer. The energy transfer rates reported in Table 1 are expressed as a percentage of the total power generation in the hot spot (600 W/m). The results in Table 1 indicate that the majority of energy flux is transported by longitudinal acoustic phonons. Summing up the boundary fluxes at the three boundaries, the contribution of the LA branch is 73.7% while the contribution of the TA branch is 26.3%. The higher frequency bands in both the LA and TA branches carry a higher proportion of the heat flux than the lower frequency bands. Additionally, about 50% of the energy from the hot spot is transported across the interface into the silicon dioxide region, mostly by the LA phonons (~40%). Interestingly, the energy flux at the interface is negative for some bands in both the LA and TA branches—meaning that when summed up over the entire interface, there is net energy transport from the interface into the silicon layer. For some of the frequency bands, the band temperatures are lower than the interface temperature. This is because the interface temperature is a weighted average of the incoming phonon temperatures and bottom boundary temperature through Eqs. (12)–(18). When the resistance of the SiO_2 layer is sufficiently high, the temperature of the interface is determined in large part as the weighted average of the incoming phonon temperatures. It is therefore possible for some bands to achieve temperatures lower than the interface temperature. Consequently, for the lower-temperature bands, there is an energy flux from the interface into the silicon layer. However, as can be seen from Table 1, in terms of overall energy balance, there is net energy entering the SiO_2 layer from the silicon, as expected.

Table 2 shows the relaxation times for the interactions between the different frequency bands. Each row represents the band *i* in the term τ_{ij} with each column representing the band *j*. As mentioned previously, higher band numbers in each branch denote higher frequency bands. The entries left blank are those for which there is no interaction between the corresponding bands due to energy conservation constraints [23–26]. All relaxation times are

Table 2 Band-wise relaxation times (ps) for the interaction of each frequency band with all other frequency bands. Each row corresponds to the index *i* in the term τ_{ij}, while each column corresponds to the index *j*.

Band		LA						TA						O
		1	2	3	4	5	6	1	2	3	4	5	6	
LA	1	5.72 *10^3		3.75 *10^3	3.08 *10^3									
	2		1.61 *10^3		4.18 *10^2	7.63 *10^2								**50.6**
	3	3.75 *10^3		1.87 *10^3		1.52 *10^2	3.25 *10^2	3.01 *10^4	4.53 *10^3	7.80 *10^4			1.88 *10^3	**37.6**
	4	3.08 *10^3	4.18 *10^2		3.91 *10^2		**77.2**			1.81 *10^3	9.51 *10^2	8.98 *10^2	1.84 *10^2	**38.5**
	5		7.63 *10^2	1.52 *10^2		1.03 *10^2	5.55 *10^2					1.82 *10^3	**75.5**	**38.5**
	6			3.25 *10^2	**77.2**	5.55 *10^2	**26.2**	3.74 *10^4	6.16 *10^3	2.81 *10^3	1.79 *10^3	1.29 *10^3	**61.1**	**20.8**
TA	1			1.12 *10^4			1.40 *10^4	5.85 *10^6						
	2			1.69 *10^3			2.30 *10^3		1.94 *10^5					
	3			2.91 *10^4	6.74 *10^2		1.05 *10^3			2.62 *10^4				
	4				3.55 *10^2		6.69 *10^2				5.17 *10^3			**81.2**
	5				3.35 *10^2	6.81 *10^2	4.81 *10^2					9.46 *10^2		**43.7**
	6			7.00 *10^2	**68.7**	**28.2**	**22.8**						**48.2**	**44.8**
O			**61.1**	**45.3**	**46.4**	**46.5**	**25.1**				2.62 *10^2	1.41 *10^2	1.45 *10^2	

Table 3 Energy transfer rates at the silicon layer boundaries in each frequency band—left hand boundary (LHB), right hand boundary (RHB), and interface; the Si/SiO_2 interface is completely transmissive

	LHB (%)		RHB (%)		Interface (%)		All Boundaries	
Band	LA	TA	LA	TA	LA	TA	LA	TA
1	0.12	0.04	0.19	0.06	-0.31	-0.10	0	0
2	0.60	0.26	0.96	0.40	0.18	-0.62	1.74	0.04
3	1.44	0.57	2.29	0.90	2.39	-1.24	6.12	0.23
4	2.49	1.05	3.96	1.67	6.50	0.96	12.95	3.68
5	4.08	1.60	6.49	2.54	12.39	5.30	22.96	9.44
6	4.39	2.79	6.95	4.35	17.79	6.52	29.13	13.66
Branch totals	13.12	6.31	20.84	9.92	38.94	10.82	72.9	27.05
Overall		19.43		30.76		49.76	99.95	

Table 4 Energy transfer rates at the silicon layer boundaries in each frequency band—left hand boundary (LHB), right hand boundary (RHB), and interface; the silicon top boundary is fully specular, and the Si/SiO_2 interface is completely transmissive

	LHB (%)		RHB (%)		Interface (%)		All Boundaries	
Band	LA	TA	LA	TA	LA	TA	LA	TA
1	0.17	0.05	0.22	0.07	-0.38	-0.12	0.01	0
2	0.76	0.36	1.16	0.47	-0.009	-0.77	1.911	0.06
3	1.71	0.80	2.66	1.08	1.89	-1.52	6.26	0.36
4	2.85	1.28	4.43	1.97	5.65	0.61	12.93	3.86
5	4.56	1.79	7.09	2.79	11.2	4.76	22.85	9.34
6	4.64	2.90	7.18	4.41	17.0	6.29	28.82	13.6
Branch totals	14.69	7.18	22.74	10.79	35.35	9.25	72.78	27.22
Overall		21.87		33.53		44.60		100.0

in ps. The lowest relaxation times ($<10^2$ ps) are highlighted for clarity. There is a wide spread in the range of the relaxation times—ranging from 5.8×10^6 to 21.0 ps. The smaller the relaxation time, the greater the impact of that particular interaction in the overall picture. Another observation is that lower frequency (i.e., lower numbered) bands in both LA and TA branches are associated with larger relaxation times than higher frequency bands. This indicates that the higher frequency bands in both LA and TA branches are more influential in dictating the thermal predictions than the lower frequency bands. This may also help explain the results in the Table 1, where higher frequency bands in both LA and TA branches carry significantly higher proportion of the energy flux.

Influence of Si/SiO_2 Interface Transmission and Boundary Scattering. Two basic resistive mechanisms operate at the horizontal boundaries of the silicon layer. At the top boundary and at the Si/SiO_2 interface, phonon boundary scattering acts to reduce the effective conductivity of the silicon layer and, consequently, to increase predicted hot spot temperatures. The Si/SiO_2 interface is not completely transmissive because of the different acoustic speeds in Si and SiO_2. This leads to an effective resistance to thermal transport at the interface and also acts to increase the hot spot temperature. It is unclear whether this mechanism plays a significant role in SOI devices where the low conductivity of the SiO_2 layer may swamp all other resistive mechanisms.

To answer this question, the impact of Si/SiO_2 interface transmission coefficient upon the thermal predictions is examined. For the full phonon dispersion model, the interface transmission coefficient is set equal to unity for all the frequency bands. Thus, there is no reflection at the interface and boundary scattering resistance is effectively eliminated. The top boundary is modeled as a diffusely reflecting boundary, as before. The temperature predictions in the domain are virtually identical to those obtained with the earlier case where the α-w plot is as shown in Fig. 8. The fluxes for the different frequency bands at the silicon layer boundaries are shown in Table 3. The flux results are almost the same as Table 1. This demonstrates that for this case, the interface resistance does not have an impact on the thermal predictions in the domain. The trends are similar for the semi-gray and gray models as well, and are not shown. Since the interface resistance appears in series with the resistance of the SiO_2 layer, the latter resistance dominates. For superlattice structures in which the adjacent layers have comparable thermal conductivity, and when the mean free path of phonons is comparable to the film thickness in both layers, the interface can be expected to play a significant role [39,40].

Next, the top boundary is made specularly reflecting while keeping the Si/SiO_2 interface completely transmissive. This eliminates all boundary scattering mechanisms as well as the interface resistance due to fractional transmissivity. For the full dispersion model, the peak temperature in the domain is 384.9 K as opposed to 393.0 K when the top wall reflection is fully diffuse; this fall in peak temperature reflects the increased effective conductivity of the silicon layer. The fluxes are shown in Table 4. The energy transmitted through the interface falls somewhat and the loss through the lateral boundaries increases as the effective resistance of the silicon layer falls. There is some change in the bandwise fluxes from the situation in Table 1. This shows that the behavior of the silicon layer top boundary is a factor, albeit not a very strong one. The trends are the same for the gray and semi-gray cases as well. For the gray case, the maximum temperatures are found to be 325.9 and 323.9 K with the diffuse and specular top boundaries, respectively. For the semi-gray case, the corresponding maximum temperatures are 504.7 and 494.3 K, respectively.

The results from these computations indicate that resistance due to silicon layer top boundary scattering and interface transmissivity are not major players in determining hot spot temperature in SOI devices at the scales and domain sizes considered here. The magnitude of the maximum temperature is determined in large part by the optical-to-acoustic relaxation time and is a very local phenomenon. For emerging ultrascaled devices at the 10–20 nm scale, phonon boundary confinement may damp group velocities, leading to low effective silicon layer thermal conductivity [26]. These effects, in addition to boundary scattering may compete with the high thermal resistance of the SiO_2 layer in future devices.

Heat Generation in the Acoustic Modes. In the results presented up to this point for the semi-gray and the full dispersion model, the heat generation (electron-phonon interaction) term has been incorporated only in the reservoir and optical modes, respectively. In reality, electrons deposit energy to both optical and acoustic modes depending on their energy level. In this section, results are presented with the electrons depositing energy only to the acoustic phonons. For the semi-gray model, the heat generation term now appears in the propagating mode BTE. It is assumed energy is dissipated equally in all directions. For the full dispersion model, energy is dissipated equally in all frequency bands in the acoustic branch so that each band receives an energy source of $(q_{vol}/12)$. Furthermore, energy is deposited equally in all directions within a frequency band.

With the semi-gray model, the maximum temperature is only 365.5 K, which is drastically different from the maximum value of 504.9 K in Fig. 9(*c*). Since energy is being deposited directly to the propagating mode, there is no bottleneck caused by the reservoir mode to propagating mode energy transfer, and a lower maximum temperature results. With the full dispersion model, a maximum temperature of 364.6 K is predicted, which is significantly lower than the value of 393.1 K in Fig. 9(*d*). This is probably a result of energy transport in the low-frequency bands, which have

Table 5 Energy transfer rates at the silicon layer boundaries in each frequency band—left hand boundary (LHB), right hand boundary (RHB), and interface; electrons deposit energy equally among the acoustic phonon bands

	LHB (%)		RHB (%)		Interface (%)		All Boundaries	
Band	LA	TA	LA	TA	LA	TA	LA	TA
1	0.13	0.05	0.37	0.25	7.68	7.97	8.18	8.27
2	0.62	0.27	0.98	0.56	4.0	7.18	5.6	8.01
3	1.46	0.59	2.28	1.02	3.15	6.09	6.89	7.7
4	2.53	1.07	3.94	1.67	2.80	3.33	9.27	6.07
5	4.14	1.63	6.45	2.54	2.42	2.07	13.01	6.24
6	4.45	2.81	6.91	4.30	2.47	-0.22	13.83	6.89
Branch totals	13.33	6.42	20.93	10.34	22.52	26.42	56.78	43.18
Overall		19.75		31.27		48.94		99.96

a higher group velocity. For the case in which the heat generation is in the optical mode, the energy is scattered from the optical to acoustic modes. The acoustic modes then transport the energy. This sequence is eliminated when all the heat generation is directly in the acoustic modes.

The band-wise fluxes at the silicon layer boundaries are presented in Table 5 for the full dispersion model. Each acoustic band receives 1/12th (i.e., 8.33%) of q_{vol} in the hot spot. Since there are equal numbers of LA and TA bands, the LA and TA modes each cumulatively start with 50% of q_{vol}. Table 5 shows that this energy is redistributed somewhat among the acoustic modes; the LA modes account for 56.78% of the outgoing heat flux, while the TA mode contribution falls to 43.18%. Furthermore, the high-energy TA bands (4–6) are the ones that predominantly lose energy to the high-frequency LA bands (4–6), though there is some contribution from the low-frequency LA bands as well. Though the precise pathways for energy exchange between bands are complex, an examination of Table 2 is instructive. Scattering between acoustic modes and the optical mode is governed by the smallest relaxation times in the table. Thus, under the present model, the optical mode appears to function as a conduit for redistributing energy among the acoustic bands, but does not itself transport any energy. Another interesting feature is the difference in band-wise distributions of fluxes between the side boundaries and the interface between the cases shown in Tables 1 and 5. These differences are due to the small aspect ratio of the silicon layer, which results in small phonon residence times in the vertical direction, and far longer residence times in the horizontal direction.

A summary of the maximum temperatures with all the different models and different cases presented in this paper is shown in Table 6. The values left blank indicate that particular case is not applicable. The base line case is one where the electrons dissipate their energy entirely to the optical mode, i.e., q_{vol} is entirely in the optical mode. The interface and boundary treatment is as described earlier. Case 1 refers to the case where the Si/SiO_2 interface is completely transmissive, and everything else is the same as in the base line case. In Case 2, in addition to the fully transmissive interface, the silicon top boundary is fully specular. For Case 3, q_{vol} is in the propagating or acoustic modes and everything else is similar to the base line case. The Fourier solution underpredicts the temperature rise from the full phonon dispersion model by as much as 350%. There is a large discrepancy between the predictions from the gray, semi-gray and the full phonon dispersion model. This is primarily a result of the inaccurate representation of optical-to-acoustic relaxation time in the simpler models.

Table 6 Comparison of maximum temperatures (K) with different models

	Baseline	Case 1	Case 2	Case 3
Fourier	320.7			
Gray	326.4	325.9	323.9	
Semi-gray	504.9	504.7	494.3	365.5
Full dispersion	393.1	393.0	384.9	364.6

Discussion and Conclusions

A comprehensive model based on the solution to the BTE, and accounting for the full details of the phonon dispersion and polarization in silicon, has been developed. This model considers longitudinal (LA) and transverse acoustic (TA) phonons, optical phonons, and the interactions among them via frequency-dependent relaxation times. The model has been validated against experimental thermal conductivity data for both bulk and thin silicon layers and shown to match the data satisfactorily. This full phonon dispersion model is used to make thermal predictions in an SOI transistor.

The results show that significantly different predictions are obtained using the Fourier, gray, semi-gray and full dispersion models. The Fourier model is unable to account for the energy accumulation in the optical mode as well as boundary scattering and ballistic phonon effects, and predicts substantially lower temperatures than the BTE-based models. The maximum temperature predicted by the BTE-based models depends in large part on the optical-to-acoustic relaxation time. The semi-gray model predicts substantially higher temperatures than the full dispersion model, primarily as a result of the long reservoir-to-propagating mode relaxation time. This suggests that using a single relaxation time derived from bulk thermal conductivity matching cannot adequately capture the rate at which energy is removed from the optical modes. More detailed modeling of phonon relaxation times [23,24] is critical. The results also show that the different phonon modes are substantially out of equilibrium in this application, as evidenced by the substantially different phonon temperatures predicted by the full dispersion model. This departure from equilibrium cannot be captured by the Fourier, gray and semi-gray models.

The transmissivity of the Si/SiO_2 interface has been found to play a negligible role in influencing thermal predictions, a trend also noted in Ref. [16]. This implies that the thermal resistance of the SiO_2 layer dominates over the interface transmission properties. The boundary treatment at the silicon top boundary has been shown to have some impact on the thermal predictions, but the impact is under 20%.

For the case in which the heat generation term is included only in the optical phonon mode, the energy from the hot spot is shown to be deposited preferentially in the high-frequency LA and TA modes due to shorter relaxation times. It is transported primarily by those modes to the boundaries of the silicon layer; the contribution of the LA modes is found to predominate. When energy is distributed to all acoustic modes, the high group velocity of the low-frequency acoustic modes serves to increase the rate of transport and results in a lower maximum temperature.

Thus, the manner in which the energy is deposited from the electrons to the phonon system is found to be critical. The precise distribution of phonon-mode energies due to electron-phonon scattering must be determined [41] in order to make reliable temperature predictions. Full-band Monte Carlo device simulators such as MOCA [42] may be used to predict the distribution of the heat source in the different phonon bands. The interplay of inter-band relaxation times and the phonon residence time will then determine the specific pathways for energy transfer as well as the rate of transport, and therefore determine the maximum device temperature.

Acknowledgments

The support of NSF Grant No. CTS-0103082, CTS-0312420, CTS-0219008 and EE-0228390 is gratefully acknowledged.

Nomenclature

C = total volumetric heat capacity ($J/m^3 K$)
C_w = volumetric specific heat per unit frequency ($Js/m^3 K$)
$D(w)$ = phonon density of states (m^{-3})
e_{total} = total energy (J/m^3)
f_w = phonon distribution function
$\hbar$ = reduced Planck's constant ($=h/(2\pi)$, 1.054×10^{-34} Js)
k_B = Boltzmann's constant (1.38e−23 J/K)
K = thermal conductivity (W/m K)
N_{LA}, N_{TA} = number of frequency bands in LA and TA branches
N_{bands} = total number of frequency bands ($N_{LA}+N_{TA}+1$)
N_θ, N_ϕ = number of θ and ϕ divisions in an octant
q_{vol} = volumetric heat generation (W/m^3)
$\mathbf{r}$ = position vector (m)
$\hat{s}$ = unit direction vector
t = time (s)
T = temperature (K)
v = phonon velocity (m/s)
w = phonon frequency (rad/s)

Greek symbols

α = transmissivity of silicon
Δw = frequency width (rad/s)
ε = emissivity
ϕ = azimuthal angle
γ = band-averaged inverse relaxation time for interaction (s^{-1})
ρ = reflection coefficient
τ = relaxation time of a phonon (s)
θ = polar angle (deg.)

Subscripts

i = ith frequency band
ij = property specific to bands i and j
L = lattice
o = optical mode
P = propagating mode
R = reservoir mode
w = phonon frequency

Superscripts

0 = equilibrium condition

References

[1] Flik, M. I., Choi, B. I., and Goodson, K. E., 1992, "Heat Transfer Regimes in Microstructures," ASME J. Heat Transfer, **114**, pp. 666–674.
[2] Majumdar, A., 1998, "Microscale Energy Transport in Solids," in *Microscale Energy Transport*, C.-L. Tien, A. Majumdar, and F. M. Gerner, eds., Taylor and Francis, Washington DC pp. 1–94.
[3] Chen, G., 1998, "Phonon Wave Effects on Heat Conduction in Thin Films," in *AIAA/ASME Joint Thermophysics and Heat Transfer Conference*.
[4] Chen, G., 2000, "Particularities of Heat Conduction in Nanostructures," J. Nanopart. Res., **2**, pp. 199–204.
[5] Majumdar, A., 1993, "Microscale Heat Conduction in Dielectric Thin Films," ASME J. Heat Transfer, **115**, pp. 7–16.
[6] Kittel, C., 1996, *Introduction to Solid State Physics*, Wiley, New York.
[7] Ashcroft, N. W., and Mermin, N. D., 1976, *Solid State Physics*, Saunders College, Philadelphia.
[8] Majumdar, A., Fushinobu, K., and Hijikata, K., 1995, "Effect of Gate Voltage on Hot-Electron and Hot-Phonon Interaction and Transport in a Submicrometer Transistor," J. Appl. Phys., **77**(12), pp. 6686–6694.
[9] Fushinobu, K., Hijikata, K., and Majumdar, A., 1995, "Heat Generation in Sub-Micron GaAs MESFETs," *Proceedings-International Intersociety Electronic Packaging Conference* EEP-Vol. 10-2, Advances in Electronic Packaging, pp. 897–902.
[10] Fushinobu, K., Majumdar, A., and Hijikata, K., 1995, "Heat Generation and Transport in Submicron Semiconductor Devices," ASME J. Heat Transfer, **117**, pp. 25–31.
[11] Lai, J., and Majumdar, A., 1996, "Concurrent Thermal and Electrical Modeling of Submicrometer Silicon Devices," J. Appl. Phys., **79**(9), pp. 7353–7361.
[12] Ju, Y. S., 1999, "Microscale Heat Conduction in Integrated Circuits and their Constituent Films," Ph.D thesis, *Department of Mechanical Engineering*, Stanford University, Stanford, CA.
[13] Sverdrup, P. G., 2000, "Simulation and Thermometry of Sub-Continuum Heat Transport in Semiconductor Devices," Ph.D thesis, *Department of Mechanical Engineering*, Stanford University, Stanford, CA.
[14] Sverdrup, P. G., Ju, Y. S., and Goodson, K. E., 1999, "Impact of Heat Source Localization on Conduction Cooling of Silicon-on-Insulator Devices," in *International Conference on Modeling and Simulation of Microsystems*.
[15] Sverdrup, P. G., Banerjee, K., Dai, C., Shih, W., Dutton, R. W., and Goodson, K. E., 2000, "Sub-Continuum Thermal Simulations of Deep Sub-Micron Devices Under ESD Conditions," in *International Conference on Simulation of Semiconductor Processes and Devices*, IEEE Electron Devices Society.
[16] Sverdrup, P. G., Ju, Y. S., and Goodson, K. E., 2001, "Sub-Continuum Simulations of Heat Conduction in Silicon-on-Insulator Transistor," ASME J. Heat Transfer, **123**, pp. 130–137.
[17] Pop, E., Banerjee, K., Sverdrup, P. G., Dutton, R., and Goodson, K. E., 2001, "Localized Heating Effects and Scaling of Sub-0.18 Micron CMOS Devices," in *IEEE International Electron Devices Meeting*.
[18] Armstrong, B. H., 1981, "Two-Fluid Theory of Thermal Conductivity of Dielectric Crystals," Phys. Rev. B, **23**(2), pp. 883–899.
[19] Armstrong, B. H., 1985, "N Processes, the Relaxation-Time Approximation, and Lattice Thermal Conductivity," Phys. Rev. B, **32**(6), pp. 3381–3390.
[20] Narumanchi, S. V. J., Murthy, J. Y., and Amon, C. H., 2003, "Simulation of Unsteady Small Heat Source Effects in Sub-Micron Heat Conduction," ASME J. Heat Transfer, **125**(5), pp. 896–903.
[21] Narumanchi, S. V. J., 2003, "Heat Transport in Sub-Micron Conduction, in Mechanical Engineering," Ph.D thesis, Department of Mechanical Engineering, Carnegie Mellon University, Pittsburgh.
[22] Narumanchi, S. V. J., Murthy, J. Y., and Amon, C. H., 2004, "Submission Heat Transfer Model in Silicon Accounting for Phonon Dispersion and Polarization," ASME J. Heat Transfer, **126**(6), pp. 946–955.
[23] Klemens, P. G., 1958, "Thermal Conductivity and Lattice Vibrational Modes," in *Solid State Physics*, F. Seitz and D. Thurnbull, eds., Academic, New York, pp. 1–98.
[24] Klemens, P. G., 1969, "Theory of Thermal Conductivity of Solids," in *Thermal Conductivity*, R. P. Tye, ed., Academic Press, London, pp. 1–68.
[25] Han, Y.-J., and Klemens, P. G., 1993, "Anharmonic Thermal Resistivity of Dielectric Crystals at Low Temperatures," Phys. Rev. B, **48**, pp. 6033–6042.
[26] Balandin, A., and Wang, K. L., 1998, "Significant Decrease of the Lattice Thermal Conductivity due to Phonon Confinement in a Free-standing Semiconductor Quantum Well," Phys. Rev. B, **58**(3), pp. 1544–1549.
[27] Holland, M. G., 1963, "Analysis of Lattice Thermal Conductivity," Phys. Rev., **132**(6), pp. 2461–2471.
[28] Ju, Y. S., and Goodson, K. E., 1999, "Phonon Scattering in Silicon Thin Films with Thickness of Order 100 nm," Appl. Phys. Lett., **74**(20), pp. 3305–3307.
[29] Asheghi, M., Touzelbaev, M. N., Goodson, K. E., Leung, Y. K., and Wong, S. S., 1998, "Temperature-Dependent Thermal Conductivity of Single-Crystal Silicon Layers in SOI Substrates," J. Heat Transfer, **120**, pp. 30–36.
[30] Asheghi, M., Kurabayashi, K., Kasnavi, R., and Goodson, K. E., 2002, "Thermal Conduction in Doped Single-Crystal Silicon Films," J. Appl. Phys., **91**(8), pp. 5079–5088.
[31] Mazumder, S., and Majumdar, A., 2001, "Monte Carlo Study of Phonon Transport in Solid Thin Films Including Dispersion and Polarization," ASME J. Heat Transfer, **123**, pp. 749–759.
[32] Swartz, E. T., and Pohl, R. O., 1989, "Thermal Boundary Resistance," Rev. Mod. Phys., **61**(3), pp. 605–668.
[33] Touloukian, Y. S., and Buyco, E. H., 1970, "Thermal Conductivity: Nonmetallic Solids," in *Thermophysical Properties of Matter*, IFI/Plenum, New York.
[34] Patankar, S. V., 1980, *Numerical Heat Transfer and Fluid Flow*, Taylor and Francis, London.
[35] Chai, J. C., Lee, H. S., and Patankar, S. V., 1994, "Finite Volume Method for Radiation Heat Transfer," J. Thermophys. Heat Transfer, **8**(3), pp. 419–425.
[36] Murthy, J. Y., and Mathur, S. R., 1998, "Finite Volume Method for Radiative Heat Transfer Using Unstructured Meshes," J. Thermophys. Heat Transfer, **12**(3), pp. 313–321.
[37] Gaskell, P. H., and Lau, A. K. C., 1988, "Curvature-Compensated Convective Transport: SMART, a New Boundedness-Preserving Transport Algorithm," Int. J. Numer. Methods Fluids, **8**, pp. 617–641.
[38] Darwish, M. S., and Moukalled, F. H., 1994, "Normalized Variable and Space Formulation Methodology for High-Resolution Schemes," Numer. Heat Transfer, Part A, **26**, pp. 79–96.
[39] Chen, G., 1997, "Size and Interface Effects on Thermal Conductivity of Superlattices and Periodic Thin-Film Structures," J. Heat Transfer, **119**, pp. 220–229.
[40] Chen, G., 1998, "Thermal Conductivity and Ballistic-Phonon Transport in the Cross-Plane Direction of Superlattices," Phys. Rev. B, **57**(23), pp. 14958–14973.
[41] Pop, E., Sinha, S., and Goodson, K. E., 2003, "Detailed Phonon Generation Simulations via the Monte Carlo Method," *Proceedings-ASME Summer Heat Transfer Conference*, Paper No. HT2003-47312.
[42] Duncan, A., Ravaioli, U., and Jakumeit, J., 1998, "Full-Band Monte Carlo Investigation of Carrier Trends in the Scaling of Metal-Oxide-Semiconductor Field-Effect Transistors," IEEE Trans. Electron Devices, **45**, pp. 867–876.

Jaewon Chung[1]
e-mail: cgrigoro@me.berkeley.edu

Seunghwan Ko

Costas P. Grigoropoulos[2]

Laser Thermal Laboratory,
Department of Mechanical Engineering,
University of California, Berkeley,
Berkeley, CA 94720-1740

Nicole R. Bieri

Cedric Dockendorf

Dimos Poulikakos

Laboratory of Thermodynamics in Emerging Technologies,
Department of Mechanical and Process Engineering,
ETH Zurich, CH-8092 Zurich, Switzerland

Damage-Free Low Temperature Pulsed Laser Printing of Gold Nanoinks On Polymers

In this study, pulsed laser based curing of a printed nanoink (nanoparticle ink) combined with moderate and controlled substrate heating was investigated to create microconductors at low enough temperatures appropriate for polymeric substrates. The present work relies on (1) the melting temperature depression of nanoparticles smaller than a critical size, (2) DOD (drop on demand) jettability of nanoparticle ink, and (3) control of the heat affected zone induced by pulsed laser heating. In the experiments, gold nanoparticles of 3–7 nm *diameter dissolved in toluene solvent were used as ink. This nanoink was printed on a polymeric substrate that was heated to evaporate the solvent during or after printing. The overall morphology of the gold microline was determined by the printing process and controlled by changing the substrate temperature during jetting. In addition, the printed line width of about* 140 μm *at the room temperature decreased to* 70–80 μm *when the substrate is heated at* 90°C. *By employing a microsecond pulsed laser, the nanoparticles were melted and coalesced at low temperature to form a conductive microline which had just 3–4 times higher resistivity than the bulk value without damaging the temperature sensitive polymeric substrate. This gold film also survived after Scotch tape test. These are remarkable results, considering the fact that the melting temperature of bulk gold is* 1064°C *and the polymeric substrate can be thermally damaged at temperatures as low as* 500°C. [DOI: 10.1115/1.1924627]

Introduction

The need-driven trend in electronics manufacturing is to develop constantly smaller and tighter packed components. On the other hand, cost is a primary consideration determining commercial success and marketability in many electronic devices, such as large area displays, RFID (Radio Frequency Identification), adaptive distributed antennas, etc. Since these electronic devices require either a large area substrate or flexibility, polymeric materials have advantages over expensive and hard, rigid substrates, such as silicon and quartz. In addition, it is important to fabricate low resistance conductors because the signal has to propagate a long distance and RC delays should be minimized. Corresponding to these requirements, direct writing (additive) processing using jet printing technology has gained significant interest as an alternative approach to conventional, subtractive integrated circuit (IC) processes [1–4].

In addition, the emergence of consistent manufacturing methods of nanoparticles [5–7] is creating a vivid activity related to the utilization of these particles. [2,8–13]. The great potential they possess through remarkable thermophysical properties can be realized in future-oriented engineering applications. Specific to this paper are gold nanosized particles (3–7 nm diameter), which possess lower melting temperatures (approx. 400–800°C compared to the melting temperature of bulk gold (1063°C) [14].

Combining the above two characteristics, several studies related to printing and curing of nanoink using a hot plate or a curing oven have been carried out [2,8–10]. Since nanoparticles melt at low temperature, there is great potential for producing microconductors at low processing temperature suitable for polymeric substrate. Compared to the evaporation and sintering alternatives using a hot plate or a curing oven, the laser curing enables local heating, so that thermally sensitive circuits in other areas of the work specimen can be protected. In previous studies, nanoink printed on glass substrate containing substantial amount of solvent was cured with continuous irradiation by a laser beam [11–13]. In many cases, a portion of nanoink was displaced ahead and behind the laser spot due to thermocapillary flow. In addition, the processing speed was relatively slow for obtaining a highly conductive gold line. Most of all, the temperature rise induced by the continuous laser irradiation was substantial, so that it was not suitable for flexible polymeric substrates.

In this work, the solvent was evaporated by heating a polymer substrate at a moderate temperature during or after printing. Subsequently, the deposited material was irradiated with a pulsed laser beam to cure the nanoparticles. In this manner, it was possible to circumvent the above problems and manufacturing of a highly conductive microconductor on a polymer film was successfully demonstrated.

Drop-on-Demand Printing System

Fine-lines of nanoink were created on a polyimide film by the generation of microdroplets using the piezoelectric drop-on-demand (DOD) printing system (Fig. 1). The DOD jetting system is composed of a backpressure controller, a purging system and a piezoelectric jetting system. The detailed description of the experimental system is given in earlier publications [11–13].

About 10 mbar vacuum is maintained in the reservoir to prevent nanoink from leaking from the nozzle of the capillary tube due to the small viscosity and low surface tension of the toluene based nanoink. A vacuum controller and a magnetic valve were connected between the vacuum pump and the reservoir to minimize the loss of toluene due to continuous evaporation. To purge the clogging, pressure controlled nitrogen gas is used and the purging pressure was controlled at 0.4 psi.

MicroFab's solder-jet head with a 50 μm nozzle diameter is used to produce microdroplets and a bipolar voltage waveform with amplitude of $\pm 13 \sim \pm 15$ V is applied as Fig. 2. Briefly, the

[1]Present address: Department of Mechanical Engineering, Korea University, Seoul, Korea.
[2]Corresponding author.
Contributed by the Heat Transfer Division for publication in the JOURNAL OF HEAT TRANSFER. Manuscript received June 9, 2004. Final manuscript received January 12, 2005. Review conducted by: Gang Chen.

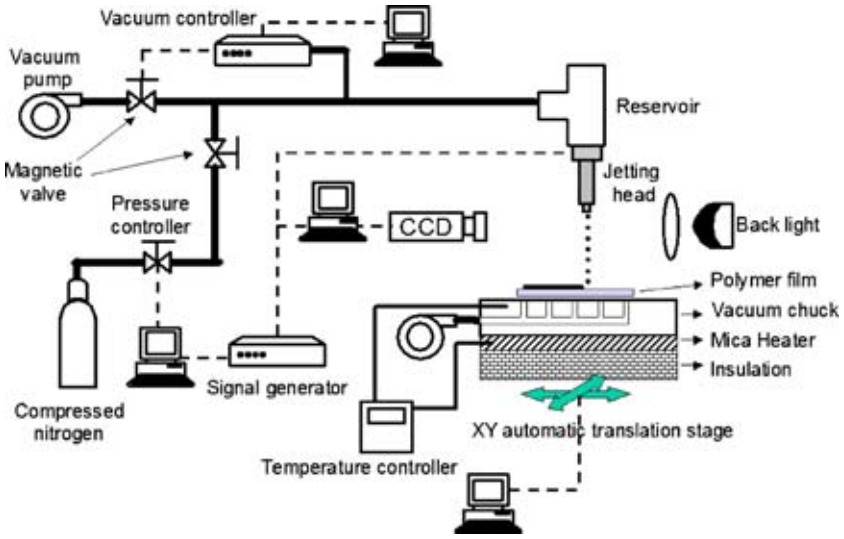

Fig. 1 Schematic of nanoink printing and curing system

first rising voltage expands the glass capillary and droplet is pushed outside the nozzle due to the falling voltage. The final rising voltage cancels some of the residual acoustic oscillations that remain after drop ejection and may cause satellite droplets [15,16]. The optimum dwelling time, t_d given by l/c (length of glass capillary/speed of sound) is about 40 μs.

The signal generator used to produce microdroplets also triggers the CCD camera, so that the CCD captures images at the droplet generation frequency. The CCD camera provides *in situ* "frozen" image of the droplet to check for satellite droplet generation as well as to measure the droplet velocity and size. After generating stable NPS droplets of 46 μm diameter (i.e., 51 pL) at 30 Hz, a continuous line was made on the glass substrate by moving a precision translation stage at 2 mm/s. The gap between the jetting head tip and the glass substrate was maintained at 2 mm.

The temperature of the vacuum chuck is controlled by thermocouple and the Mica heater. Vacuum (300 mbar) is applied through 0.5 mm diameter holes to attach the polymer film on the vacuum chuck (Fig. 1).

Printing on a Heated Substrate

Printing on a heated substrate has advantages over room temperature printing. The solvent evaporates soon after contact, so that a thick layer can be deposited with high jetting frequency while maintaining a small feature size. The rapid liquid evaporation also eliminated wetting problems in room temperature printing, such as uneven wetting in response to minute contamination of the substrate. In addition, it enables multilayer deposition without intervention of heating and cooling schedule. However, there

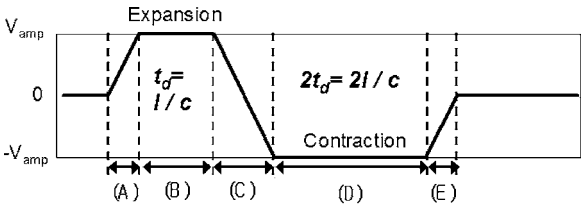

	(A)	(B)	(C)	(D)	(E)
Time(μs)	2	40	4	80	2

Fig. 2 Bipolar voltage waveform applied to piezoelectric actuator

are limitations in printing on a heated substrate. For stable droplet generation and impact (which is directly related to the spatial resolution), the nozzle to substrate distance should be maintained less than 2–3 mm. This causes temperature rise in the nozzle (and corresponding decrease in both viscosity and surface tension of fluid) due to heat transfer from the hot substrate. Therefore, the maximum temperature of the hot substrate for stable droplet generation is limited. In addition, unless the droplet is jetted in a continuous mode, the solvent evaporates in the nozzle, increasing the possibility of partial or complete nanoparticle clogging.

Related to the above topic, the variation of jetting conditions by substrate heating is discussed and the temperature rise at the nozzle is quantified in the following section. In addition, the morphology change of the printed nanoink due to substrate heating are shown.

Jetting Condition Variation due to Substrate Heating. When the substrate is heated during jetting, the jetting velocity changes due to significant heat transfer from the heated substrate to the nozzle of the jet head. Specifically, conductive heat transfer across the 1–2 mm thick air gap elevates the temperature of the nozzle and nearby fluid. Note that the Rayleigh number is of the order of 10^{-4}, when the gap distance between the jetting head and the substrate is used as length scale, so that heat conduction in the air medium is dominant over natural convection. This temperature rise decreases the viscosity and surface tension of the fluid near the nozzle, so that the ejecting droplet velocity increases dramatically. In the case of toluene, a 50°C temperature rise from room temperature decreases the viscosity and surface tension by about 40% and 10%, respectively, while the ejecting velocity increases about 3–5 times. The temperature rise at the nozzle can be minimized by increasing the gap distance between the nozzle and the substrate. However, the impact velocity of the droplet also decreases and good control on droplet placement cannot be guaranteed. In addition, when the gap is large, natural convection becomes more significant. Consequently, the directionality of droplet impact is not perfectly stable according to observation.

The temperature rise at the nozzle, T_n (i.e., the temperature of the droplet) due to the substrate heating is quantified both experimentally and numerically. In this experiment, α-terpineol instead of toluene is used, since the jettable temperature range of α-terpineol is wider. However, it is noted that the evaporation rate of α-terpineol is slower than that of toluene, since the boiling temperature is higher. Therefore, the substitution of α-terpineol for toluene weakens several of the above mentioned advantages of printing on a heated substrate. Figure 3 shows the configuration of

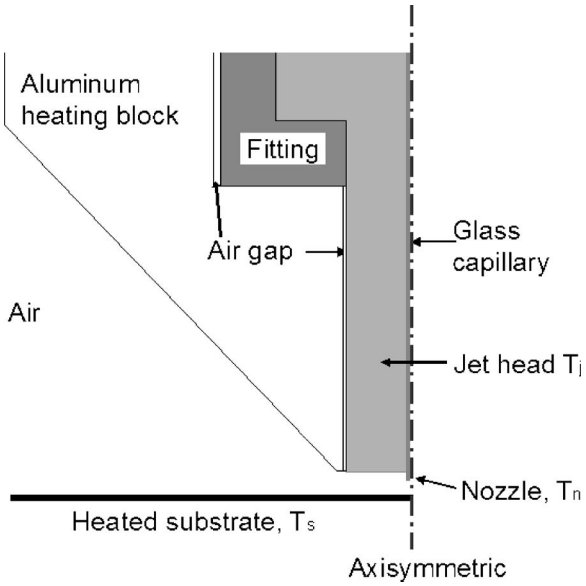

Fig. 3 Configuration of jet head and aluminum heating block. The nozzle to substrate distance was 1.2 mm and in addition to T_j and T_s, the temperature at the aluminum heating block and the fluid temperature at the reservoir were measured to use as boundary conditions for numerical simulations. This configuration was used for numerical simulations.

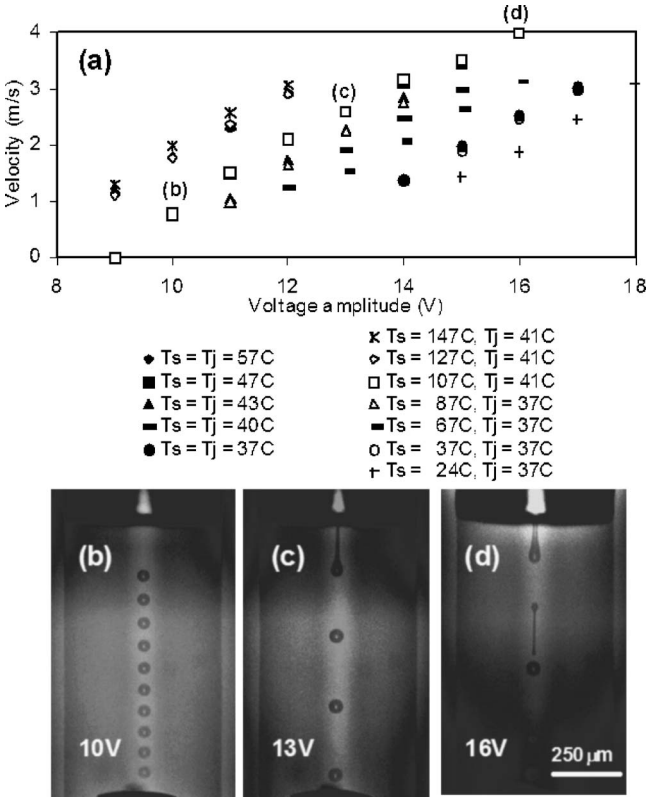

Fig. 4 (a) Variation of droplet velocity at 1 mm from the nozzle in response to changing voltage amplitude and temperature of jetting head and substrate. Gap distance between the substrate and nozzle is 1.2 mm. T_s and T_j represent the temperature of the substrate and the jetting head. When only T_s is changed, T_j is set to 37°C. However, T_j increases to 41°C when $T_s \geqslant 107$°C. Note that the nozzle temperature (T_n) is approximately equal to T_j when $T_s = T_j$, and that T_n is higher than T_j when $T_s > T_j$ due to heat conduction from the substrate. Images (*b*), (*c*), (*d*) are obtained by multiple 2 μs exposures with a 98 μs delay when $T_s = 107$°C and $T_j = 41$°C.

the jet head and the aluminum heating block. Since the temperature rise at the nozzle changes the viscosity and surface tension of the fluid in the nozzle, hence directly affecting the droplet velocity, the temperature rise at the nozzle due to only substrate heating can be estimated by comparing the velocity. First, the droplet velocity at the known nozzle temperature (T_n) was obtained by setting the substrate temperature (T_s) and the temperature of the jet head (T_j) equal to each other (i.e., $T_s = T_j \approx T_n$). Since the nozzle is located between the jet head and the substrate, T_n should be equal to $T_j = T_s$ in this case. Consequently, T_n in the case of $T_s T_j$ was estimated by matching the droplet velocity curve for $T_s = T_j (\approx T_n)$. For example, the velocity versus voltage curve for $T_s = 107$°C and $T_j = 41$°C matches well to the curve for $T_s = T_j = 47$ °C ($= T_n$). Therefore, T_n is approximately 47°C when $T_s = 107$°C and $T_j = 41$°C.

The impact velocity of the droplet increases with the voltage amplitude and temperature [Fig. 4(*a*)]. In the range of 1–3 m/s, each curve in Fig. 4(*a*) is almost linear, while over 3 m/s, the slope of the velocity vs voltage curve slightly decreases [e.g., $T_s = 107$°C and $T_j = 41$°C case in Fig. 4(*a*)] with the generation of a satellite droplet behind the main droplet [Fig. 4(*d*)]. The droplet diameter is about 50–55 μm in most of the temperature and voltage ranges, and slightly decreases to about 45 μm when the velocity is under 1 m/s.

Figure 5 shows the droplet velocity versus the dwelling time (t_d). The optimum dwelling time corresponding to maximum droplet velocity does not change with the substrate temperature. Similar results were obtained when both T_s and T_j were changed while maintaining $T_s = T_j$. In other words, the change of the speed of sound in the suspension fluid due to temperature change is not sufficiently significant to affect the droplet velocity. It is noted that when t_d is larger or smaller than the optimum t_d, the droplet velocity decreases. Satellite droplets which do not collapse to the main droplet were generated at short dwell times (inset picture in Fig. 4).

A steady-state axisymmetric, two-dimensional numerical simulation considering convection in air and conduction in the stationary jetting structure (Fig. 3) was carried out using FLUENT to predict the nozzle temperature. The boundary conditions at the top surface of the substrate is set at the constant temperature at T_s and the upper boundary of jetting structure (Fig. 3) is set to T_j, since the difference between the temperature of the upper boundary of jetting structure and the temperature of the jet head is negligible. Figure 6 shows the velocity and temperature profile in the vicinity

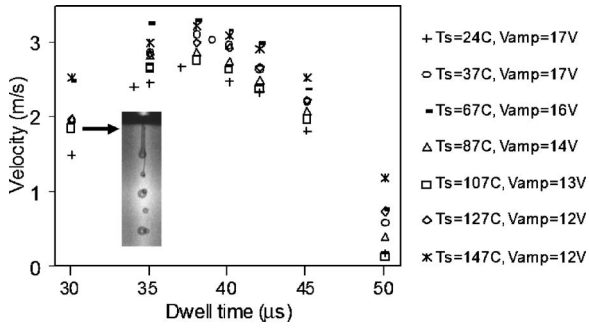

Fig. 5 Variation of droplet velocity at 1 mm from the nozzle changing dwell time, t_d [(B) in Fig. 2]. T_s changes and T_j is set to 37°C. Inset picture corresponds to the case for $T_s = 107$°C and $V_{amp} = 13$ V and similar satellite droplet was observed at the dwell time of 30 μs at different substrate temperatures and voltages.

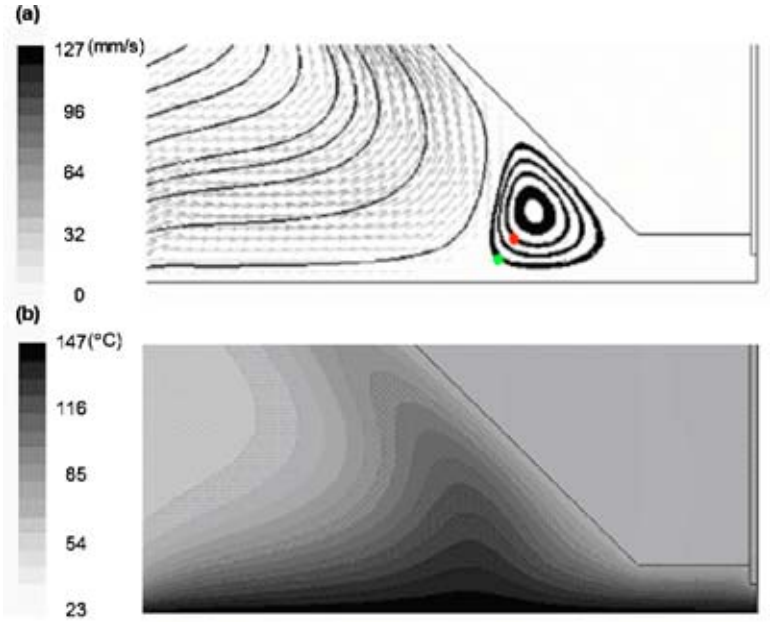

Fig. 6 Numerical result when T_s=147°C and T_j=37°C. (*a*) Velocity profile with stream lines. (*b*) temperature profile.

of the nozzle for T_s=147°C and T_j=37°C. As predicted from the calculated Rayleigh number, conductive heat transfer is dominant between the nozzle and the substrate [Fig. 6(*a*)]. Figure 6(*b*) shows the temperature profile. The nozzle temperature (T_n) calculated from numerical simulation also agrees well with values estimated from experiment (Fig. 7). Numerical simulation considering surface radiative heat transfer was also carried out and the nozzle temperature for T_s=147°C and T_j=37°C was calculated and found to be 2–3°C higher than when surface radiative heat transfer was neglected.

Morphology of Printed Nanoink. Nanoink was printed on a substrate moving at 2 mm/s. The ink is composed of monolayer protected gold particles (30% in weight, 1.9% volume) diluted in toluene. Nanoink was purchased from ULVAC Corporation in Japan. The size distribution of nanoparticles is similar to log normal distribution. The mean diameter and the standard deviation are 5.3 nm and 2.4 nm, respectively. About 50% and 80% nanoparticles are smaller than 5 nm and 7 nm, respectively. Nanoparticles were made by gas evaporation method (gas phase condensation) and covered by surface monolayer (organic acid based material) to prevent agglomeration [5].

The same bipolar voltage waveform in Fig. 2 was used and V_{amp} was 14 V. The jetting frequency is 30 Hz, so that the distance between each droplet is 67 μm [except in Fig. 8(*b*)]. The jet head was not heated (i.e., T_j=25°C). At 25°C of substrate temperature, the droplet diameter is 46 μm (i.e., 51 pL) and the impact velocity at 1.2 mm below the nozzle is 1–2 m/s.

The morphology of printed and cured lines of gold nanoink is seriously affected as the substrate temperature increases (Fig. 8). At room temperature, an impacted droplet evaporates and forms a circular ridge pattern as in Fig. 8(*a*). When droplets overlap to form a continuous line, the printed ink reflows to form a double ridge pattern as in Fig. 8(*b*). When the substrate is heated at 50°C, the nanoink solvent evaporates before the arrival of the next droplet (within 33 ms≈1/30 Hz), so that the circular ridge pattern reappears [Fig. 8(*c*)]. At 90°C, the droplet is flash-evaporated during impact and spreading, so that the circular ridge disappears and the printed line width reduces by half compared to room temperature case [Fig. 8(*d*)]. When the substrate is heated at 110°C, droplet generation becomes unstable. The droplet spreading and evaporation upon impact on a heated substrate is currently under further investigation.

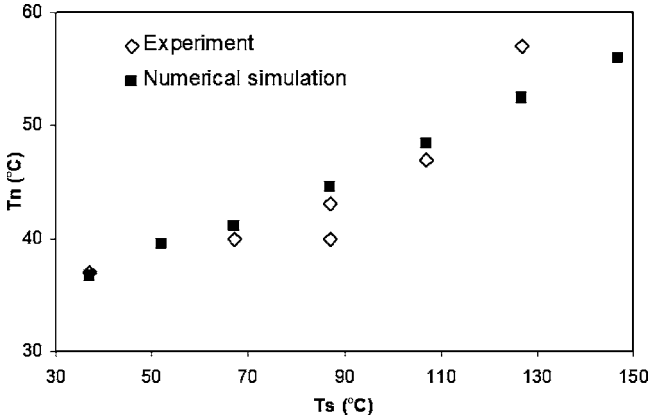

Fig. 7 Estimated nozzle temperature (T_n) from experiment and numerical simulation due to substrate heating at T_j=37°C.

Curing Printed Nanoink

Curing by Substrate Heating. Figure 9(*a*) shows the resistance per length, R_L, and the rms roughness of printed and cured nanoink by substrate heating at different temperatures for at least 10 min. Resistances were measured varying the distance with 10 mm long microlines and R_L was obtained from the slope of linear fit of measured resistances where the correlation coefficient was over 99%. Nanoparticle lines printed at room temperature in Fig. 10(*b*) were used. The resistance per length is about 10^6 Ω/mm at 150°C of curing temperature, and decreases below 10^2 Ω/mm from 160 to 170°C [Fig. 9(*a*)]. In addition, the reflectivity of the printed line dramatically increases at 160–170°C as the printed line color changes from black to dull gold. Note that similar phenomena were observed for octanethiol or dodecanethiol protected gold nanoparticles with 5 nm diameter [10]. Additional heating decreases the resistance per length to 5 Ω/mm at 450–500°C and the color changes to shiny gold. rms roughness

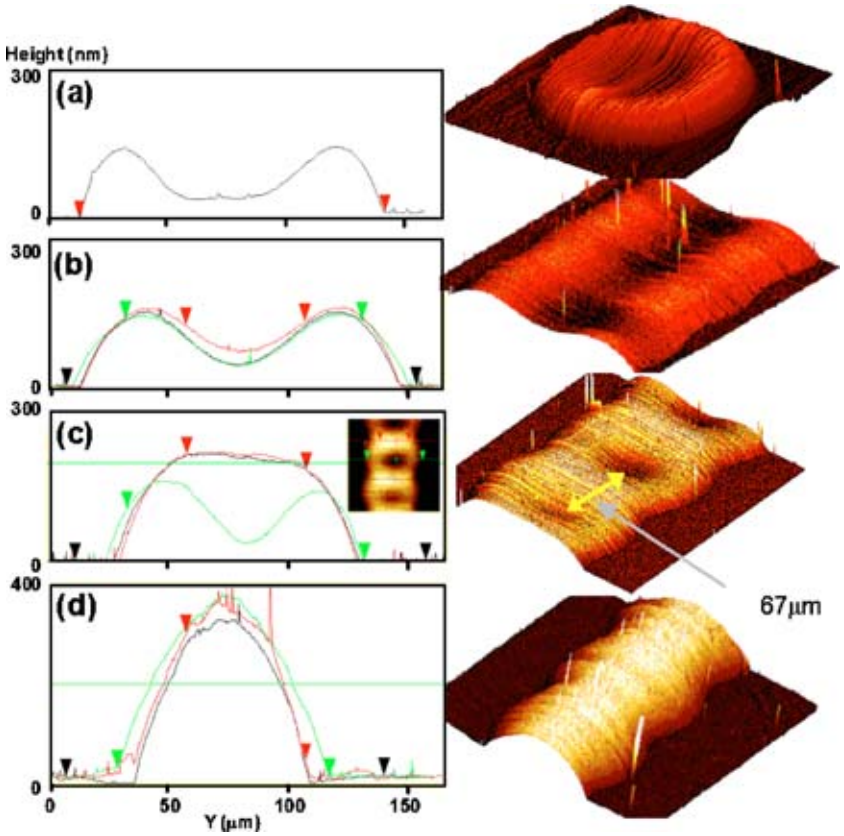

Fig. 8 Morphology of printed and cured nanoink on polyimide film. The same voltage waveform in Fig. 2 was used with V_{amp}=14 V. Before AFM (atomic force microscopy) scans, all lines were cured at 200°C to evaporate toluene solvent. (*a*) Shows the morphology of a single droplet deposition obtained at T_s=25°C. In (*b–d*), the translation speed and jetting frequency were 2 mm/s and 30 Hz, respectively. Therefore, the distance between the droplet centers is 67 μm. T_s for (*b*), (*c*), and (*d*) was 25, 50, and 90°C, respectively.

obtained from AFM image increases with the curing temperature [Fig. 9(*a*)]. Curing at higher temperature was carried out for the printed line on glass substrate, but the resistance per length did not decrease further. However, the roughness increased continuously. Though not shown here, the cross-sectional area of printed line on glass was almost reduced by half when the curing temperature increased from 150°C to 450–500°C, while it did not decrease further in the temperature range of 450–500°C. An erosion whose origin is unknown, even though chemical reaction is speculated as a possibility, was observed on the polyimide film for temperatures exceeding 400°C, so that the region of printed line sank into the substrate as shown in Fig. 9(*b*). However, the resistance per length still decreased as the curing temperature increased above 400°C [Fig. 9(*a*)] as it could be seen on the glass substrate. In addition, the double ridge profiles of gold film could be still observed. These imply that gold was neither removed nor diffused into the polyimide film.

The cross-sectional area of the printed line cured at 350°C was measured as 9.5–10.5 μm^2 from Fig. 9(*b*) and the resistivity was calculated as 9.8–11.6 $\mu\Omega$ cm. For higher curing temperatures, the cross-sectional area could not be measured due to the erosion of the polyimide film. When the same cross-sectional area was used for the printed line cured at 520°C, the resistivity was 4.7–5.7 $\mu\Omega$ cm. This value is about 2–2.5 times the resistivity of bulk gold. It is noted that the cross-sectional area decreases as the curing temperature increases, so that the resistivity of the printed line cured at 520°C would be lower than the above calculated value.

Curing by Pulsed Laser Heating. In earlier work, printed nanoink that was still wet and thus contained a substantial amount of solvent was cured with continuous laser irradiation [11–13]. In many cases, a portion of the nanoink was displaced ahead and behind the laser spot due to thermocapillary flow, so that expensive nanoink was not 100% used. An extra washing process was also necessary to remove the left-over nanoink that was pushed behind the laser spot. Even though an intensity-modulated laser beam could tailor the temperature profile to circumvent the above problems, the scanning speed for obtaining a highly conductive gold line was still slow. As a result, the temperature rise induced by the continuous laser irradiation was substantial, so that it was not suitable for application on flexible polymeric substrates having low deformation temperature.

By employing irradiation of the pulsed laser beam on printed and partially cured nanoink, it is possible to eliminate these problems. Since the solvent is evaporated by heating the substrate at a moderate temperature before irradiation of the pulsed laser, thermocapillary flow problems can be avoided. In addition, the pulsed laser can effectively minimize the heat-affected zone. In the experiment, a line of nanoink on polyimide film [17] printed at room temperature was heated in order to evaporate the solvent [Fig. 10(*b*)]. Pulsed laser irradiation was then applied, while the temperature of polyimide film was maintained at 200°C to decrease the required laser pulse energy. Obviously, printing and laser curing at the same temperature will benefit the processing speed/simplicity and feature size.

Using an acousto-optic modulator, pulsed irradiation of the con-

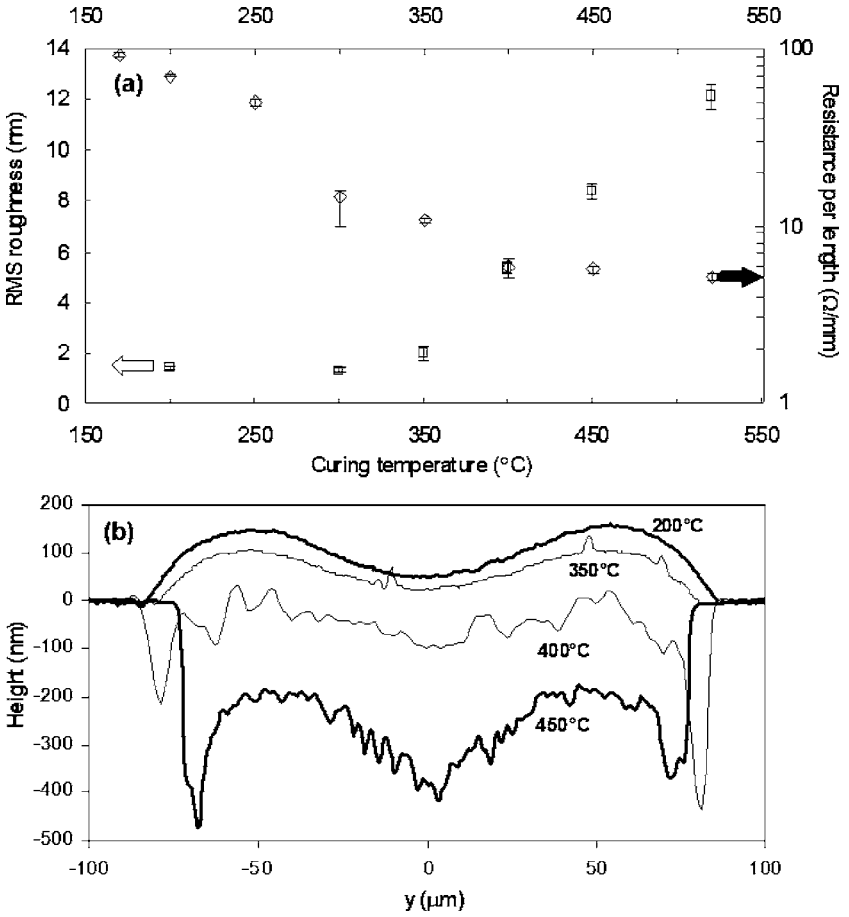

Fig. 9 (*a*) rms (root mean square) roughness and resistance per length of printed lines cured at different temperatures. (*b*) Cross-sectional profiles of printed lines cured at different temperatures.

tinuous argon laser (514 nm) was applied at the incidence angle of 45 deg. The polyimide film was placed on a moving vacuum chuck heated at 200°C and the laser curing process was observed from the top by an upright fixed microscope and a CCD camera. A long working objective lens (20×) was used and a filter eliminated scattered argon laser during curing. Since the focused beam waist ($1/e^2$) of 30 μm is smaller than the width of the printed line (about 160 μm), the pulsed laser spot had to scan several times parallel to the line to cure the entire width of the printed nanoink line [Fig. 10(*a*)]. Experiments were carried out varying the laser power, pulse duration (t_{pulse}), frequency, beam waist, scanning speed, and scanning gap (d_{gap}).

Figure 10 shows the results of a pulsed laser cured printed line at different scanning gaps. Nanoparticle lines printed at a room temperature in Fig. 10(*b*) were used. In this experiment, the laser frequency was set at 100 Hz allowing a sufficiently long time interval between pulses for the heated area to cool down to near the original substrate temperature of 200°C. As the scanning gap increases, the resistance per length, R_L increases [Fig. 10(*a*)]. When the scanning gap is larger than the diameter of the focused beam (60 μm), dark lines appear indicating low curing level, separated by a distance matching the scanning gap [see reflection image in Fig. 10(*a*)]. These dark lines correspond to small ridges in AFM images [Fig. 10(*c*)]. Note that the cross-sectional area decreases as the curing temperature increases. When the scanning gap is reduced, these ridges are not clearly observed, but the rough morphology in Fig. 10(*d*) is attributed to the same reason. When the scanning gap is 10 μm at $t_{\text{pulse}}=20$ μs [Fig. 10(*d*)], R_L and RMS roughness are 9 Ω/mm and 2.7 nm, respectively. Both values match well with the interpolated values at the curing temperature of 370°C in Fig. 9.

Figure 11 depicts a pulsed laser cured line for varying laser pulse duration, t_{pulse}. The printed lines shown in Fig. 10(*b*) were cured by pulsed laser using a scanning gap of 10 μm. The other conditions are the same as those in Fig. 10. As t_{pulse} increases up to 40 μs, the resistance per length, R_L, decreases to 7.5 Ω/mm, which is 10 times smaller than R_L ($\approx$75 Ω/mm) at the curing temperature of 200°C. Note that this value corresponds to the curing temperature of 400°C in Fig. 9. At 35 μs, "blister" spots start to appear [Fig. 11(*b*)]. Though not shown here, it was observed from in-situ imaging that these spots rapidly expanded upon irradiation of pulsed laser and then slowly contracted as the laser passed by. At 50 μs, R_L increases due to delamination of gold layer [Fig. 11(*c*)]. The surface inside the crater in Fig. 11(*c*) is flat, indicating that the substrate is exposed by the gold film delamination. Sometimes, this delaminated film breaks, so that an open hole is observed instead of the crater shape in Fig. 11(*c*). Note that the polyimide film did not show a significant deformation even at $t_{\text{pulse}}=50$ μs. Therefore, the limiting factor for obtaining lower resistance (i.e., more complete curing of nanoparticles) is not the deformation of the polymer film, but the gold film delamination (peeling off). Upon pulsed laser irradiation, it appears that rapid expansion of the trapped vapor bulges and occasionally explodes the gold film. In contrast, when the nanoparticles are cured at 500°C with substrate heating, the trapped vapor expands slowly and can escape due to the slow heating rate. The

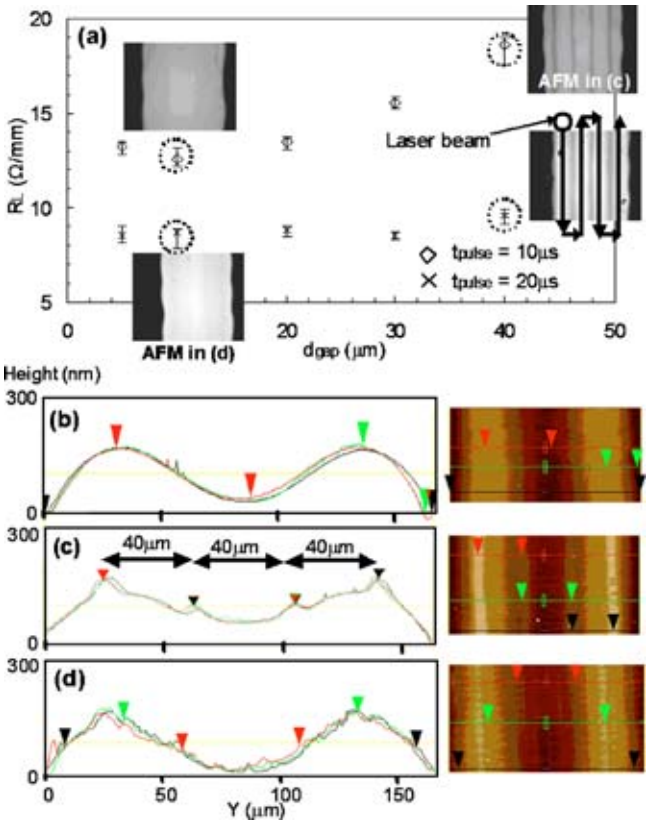

Fig. 10 Pulsed laser cured printed line at different scanning gaps, d_{gap}. The same voltage waveform in Fig. 2 was used and V_{amp}=15 V. Nanoink was printed on a polyimide film at room temperature and cured by a substrate heating at 200°C. During laser curing, the film was heated at 200°C using the vacuum chuck in Fig. 1. Laser power, beam waist ($1/e^2$), frequency and translation speed are 0.85 W, 30 μm, 100 Hz, and 0.5 mm/s, respectively. (*a*) R_L versus scanning gap of laser beam. Inset pictures are reflection images corresponding to cases circled with a dotted line. (*b*) AFM image before pulsed laser irradiation. (*c*) AFM image after pulsed laser irradiation at t_{pulse}=10 μs and d_{gap}=40 μm. (d) AFM image after pulsed laser irradiation at t_{pulse}=20 μs and d_{gap}=10 μm. rms roughness is 2.7 nm.

right insert picture in Fig. 11(*a*) shows that most craters are formed near the edge of the printed line where it may be harder for the expanded fluid to escape. The origin of trapped vapor is attributed to decomposed polymer due to chemical reaction between gold and polymer at elevated temperature. This decomposition is mentioned with regard to the erosion of polymer shown in Fig. 9(*b*). It is noted that similar resistances per length to Fig. 11(*a*) were obtained at the scanning speed of 20 mm/s with 30 μs pulse by increasing the laser frequency to about 3000 Hz.

A transient axisymmetric, two-dimensional conductive heat transfer numerical simulation was carried out using FLUENT to estimate the approximate temperature rise due to pulsed Gaussian profile heating and the required cooling time. Table 1 summarizes the material properties and parameters used in the simulation. A grid-dependence test was carried out using one dimensional analytic solution for pulsed laser heating in two layers with constant surface absorption [18] and the inaccuracy of the numerical simulation was found to be less than 5%. Figure 12 shows the transient temperature profile with respect to depth along the central beam axis for a 40 μs heating time. Since the latent heat consumed to melt nanoparticles was not considered, the maximum temperature rise at the surface was overestimated. As cooling starts after the end of the laser pulse at 40 μs, the temperature at the surface drops below the maximum temperature inside the polymer due to radial heat diffusion through the highly conductive gold film. It took about 300 μs for polymer film to cool down to below 10% of the maximum temperature rise. It is noted that as temperature increases during pulsed laser heating, nanoparticles tend to coalesce in clusters with a wider size distribution. Accordingly, more precise calculations of the induced temperature field upon the laser irradiation would require accounting of the latent heat of fusion for the nanoparticles. As the latent heat is a function of nanoparticle size, the employed nanoparticle size distribution has to be considered.

Conclusions and Outlook

Pulsed laser-based curing of printed nanoink combined with moderate and controlled substrate heating was investigated and shown to produce conductive microlines having 3–4 times higher resistivity than the bulk value at low enough temperatures, hence avoiding unwanted deformation of the employed polymeric substrates.

The overall morphology of the gold microlines was determined by the printing process and could be controlled by changing the substrate temperature during printing. In addition, printing on the heated substrate speeds up the process and reduces the feature size. However, the jetting environment also changes as the substrate temperature is elevated. At 110°C substrate temperature, the droplet generation becomes unstable, so that the range of substrate heating is limited. In addition, the nanoink orifice often clogged due to evaporation at the nozzle unless the jetting was performed in a continuous mode. Therefore, it would be beneficial if the temperature at the nozzle could be kept low while the substrate temperature is high. To this end, the variation of jetting conditions due to substrate heating was studied and the temperature rise at the nozzle estimated. It is noted that conductive heat transfer across the air gap is dominant in this situation. An active cooling system is required to decrease the nozzle temperature effectively. The printed nanoink was first cured by heating the substrate. Reflectivity is a good *in situ* indicator for curing while resistance and surface roughness are good postprocessing indica-

Table 1 Material properties and parameters used in the simulation

Material thermal properties				
	ρ (kg/m^3)	k (W/mK)	c_p (J/kgK)	
Gold film	19320	315	251	[18]
Polyimide	1470	0.287	1130	at 300K [17]
	constant	$k(T)= k_{300K}(T/300)^{0.22}$	$c_p(T) = c_{p,300K}$ [1+0.003 (T-300)]	[19]

Parameters used in the simulation			
Irradiated laser power	0.85W	Gold film thickness	200nm
Reflectance	0.65	Initial temperature	200°C
Beam waist ($1/e^2$)	36μm		

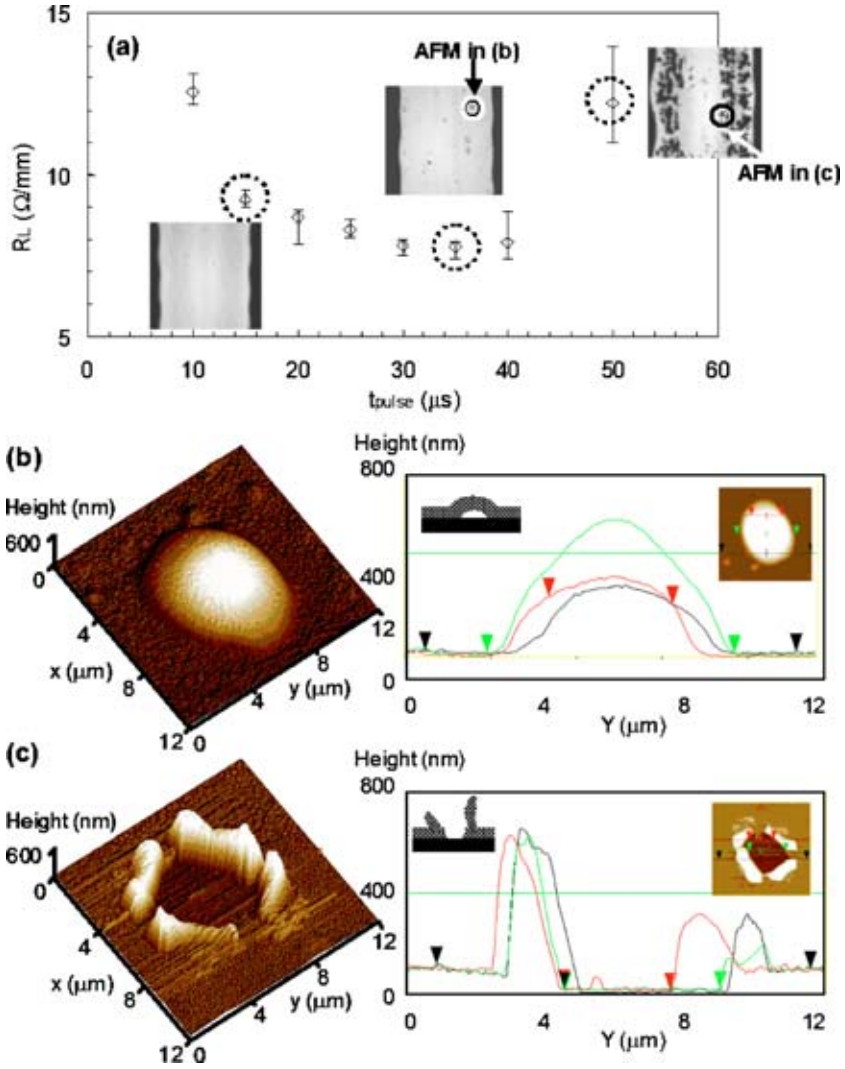

Fig. 11 Pulsed laser cured printed line at different laser pulse durations. Printed lines in Fig. 10(*b*) were used. During laser curing, the polyimide film was heated at 200°C using the vacuum chuck in Fig. 1. Laser power, beam waist ($1/e^2$), frequency, translation speed and scanning gap are 0.85 W, 30 μm, 100 Hz, 0.5 mm/s, and 10 μm, respectively. Inset pictures in (*a*) are reflection images corresponding to cases circled with dotted line. (*b*) and (*c*) are AFM images of the areas circled with a white line in (*a*).

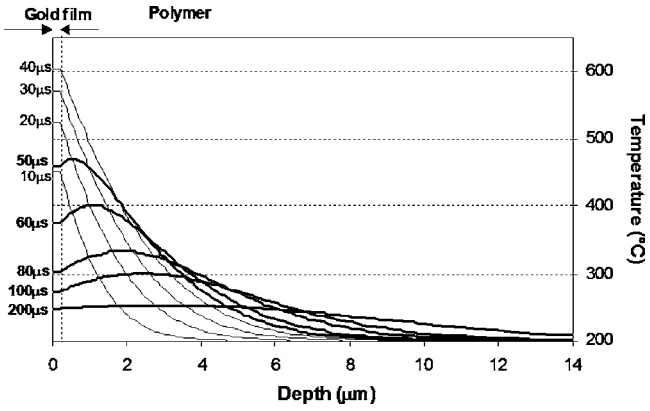

Fig. 12 Transient temperature profiles in depth with 40 μs heating time

tors. In addition, the volume of printed nanoink decreases as the curing temperature rises.

By employing a microsecond pulsed laser, the nanoparticles were melted and coalesced to form a highly conductive microline without damaging the polymeric substrate. The resistance per length ($R_L = 7.5\ \Omega/\text{mm}$) obtained by pulsed laser heating was 10 times smaller than R_L at the curing temperature of 200°C, although still larger than R_L at the curing temperature of 450–500°C. It appears that rapid heating of trapped vapor and the resulting expansion may cause delamination of the gold film if the laser heating time is prolonged and the induced thermal load is increased. The exact mechanism of this delamination is currently under investigation. Similar resistances per length were obtained by increasing both the scanning speed and laser frequency, so that R_L of about 7 Ω/mm was demonstrated up to the scanning speed of 20 mm/s. For the current experimental setup and due to the limited average laser power, the pulsed laser spot needs to scan about 10–15 times parallel to the line to cover the entire width of the printed nanoink line. While this is not an issue in the current basic study focusing on the understanding of the phenomena in-

volved, for practical application, it can be overcome by using a fast galvanometric mirror to rapidly scan the laser beam in the direction perpendicular to the printed line, while the translation stage moves parallel to the printed line.

Acknowledgment

The authors wish to especially thank Professor Vivek Subramanian of the Department of Electrical Engineering and Computer Sciences, University of California, Berkeley for valuable discussions. Financial support to the University of California, Berkeley by the U.S. National Science Foundation under Grant No. CTS-0417563 and to the Swiss Federal Institute of Technology in Zurich by the Swiss National Science Foundation under Grant No. 2000-063580.00 is gratefully acknowledged.

Nomenclature

c = speed of sound in pure toluene
c_p = heat capacity
d_{gap} = scanning gap of laser beam
g = gravitational acceleration
k = thermal conductivity
L = gap between jetting head and substrate
l = length of glass capillary tube
P = total laser power
Ra = Rayleigh number ($=g\beta\Delta TL^3/\alpha\nu$)
R_L = resistance per length
$R_{L,\text{Min}}$ = minimum R_L calculated from the bulk resistivity
t_d = dwell time
T_j = jet head temperature
T_n = nozzle temperature
T_s = substrate temperature
V_{amp} = voltage amplitude
w_0 = beam waist where the intensity is $1/e^2$ of a maximum

Greek symbols

ρ = density
β = expansion coefficient
ν = kinematic viscosity
α = thermal diffusivity
ΔT = temperature difference

References

[1] Sirringhaus, H., and Shimoda, T., 2003, "Inkjet Printing of Functional Materials," MRS Bull., **28**(11), pp. 802–803.
[2] Burns, S. E., Cain, P., Mills, J., Wang, J., and Sirringhaus, H., 2003, "Inkjet Printing of Polymer Thin-Film Transistor Circuits," MRS Bull., **28**(11), pp. 829–834.
[3] Bharathan, J., and Yang, Y., 1998, "Polymer Electroluminescent Devices Processed by Inkjet Printing. I. Polymer Light-Emitting Logo," Appl. Phys. Lett., **72**(21), pp. 2660–2662.
[4] Hebner, T. R., Wu, C. C., Marcy, D., Lu, M. H., and Sturm, J. C., 1998, "Ink-Jet Printing of Doped Polymers for Organic Light Emitting Devices," Appl. Phys. Lett., **72**(5), pp. 519–521.
[5] Oda, M., Abe, T., Suzuki, T., Saito, N., Iwashige, H., and Kutluk, G., 2002, "Application of Dispersed Nano Particles," Nanoparticulate Materials Symposium, MRS Symposium Proc., Warrendale, PA, Vol. 704, pp. 3–10.
[6] Brust, M., Walker, M., Bethell, D., Schriffin, D. J., and Whyman, R. J., 1994, "Synthesis of Thiol-Derivatized Gold Nanoparticles in a Two-Phase Liquid-Liquid System," J. Chem. Soc., Chem. Commun., **7**, pp. 801–802.
[7] Hostetler, M. J., Wingate, J. E., Zhong, C., Harris, J. E., Vachet, R. W., Clark, M. R., Londono, J. D., Green, S. J., Stokes, J. J., Wignall, G. D., Glish, G. L., Porter, M. D., Evans, N. D., and Murray, R. W., 1998, "Alkanethiolate Gold Cluster Molecules With Core Diameters From 1.5 to 5.2 nm: Core and Monolayer Properties as a Function of Core Size," Langmuir, **14**, pp. 17–30.
[8] Szczech, J. B., Megaridis, C. M., Gamota, D. R., and Zhang, J., 2002, "Fine-Line Conductor Manufacturing Using Drop-on Demand PZT Printing Technology," IEEE Transactions on Electronics Packaging Manufacturing, **25**(1), pp. 26–33.
[9] Fuller, S. B., Wilhelm, E. J., and Jacobson, J. M., 2002, "Ink-Jet Printed Nanoparticle Microelectromechanical Systems," J. of MEMS, **11**(1), pp. 54–60.
[10] Huang, D., Liao, F., Molesa, S., Redinger, D., and Subramanian, V., 2003, "Plastic-Compatible Low Resistance Printable Gold Nanoparticle Conductors for Flexible Electronics," J. Electrochem. Soc., **150**(7), pp. G412–G417.
[11] Bieri, N. R., Chung, J., Haferl, S. E., Poulikakos, D., and Grigoropoulos, C. P., 2003, "Microstructuring by Printing and Laser Curing of Nanoparticle Solutions," Appl. Phys. Lett., **82**(20), pp. 3529–3531.
[12] Chung, J., Ko, S., Bieri, N. R., Grigoropoulos, C. P., and Poulikakos, D., 2004, "Conductor Microstructures by Laser Curing of Printed Gold Nanoparticle Ink," Appl. Phys. Lett., **84**(5), pp. 801–803.
[13] Chung, J., Ko, S., Bieri, N. R., Grigoropoulos, C. P., and Poulikakos, D., 2003, "Laser Curing of Nanoparticle Suspended Solution," in Proceedings of the 2003 ASME IMECE, Washington, D.C., November.
[14] Buffat, P. A., and Borel, J. P., 1976, "Size Effect on the Melting Temperature of Gold Particles," Phys. Rev. A, **13**(6), pp. 2287–2298.
[15] Dijksman, J. F., 1984, "Hydrodynamics of Small Tubular Pumps," J. Fluid Mech., **139**, pp. 173–191.
[16] Bogy, D. B., and Talke, F. E., 1984, "Experimental and Theoretical Study of Wave Propagation Phenomena in Drop-on-Demand Ink Jet Devices," IBM J. Res. Dev., **28**(3), pp. 314–321.
[17] Upilex-S, Ultra-high heat-resistant polyimide film (50 μm thick), UBE industries. The minimum glass transition temperature is 500°C.
[18] El-adawi, M. K., Abdel-naby, M. A., and Shalaby, S. A., 1995, "Laser Heating of a Two Layer System With Constant Surface Absorption: An Exact Solution," Int. J. Heat Mass Transfer, **38**(5), pp. 947–952.
[19] Bicerano, J., 1993, *Prediction of Polymer Properties*, Marcel Dekker, New York.

Laminar Natural Convection Heat Transfer From a Vertical Baffled Plate Subjected to a Periodic Oscillation

Xinrong Zhang
Department of Mechanical Engineering, Doshisha University, Kyoto 610-0321, Japan

Shigenao Maruyama
Institute of Fluid Science, Tohoku University, Katahira 2-1-1, Aoba-ku, Sendai 980-8577, Japan

Hiroshi Yamaguchi
Department of Mechanical Engineering, Doshisha University, Kyoto 610-0321, Japan

The problem of laminar natural convection on a vertical baffled plate subjected to a periodic oscillation is investigated numerically. Of particular interest of this paper is the heat transfer characteristic with the oscillatory velocity being close to the flow velocity in the velocity boundary layer under nonoscillation condition. The results show that a sevenfold increase in space-time averaged Nusselt number is achieved. Three mechanisms that are responsible for the heat transfer enhancement are identified. In addition, the effects of the governing parameters on the heat transfer are studied over a wide range. The heat transfer enhancement is found to be increased with dimensionless oscillation frequency and amplitude, but decreased with the Grashof number. Another interest of this paper is to optimize the geometry of baffle plates and an optimal baffle height-spacing ratio 0.25–0.50 is found for higher heat transfer rate. [DOI: 10.1115/1.1924570]

Keywords: Baffled Plate, Heat Transfer, Natural Convection, Oscillation

1 Introduction

The oscillation-induced heat transport has been studied by a number of researchers due to its many industrial applications, such as bioengineering and chemical industrial engineering, etc. Continuous attention received for the problem started with the early work of Kurzweg et al. [1–3], in which a new technology has been developed for the heat transfer enhancement by sinusoidal oscillation of a fluid, i.e., heat transfer in a pipe connected to hot and cold reservoirs at both ends was highly enhanced by imposing sinusoidal oscillation. Very large effective axial heat conduction rates, exceeding those possible with heat pipes by several orders of magnitude, were found to be achievable. These systems were proposed as "dream pipe." Ozawa and Kawamoto [4] conducted numerical simulation and visualization experiment to investigate the fundamental heat transfer mechanisms of the dream pipe, which were found to be mainly owing to lateral diffusion of heat, accumulation capacity of heat in a region of depth of penetration formed near the wall and convective motion forced by the oscillation. Furthermore, Nishio et al. [5] proposed phase shifted oscillation-controlled heat transport tubes to further increase the thermal conductivity. In addition, Walsh et al. [6], Liao et al. [7] and Fusegi [8] showed that the forced convection heat transfer in tubes can also be significantly enhanced using oscillatory flow techniques.

The combination of oscillatory flow and a series of sharp edges in a tube or channel for heat transfer enhancement has already been investigated by Brunold et al. [9], Howes et al. [10], Mackly and Stonestreet [11], and Stephen and Mackley [12]. This kind of oscillatory flow promotes chaotic mixing in the tube, of which radial velocity components are significant [9,10]. Mackley and Stonestreet reported that significant heat transfer enhancement can be achieved in tubes with a series of baffles due to oscillatory flows, especially for low net flow Reynolds number and a 30-fold improvement in Nusselt number was achieved [11]. The oscillatory flow and baffles both had to be present to produce this effect. Stephen and Mackley further presented heat transfer data obtained from two oscillatory flow methods, the first being the fluid oscillation in which the baffles remain stationary, whereas the second employing oscillating baffles [12]. The energy efficient heat transfer can be obtained for the two situations, due to the mechanisms of vortex interaction. In addition, Fu et al. investigated some flow and heat transfer enhancement phenomena under oscillation conditions [13–16], for example, heat transfer problem of a body moving in opposition to a flowing fluid [13]; heat transfer characteristics of a heated transversely oscillating cylinder in a cross flow [14]; the influence of an oscillating cylinder on the heat transfer from heated blocks in a channel flow [15].

Almost all the previous studies were relevant to forced convection. But these are many technological applications that can be simplified into models of baffled walls subjected to oscillatory conditions under the natural convection. For example, the upwelling flow of deep seawater using the perpetual salt fountain is a kind of natural convection produced by the temperature and salinity differences between the seawater inside and outside a pipe [17]. The upwelling velocity is strongly dependent on the heat transfer between the pipe wall and the deep seawater in the pipe, which is significantly enhanced by a combination of baffled pipe surface and its oscillation due to wave motion [18,19]. However, only a few published works could be located that discusses the natural convection heat transfer under the combination of oscillatory flow or oscillatory wall and baffles. For example, Iwatsu et al. [20] examined the flow and heat transfer characteristics in a differentially heated cavity with an oscillating lid and found a suitable frequency to achieve heat transfer enhancement. Fu and Shieh [21] studied thermal convection in a square enclosure induced simultaneously by gravity and vertical vibration and the numerical results show that in the low Rayleigh number case, the vibration enhances the heat transfer enhancement significantly.

The present study is a logical extension of the recent work of the authors [22] who reported a numerical study of natural convection on a flat plate subjected to a periodic oscillation. A major objective of this study is to obtain a fundamental understanding and estimation of natural convection heat transfer characteristics under the oscillating wall conditions imposed on baffled plates. Particular interest is focused on the heat transfer characteristics

Contributed by the Heat Transfer Division for publication in the JOURNAL OF HEAT TRANSFER. Manuscript received April 27, 2004; final manuscript received February 2, 2005. Review conducted by: Jay Khodadadi.

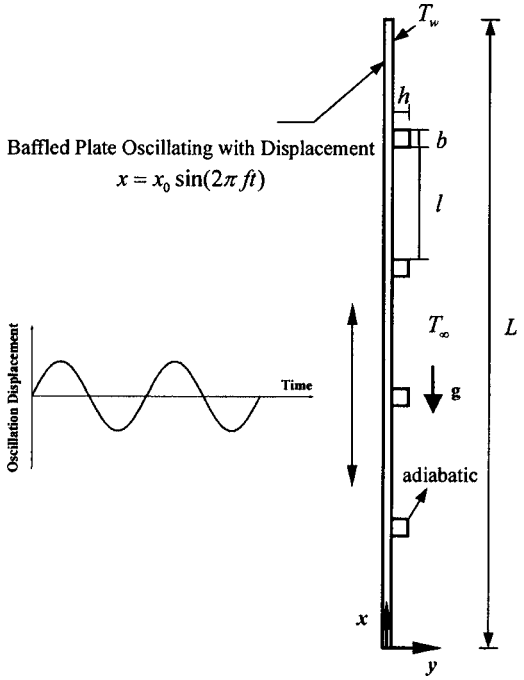

Fig. 1 Schematic diagram of oscillating baffled plate problem

with oscillatory velocity being close to the flow velocity in the velocity boundary layer under nonoscillation condition. In addition, influences of the governing parameters on the heat transfer are examined and optimal values are found for higher heat transfer rate.

2 Problem Formulation

The schematic of the problem under study and the coordinates are shown in Fig. 1. The baffle spacing, height and width are denoted by ℓ, h and b, respectively. A zero-thickness base plate (length L) is assumed in the simulation. At time $t \leqslant 0$, the plate is assumed to be at rest and the fluid is assumed to be at the temperature T_∞ and the fluid is still. For time $t > 0$ the plate temperature is suddenly raised to a higher constant temperature T_w than the surrounding fluid T_∞, and the plate starts moving in its own plane. The resultant density difference in the presence of a gravitational field causes the fluid to rise. It is assumed that $(T_w - T_\infty)$ is sufficiently small that the Boussinesq approximation can be made. It is also assumed that all other relevant thermodynamic and transport properties are independent of temperature and that compressibility and dissipation effects can be neglected. And heat transfer by radiation is not considered in this study. The subsequent fluid motion can be described by the following governing equations:

$$\nabla \cdot (\rho \mathbf{V}) = 0, \tag{1}$$

$$\frac{\partial(\rho \mathbf{V})}{\partial t} + \nabla \cdot (\rho \mathbf{V}\mathbf{V}) = \mu \nabla^2 \mathbf{V} - \nabla P - \rho\beta(T - T_0)\mathbf{g}, \tag{2}$$

$$\frac{\partial(\rho T)}{\partial t} + \nabla \cdot (\rho \mathbf{V} T) = \frac{k}{c_p} \nabla^2 T. \tag{3}$$

The domain of interest is a two-dimensional rectangular geometry in which the plate is kept in the center. The dimensions of height and width for the geometry are respectively set eight and five times of the baseplate length, wide enough to simulate the flow and heat transfer in the case of the plate oscillating within an unbounded viscous fluid. In this paper, the baffles do not work as extended heat transfer surfaces but redirecting the flow and they are assumed to be adiabatic. The left and right side walls of the geometry are specified with uniform temperature T_∞, and the top and bottom horizontal walls are assumed to be adiabatic. The velocity boundary conditions considered here are the nonslip conditions on all the solid walls. The plate motion is governed by the time-dependent equations, in which the displacement of oscillation and the oscillatory velocity are in forms of

$$x = x_0 \sin(2\pi ft), \tag{4}$$

$$u = u_0 \cos(2\pi ft) = 2\pi f x_0 \cos(2\pi ft). \tag{5}$$

This oscillation boundary condition is governed by two-dimensionless parameters

$$A_0 = x_0 / \delta_{\max}, \tag{6}$$

$$w_0 = \delta_{\max} / \sqrt{\upsilon / \pi f}, \tag{7}$$

where A_0 is the dimensionless oscillation amplitude, which represents a ratio of the oscillation amplitude to the maximum of velocity boundary layer thickness of a stationary baffled plate. The term w_0 is the dimensionless oscillation frequency, which describes a comparison of the velocity boundary layer thickness between nonoscillation and oscillation condition. The value of $\sqrt{\upsilon / \pi f}$ approximately corresponds to the thickness of the velocity boundary layer of an oscillating plate [4].

In addition, the dimensionless coordinate, time, temperature, oscillation velocity, baffle height and spacing are defined as

$$X = x/L, \quad Y = y/\sqrt{\upsilon/\pi f}, \quad \phi = 2\pi ft, \quad \theta = (T - T_\infty)/(T_w - T_\infty),$$

$$U = \frac{2\pi f x_0}{u_{\max}}, \quad St = h/\pi x_0, \quad Sr = 2x_0/\ell, \tag{8}$$

where U represents a ratio of the oscillation velocity to the maximum flow velocity in the velocity boundary layer of a stationary baffled plate. The Strouhal number St represents a ratio of baffle height to oscillation amplitude and the Stroke ratio Sr measures a ratio of oscillation amplitude to baffle spacing.

In this paper, only such an oscillation condition is mainly investigated as the oscillatory velocity and amplitude being respectively less than and close to the flow velocity and the thickness of velocity boundary layer under nonoscillation condition. Therefore, the oscillation amplitude and velocity are respectively limited to $A_0 \leqslant 1$ and $U \leqslant 1$.

The definition of local instantaneous Nusselt number along the heated plate is given as follows:

$$Nu_{x,t} = \frac{h_{x,t} L}{k} = \frac{q_{x,t} L}{(T_w - T_\infty)k}. \tag{9}$$

For the purpose of generalizing the spatially and temporally averaged heat transfer data, based on the time and area weighted average of a quantity, the time-averaged local Nusselt number $\overline{Nu}_x$, the space-averaged instantaneous Nusselt number $\overline{Nu}_t$, and the space-time averaged Nusselt number $\overline{Nu}$ can be defined, respectively, as

$$\overline{Nu}_x = \frac{1}{2\pi} \int_0^{2\pi} Nu_{x,t} d\phi, \quad \overline{Nu}_t = \frac{1}{L} \int_0^L Nu_{x,t} dx,$$

$$\overline{Nu} = \frac{1}{2\pi L} \int_0^{2\pi} \int_0^L Nu_{x,t} dx d\phi. \tag{10}$$

3 Computational Details

A finite-volume numerical solution technique based on integration over the control volume is used to solve the model Eqs. (1)–(3) subject to the appropriate boundary conditions. This numerical technique is essentially based on the previous work [23]. A structured nonuniform grid arrangement is employed to solve

the discretized equation. The grid is made finer towards the wall in order to model accurately the solution variables with large gradients in the near-wall region and capture adequately solutions under the oscillation conditions. Because of the extremely thin velocity and thermal boundary layer at a high dimensionless oscillation frequency, a highly nonuniform grid is deployed. The corresponding grid independence of the results is established by employing various number of mesh points, ranging from 30 000 to 120 000. The time step independence of the solutions is tested, and the typical implicit time step used is 0.001–0.01 s, which is chosen as the uppermost value on balance of convergence and CPU time. All the computations in this paper are carried out on the SGI Origin2000 workstation in the Advanced Fluid Information Research Center at Tohoku University, Japan.

The formulation of numerical model above is expected to have a capability of reasonably dealing with the laminar natural convection under an oscillating-wall boundary condition. Therefore, for validation of the proposed numerical model, the similarity solutions by Ostrach [24] and the exact solutions for the classical Stoke's second problem [25] are used. A uniform temperature boundary condition is applied on the plate wall when using Ostrach's solution, which describes the velocity and temperature field of bouyant convection on a stationary vertical plate. A moving boundary condition $u=u_0\cos(2\pi ft)$ is used to compare with the exact solutions for the Stoke's problem, in which the flow solutions about a flat plate which executes linear harmonic oscillations parallel to itself are given. Excellent agreements between the present predictions and those of Ostrach and Stoke are found [22,23]. Through these program tests, it is found that the present numerical method is suitable for this study.

4 Results and Discussion

An examination of the governing equations and boundary conditions shows that the important governing parameters for the problem under consideration are the dimensionless oscillation frequency w_0 and amplitude A_0, the dimensionless baffle height St and spacing Sr, and the Grashof number Gr. In order to study the effects of the parameters on heat transfer characteristics, numerical calculations are carried out for a wide range of various parameters. In the present study, however, the parameters for the numerical treatment are chosen in such a way that the Grashof number is less than the critical value for the onset of turbulence, and that the magnitude of oscillation velocity is similar to the flow velocity in velocity boundary layer of a baffled stationary plate. In this work, the results of the baseplate length ranging from 0.3 to 0.8 m, oscillation frequency from 0.2 to 10.0 Hz, amplitude from 0.002 to 0.1 m, baffle height from 0.004 to 0.06 m, baffle spacing from 0.04 to 0.10 m and temperature difference from 0.1 to 20 °C are presented. The numerical simulations are performed for a laminar flow of air ($Pr=0.7$).

In the present study, the main concern is focused on the case of the oscillation velocity and amplitude close to the flow velocity and the thickness of the velocity boundary layer of a stationary baffled plate. A comparison of the space-time averaged Nusselt number for $U=0.95$ and for a stationary flat plate at $St=0.24$, $Sr=0.32$ and $Gr=10^7$ are shown in Fig. 2. Figure 2 is for the value of w_0 from 10.0 to 70.0 and corresponding oscillation amplitude A_0 from 1.66 to 0.03. The results show that a sevenfold increase of the space-time averaged Nusselt number is achieved under such an oscillation boundary condition. Figure 2 also shows that, at a fixed oscillation velocity, the space-time averaged Nusselt numbers only decrease a little with the frequency w_0. The oscillation amplitude drops rapidly with the increase of frequency at a fixed oscillation velocity, which may lead to such a change of the averaged Nusselt number as shown in Fig. 2.

Figures 3(*a*) and 3(*b*), illustrate the temperature profiles for a stationary baffled plate and an oscillatory baffled plate, respectively. For the stationary flat plate, the thermal boundary layer develops along the plate and its thickness becomes thicker towards the trailing edge of the plate ($X=1.0$). For the stationary baffled plate (the baffles are at $X=0.2$, 0.4, 0.6 and 0.8), the thermal boundary layer is efficiently interrupted by the baffles which form on the plate surface, thereby creating a fresh boundary layer that increases near-wall temperature gradient. For the oscillatory baffled plate, it is found from a comparison of Figs. 3(*a*) and 3(*b*) that during one oscillation cycle, not only is the thermal boundary layer continuously interrupted by the baffles and periodic redevelopment of boundary layers created, but also the temperature gradient near the plate wall is further increased by simultaneous use of the oscillatory boundary conditions and baffles.

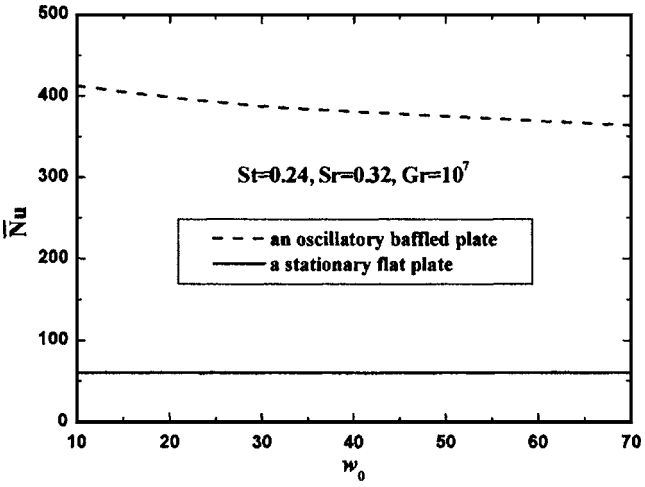

Fig. 2 Comparison of the space-time averaged Nusselt number between a stationary flat plate and an oscillatory baffled plate at a fixed velocity ($U=0.95$) for $St=0.24$, $Sr=0.32$ and $Gr=10^7$

Here, flow patterns from the numerical prediction of the oscillatory baffled plate are given using plots of instantaneous streamlines. Figure 4 is a time sequence of the streamlines showing fluid motion in the (x,y) plane under the oscillating-wall condition imposed on the baffled plate at $St=0.24$, $Sr=0.32$, $w_0=22.0$, $A_0=0.9$ and $Gr=10^7$. The instantaneous streamlines of phase angle $2\pi ft=0$, 72, 144, 216, 288 and 360 deg during one oscillation cycle are respectively shown in Figs. 4(*a*)–4(*f*). The kinematics of the flow is important in understanding of mechanisms for heat transport. It can be clearly seen that the two-dimensional unsteady flow caused by the oscillatory condition of the baffled plate is extremely complex. The flow patterns of Fig. 4 indicate that the flow is fully periodic over one oscillation cycle. This is clear from comparison of Figs. 4(*a*) and 4(*f*). In addition, it is obvious that the strong vortices exist through both the flow regime and the oscillation cycle. Further observation of the flow at successive plate oscillations indicates that the observed vortex structure is time periodic. Efficient mixing appears to have occurred, which is not exclusively in the near-wall region but extends well into the ambient region. The basic mechanism of mixing is caused by the baffles and oscillatory plate leading to this complex process. The flow patterns in this figure give a clear picture of complex and continuous interactions between the ambient fluid and the boundary-layer fluid through the boundary-layer destabilization caused by these vortices. These vortices transfer near-wall fluid to the ambient region and hence enhance the rate of heat transfer. Therefore, we believe that the fluid flow pattern caused by the oscillating-wall condition imposed on the baffled plate can be a very efficient way of enhancing heat transfer.

At the fixed oscillation velocity $U=0.95$, the variations of the time-averaged local Nusselt number $\overline{Nu}_x$ and the space-averaged instantaneous Nusselt number $\overline{Nu}_t$ for $w_0=22.0$, $A_0=0.9$, $St=0.24$, $Sr=0.32$ and $Gr=10^7$ are, respectively, given in Figs. 5(*a*)

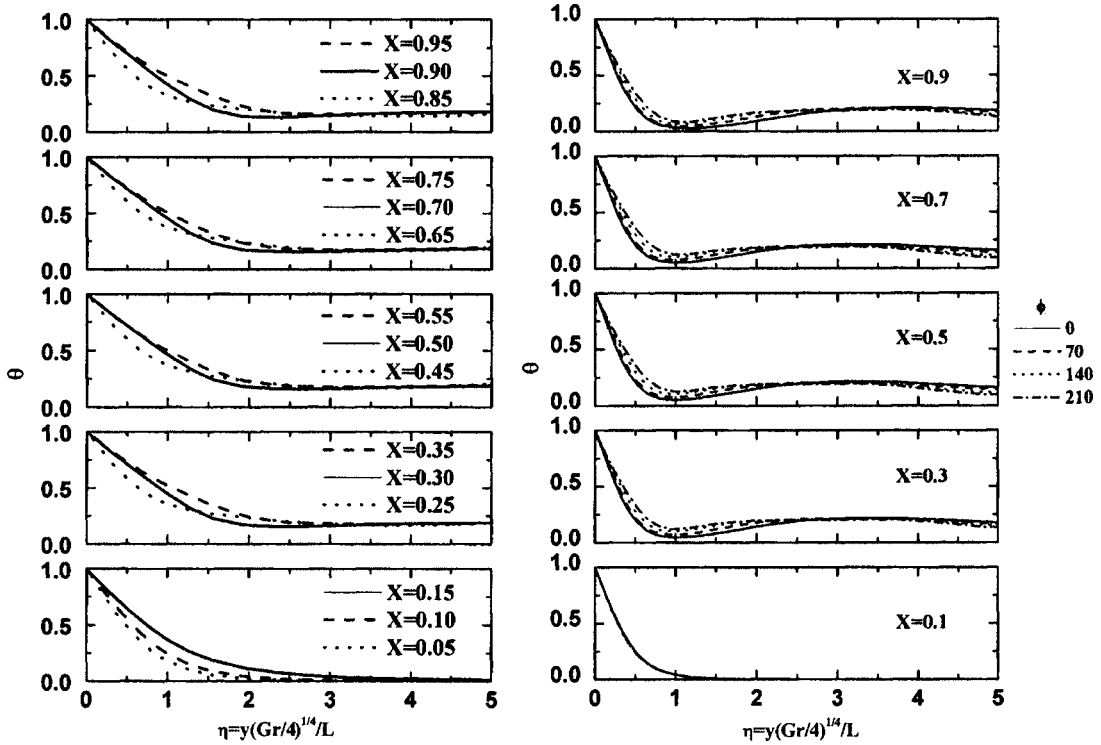

Fig. 3 Evolutions of the temperature profile (θ) during one oscillation cycle for $Gr=10^7$. (a) A stationary baffle plate; (b) an oscillatory baffled plate at $w_0=22.0$, $A_0=0.9$, $St=0.24$, and $Sr=0.32$.

and 5(b). Comparing the two $\overline{Nu}_x$ curves in Fig. 5(a), it is found that $\overline{Nu}_x$ can be enhanced greatly along the whole plate. The heat transfer enhancement due to periodic redevelopment of the thermal boundary layer can be seen clearly from this figure. Comparing two $\overline{Nu}_t$ curves in Fig. 5(b), it is seen that $\overline{Nu}_t$ can be enhanced greatly throughout all the time of the whole cycle. We believe there are three competing mechanisms that are responsible for these heat transfer enhancements. First, under the oscillation conditions, the thickness of thermal boundary layer becomes much thinner than that with no oscillation. In this case, the value of w_0 is 22.0, according to the physical meaning of w_0, implying that the thermal boundary thickness becomes thinner than that of a stationary plate due to such as oscillating wall, which may contribute to the heat transfer enhancements. Second, introduction of the baffles effectively interrupts the boundary layer that forms on the plate surface and replaces it with fluid from the ambient, thereby creating a fresh boundary layer that increases near-wall temperature gradients. In addition, a simultaneous use of baffles and oscillating-wall conditions will result in strong vortices giving an efficient mixing, shown in the Fig. 4. And these vortices can transfer near-wall fluid to the ambient region and therefore greatly enhance the heat transfer rate. All of the above mechanisms may lead to such high heat transfer phenomena.

Figure 6 demonstrates the time variation trends of Nusselt number in a complete cycle, from the bottom side to the top side of the plate. At each location, $Nu_{x,t}$ changes with phase angle ϕ with a maximum value (peak) and a minimum value (valley) during one cycle. And the closer to the two ends of the plate, the greater the variation amplitude of the Nusselt number during one cycle is. It can be physically explained that the boundary layer of the middle part of the plate is more difficult to change with time than that of the two end parts of the plate. Figure 6 also demonstrates that the heat transfer at the top part of the plate is greatly increased, which even exceeds those at lower locations of the plate.

The results for the space-time averaged Nusselt numbers under a wide range of the oscillation velocities U are shown in Fig. 7. It can be seen that the average Nusselt number increases with the value of U. When the oscillation velocity u_0 is about ten times larger than the magnitude of fluid flow velocity $u_{\max}$ of a stationary baffled plate, about 16-fold increase in the average Nusselt number is observed. Even when u_0 is the one-tenth of the value of $u_{\max}$, about 30% increase over the nonoscillatory heat transfer can be achieved. Therefore, by imposing an oscillatory motion on the baffled plate under the buoyant convection, heat transfer performance is kept at a high level. Moreover, heat transfer depends significantly on the dimensionless oscillation velocity U imposed. Regulating the frequency and amplitude under the certain buoyant convection, the heat transfer performance can be brought to a predetermined level. In addition, it can also be seen that the lower the oscillation velocity is, the closer to the stationary-state condition the heat transfer performance is.

The effects of varying baffle spacing and baffle height on the enhancement ratio (defined as the ratio of the space-time averaged Nusselt number $\overline{Nu}$ of the oscillating baffled plate and the stationary flat plate) for $w_0=22.0$, $A_0=0.9$, and $Gr=10^7$ is shown in Fig. 8. This figure includes a wide range varying baffle height from one-fifth to two times the thickness of the thermal boundary layer and baffle length from one-tenth to one-fourth of the baseplate length. It is seen that the enhancement ratio changes from 5.2 to 7.7, depending on the baffle spacing and baffle height. It is obvious that for short baffles (the cases of $St=0.04$ and 0.10), when the baffle spacing increases, the enhancement ratio decreases; however, at a higher baffle (the cases of $St=0.24$ and 0.40), the heat transfer enhancement increase is observed as the baffle spacing is increased. It means that smaller baffle height results in a higher enhancement ratio at smaller baffle spacing and higher baffle provides a higher enhancement at bigger baffle spacing. It can be explained based on the three competing mechanisms described above which are responsible for the heat transfer enhancement. For the shorter baffles, because the vortices which transfer near-wall fluid to the ambient region are always easy to be generated due to the baffles being short, the differences in the enhancement

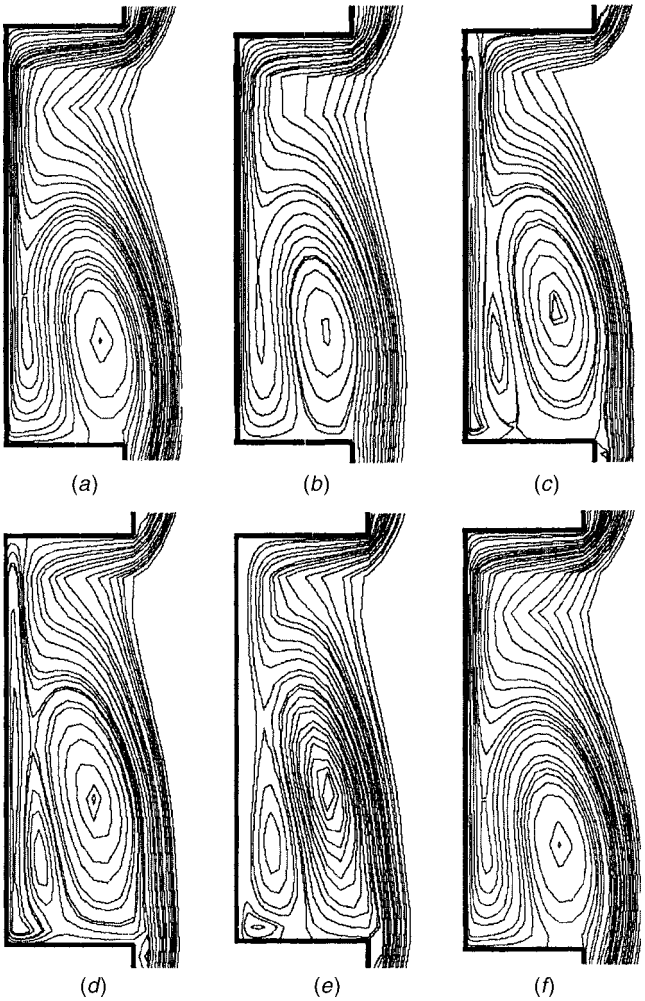

Fig. 4 A time sequence of instantaneous streamlines in the (x,y) plane for one oscillation cycle. The dimensionless oscillation frequency, amplitude, baffle height, spacing and the Grashof number are 22.0, 0.9, 0.24, 0.32 and 10^7, respectively. (a) $t=t_0$ (an integer), (b) $t=t_0+0.2$, (c) $t=t_0+0.4$, (d) $t=t_0+0.6$, (e) $t=t_0+0.8$, and (f) $t=t_0+1.0$.

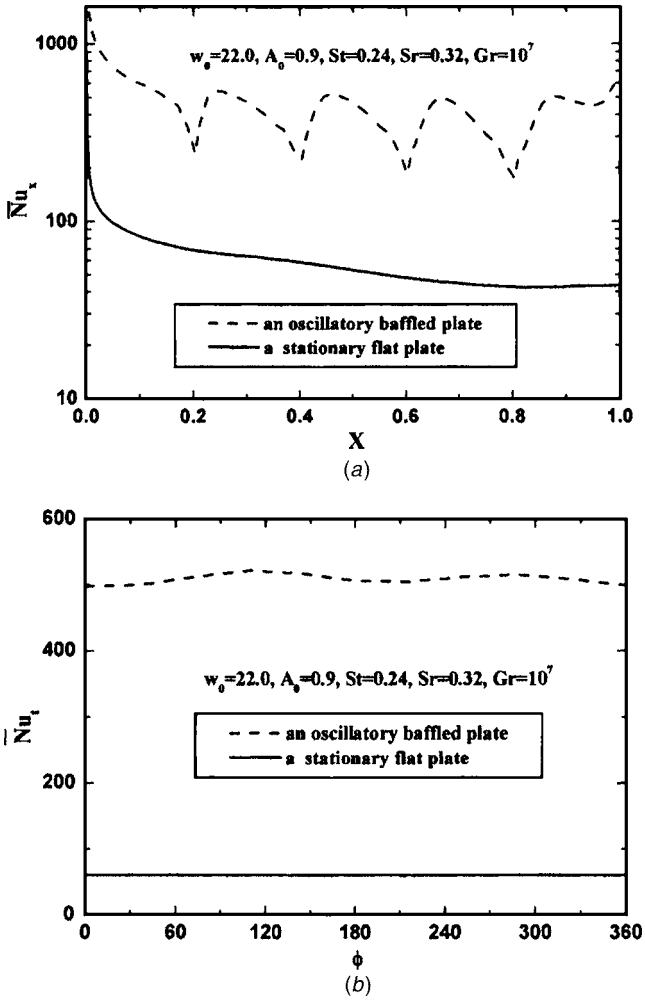

Fig. 5 Variations of Nusselt number during one oscillation cycle for $w_0=22.0$, $A_0=0.9$, $St=0.24$, $Sr=0.32$ and $Gr=10^7$. (a) The time-averaged local Nusselt number $\bar{Nu}_x$; (b) the space-averaged instantaneous Nusselt number $\bar{Nu}_t$.

ratio are mainly based on how often the boundary layer is efficiently interrupted. Thus, a higher enhancement ratio can be achieved when spacing is decreased. However, for the higher baffles, bigger than the thermal boundary layer thickness, small baffle spacing will prevent the ambient flow from flowing into the near-wall region and it is difficult to carry heat from near-wall fluid to the ambient region. However, for bigger baffle spacing, the vortices which transfer heat from near-wall region to the ambient are easier to generate by a simultaneous use of oscillatory plate and baffles. Thus, the differences in the enhancement ratio for the higher baffles are mainly due to variations in flow patterns. Furthermore, it can be concluded from Fig. 8 that a higher enhancement ratio can be achieved for the baffle height-spacing ratio which falls into 0.25–0.50. Therefore, if the geometry of baffled plate is properly designed, it is very attractive for achieving significant heat transfer enhancement.

The effect of the Grashof number on the enhancement ratio for $w_0=22.0$, $A_0=0.9$, $St=0.08$ and $Sr=2.0$ (the baffle height-spacing ratio is at 0.25) is shown in Fig. 9. The solid line represents the enhancement ratio when the oscillation velocity u_0 is fixed at the value close to u_{max} at $Gr=10^7$. It can be seen that the ratios increase with the decrease of Grashof number. At the fixed oscillation frequency and amplitude, under a smaller buoyant force, a higher heat transfer enhancement is obtained. The reason given for this behavior is that the ratio of the oscillation velocity u_0 and the flow velocity u_{max} in the boundary layer under nonoscillation condition becomes smaller and smaller with the increase of the Grashof number. As described in Fig. 7, the heat transfer enhancement by an oscillating-wall condition is appreciably related to the relative size of the value of u_0 and u_{max}. The dashed line in Fig. 9 is the calculated results when the ratios u_0/u_{max} under different buoyancy forces are all fixed at 1.0, which means oscillation velocity u_0 is almost same with the flow velocity u_{max} in the velocity boundary layer under nonoscillation conditions. It can be seen that the enhancement ratio is inversely proportional to the Grashof number. This is because, under smaller buoyancy forces, the vortices are easier to generate by a simultaneous use of oscillating wall and baffles. Therefore, the heat transfer performance can be kept at a higher level for a small buoyancy force. This phenomenon is similar to the conclusion shown in the research of forced convection [11], in which the greater advantage for the heat transfer enhancement of oscillatory flow appears to be found at low net flow Reynolds number.

5 Concluding Remarks

A numerical investigation of the laminar natural convection on a periodically oscillating baffled plate has been presented. The following remarks are made from the results of this study:

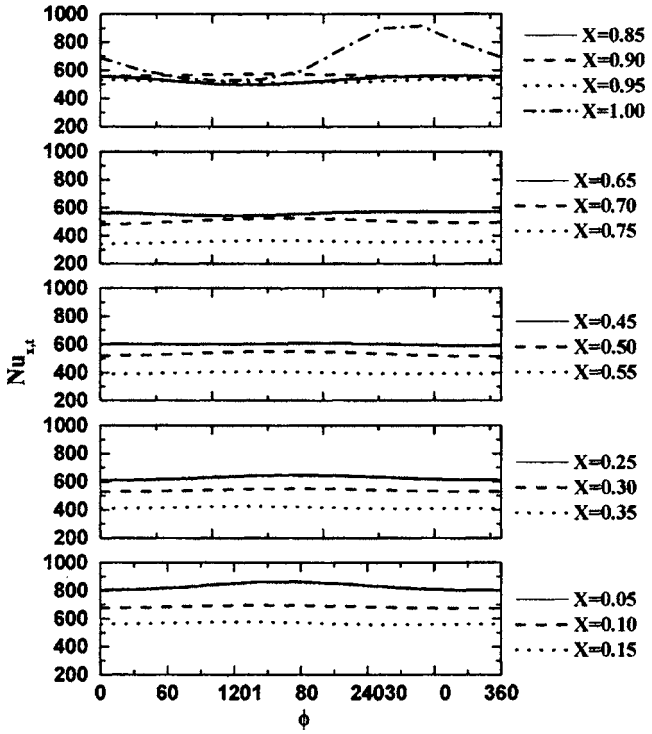

Fig. 6 Variations of the local instantaneous Nusselt number along the plate during one oscillation cycle for $w_0=22.0$, $A_0=0.9$, $St=0.24$, $Sr=0.32$ and $Gr=10^7$

1. This paper focused on the investigation of heat transfer characteristics under such an oscillation condition as the magnitude of oscillation velocity close to the flow velocity in the velocity boundary layer of a stationary baffled plate. The results show that a sevenfold increase in the space-time averaged Nusselt number is obtained.

2. Three competing mechanisms that are responsible for the heat transfer enhancement are observed. The first mechanism of the enhancements is due to periodic redevelopment of the thermal boundary layer. The second is that the thickness of thermal boundary layer becomes thinner under oscillating-wall conditions. In addition, a highly complex flow pattern including strong vortices produced by a simultaneous use of oscillation plate and baffles may contribute much to the heat transfer enhancements.

3. The heat transfer performance of an oscillatory baffled plate depends significantly on the dimensionless oscillation frequency and amplitude. The larger the dimensionless oscillation velocity, the higher heat transfer can be achieved. But the heat transfer enhancement decreases with the increase of the Groshof number.

4. Changes in the enhancement ratio at different combinations of baffle spacing and baffle height are reported. The results indicate that the enhancement ratio can be varied from 5.2 to 7.7, depending on the baffle spacing and baffle height. An optimal baffled height-spacing ratio 0.25–0.50 is found for a higher heat transfer enhancement ratio.

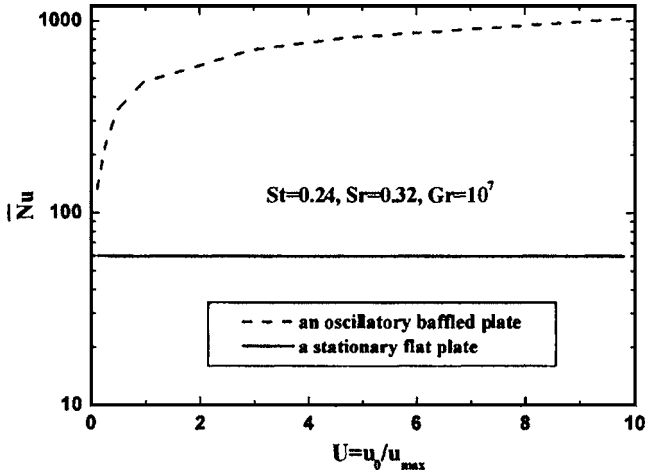

Fig. 7 Variations of the space-time averaged Nusselt number with the dimensionless oscillation velocity ($U=u_0/u_{max}$) for $St=0.24$, $Sr=0.32$ and $Gr=10^7$

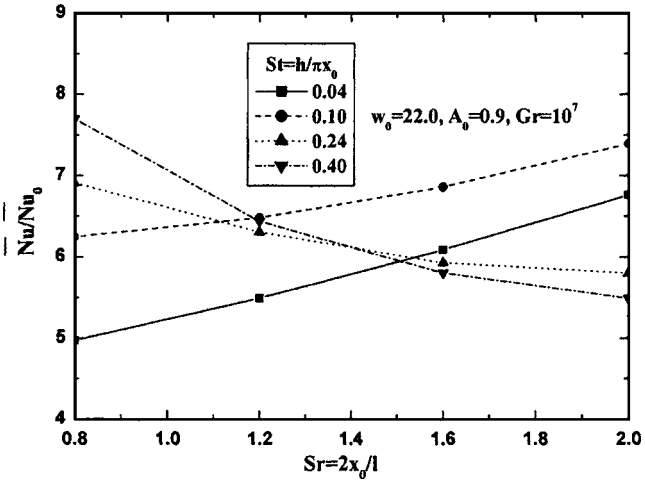

Fig. 8 Variations of the enhancement ratio with the baffle spacing ($Sr=2x_0/\ell$) for different baffle height ($St=h/\pi x_0$) for $w_0=22.0$, $A_0=0.9$ and $Gr=10^7$

Acknowledgment

The calculations were performed using the ORIGIN 2000 (or SX-5) in the Institute of Fluid Science, Tohoku University.

Nomenclature

A_0 = dimensionless oscillation amplitude, Eq. (6)
b = dimensionless baffle width
c_p = specific heat

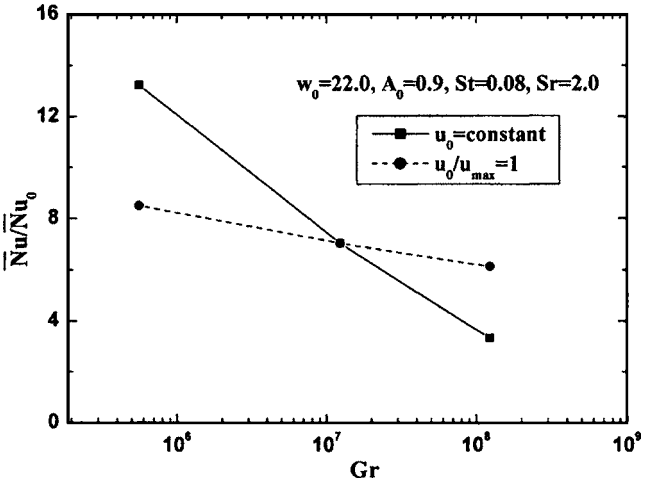

Fig. 9 Effect of the Grashof number on the enhancement ratio for $w_0=22.0$, $A_0=0.9$, $St=0.10$ and $Sr=2.0$

f = dimensional oscillation frequency
g = gravity vector
Gr = Grashof number, $Gr=g\beta(T_w-T_\infty)L^3/\nu^2$
h = dimensional baffle height
k = thermal conductivity for fluid
ℓ = dimensional baffle spacing
L = base plate length
$Nu_{x,t}$ = local instantaneous Nusselt number, Eq. (9)
$\overline{Nu}_x$ = time-averaged local Nusselt number, Eq. (10)
$\overline{Nu}_t$ = space-averaged instantaneous Nusselt number, Eq. (10)
$\overline{Nu}_0$ = space-averaged Nusselt number of a stationary flat plate
$\overline{Nu}$ = space-time averaged Nusselt number, Eq. (10)
P = dimensional pressure of the fluid
Pr = Prandtl number of the fluid
$q_{x,t}$ = local instantaneous convective heat flux
St = dimensionless baffle height, Eq. (8)
Sr = dimensionless baffle spacing, Eq. (8)
T = dimensional temperature; T_0 (reference temperature)
t = dimensional time
u = dimensional oscillation velocity, Eq. (5)
U = dimensionless oscillation velocity, Eq. (8)
$u_{\max}$ = the maximum flow velocity in the velocity boundary layer of a stationary baffled plate
V = dimensional velocity vector
w_0 = dimensionless oscillation frequency, Eq. (7)
x = dimensional vertical coordinate; the displacement of oscillation, Eq. (4)
x_0 = dimensional oscillation amplitude
X = dimensionless vertical coordinate, Eq. (8)
y = dimensional horizontal coordinate
Y = dimensionless horizontal coordinate, Eq. (8)

Greek Symbols

$\delta_{\max}$ = the maximum thickness of velocity boundary layer of a stationary baffled plate
μ = dynamic viscosity
ρ = density
β = volumetric thermal expansion coefficient
ν = kinematic viscosity
ϕ = dimensionless time (phase angle), Eq. (8)
θ = dimensionless temperature, Eq. (8)

References

[1] Kurzweg, U. H., and Zhao, L. D., 1984, "Heat Transfer by High Frequency Oscillations: A New Hydrodynamic Technique for Achieving Large Effective Thermal Conductivities," Phys. Fluids, **27**, pp. 2624–2627.
[2] Kurzweg, U. H., 1985, "Enhanced Heat Conduction in Fluids Subjected to Sinusoidal Oscillations," J. Heat Transfer, **107**, pp. 459–462.
[3] Kurzweg, U. H., 1986, "Temporal and Spatial Distribution of Heat Flux in Oscillating Flow Subjected to an Axial Temperature Gradient," Int. J. Heat Mass Transfer, **29**, pp. 1969–1977.
[4] Ozawa, M., and Kawamoto, A., 1991, "Lumped-Parameter Modeling of Heat Transfer Enhanced by Sinusoidal Motion of Fluid," Int. J. Heat Mass Transfer, **34**, pp. 3083–3094.
[5] Nishio, S., Shi, X. H., and Zhang, W. M., 1995, "Oscillation-Induced Heat Transport: Heat Transport Characteristics Along Liquid-Columns of Oscillation-Controlled Heat Transport Tubes," Int. J. Heat Mass Transfer, **38**, pp. 2457–2470.
[6] Walsh, T. E., Yang, K. T., Nee, V. W., and Liao, Q. D., 1993, "Forced Convection Cooling in Microelectronic Cabinets via Oscillatory Flow Techniques," Exp. Heat Transfer, pp. 641–648.
[7] Liao, Q. D., Yang, K. T., and Nee, V. W., 1995, "Enhanced Microprocessor Chip Cooling by Channeled Zero-Mean Oscillatory Air Flow," *Advances in Electronic Packaging*, Vol. 2, pp. 789–794.
[8] Fusegi, T., 1996, "Mixed Convection in Periodic Open Cavities With Oscillatory Throughflow," Numer. Heat Transfer, Part A, **29**, pp. 33–47.
[9] Brunold, C. R., Hunns, J. C. B., Mackley, M. R., and Thompson, J. W., 1989, "Experimental Observations on Flow Patterns and Energy Losses for Oscillatory Flows in Ducts with Sharp Edges," Chem. Eng. Sci., **44**, pp. 1227–1244.
[10] Howes, T., Mackley, M. R., and Roberts, E. P. L., 1991, "The Simulation of Chaotic Mixing and Dispersion for Periodic Flows in Baffled Channels," Chem. Eng. Sci., **46**, pp. 1669–1677.
[11] Mackley, M. R., and Stonestreet, P., 1995, "Heat Transfer and Associated Energy Dissipation for Oscillatory Flow in Baffled Tubes," Chem. Eng. Sci., **50**, pp. 2211–2224.
[12] Stephens, G. G., and Mackley, M. R., 2002, "Heat Transfer Performance for Batch Oscillatory Flow Mixing," Exp. Therm. Fluid Sci., **25**, pp. 583–594.
[13] Fu, W. S., and Yang, S. J., 2001, "Heat Transfer Induced by a Body Moving in Opposition to a Flowing Fluid," Int. J. Heat Mass Transfer, **44**, pp. 89–98.
[14] Fu, W. S., and Tong, B. H., 2002, "Numerical Investigation of Heat Transfer from a Heated Oscillating Cylinder in a Cross Flow," Int. J. Heat Mass Transfer, **45**, pp. 3033–3043.
[15] Fu, W. S., and Tong, B. H., 2004, "Numerical Investigation of Heat Transfer Characteristics of the Heated Blocks in the Channel with a Transversely Oscillating Cylinder," Int. J. Heat Mass Transfer, **47**, pp. 341–351.
[16] Fu, W. S., and Yang, S. J., 2001, "A New Model for Heat Transfer of Fins Swinging Back and Forth in a Flow," Int. J. Heat Mass Transfer, **44**, pp. 1687–1697.
[17] Maruyama, S., Ishikawa, M., and Taira, K., 2000, Japanese patent No. 158594.
[18] Maruyama, S., Tsubaki, K., Taira, K., and Sakai, S., 2004, "Artificial Upwelling of Deep Seawater Using the Perpetual Salt Fountain for Cultivation of Ocean Desert," J. Oceanogr., **60**, pp. 563–568.
[19] Zhang, X. R., Maruyama, S., Sakai, S., Tsubaki, K., and Behnia, M., 2004, "Flow Prediction in Upwelling Deep Seawater—the Perpetual Salt Fountain," Deep-Sea Res., Part I, **51**, pp. 1145–1157.
[20] Iwatsu, R., Hyun, J. M., and Kuwahara, K., 1992, "Convection in a Differentially-Heated Square Cavity with a Torsionally-Oscillating Lid," Int. J. Heat Mass Transfer, **35**, pp. 1069–1076.
[21] Fu, W. S., and Shieh, W. J., 1992, "A Study of Thermal Convection in an Enclosure Induced Simultaneously by Gravity and Vibration," Int. J. Heat Mass Transfer, **35**, pp. 1695–1710.
[22] Zhang, X. R., Maruyama, S., and Sakai, S., 2004, "Numerical Investigation of Laminar Natural Convection on a Heated Vertical Plate Subjected to a Periodic Oscillation," Int. J. Heat Mass Transfer, **47**, pp. 4439–4448.
[23] Zhang, X. R., Maruyama, S., Sakai, S., Tsubaki, K., and Behnia, M., 2004, "Mechanism of Turbulent Transport in Upwelling Deep Seawater Using the Perpetual Salt Fountain," Deep-Sea Res., Part I, (to be published).
[24] Ostrach, S. S., 1953, "An Analysis of Laminar Free Convection Flow and Heat Transfer About a Flat Plate Parallel to the Direction of the Generating Body Force," NASA Report, pp. 63–79.
[25] Schlichting, H., 1979, *Boundary-Layer Theory*, seventh edition, McGraw-Hill, New York, pp. 93–95.

Narrow-Band Based Multiscale Full-Spectrum *k*-Distribution Method for Radiative Transfer in Inhomogeneous Gas Mixtures

Liangyu Wang

Michael F. Modest[1]
Fellow ASME

The Pennsylvania State University,
Department of Mechanical
and Nuclear Engineering,
University Park, PA 16802

The full-spectrum k-distribution (FSK) method has become the most promising model for radiative transfer in participating media since its introduction a few years ago. It achieves line-by-line (LBL) accuracy for homogeneous media with only a tiny fraction of LBL's computational cost. Among the variants of the FSK method for dealing with inhomogeneous media, the multiscale FSK (MSFSK) method not only provides a strategy to treat the inhomogeneity problem by introducing an overlap coefficient, it also accommodates a solution to the so-called mixing problem (mixing of k-distributions for different gas species). The evaluation of MSFSK parameters, however, is tedious and excludes the MSFSK method from practical applications. In this paper a new scheme of evaluating k-distributions and overlap coefficients from a database of narrow-band k-distributions is formulated, treating each gas specie as a single scale. The new scheme makes the MSFSK method efficient and convenient for practical applications, and ready to accommodate nongray absorbing particles (such as soot) in the medium. The method virtually eliminates errors caused by uncorrelatedness due to independently varying species concentrations. It was also found that, in addition, breaking up a gas mixture into gas scales reduces the error caused by temperature inhomogeneities. The mathematical development of the new scheme is described and validated; the concept and the implication of the overlap coefficient are discussed. Sample calculations for inhomogeneous media with step changes in species mole fraction and temperature are performed to demonstrate the accuracy of the new scheme by comparison with LBL calculations. [DOI: 10.1115/1.1925281]

Keywords: k-Distribution Method, Inhomogeneous Gas Mixture, Multiscale Approach

1 Introduction

The concepts of reordering absorption coefficients has greatly reduced the computational cost of predicting radiative transfer in gas mixtures [1,2]. Several models have been put forward to apply the concept to the entire spectrum and these include the spectral-line-based weighted-sum-of-gray-gases (SLW) model [3,4], the absorption distribution function (ADF) method [5,6], and the recent full-spectrum *k*-distribution (FSK) method [7]. Whereas the SLW and ADF methods are weighted-sum-of-gray-gases approaches (i.e., the—assumed to be correlated—absorption coefficient is reduced to a few discrete values) the FSK method distinguishes itself in that it is an *exact* method for a correlated absorption coefficient, utilizing a continuous *k*-distribution over the whole spectrum, and this allows a quadrature scheme of arbitrary order of accuracy to be employed. The FSK method achieves line-by-line (LBL) accuracy for homogeneous media with only a tiny fraction of LBL's computational cost. Since its introduction, the FSK method has undergone several major developments, including the formal mathematical development of full-spectrum correlated-*k* (FSCK) and scaled-*k* (FSSK) methods [8], the proposal of a multiscale FSK (MSFSK) method [9], the development of the multigroup FSK (MGFSK) method [10], and the assembly of full-spectrum *k*-distributions from narrow-band *k*-distributions [11].

The FSCK, FSSK, MSFSK, and MGFSK methods are designed to apply the FSK scheme to radiative transfer problems in inhomogeneous media, which remains a challenging topic for reordering models and any other global methods. The challenge is that inhomogeneities in total pressure, temperature, and component gas mole fraction (partial pressure) change the spectral distribution of the absorption coefficient, which is critical to the FSK reordering process. The effect of varying total pressure on the FSK reordering process is relatively small, as evidenced by the success of applying the correlated-*k* method in the field of meteorology, where strong total pressure variations occur while temperatures stay relatively uniform [1,12,13]. The effect of varying temperature can be substantial, as first recognized by Rivière et al. [14–16]: Spectral lines that are negligible at room temperatures become more and more important at elevated temperatures, giving rise to the so-called "hot lines." The effect of varying gas concentrations can also be substantial, as first recognized by Modest and Zhang [7]: At one spatial location the absorption coefficient may be dominated by one specie, but by another (with totally different spectral lines) at a different location.

The FSCK and FSSK methods can produce accurate results for media that have large variations in total pressure but small variations in temperature and partial pressure. For media that have large temperature and partial pressure variations, sophisticated MSFSK and MGFSK methods have been developed to improve the accuracy of the FSK method. The MSFSK method deals with the inhomogeneity problem by grouping individual spectral lines comprising the absorption coefficient into *M* separate scales according to their temperature dependence [9]. The overlap in spectrum between different scales is treated in an approximate way so

[1]Author to whom all correspondence should be addressed. Fax: (814) 863-4848; e-mail: MFModest@psu.edu

Contributed by the Heat Transfer division for publication in the JOURNAL OF HEAT TRANSFER. Manuscript received: August 27, 2004. Final manuscript received: December 7, 2004. Review conducted by: Stefan Thynell.

that a number of M independent radiative transfer equations (RTEs) (instead of M^2 required for the fictitious gas approach [5,6]) need to be solved. In contrast to the MSFSK method, which organizes spectral lines into groups, the MGFSK method places spectral positions into M separate groups according to their temperature and partial pressure dependencies [10]. This avoids the problem of overlap among different groups and, therefore, also requires only M RTE evaluations but without any further approximation. However, with the MGFSK method it appears impossible to obtain k-distributions for arbitrary gas mixtures from mixing those of individual species.

The need for mixing comes from practical considerations, since it would be impossible to precalculate and database the infinite number of possible k-g distributions that are required in a practical heat transfer calculation. In practice, the k-g distributions of individual gases are precalculated and then are mixed during the calculation to obtain arbitrary mixture k-g distributions. Although the MGFSK method can achieve great accuracy for individual gases, groups from different gases are incompatible, making its application to inhomogeneous mixtures problematic. The MSFSK method, on the other hand, can treat the absorption coefficient of an individual specie in a mixture as one of its scales. The problem of mixing FSKs of individual species in a gas mixture is thus transformed into a problem of resolving the overlap among scales.

The originally formulated MSFSK method proposed an approximate but elegant solution to the overlap problem by introducing an overlap coefficient. The calculation of this overlap coefficient, however, is cumbersome, and must be obtained from a spectral database for every location in an inhomogeneous medium. Therefore, the MSFSK method in its original form is not useful for practical calculations. It is the purpose of the present paper to develop a scheme to calculate the overlap coefficient efficiently from a database of narrow-band k-distributions, rather than from high-resolution spectral databases. This will allow the MSFSK parameters to be calculated on-the-fly, making the MSFSK method the most powerful method to deal with radiative transfer in strongly inhomogeneous gaseous media. In addition, the new scheme described here makes the MSFSK method ready to accommodate nongray absorbing particles (such as soot) in the medium. The original development of the MSFSK method does not consider nongray particles, and in addition, the boundaries were treated as black and cold. These issues will be addressed in a follow-up paper.

2 Theoretical Development

In the following, the original MSFSK method is reformulated for the convenience of further development. Many key points are clarified and improvements are indicated. All developments are in context of a radiatively participating medium contained in an opaque enclosure.

2.1 MSFSK Formulation for Gas Mixture. Although the following development can be easily extended to include gray absorbing and scattering particles as done in the original MSFSK development, for clarity, a medium consisting of a mixture of molecular gases is considered, and the radiative transfer equation (RTE) is then written as [17]

$$\frac{\mathrm{d}I_\eta}{\mathrm{d}s} = \kappa_\eta(\underline{\phi})(I_{b\eta} - I_\eta), \tag{1}$$

subject to the boundary condition

$$\text{at } s = 0: \quad I_\eta = I_{w\eta} \tag{2}$$

Here, I_η is the spectral radiative intensity, κ_η the absorption coefficient, $I_{b\eta}$ the spectral blackbody intensity (or Planck function), and wave number η is the spectral variable. The term $\underline{\phi}$ is a vector of state variables that affect κ_η, which include temperature T, total pressure P, and gas mole fractions $\underline{x}$: $\underline{\phi}=(T,P,\underline{x})$. The boundary intensity $I_{w\eta}$ is due to the emission and/or reflection from the enclosure wall. If we separate the contributions to κ_η from the M component gases and break up the radiative intensity I_η accordingly, i.e.,

$$\kappa_\eta = \sum_{m=1}^{M} \kappa_{m\eta}, \quad I_\eta = \sum_{m=1}^{M} I_{m\eta}, \tag{3}$$

then the RTE (1) is transformed into M component RTE's, one for each gas or scale. In this paper we will deal only with the treatment of concentration inhomogeneities, i.e., each gas specie will be treated as a single scale. Then the RTE for each gas scale is

$$\frac{\mathrm{d}I_{m\eta}}{\mathrm{d}s} = \kappa_{m\eta}(\underline{\phi})I_{b\eta} - \kappa_\eta(\underline{\phi})I_{m\eta}, \quad \text{for } m = 1,\ldots,M. \tag{4}$$

It is observed, physically, the intensity $I_{m\eta}$ for the mth scale is due to emission from the mth gas specie but subject to absorption from all gases.

We now apply the FSK scheme [8] to the RTE of each scale: First Eq. (4) is multiplied by Dirac's delta function $\delta(k_m - \kappa_{m\eta}(\underline{\phi}_0))$, followed by division with

$$f_m(T_0,\underline{\phi}_0,k_m) = \frac{1}{I_b(T_0)}\int_0^\infty I_{b\eta}(T_0)\,\delta(k_m - \kappa_{m\eta}(\underline{\phi}_0))\mathrm{d}\eta, \tag{5}$$

where, $\underline{\phi}_0$ and T_0 refer to a reference state. The resulting equation is then integrated over the whole spectrum, leading to

$$\frac{\mathrm{d}I_{mg}}{\mathrm{d}s} = k_m a_m I_b - \lambda_m I_{mg}, \quad \text{for } m = 1,\ldots,M, \tag{6}$$

where

$$I_{mg} = \int_0^\infty I_{m\eta}\delta(k_m - \kappa_{m\eta}(\underline{\phi}_0))\mathrm{d}\eta \Big/ f_m(T_0,\underline{\phi}_0,k_m), \tag{7}$$

$$g_m = \int_0^{k_m} f_m(T_0,\underline{\phi}_0,k)\mathrm{d}k \tag{8}$$

$$a_m = \frac{f_m(T,\underline{\phi}_0,k_m)}{f_m(T_0,\underline{\phi}_0,k_m)}, \tag{9}$$

$$\lambda_m I_{mg} = k_m I_{mg} + \int_0^\infty \left(\sum_{n\neq m}\kappa_{n\eta}(\underline{\phi})\right) I_{m\eta}\delta(k_m - \kappa_{m\eta}(\underline{\phi}_0))\mathrm{d}\eta \Big/ f_m(T_0,\underline{\phi}_0,k_m). \tag{10}$$

Here the correlated-k (FSCK) approach has been taken, in which the correlated-k assumption deals with the inhomogeneity due to temperature change only. This implies that $k_m = k_m(T_0,\underline{\phi},g_m)$ is evaluated from the k-distribution of the *local* absorption coefficient weighted by the Planck function at the *reference* temperature [8]. The second term in Eq. (10) is due to the overlap of the absorption coefficient of the mth scale, $\kappa_{m\eta}$, with those of all other scales, which occurs over part of the spectrum. Physically, the overlap coefficient λ_m is a reordered absorption coefficient of the mth scale taking into account the overlap with all other scales. In the MSFSK approach, the λ_m are determined approximately, based on the argument that overlap effects between scales (individual gas species in this work) are relatively small. There are many ways of approximating λ_m. Here we follow the approach used in the original MSFSK development, that is, the overlap coefficient λ_m is determined in such a way that the emitted intensity emanating from a homogeneous layer bounded by cold black walls is predicted exactly.

In Eq. (7), the reordering is performed in terms of $\kappa_{m\eta}$ and the interaction between $\kappa_{m\eta}$ and κ_η during the reordering process is lumped into λ_m. The reordering can also be performed in terms of κ_η, which for a homogeneous layer at temperature T leads to

$$\frac{dI^*_{mg}}{ds} = \frac{k^*_m I_b}{f(T,\underline{\phi},k)} - kI^*_{mg}, \quad \text{for } m = 1,\ldots,M, \tag{11}$$

where

$$f(T,\underline{\phi},k) = \frac{1}{I_b(T)}\int_0^\infty I_{b\eta}(T)\,\delta(k-\kappa_\eta(\underline{\phi}))\,d\eta, \tag{12}$$

$$I^*_{mg} = \int_0^\infty I_{m\eta}\,\delta(k-\kappa_\eta(\underline{\phi}))\,d\eta \big/ f(T,\underline{\phi},k), \tag{13}$$

$$k^*_m = \frac{1}{I_b}\int_0^\infty I_{b\eta}(T)\kappa_{m\eta}\,\delta(k-\kappa_\eta(\underline{\phi}))\,d\eta. \tag{14}$$

In Eq. (11), the interaction between $\kappa_{m\eta}$ and κ_η is lumped into k^*_m. The solutions to Eqs. (6) and (11) for a homogeneous layer at temperature T bounded by cold black walls can be obtained analytically, and the total exiting intensities at $s=L$ are

$$I_m = \int_0^1 I_{mg}\,dg = \int_0^\infty \frac{k_m}{\lambda_m} I_b[1-\exp(-\lambda_m s)] f_m(T,\underline{\phi},k_m)\,dk_m \tag{15}$$

and

$$I^*_m = \int_0^1 I^*_{mg}\,dg = \int_0^\infty \frac{k^*_m}{k} I_b[1-\exp(-ks)]\,dk, \tag{16}$$

respectively. The spectrally integrated intensity, I_m, should be equal to I^*_m, and this requirement leads to

$$\lambda_m = k \quad \text{and} \quad k_m f_m(T,\underline{\phi},k_m)\,dk_m = k^*_m(k)\,dk, \tag{17}$$

or

$$k^*_m(\lambda_m)\,d\lambda_m = k_m f_m(T,\underline{\phi},k_m)\,dk_m. \tag{18}$$

Equation (18) provides the relationship between λ_m and k_m that is required to solve Eq. (6). One convenient way of determining λ_m is using the relationship [9]

$$\int_0^{k_m} k'_m f_m(T,\underline{\phi},k'_m)\,dk'_m = \int_0^{k'=\lambda_m} k^*_m(k')\,dk'. \tag{19}$$

In wavenumber space this may also be expressed as

$$\int_{\eta|\kappa_{m\eta}\le k_m} \kappa_{m\eta} I_{b\eta}(T)\,d\eta = \int_{\eta|\kappa_\eta\le\lambda_m} \kappa_{m\eta} I_{b\eta}(T)\,d\eta \tag{20}$$

Equation (19) is an implicit equation for the $\lambda_m - k_m$ relationship. In practice, the left and right hand sides of Eq. (19) are evaluated for a set of predetermined k_m and λ_m values and the results are stored in two arrays. The corresponding λ_m values for the k_m values used in the RTE evaluations are determined by interpolation from the two arrays. The so-determined λ_m will be a function of the state variables (i.e., temperature and gas species concentration) as well as k_m (or g_m).

2.2 Evaluation of Overlap Coefficient λ_m. In the original MSFSK development, the k^*_m are calculated directly from Eq. (14), using high-resolution spectral databases, making their evaluation extremely tedious and, thus, impractical for use in general problems with strongly varying concentrations. In the present work, it will be shown how the k^*_m can be determined efficiently and accurately from a database of narrow-band (NB) k-distributions of individual species (scales). The advantages of using NB k-distributions have been demonstrated by Modest and Riazzi [11]: Assembling mixture FS k-distributions from NB k-distributions of individual gas species mixed at the narrow-band level is more accurate than mixing entire FS k-distributions of individual species. In addition, the use of NB k-distributions of individual species allows the inclusion of nongray absorbing particles in the participating medium, and can accommodate nongray scattering and nongray walls.

Substituting Eq. (14), the right-hand side (RHS) of Eq. (19) may be rewritten in terms of narrow-band k^*_m

$$\begin{aligned}\text{RHS} &= \int_0^{k=\lambda_m} \sum_{i=1}^{N_{\text{nb}}} \frac{I_{bi}}{I_b}\frac{1}{\Delta\eta}\int_{\Delta\eta} \kappa_{m\eta}\,\delta(k-\kappa_\eta)\,d\eta\,dk \\ &= \sum_{i=1}^{N_{\text{nb}}} \frac{I_{bi}}{I_b}\int_0^{k=\lambda_m} k^*_{m,i}(k)\,dk,\end{aligned} \tag{21}$$

where $k^*_{m,i}$ is the narrow-band counterpart of k^*_m, N_{nb} is the number of narrow-bands comprising the entire spectrum, and the NB Planck function I_{bi} is defined as

$$I_{bi} = \int_{\Delta\eta} I_{b\eta}\,d\eta. \tag{22}$$

As always in the NB k-distribution approach, we have assumed that $I_{b\eta}$ is constant over $\Delta\eta$ and can be approximated by $I_{bi}/\Delta\eta$.

In order to evaluate the integrals involving $k^*_{m,i}$ in Eq. (21) in terms of NB k-distributions, we consider the quantity Q_m

$$Q_m = \frac{1}{\Delta\eta}\int_{\Delta\eta} \kappa_{m\eta}\exp(-\kappa_\eta L)\,d\eta \tag{23}$$

for the ith narrow band. Physically, Q_m is related to narrow-band emission from scale m, attenuated over path L by the entire gas mixture. Q_m can be rewritten as

$$\begin{aligned}Q_m &= \frac{1}{\Delta\eta}\int_{\Delta\eta}\kappa_{m\eta}\int_0^\infty \exp(-kL)\,\delta(k-\kappa_\eta)\,dk\,d\eta \\ &= \int_0^\infty k^*_{m,i}\exp(-kL)\,dk = \mathcal{L}(k^*_{m,i}),\end{aligned} \tag{24}$$

i.e., Q_m is the Laplace transform of $k^*_{m,i}$.

Modest and Riazzi [11] have shown that, on a narrow-band basis, the spectral behavior of different species is essentially statistically uncorrelated. With this assumption, Q_m can also be written as

$$\begin{aligned}Q_m &= \frac{1}{\Delta\eta}\int_{\Delta\eta}\kappa_{m\eta}\exp(-\kappa_{m\eta}L)\prod_{n\ne m}\exp(-\kappa_{n\eta}L)\,d\eta \\ &\approx \frac{1}{\Delta\eta}\int_{\Delta\eta}\kappa_{m\eta}\exp(-\kappa_{m\eta}L)\,d\eta\prod_{n\ne m}\left(\frac{1}{\Delta\eta}\int_{\Delta\eta}\exp(-\kappa_{n\eta}L)\,d\eta\right).\end{aligned} \tag{25}$$

The second step follows by recognizing that the integration in the first step is an averaging operator, together with the assumption that the absorption coefficients of different scales are statistically uncorrelated. The k-distribution method can then be applied to Eq. (25) and we obtain

$$\begin{aligned}Q_m &\approx \int_0^1 k_{m,i}\exp(-k_{m,i}L)\,dg_m\prod_{n\ne m}\left(\int_0^1\exp(-k_{n,i}L)\,dg_n\right) \\ &= \int_{g_1=0}^1\cdots\int_{g_M=0}^1 k_{m,i}\exp\left(-\sum_{n=1}^M k_{n,i}L\right)dg_1\cdots dg_M.\end{aligned} \tag{26}$$

Equating Eqs. (24) and (26), we have

$$\mathcal{L}(k^*_{m,i}) \approx \int_{g_1=0}^{1} \cdots \int_{g_M=0}^{1} k_m \exp\left(-\sum_{n=1}^{M} k_n L\right) \mathrm{d}g_1 \cdots \mathrm{d}g_M, \tag{27}$$

and, using the integral property of the Laplace transform,

$$\mathcal{L}\left(\int_0^{k=\lambda_m} k^*_{m,i}(k)\mathrm{d}k\right) \approx \int_{g_1=0}^{1} \cdots \int_{g_M=0}^{1} k_m \frac{\exp\left(-\sum_{n=1}^{M} k_n L\right)}{L} \mathrm{d}g_1 \cdots \mathrm{d}g_M. \tag{28}$$

Finally, taking the inverse Laplace transform, we obtain

$$\int_0^{k=\lambda_m} k^*_{m,i}(k)\mathrm{d}k \approx \int_{g_1=0}^{1} \cdots \int_{g_M=0}^{1} k_m H\left(k - \sum_{n=1}^{M} k_n\right) \mathrm{d}g_1 \cdots \mathrm{d}g_M, \tag{29}$$

where H is the Heaviside step function.

The LHS of Eq. (19) is also readily expressed in terms of NB k-distributions,

$$\begin{aligned} \mathrm{LHS} &= \int_0^{k_m} k'_m \frac{1}{I_b} \int_0^{\infty} I_{b\eta} \delta(k'_m - \kappa_{m\eta}) \mathrm{d}\eta \, \mathrm{d}k'_m \\ &= \sum_{i=1}^{N_{\mathrm{nb}}} \frac{I_{bi}}{I_b} \int_0^{k_m} k'_m \frac{1}{\Delta\eta} \int_{\Delta\eta} \delta(k'_m - \kappa_{m\eta}) \mathrm{d}\eta \, \mathrm{d}k'_m \\ &= \sum_{i=1}^{N_{\mathrm{nb}}} \frac{I_{bi}}{I_b} \int_0^{g_{m,i}(k_m)} k_{m,i} \, \mathrm{d}g_{m,i}. \end{aligned} \tag{30}$$

Equating the LHS and RHS, we obtain a generic expression for the determination of the overlap coefficient λ_m based on NB k-distributions of individual gases as

$$\begin{aligned} &\sum_{i=1}^{N_{\mathrm{nb}}} \frac{I_{bi}}{I_b} \int_0^{g_{m,i}(k_m)} k_{m,i} \, \mathrm{d}g_{m,i} \\ &\quad = \sum_{i=1}^{N_{\mathrm{nb}}} \frac{I_{bi}}{I_b} \int_{g_{1,i}=0}^{1} \cdots \int_{g_{M,i}=0}^{1} k_{m,i} H\left(\lambda_m - \sum_{n=1}^{M} k_{n,i}\right) \mathrm{d}g_{1,i} \cdots \mathrm{d}g_{M,i}, \\ &\quad \text{for } m = 1, \ldots, M. \end{aligned} \tag{31}$$

For special cases, for example, for a mixture of two gases, the $\lambda_1 - k_1$ relation for gas 1 can be found from

$$\sum_{i=1}^{N_{\mathrm{nb}}} \frac{I_{bi}}{I_b} \int_0^{g_{1,i}(k_1)} k_{1,i} \, \mathrm{d}g_{1,i} = \sum_{i=1}^{N_{\mathrm{nb}}} \frac{I_{bi}}{I_b} \int_{g_{1,i}=0}^{1} k_{1,i} g_{2,i}(\lambda_1 - k_{1,i}) \mathrm{d}g_{1,i}, \tag{32}$$

and similarly for gas 2.

In the narrow-band k-g database published by Wang and Modest [18], the data are organized in such a way that the narrow-band k-g pairs obtained from the database for a certain condition correspond to the quadrature points of a Gaussian quadrature scheme. Therefore, the integrals in Eqs. (31) and (32) can be evaluated efficiently based on the narrow-band database.

2.3 Uncorrelatedness of Gas Absorption Coefficients. In order to reach the result of Eq. (31), the absorption coefficients of different scales (component gases) have been assumed to be uncorrelated on a narrow-band basis, Eq. (25). Taine and Soufiani [19] have discovered that multiplying the transmissivities of two individual gas species to obtain a binary mixture transmissivity is very accurate for nearly all spectral locations, i.e.,

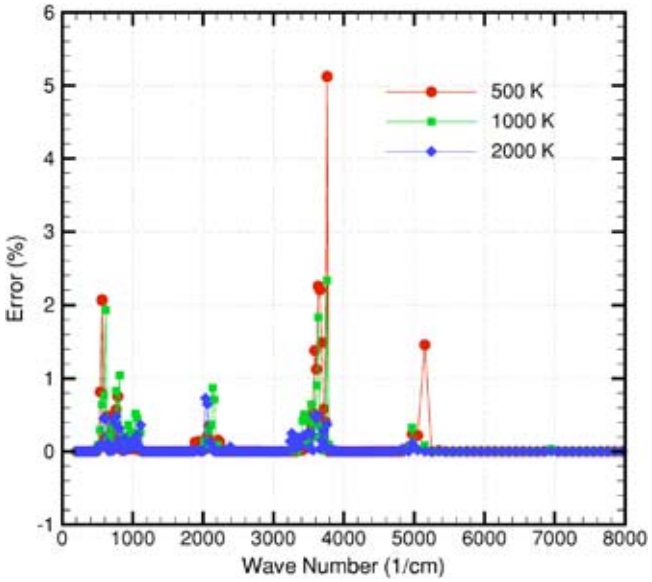

Fig. 1 Error introduced by Eq. (33) for a mixture of 10% CO_2–10% H_2O–80% N_2 at 1 bar

$$\begin{aligned} &\frac{1}{\Delta\eta} \int_{\Delta\eta} \exp[-(\kappa_{1\eta} + \kappa_{2\eta})L] \mathrm{d}\eta \\ &\quad \approx \frac{1}{\Delta\eta} \int_{\Delta\eta} \exp(-\kappa_{1\eta} L) \mathrm{d}\eta \, \frac{1}{\Delta\eta} \int_{\Delta\eta} \exp(-\kappa_{2\eta} L) \mathrm{d}\eta. \end{aligned} \tag{33}$$

Equation (33) does not imply that the absorption coefficients of the two gases are statistically uncorrelated, but if they are uncorrelated, Eq. (33) will follow. Figure 1 shows the relative errors of using the product of individual gas transmissivities as the mixture transmissivity when compared to the directly calculated mixture transmissivity from the LBL database. In the figure, the mixture contains 10% H_2O and 10% CO_2, and the HITEMP [20] and CDSD [21] spectral databases are used to evaluate the absorption coefficients of the two gas species, respectively. Following Wang and Modest [18], a total number of 248 narrow bands are considered, and the spectral range of each narrow band is selected such that the Planck function is nearly constant over the range (within 0.5% error for temperatures from 300 to 2500 K). The path length L is determined in such a way that the mixture transmissivity is around 0.5 for each narrow band, except for those cases where the length would be too large or too small (allowing lengths between 0.01 and 1000 cm). Each symbol in the figure represents the error for one narrow band. The errors stay below 1% for most NBs and this is true for all mixture temperatures. The error becomes smaller as the mixture temperature is increased, suggesting that Eq. (33) is more accurate for high temperature situations.

In order to ascertain the accuracy of Eq. (31), the uncorrelatedness between gas species will be tested by considering a binary mixture of the most important combustion gases, H_2O and CO_2. Equation (25) for a two-gas mixture reduces to

$$\begin{aligned} &\frac{1}{\Delta\eta} \int_{\Delta\eta} \kappa_{1\eta} \exp[-(\kappa_{1\eta} + \kappa_{2\eta})L] \mathrm{d}\eta \\ &\quad \approx \frac{1}{\Delta\eta} \int_{\Delta\eta} \kappa_{1\eta} \exp(-\kappa_{1\eta} L) \mathrm{d}\eta \\ &\qquad \frac{1}{\Delta\eta} \int_{\Delta\eta} \exp(-\kappa_{2\eta} L) \mathrm{d}\eta. \end{aligned} \tag{34}$$

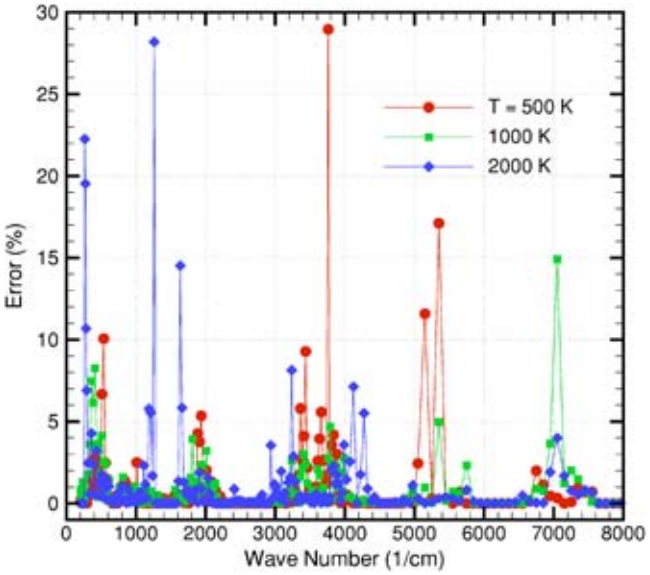

Fig. 2 Error introduced by Eq (34) for a mixture of 10% CO_2–10% H_2O–80% N_2 at 1 bar

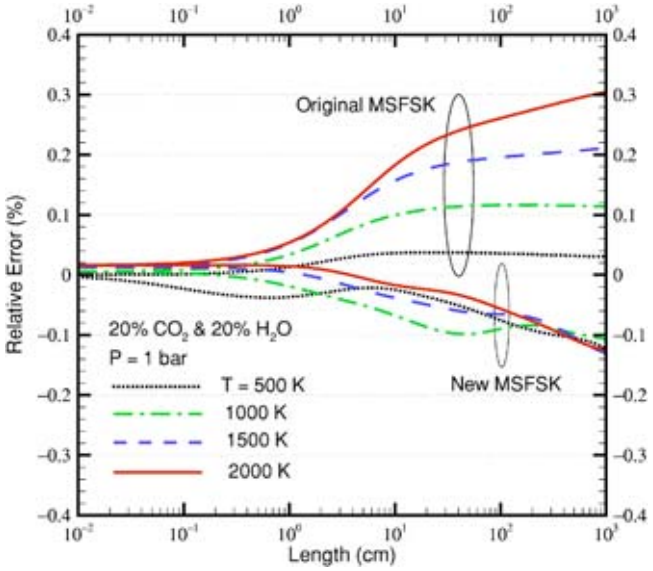

Fig. 3 Validation of the new MSFSK scheme

This relation differs from Eq. (33) in that the absorption coefficient of one gas appears in front of the exponential in the integrand of the LHS; the first part of the RHS can be recognized as the derivative of the transmissivity of gas 1 with respect to the path length. Equation (34) is exact if $\kappa_{1\eta}$ and $\kappa_{2\eta}$ are statically uncorrelated. The errors introduced by this approximation for all the narrow bands are shown in Fig. 2, using the same parameters as those for Fig. 1. The errors are considerably larger than the errors shown in Fig. 1, indicating that the absorption coefficients of different gases are not truly uncorrelated. The maximum errors for different mixture temperatures occur at different spectral locations. Since the introduced error will be weighted by the Planck function [RHS in Eq. (31)], the overall error from using Eq. (31) to determine the overlap coefficient λ_m is still expected to be relatively small. This is shown to be true in the following validating calculations.

2.4 Validation of Approach. To test the new scheme of evaluating the overlap coefficient from narrow-band *k*-distributions for individual species, the radiative intensity emerging from a homogeneous gas layer bounded by cold black walls is calculated in three ways: Using LBL calculations, using the MSFSK method with Eqs. (14) and (19) to determine the overlap coefficient directly from the HITEMP and CDSD databases (the original MSFSK method), and, finally, using the MSFSK method, but employing Eq. (31) to determine the overlap coefficient (present approach), with the required narrow-band *k*-distributions obtained also from HITEMP and CDSD. In the MSFSK calculations, all (5000) *k-g* points have been used for numerical integration, and, therefore, the results from the original MSFSK are as "exact" as the LBL calculations (which were obtained using trapezoidal rule quadrature with 1 million data points) for such a homogeneous layer and the differences between the two come only from numerical inaccuracies. The present approach contains the approximation made in Eq. (25) and differences from the LBL calculations show the error introduced by this simplification and, consequently, the validity of the new scheme to determine the overlap parameter.

Figure 3 shows the relative errors of the two MSFSK calculations compared to LBL, with errors plotted against the path length of the homogeneous layer for several temperatures. For the original MSFSK method, in which the overlap coefficient is determined "exactly," the error increases with path length, but at a slow rate; the error also increases with temperature. Since the method is exact, the error comes only from numerical inaccuracies in the evaluation of *k*-distributions. For the new MSFSK implementation, in which the assumption of uncorrelated absorption coefficients between species is introduced, the error also increases with path length, but the variation with path length and temperature is not monotonic and smooth. This error comes from two sources: one is the error introduced by the uncorrelated-absorption-coefficient assumption (Fig. 2), which is weighted by the Planck function; the other is the numerical error introduced by assembling the LHS and RHS of Eq. (31) from narrow-band data. Overall, the error using the new MSFSK implementation is equivalent to the error using the original MSFSK method, proving the new scheme's validity.

2.5 Overlap Coefficient λ_m. Figures 4 and 5 show the $\lambda_m - k_m$ relations of CO_2 and of H_2O for the same homogeneous binary mixture as used in Fig. 3. As seen from Eq. (10), λ_m is the sum of k_m and the contribution from overlap with all other scales, i.e., $\lambda_m > k_m$ always. For example, Fig. 4 shows the overlap coef-

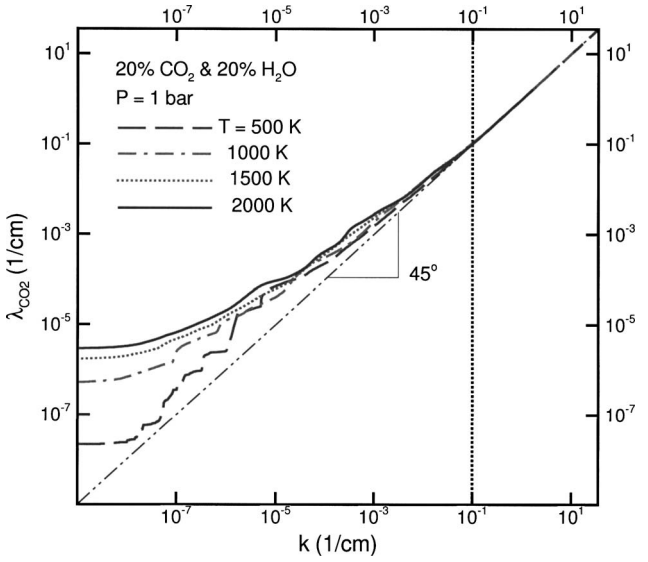

Fig. 4 $\lambda_m - k_m$ relation for CO_2

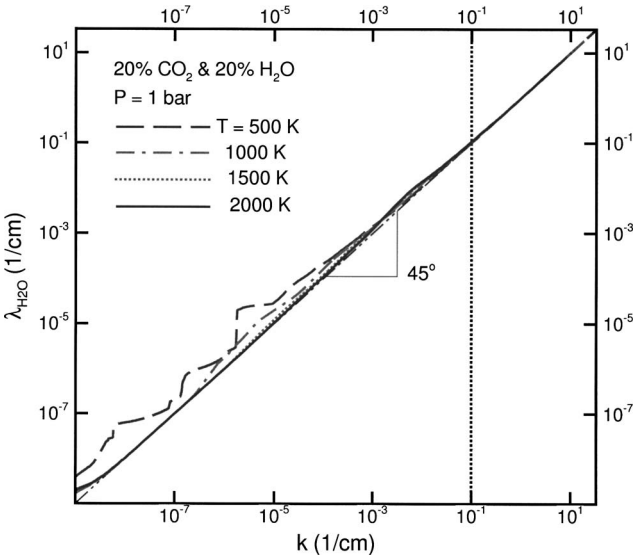

Fig. 5 $\lambda_m - k_m$ relation for H_2O

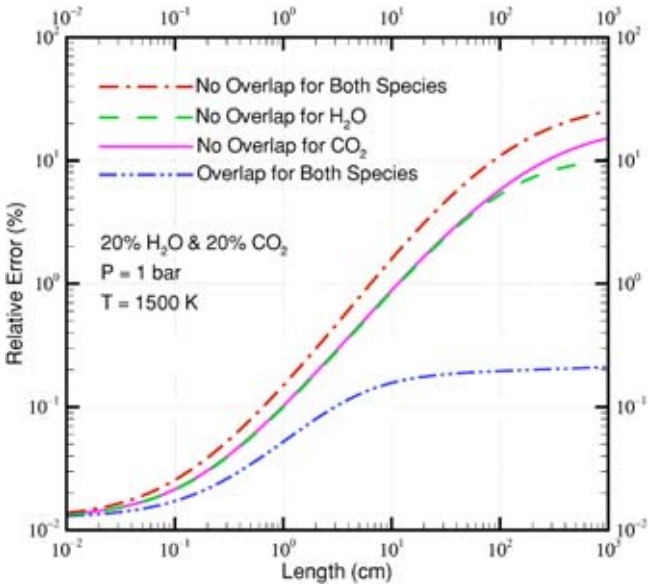

Fig. 6 Importance of neglect of overlap for one or all scales

ficient λ for CO_2 as the *k*-distribution of CO_2 plus the overlap contribution from H_2O. Both figures show that overlap is appreciable for *k*-values less than about 0.1 cm^{-1} and becomes more and more prominent as *k*-values decrease. This is understood by realizing that overlap occurs mostly in the wings of spectral lines. It is seen that the λ for CO_2 increases with temperature, since more and more spectral lines appear at elevated temperatures. The λ for H_2O, however, decreases with temperature. It is known that H_2O spectral lines exist almost everywhere across the entire spectrum, while CO_2 spectral lines occupy only small parts (bands) of the spectrum. At high temperatures the spectrum becomes more and more populated while the spectral lines become narrower and narrower. The portion of the H_2O spectrum that is overlapped by CO_2 apparently becomes smaller and smaller, as indicated in the figure. It is tempting to consider that for H_2O the overlap with other gases may be neglected within certain tolerance limits.

To explore the idea of neglecting overlap for H_2O, the same calculation as in Fig. 3 is performed but with overlap turned off for one or both scales (gases). The results for a mixture temperature of 1500 K are shown in Fig. 6. Even though $\lambda_{H_2O} \approx k$ (Fig. 5), not considering overlap for H_2O produces almost the same error than not considering overlap for CO_2, and is even larger at large path lengths. The explanation is found in Fig. 7, in which the *k*-*g* and λ-*g* distributions for H_2O and CO_2 are plotted for the same condition. The absorption coefficient of H_2O is much larger than that of CO_2 for a large part of *g*-space, making the small overlap in the H_2O equation more important than the overlap in CO_2.

Figure 6 also shows that the error by neglecting overlap from one or the other gas is less than about 1% for path lengths less than 10 cm, but then increases dramatically with path length. This was expected since, for path lengths less than 10 cm, the gas mixture is optically thin at nearly all wavelengths.

3 Sample Calculations

In the original development of the MSFSK method several sample calculations were conducted to demonstrate the performance of the MSFSK method. The present purpose is to improve the efficiency and convenience of the MSFSK method, by evaluating overlap coefficients and *k*-distributions from a narrow-band *k*-distribution database. In particular, we want to emphasize the accuracy of the MSFSK method in dealing with inhomogeneous media with strong partial pressure variations, i.e., in situations where the (single scale) FSK method encounters large errors. Therefore, two one-dimensional sample calculations are considered, one with step changes in species mole fraction, the other with step changes in both species mole fraction and mixture temperature.

Both sample calculations consider a mixture of CO_2–H_2O–N_2 confined between two cold, black walls. The mixture is at a total pressure of 1 bar and consists of two different homogeneous layers (denoted as left and right layer/column). The left layer has a fixed width of $L_L = 50$ cm, and the right layer a variable width of L_R. The radiative heat flux leaving from the right layer is calculated. Five methods are used to calculate the exiting flux: The LBL, FSK (using both the correlated-*k*, FSCK, and the scaled-*k*, FSSK, approaches), and MSFSK (using correlated-*k*, both, with the overlap coefficient calculated directly from the spectral database, MSFSKdir, and calculated from a narrow-band database, MSFSKnb) methods. In the LBL calculations, the HITEMP and CDSD spectral databases are used for the absorption coefficients of H_2O and CO_2, respectively. In the FSK calculations, the *k*-*g* distributions are constructed directly from the spectral databases;

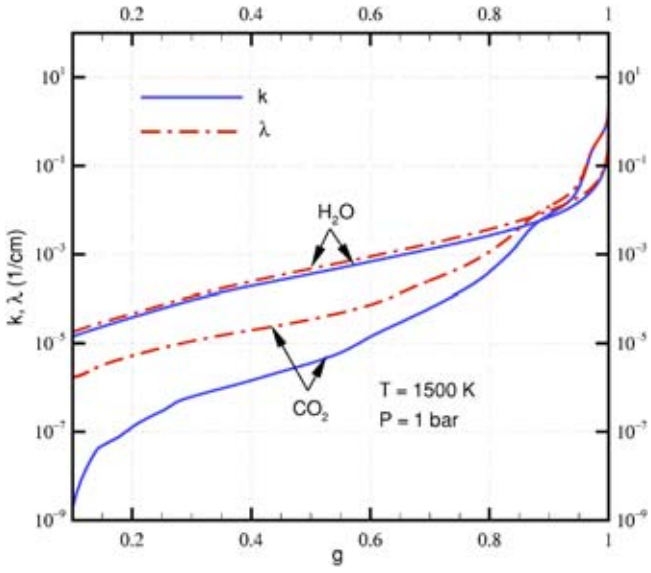

Fig. 7 *k*-*g* and λ-*g* distributions for water and carbon dioxide

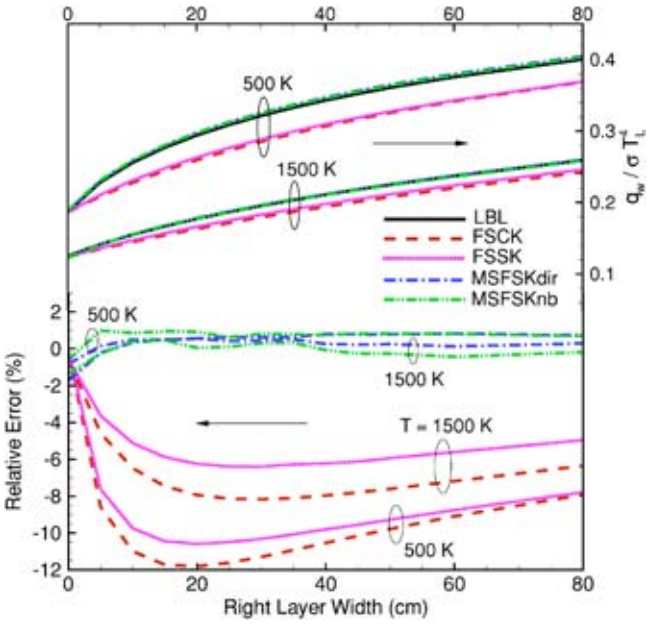

Fig. 8 Relative errors of the FSCK, FSSK, MSFSKdir, and MSFSKnb calculations for step changes in mole fraction, left layer: 20% CO_2 and 2% H_2O, right layer: 2% CO_2 and 20% H_2O

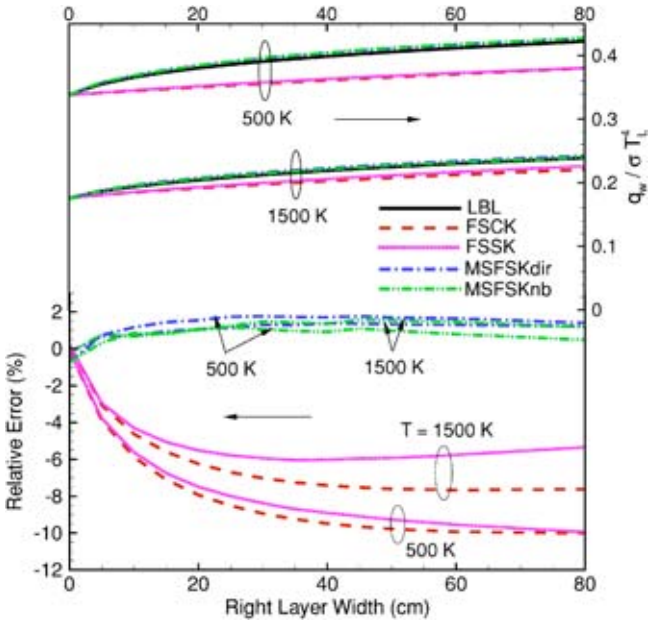

Fig. 9 Relative errors of the FSCK, FSSK, MSFSKdir, and MSFSKnb calculations for step changes in mole fraction, left layer: 2% CO_2 and 20% H_2O, right layer: 20% CO_2 and 2% H_2O

the reference states and the scaling functions are determined according to the formulas in Modest and Zhang [7]. Both correlated-*k* and scaled-*k* FSK approaches are employed since, while a little more cumbersome to use, FSSK generally performs better than FSCK. While both approaches can also be applied to the MSFSK methods, Zhang and Modest [22] have shown that scaled-*k* loses its advantages if multiple scales are used. Thus, only correlated-*k* is considered for the present MSFSK examples; for the MSFSKdir calculations the overlap coefficients (and *k*-distributions) are obtained directly from HITEMP and CDSD; for the MSFSKnb calculation the overlap coefficients and *k*-distributions are obtained from narrow-band *k*-*g* distributions read from the NB *k*-*g* database of Wang and Modest [18]. A ten point Gaussian quadrature scheme is used for the spectral integrations in all FSCK, FSSK, MSFSKdir, and MSFSKnb calculations.

In the first example, the temperatures of both layers (T_L and T_R) are set equal, but the species mole fractions change sharply: the left layer contains 20% CO_2 and 2% H_2O, while the right layer has 2% CO_2 and 20% H_2O. The nondimensional heat flux exiting from the right layer is plotted in the upper half of Fig. 8 as a function of the right layer width (i.e., the optical thickness of the right layer). The figure includes the results for two mixture temperatures (1500 and 500 K). The heat flux increases with increasing the thickness of the right layer as the emission from the right layer builds up. The MSFSK results follow the LBL calculations closely, while the FSK methods show significant departures. The relative errors of the FSCK, FSSK, MSFSKdir, and MSFSKnb calculations compared to LBL calculations are shown in the lower half of the figure. For the case of homogeneous temperature with strongly inhomogeneous gas concentration, the MSFSK method gives errors less than 1% with 10 quadrature points (and, thus, RTE evaluations) for various optical thicknesses, while the FSCK and FSSK methods reach errors of 10%–12%. As the width of the right layer increases, the FSCK and FSSK errors decrease, indicating that emission from the homogeneous right layer becomes dominant, and that limit can be predicted exactly by the FSCK and FSSK methods. In Fig. 9, the compositions of the two layers are switched (i.e., 2% CO_2 and 20% H_2O in the left layer and 20% CO_2 and 2% H_2O in the right layer). Again, the MSFSK method gives errors less than 2% for all optical thicknesses. This sample calculation demonstrates that in this extreme case of inhomogeneous gas concentration (partial pressure) discontinuities, the accuracy of the MSFSK method rivals that of LBL calculations, and that the new scheme of using narrow-band *k*-distributions for the evaluation of overlap coefficients is successful.

In the second example, in addition to a step change in species mole fraction, a step change in mixture temperature is introduced. The temperature of the left layer is set to 1500 K, and the right layer to 500 K, with the same mixture as given in Fig. 8, that is, 20% CO_2 and 2% H_2O in the left hot layer and 2% CO_2 and 20% H_2O in the right cold layer. Thus, in this example the absorption coefficients of both layers is uncorrelated due to, both, species concentration and temperature effects. Heat flux leaving the right layer is now due to emission by the left hot layer, which is attenuated by the (strongly uncorrelated) right layer. The nondimensional heat fluxes calculated by the LBL, FSCK, FSSK, MSFSKdir, and MSFSKnb methods are shown in Fig. 10 against the width of the right layer. In the MSFSK calculations, the reference states are determined separately for each scale. The heat flux decreases with increasing width of the right absorption layer. For this extreme case of strong inhomogeneity in both species concentration and temperature, the FSCK and FSSK methods fail completely, while the present MSFSK method, although designed for just dealing with strong inhomogeneities in gas concentration, has a maximum error of only about 12% with 10 quadrature points for various optical thickness. The difference between MSFSKdir and MSFSKnb calculations is small, indicating that the new scheme of using a database of narrow-band *k*-distributions to evaluate overlap coefficients is robust.

The error from the present MSFSK method can be mostly attributed to the temperature inhomogeneity and the uncorrelatedness it causes. To highlight this, the mole fraction step changes in Fig. 10 were removed and the same calculations were performed again for constant concentrations throughout. Figure 11 shows the nondimensional heat fluxes calculated by the LBL, FSCK, and MSFSKnb methods for two homogeneous compositions. The differences between MSFSK and LBL calculations are similar to those in Fig. 10, in which mole fraction inhomogeneities are also present. Furthermore, it can be seen that, in addition to greatly reducing the error caused by mole fraction inhomogeneities (com-

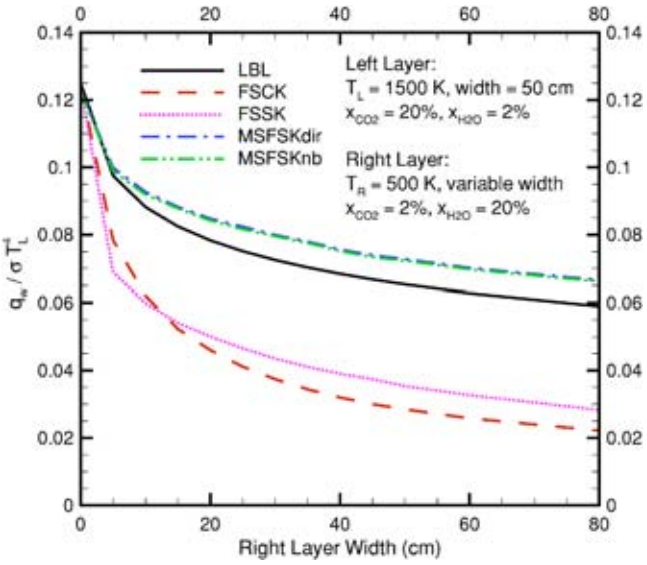

Fig. 10 Nondimensional heat flux leaving an inhomogeneous medium with step changes in species mole fraction and temperature

paring Figs. 10 and 11), the MSFSK approach (breaking up a gas mixture into gas scales) also reduces the error caused by temperature inhomogeneities: The absorption coefficient of a single gas specie is more correlated than that of a mixture that combines the spectral lines from different species. The MSFSK error can be further reduced by breaking up each gas scale into subscales to remedy temperature-caused uncorrelatedness ("hot lines"), by grouping the spectral lines of each gas according to their temperature dependencies [6,9,14]. Such breaking up into subscales in the framework of a narrow-band *k*-distribution database will be addressed in future work.

4 Summary and Conclusions

A new scheme has been developed and validated for the evaluation of the overlap coefficient in the multiscale full-spectrum *k*-distribution (MSFSK) method applied to inhomogeneous gas mixtures with each component gas treated as one scale. The new scheme exploits the uncorrelatedness of absorption coefficients of different gas species on the narrow-band level, and therefore, facilitate the use of narrow-band *k*-distributions. This enables the MSFSK method to be employed efficiently and conveniently in practical applications. The newly formulated MSFSK method was tested by performing radiation calculations in media with strong inhomogeneities in species mole fraction and in temperature. It was found that at isothermal conditions, the MSFSK approach essentially obtains line-by-line accuracy for inhomogeneous mixtures with extreme variations in gas concentration by treating each individual gas specie as one scale. It was also found that treating each individual gas specie as an independent scale reduces the errors caused by temperature inhomogeneities.

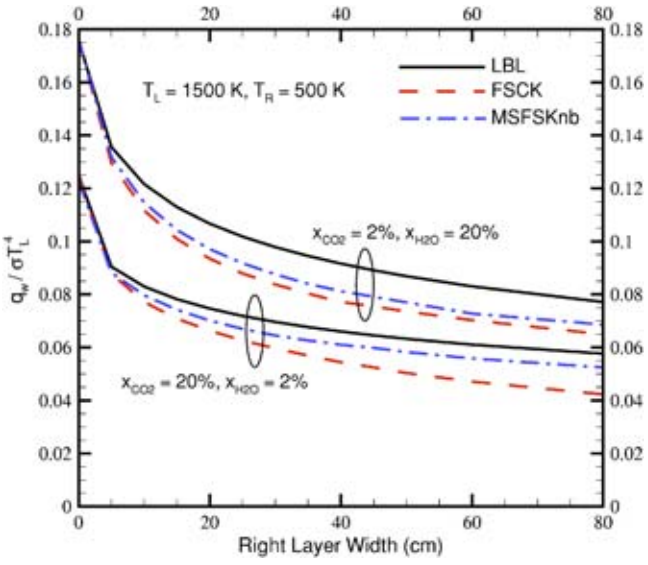

Fig. 11 Nondimensional heat flux leaving an inhomogeneous medium with step changes in temperature only

Acknowledgment

This research has been sponsored by National Science Foundation under Grant Nos. CTS-0121573 and CTS-0112423.

Nomenclature

a = stretching factor for FSK method
f = *k*-distribution function, cm
g = cumulative *k*-distribution
H = Heaviside step function
I = radiative intensity, W/m^2sr
k = absorption coefficient variable, cm^{-1}
k^* = overlap parameter defined in Eq. (14)
L = geometric length, cm
M = total number of scales
P = pressure, bar
q = radiative heat flux, W/m^2
Q = quantity defined by Eq. (23)
s = distance along path, m
T = temperature, K
x, $\underline{x}$ = mole fraction (vector)
$\mathcal{L}$ = Laplace transform

Greek Symbols

η = wave number, cm^{-1}
$\underline{\phi}$ = composition variable vector
δ = Dirac's delta function
$\Delta\eta$ = spectral interval, cm^{-1}
λ = overlap coefficient defined in Eq. (10), cm^{-1}
κ = absorption coefficient, cm^{-1}
σ = Stefan–Boltzmann constant

Subscripts

0 = reference condition
b = blackbody emission
i = *i*th narrow band
L = left layer
m = *m*th scale
R = right layer
w = wall
η = spectral in wavenumber space
g = spectral in g space

References

[1] Lacis, A. A. and Oinas, V., 1991, "A Description of the Correlated-*k* Distribution Method for Modeling Nongray Gaseous Absorption, Thermal Emission, and Multiple Scattering in Vertically Inhomogeneous Atmospheres," J. Geophys. Res., **96**(D5), pp. 9027–9063.

[2] Goody, R. M. and Yung, Y. L., 1989, *Atmospheric Radiation—Theoretical Basis*, Oxford University Press, New York, 2nd ed.

[3] Denison, M. K. and Webb, B. W., 1993, "A Spectral Line Based Weighted-Sum-of-Gray-gases Model for Arbitrary RTE Solvers," ASME J. Heat Transfer, **115**, pp. 1004–1012.

[4] Denison, M. K. and Webb, B. W., 1995, "The Spectral-Line-Based Weighted-Sum-of-Gray-Gases Model in Nonisothermal Nonhomogeneous Media," ASME J. Heat Transfer, **117**, pp. 359–365.

[5] Rivière, Ph., Soufiani, A., Perrin, M. Y., Riad, H., and Gleizes, A., 1996, "Air

Mixture Radiative Property Modelling in the Temperature Range 10,000–40,000 K," J. Quant. Spectrosc. Radiat. Transf., **56**, pp. 29–45.
[6] Pierrot, L., Rivière, Ph., Soufiani, A., and Taine, J., 1999, "A Fictitious-gas-based Absorption Distribution Function Global Model for Radiative Transfer in Hot Gases," J. Quant. Spectrosc. Radiat. Transf., **62**, pp. 609–624.
[7] Modest, M. F. and Zhang, H., 2002, "The Full-Spectrum Correlated-*k* Distribution For Thermal Radiation from Molecular Gas-Particulate Mixtures," ASME J. Heat Transfer, **124**(1), pp. 30–38.
[8] Modest, M. F., 2003, "Narrow-Band and Full-Spectrum *k*-Distributions for Radiative Heat Transfer-Correlated-*k* Versus scaling approximation," J. Quant. Spectrosc. Radiat. Transf., **76**(1), pp. 69–83.
[9] Zhang, H. and Modest, M. F., 2002, "A Multi-Scale Full-Spectrum Correlated-*k* Distribution For Radiative Heat Transfer in Inhomogeneous Gas Mixtures," J. Quant. Spectrosc. Radiat. Transf., **73**(2-5), pp. 349–360.
[10] Zhang, H. and Modest, M. F., 2003, "Scalable Multi-Group Full-Spectrum Correlated-*k* Distributions For Radiative Heat Transfer," ASME J. Heat Transfer, **125**(3), pp. 454–461.
[11] Modest, M. F. and Riazzi, R. J., 2004, "Assembly of Full-Spectrum *k*-Distributions From a Narrow-Band Database; Effects of Mixing Gases, Gases and Nongray Absorbing Particles, and Mixtures with Nongray Scatterers in Nongray Enclosures," J. Quant. Spectrosc. Radiat. Transf., **90**(2), pp. 169–189.
[12] Goody, R. M., West, R., Chen, L., and Crisp, D., 1989, "The Correlated *k* Method for Radiation Calculations in Nonhomogeneous Atmospheres," J. Quant. Spectrosc. Radiat. Transf., **42**, pp. 539–550.
[13] Fu, Q. and Liou, K. N., 1992, "On the Correlated *k*-Distribution Method for Radiative Transfer in Nonhomogeneous Atmospheres," J. Atmos. Sci., **49**(22), pp. 2139-2156.
[14] Rivière, P., Soufiani, A., and Taine, J., 1992, "Correlated-*k* and Fictitious Gas Methods for H_2O near 2.7 μm," J. Quant. Spectrosc. Radiat. Transf., **48**, pp. 187–203.
[15] Rivière, P., Scutaru, D., Soufiani, A., and Taine, J., 1994, "A New $c-k$ Data Base Suitable from 300 to 2500 K for Spectrally Correlated Radiative Transfer in CO_2–H_2O Transparent Gas Mixtures," in *Tenth International Heat Transfer Conference*, Taylor & Francis, pp. 129–134.
[16] Rivière, P., Soufiani, A., and Taine, J., 1995, "Correlated-*k* and Fictitious Gas Model for H_2O Infrared Radiation in the Voigt Regime," J. Quant. Spectrosc. Radiat. Transf., **53**, pp. 335–346.
[17] Modest, M. F., 2003, *Radiative Heat Transfer*, Academic Press, New York, 2nd ed.
[18] Wang, A. and Modest, M. F., 2005, "High Accuracy, Compact Database of Narrow-Band *k*-Distributions for Water Vapor and Carbon Dioxide," J. Quant. Spectrosc. Radiat. Transf., **93**(1–3), pp. 245–261.
[19] Taine, J. and Soufiani, A., 1999, "Gas IR Radiative Properties: From Spectroscopic Data to Approximate Models," in *Advances in Heat Transfer*, 33, Academic Press, New York, pp. 295–414.
[20] Rothman, L. S., Camy-Peyret, C., Flaud, J.-M., Gamache, R. R., Goldman, A., Goorvitch, D., Hawkins, R. L., Schroeder, J., Selby, J. E. A., and Wattson, R. B., 2000, "HITEMP, the High-Temperature Molecular Spectroscopic Database," available through http://www.hitran.com.
[21] Tashkun, S. A., Perevalov, V. I., Bykov, A. D., Lavrentieva, N. N., and Teffo, J.-L., 2002, "Carbon Dioxide Spectroscopic Databank (CDSD)," available from ftp://ftp.iao.ru/pub/CDSD-1000.
[22] Zhang, H. and Modest, M. F., 2003, "Multi-Group Full-Spectrum *k*-Distribution Database For Water Vapor Mixtures in Radiative Transfer Calculations," Int. J. Heat Mass Transfer, **46**(19), pp. 3593–3603.

N. M. Rao[1]
e-mail: nmuralidhararao@yahoo.com
Department of Mechanical Engineering,
Dr. Babasaheb Ambedkar Technological University,
"Vidyavihar," Lonere-402 103 Maharashtra State, India

B. Maiti
e-mail: bmaiti@mech.iitkgp.ernet.in

P. K. Das
e-mail: pkd@mech.iitkgp.ernet.in

Indian Institute of Technology, Kharagpur,
Kharagpur-721 302, West Bengal, India

Stability Behavior of a Natural Circulation Loop With End Heat Exchangers

The present investigation describes the stability behavior of NCL with end heat exchangers. The one-dimensional transient conservation equations of the loop fluid and the two fluid streams of cold end and hot end heat exchangers are solved simultaneously using the finite element program. For the stability analysis the loop response is found for an imposed finite perturbation to the loop circulation rate. Though the stability may depend on the number of parameters, variation of two nondimensional parameters, namely C_h^* *and* Gr_L*, is studied. Selecting the specific combinations of the above two parameters three different cases of stability, namely, stable, neutrally stable, and unstable, are demonstrated. The stability behavior is scanned over a wide range of* C_h^* *and* Gr_L *values and the stability envelope is also constructed.* [DOI: 10.1115/1.1924569]

Keywords: stability, natural circulation loop, end heat exchangers, finite element method

Introduction

In the most common configuration of natural circulation loops (NCLs), the loop fluid flow is driven by thermally generated density gradient so that a pump is not required. The generation of density gradient is caused by temperature variations of fluid due to simultaneous heating and cooling at different parts of the loop. The loops are often heated from below and cooled from above, which then establishes stable density gradient in the fluid. Side heating and cooling are also common configurations. Under the influence of gravitational force the lighter fluid rises and heavier fluid falls. Under the stable operation of the loop the fluid experiences a continuous unidirectional flow through the loop. As these loops do not require any auxiliary power they can be designed as highly reliable and self-contained systems. They find wide applications in varied engineering systems, ranging from low capacity boilers and micro-coolers to large nuclear power plants and space heat sinks.

As the flow in a NCL is self-developed and not known a priori, its designs possess a challenging problem of coupled momentum and energy transfer. Stability analysis becomes an essential and unavoidable issue in the design of NCLs in order to maintain its reliability and keep it in smooth operation. It mainly highlights the system's strange characteristics, which comes from neither steady-state nor transient analysis. One can find an adequate literature and growing interest on stability analysis of NCLs having various configurations and operating conditions.

The earliest reported observation of free convection instability for a near critical fluid was made by Schmidt et al. [1] using pressurized ammonia. This unexpected behavior was later observed for other near critical fluids in free convection loops, first by Holman and Boggs [2] for Freon-12 and then by Van Putte [3] for water. Harden [4] and Cornelius [5] specifically studied instabilities of near critical Freon-114 in free convection loops. The references cited above treated only the instabilities encountered in the vicinity of the critical point. In each of these cases it was assumed that the instability was caused by the large fluid property variations in this region. Further, Alstad et al. [6] measured the transient response of a free convection loop containing ordinary water and did not observe any instability.

The stability studies of the steady-state motion by Keller [7] and Welander [8] for the simple geometry (rectangular shape) consisting of a point heat source and sink with two vertical branches was a very informative model. They had shown analytically that loop flow instabilities could occur in the absence of inertial effects, merely requiring an interplay between frictional and buoyancy forces. On the basis of these analyses instabilities should exist under certain conditions for ordinary fluids, as well as near critical fluids, even though one may not intuitively expect them. Further, Welander [8] provided a plausible argument to explain the existing unstable situation. Creveling et al. [9] considered a toroidal loop and demonstrated, experimentally and theoretically the presence and importance of the instabilities. The loop was heated continuously by a constant heat flux over the bottom half of its area and cooled continuously over the top half. He found that there were two ranges of heat input in which the system was stable: A low heat input range in which the flow appeared laminar, and a high heat input range which was accompanied by turbulent flow. At intermediate values of the heating the flow was unstable. He strongly defended the argument of Welander [8] regarding the origin of instability. Greif et al. [10] carried out a numerical study on stability behavior of a toroidal. They carried out the study based on the finite difference method using the steady-state temperature distributions and small perturbations from the steady-state values of the velocity as initial condition.

Later, Mertol et al. [11] studied the stability of a toroidal loop with similar heating and cooling modes as stated earlier. In this study they investigated the effect of constant and continuous addition and withdrawal of loop fluid, which was one type of open loop. Interestingly, this work revealed another type of instability (metastable) where the model had multiple solutions (double or triple) for a certain range of systems and through flow parameters. The existence of multiple solutions was also observed by Damerell and Schoenhals [12] for a toroidal asymmetrical loop and by Zvirin [13] for the vertical loop with a point heat source and a heat sink. Sen et al. [14] reported the transient and stability behavior of a toroidal loop with known heat flux over the whole loop. Hart [15] developed a model for a flow in a toroidal loop with the inclusion of soret effect and also studied (Hart [16]) the complex oscillations in a closed tubular thermosyphon. Control of the chaotic nature in a thermal convection (torodial) loop was

[1]Corresponding author.

Contributed by the Heat Transfer Division for publication in the JOURNAL OF HEAT TRANSFER. Manuscript received April 30, 2004. Final manuscript received January 10, 2005. Review conducted by: N. K. Annand.

studied by Singer et al. [17] and Wang et al. [18]. Other studies by Japikse [19], Sen et al. [20], Bernier and Baliga [21] and review articles by Zvirin [22], Mertol and Greif [23], and Greif [24] should also be noted.

The references cited above refer to closed toroidal loops, however, adequate information was also available on open thermosyphons. Torrance [25] studied the steady flow and heat transfer in an open geothermal system where the inlet and outlet were at boundary of the medium. The transient and steady behavior of an open, symmetrically heated, free convection loop was reported by Bau and Torrance [26]. In their study they considered a U-shaped loop with adiabatic vertical legs connected to an isothermal reservoir, which was open to the atmosphere. Heating was provided at the lower segment of the loop. In another study, Bau and Torrance [27] carried out both the theoretical and experimental study on the stability analysis of an asymmetrically heated open convection loop. The difference of the later from the earlier work was that the horizontal leg and one of the vertical legs were subjected to different heat transfer rates. The effect of viscous dissipation on free convection loops was also studied by Zvirin [28] and Bau and Torrance [29]. Loops of different geometrical configurations such as figure of eight (Vijayan et al. [30]) and triangular in the study of thermosiphon-based PCR reactor by Chen et al. [31] were also considered. Little work could be seen on rectangular closed configuration (Huang and Zelaya [32], Vijayan [33], Nayak et al. [34], and Fichera and Pagano [35]). Huang and Zelaya [32] studied the heat transfer behavior of a rectangular thermosyphon loop whereas Vijayan [33] studied theoretically and experimentally the steady state and stability behavior of nonuniform diameter single phase rectangular NCL. In recent times efforts were also made to simulate NCLs based on two-dimensional (2D) and three-dimensional (3D) formulation. Chen et al. [31] 3D formulation for the analysis of PCR reactor is worth mentioning.

In most of the above investigations toroidal geometry was considered. Only a few of the investigations were based on rectangular configuration. However, in all these investigations heat exchange was assumed to take place either by constant heat flux or constant wall temperature. However, a number of practical systems deviate from these idealizations. For example, in most of the chemical plants due to their typical plant design or process requirement, the transfer of thermal energy from hot fluid stream to cold fluid stream is not possible since these two fluids cannot be brought together to their closed proximity. In this situation, the transfer of thermal energy is still possible through an intermediate fluid passing through a closed loop. Generally, closed loop would be a rectangular configuration having two heat exchangers located at different places for exchanging the heat from hot fluid to cold fluid. Loop fluid circulation may be forced or due to thermal convection. If loop fluid flow is due to thermal convection then the loop would become a natural circulation loop (NCL) and heating and cooling would take place by hot and cold fluid streams with finite heat capacity rates. In some distinctive situations where the contamination of one fluid (hot–cold) to another (cold–hot) is a serious issue, and in waste heat recovery systems, a NCL with end heat exchangers is the only appropriate solution. Therefore, rectangular loops exchanging heat with flowing fluid streams in single phase are often designed. Stability of such loops is not studied in detail. Recently, Rao et al. [36,37] studied the steady-state performance of a rectangular NCL with end heat exchangers as well as its total and dynamic pressure variation under steady-state and transient conditions. However, so far no studies are taken up to analyze the stability behavior of the NCL with end heat exchangers. In the present work, the stability analysis of a vertical rectangular loop with end heat exchangers is described. Further, from this model one can also study the stability behavior of the hot and cold streams (i.e., exit temperatures) along with that of the loop.

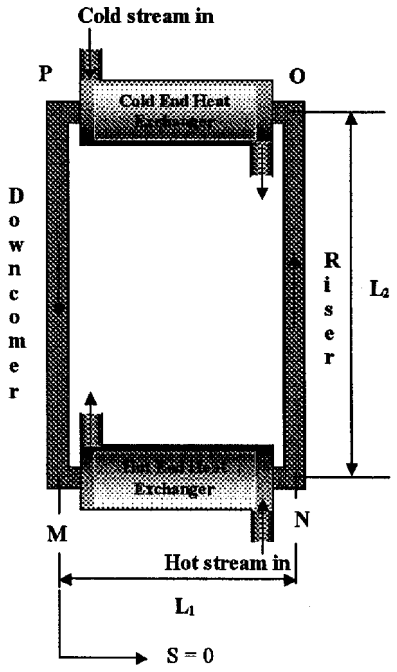

Fig. 1 Schematic diagram of a NCL with end heat exchangers

Theoretical Formulation

A schematic diagram of the NCL with end heat exchangers considered for the present study is shown in Fig. 1. The natural circulation system is idealized as a vertical rectangular loop with constant cross-sectional area. The hot end heat exchanger (HEHE) is located at the bottom of the loop while the cold end heat exchanger (CEHE) is at the top as depicted in figure. During steady-state operation four prominent zones can be identified in the loop. The coupling fluid enters the bottom section (M–N) with a temperature T_{cf1} and density ρ_{cf1}. The fluid gets heated up while passing through the hot end heat exchanger by absorbing heat from the hot stream and leaves with temperature and density T_{cf2} and ρ_{cf2} ($T_{cf2} > T_{cf1}$ and $\rho_{cf2} < \rho_{cf1}$), respectively. The lighter fluid ascends through the adiabatic riser (N–O) without changing its density. While flowing through the top section (O–P) the coupling fluid rejects heat to the cold stream and finally attains a temperature T_{cf1}. A downward flow of the coupling fluid through the adiabatic downcomer (P–M) completes the circulation loop.

For the analysis of the loop following assumptions may be made.

- The hot and cold stream heat capacity rates remain constant.
- The over-all heat transfer coefficients and the surface area per unit length for the heat exchangers are constant throughout their length.
- The thermal properties of all the fluid streams are uniform and constant.
- Density of the coupling fluid is a linear function of its temperature.
- The density variation in the coupling fluid is considered only in the body force term (Boussinesq approximation).
- For the transient analysis, it is assumed that flow inside the loop is turbulent and the friction factor is a sole function of Reynolds number.
- Flow at a cross section is well mixed so that there is no variation of temperature and velocity. Variations only along the loop length are considered.
- The wall capacitance is neglected.
- No heat is conducted along the axial directions of the three fluids and the viscous dissipation is neglected.

- Vertical limbs (riser and downcomer) are adiabatic.
- Minor losses due to bends and fittings are neglected.

Based on the above idealizations following conservation equations may be written.

As the velocity depends only on time, the continuity equation may be written for the incompressible flow of the coupling fluid as

$$u_{cf} = u_{cf}(t). \tag{1}$$

The momentum equation for a differential fluid element inside the loop can be written as

$$\frac{\partial P}{\partial s} = -\left[\rho_{cf}\frac{\partial u_{cf}}{\partial t} + \rho_{cf} g \sin\phi + \frac{2C_f \rho_{cf} u_{cf}^2}{D}\right]. \tag{2}$$

One can now introduce a functional relationship between friction factor, C_f, and Reynolds number, Re, in the following form,

$$C_f = a\,\mathrm{Re}^{-b} \tag{3}$$

where "a" and "b" are constants. Relationship of this form is valid over a wide range of Reynolds number covering both laminar and turbulent regions. However, the constants have different values for these two regions. Incorporating the relationship for friction factor in the differential momentum equation, one gets

$$\frac{\partial P}{\partial s} = -\left[\rho_{cf}\frac{\partial u_{cf}}{\partial t} + \rho_{cf} g \sin\phi + \frac{2a\mu_{cf}^{b}\rho_{cf}^{1-b}}{D^{1+b}} u_{cf}^{2-b}\right]. \tag{4}$$

The density variation in the body force term may be assumed a linear function of temperature (Greif et al. [10], Zvirin and Greif [38], and Mertol et al. [39])

$$\rho_{cf} = \rho_0[1 - \beta(T_{cf} - T_0)] \tag{5}$$

Integrating Eq. (4) around the loop and substituting Eq. (5) in the body force term, one gets the momentum equation in an integral form

$$\frac{2(L_1+L_2)}{(A_s c)_{cf}}\frac{\partial C_{cf}}{\partial t} + \frac{4a\mu_{cf}^{b}(L_1+L_2)}{\rho_{cf}(A_s c)_{cf}^{2-b}} C_{cf}^{2-b} + \rho_0 g\beta\left[\int_{(2L_1+L_2)}^{2(L_1+L_2)} T_{cf}\,ds - \int_{L_1}^{(L_1+L_2)} T_{cf}\,ds\right] = 0 \tag{6}$$

where "$C_{cf}=c\rho_{cf}u_{cf}A_s$" is coupling fluid heat capacity rate.

The energy balance for the hot stream and the coupling fluid can be derived considering a differential element (Δs) of HEHE of the NCL [Fig. 2(a)] in Eqs. (7) and (8)

$$\frac{\partial T_h}{\partial t} - u_h\frac{\partial T_h}{\partial s} + \frac{(UA)_h}{(\rho A_s c)_h L_1}(T_h - T_{cf}) = 0 \quad 0 \leqslant s \leqslant L_1 \tag{7}$$

$$\frac{\partial T_{cf}}{\partial t} + u_{cf}\frac{\partial T_{cf}}{\partial s} + \frac{(UA)_h}{(\rho A_s c)_{cf} L_1}(T_{cf} - T_h) = 0 \quad 0 \leqslant s \leqslant L_1 \tag{8}$$

Similarly, the energy balance of the cold stream and the coupling fluid inside CEHE [Fig. 2(b)] can be expressed in Eqs. (9) and (10), respectively,

$$\frac{\partial T_c}{\partial t} - u_c\frac{\partial T_c}{\partial s} + \frac{(UA)_c}{(\rho A_s c)_c L_1}(T_c - T_{cf}) = 0$$

$$(L_1 + L_2) \leqslant s \leqslant (2L_1 + L_2) \tag{9}$$

$$\frac{\partial T_{cf}}{\partial t} + u_{cf}\frac{\partial T_{cf}}{\partial s} + \frac{(UA)_c}{(\rho A_s c)_{cf} L_1}(T_{cf} - T_c) = 0$$

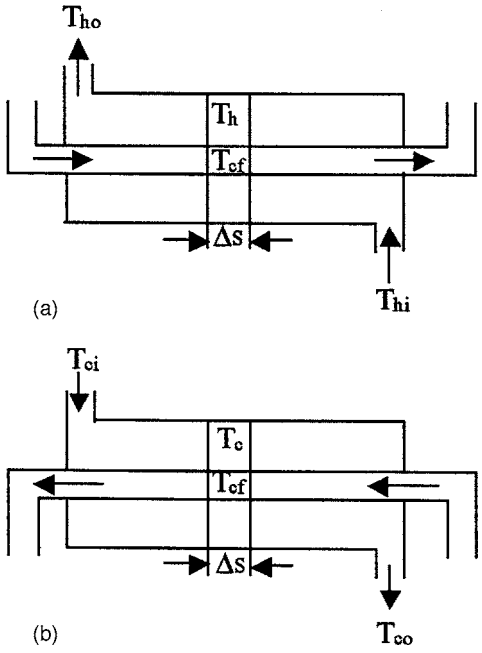

Fig. 2 Schematic diagrams of end heat exchanger of NCL: (*a*) hot end heat exchanger (HEHE), (*b*) cold end heat exchanger (CEHE)

$$(L_1 + L_2) \leqslant s \leqslant (2L_1 + L_2) \tag{10}$$

The energy equation can be written for the coupling fluid within a differential element (Δs) of the fluid in the adiabatic riser and downcomer in the following form:

$$\frac{\partial T_{cf}}{\partial t} + u_{cf}\frac{\partial T_{cf}}{\partial s} = 0 \quad L_1 \leqslant s \leqslant (L_1 + L_2) \text{ and}$$

$$(2L_1 + L_2) \leqslant s \leqslant 2(L_1 + L_2) \tag{11}$$

The only boundary conditions needed to analyze the loop performance are the inlet temperatures of the hot and cold streams. They may be specified as follows:

$$T_h(s,t) = T_h(t), \quad \text{at } s = L_1 \quad \text{i.e., at a station "}N\text{"} \tag{12}$$

$$T_c(s,t) = T_{ci}(t), \quad \text{at } s = (2L_1 + L_2) \quad \text{i.e., at a station "}P\text{"} \tag{13}$$

The initial conditions are

$$T_{h,c,cf}(s,0) = \text{constant (known temperature) at } s = s \text{ and } t = 0 \tag{14}$$

Momentum and energy equations along with the boundary conditions can be nondimensionalized by using the following substitutions:

$$C^*_{h,c,cf} = \frac{C_{h,c,cf}}{(\mu c D)_{cf}} \tag{15a}$$

where C_{cf}, C_h, and C_c are the heat capacity rates of coupling fluid, hot and cold fluid streams, respectively,

$$(UA)^*_{h,c} = \frac{(UA)_{h,c}}{(\mu c D)_{cf}} \tag{15b}$$

$$\theta_{h,c,cf} = \frac{(T_{h,c,cf} - T_{ci})}{(T_0 - T_{ci})} \tag{15c}$$

$$\tau = t\left[\left(\frac{\mu D}{\rho A_s}\right)_{cf}\frac{1}{L_1}\right] \tag{15d}$$

$$S = \frac{s}{L_1};\ K_1 = \frac{L_2}{L_1};\ K_2 = \frac{L_1}{D} \tag{15e}$$

$$Ntu^*_{h,c} = \frac{(UA)^*_{h,c}}{C^*_{h,c}} \tag{15f}$$

$$Gr_L = \frac{\rho_0^2 g\beta D^3(T_0 - T_{ci})}{\mu^2_{cf}} \tag{15g}$$

Using the above nondimensional parameters equations (6)–(11) can be represented as (16)–(21), respectively.

$$\frac{\partial C^*_{cf}}{\partial\tau} + \frac{\pi^b aK_2}{2^{2b-1}}(C^*_{cf})^{2-b} + \frac{\pi^2}{2^5}Gr_L K_2\frac{1}{(1+K_1)}\left[\int_{(K_1+2)}^{2(K_1+1)}\theta_{cf}dS - \int_1^{(K_1+1)}\theta_{cf}dS\right] = 0 \tag{16}$$

$$\frac{\partial\theta_h}{\partial\tau} - C^*_h R_h\frac{\partial\theta_h}{\partial S} + Ntu^*_h C^*_h R_h(\theta_h - \theta_{cf}) = 0 \tag{17}$$

$$\frac{\partial\theta_{cf}}{\partial\tau} + C^*_{cf}\frac{\partial\theta_{cf}}{\partial S} + Ntu^*_h C^*_h(\theta_{cf} - \theta_h) = 0 \tag{18}$$

$$\frac{\partial\theta_c}{\partial\tau} - C^*_c R_c\frac{\partial\theta_c}{\partial S} + Ntu^*_c C^*_c R_c(\theta_c - \theta_{cf}) = 0 \tag{19}$$

$$\frac{\partial\theta_{cf}}{\partial\tau} + C^*_{cf}\frac{\partial\theta_{cf}}{\partial S} + Ntu^*_c C^*_c(\theta_{cf} - \theta_c) = 0 \tag{20}$$

$$\frac{\partial\theta_{cf}}{\partial\tau} + C^*_{cf}\frac{\partial\theta_{cf}}{\partial S} = 0 \tag{21}$$

where $R_{h,c}=(\rho A_s c)_{cf}/(\rho A_s c)_{h,c}$ ratio of coupling fluid heat capacitance to hot–cold stream heat capacitance per unit length.

The boundary conditions become in nondimensional form as

$$\theta_h(S,\tau) = \theta_h(\tau), \quad \text{at } S = 1.0 \tag{22a}$$

$$\theta_c(S,\tau) = \theta_c(\tau), \quad \text{at } S = (K_1 + 2) \tag{22b}$$

The nondimensional initial conditions are

$$\theta_{h,c,cf}(S,\tau) = 0.0, \quad \text{at } \tau = 0 \tag{22c}$$

Methods of Solution

Steady-State Solution. Steady-state characteristics of the loop (the flow rate of the coupling fluid and the temperature distributions of all the three fluid streams) can be obtained solving Eqs. (16)–(21) putting the time derivative equal to zero ($\partial/\partial\tau=0$). Two boundary conditions namely, inlet temperatures of the hot and cold streams are specified in nondimensional form. These are

$$\theta_{hi} = 1.0, \tag{23a}$$

$$\text{and } \theta_{ci} = 0.0. \tag{23b}$$

Under the steady state, Eqs. (16)–(21) will reduce to a set of five coupled algebraic equations and they can be solved using a suitable iterative guess-and-correct procedure as explained in Rao [40]. These steady-state equations are:

$$C^*_{cfSS} = \left[NGr_L\frac{K_1}{(1+K_1)}[\theta_{cf2} - \theta_{cf1}]\right]^{1/(2-b)} \quad \text{for steady-state coupling fluid} \tag{24}$$

$$\theta_{cf2} = \theta_{cf1} + \left\{[1 - \theta_{cf1}]\frac{C^*_{\min,h}}{C^*_{cf}}\varepsilon^*_h\right\} \quad \text{for riser temperature} \tag{25}$$

$$\theta_{cf1} = \theta_{cf2}\left[1 - \frac{C^*_{\min.c}}{C^*_{cf}}\varepsilon^*_c\right] \quad \text{for downcomer temperature} \tag{26}$$

The outlet temperatures of hot and cold fluid streams are obtained from the following equations:

$$\theta_{ho} = \left[\theta_{hi} - \frac{C^*_{cf}}{C^*_h}[\theta_{cf2} - \theta_{cf1}]\right] \tag{27}$$

$$\theta_{co} = \left[\theta_{ci} + \frac{C^*_{cf}}{C^*_c}[\theta_{cf2} - \theta_{cf1}]\right] \tag{28}$$

The temperature profile for coupling fluid is determined from the following equation:

$$\theta_{cfS} = \begin{cases} \left\{\dfrac{C^*_{\min,h}}{C^*_{cf}}\dfrac{\varepsilon_h{*}_S}{\left[1 - \dfrac{C^*_{\min,h}}{C^*_h}\varepsilon_h{*}_S\right]}\theta_{ho} + \theta_{cf1}\left[1 - \dfrac{C^*_{\min,h}}{C^*_{cf}}\dfrac{\varepsilon_h{*}_S}{\left[1 - \dfrac{C^*_{\min,h}}{C^*_h}\varepsilon_h{*}_S\right]}\right]\right\} \ldots\ \ldots\ \ldots 0 \leqslant S \leqslant 1.0 \\ \theta_{cf2} \ldots\ .\ 1.0 \leqslant S \leqslant (1.0 + K_1) \\ \left\{\dfrac{C^*_{\min,c}}{C^*_{cf}}\dfrac{\varepsilon_c{*}_S}{\left[1 - \dfrac{C^*_{\min,c}}{C^*_c}\varepsilon_c{*}_S\right]}\theta_{co} + \theta_{cf2}\left[1 - \dfrac{C^*_{\min,c}}{C^*_{cf}}\dfrac{\varepsilon_c{*}_S}{\left[1 - \dfrac{C^*_{\min,c}}{C^*_c}\varepsilon_c{*}_S\right]}\right]\right\} \ldots\ \ldots\ \ldots\ \ldots\ .\ (1.0 + K_1) \leqslant S \leqslant (2.0 + K_1) \\ \theta_{cf1} \ldots\ .\ .\ (2.0 + K_1) \leqslant S \leqslant 2.0(1.0 + K_1) \end{cases} \tag{29}$$

where $\varepsilon^*_{h,c\ S}=[1-e^{-Ntu^*_{h,c}(C^*_{h,c}/C^*_{\min,h,c})S(1-CR^*_{h,c})}]/[1-CR^*_{h,c}e^{-Ntu^*_{h,c}(C^*_{h,c}/C^*_{\min,h,c})S(1-CR^*_{h,c})}]$

Finally, hot and cold fluid streams temperature profiles along the respective heat exchangers are determined from the following two equations, respectively,

$$\theta_{hS} = \left[\frac{C^*_{cf}}{C^*_h} [\theta_{cfS} - \theta_{cf1}] \right] + \theta_{ho} \quad 0 \leqslant S \leqslant 1.0 \tag{30}$$

$$\theta_{cS} = \theta_{co} - \left[\frac{C^*_{cf}}{C^*_c} [\theta_{cf2} - \theta_{cfS}] \right] \quad (1.0 + K_1) \leqslant S \leqslant (2.0 + K_1) \tag{31}$$

Stability Analysis. To study the time varying behavior of the loop, one needs to solve Eqs. (16)–(21) in its full form. Finite element method (FEM) is adopted to solve the one-dimensional momentum and energy equations in the transient state. The whole NCL is discretized by a number of one-dimensional three node quadratic elements and the temperature variation over an element is taken as a quadratic function of space coordinate. The coefficients of the quadratic function are evaluated in terms of three nodal temperatures. The finite element solution eventually evaluates the unknown nodal temperatures. Each node of horizontal sides (having two fluids) of the loop has two degrees of freedom and the nodes on vertical side (having single fluid) have single degree of freedom. In the present analysis, weighted integral formulation is used. The solution of weighted integral form of energy equations is approximated by $\theta(S,\tau) = \Sigma_{j=1}^{3} \theta_j^e(\tau) \psi_j^e(S)$ where, $\psi_j^e(S)$ are the Lagrange quadratic interpolation functions developed for three nodal points of any element. Energy equations are solved using the Crank–Nicholsan scheme for time-dependent problem. Standard routines are written for each element for computation of energy as well as momentum equation and they are assembled to obtain a global matrix of the form, $[M]\{\dot{\theta}\} + [K]\{\theta\} = 0$, where $[M]$ is the global mass matrix and $\{K\}$ is the global coefficient matrix. Since, the discritized domain consists of elements of two degrees of freedom and also elements of one degree of freedom, a typical assembly routine is written so that elements with different degrees of freedom can be accommodated. The integrals in the momentum equation are carried out by the Gauss–Legendre quadrature. The solution of the momentum equation is carried out iteratively by using the Newton–Raphson method.

The solution of the problem is carried out for discritization of the NCL with 40 elements (10 for each side of the loop) to 120 elements (30 for each side). No appreciable change in the solution was noticed both for transient and stability if the number of elements are 10 or more than 10. Time step variation 1×10^{-7} to 1×10^{-9} (nondimensional) is taken. Again, no appreciable change in the results is seen in above time step variation. However, for determining the stability envelope further finer time steps are taken for an accurate prediction of the neutrally stable zone. Since the present numerical code consists of two error criteria for the convergence of temperature as well as the coupling fluid rate, the temperature error criteria induces the maximum uncertainty in the calculation of temperature is ±0.006% and in the flow rate is ±0.004%.

In the present case, the momentum and energy equations are coupled with each other and the system is having only two natural boundary conditions (hot and cold stream nondimensional inlet temperatures). The node "*M*" of the loop MNOP is treated as two separate nodes (open node) though, these two nodes are physically one and the same. That means, "*M*" is the first node of the first element as well as the third node of the last element of the loop MNOP (loop starts from "*M*"). To start with, the steady-state values of the coupling fluid velocity, loop temperature profile, and the temperature distributions for hot and cold streams are considered for specified loop configuration and operating conditions. These are given in Eqs. (24) and (26)–(31) respectively. A finite perturbation is given to the circulation velocity. The perturbed steady-state value of the circulation velocity and unperturbed values of the temperature distributions are taken as the initial conditions for the set of transient, one-dimensional energy and momentum equations mentioned earlier. FEM solutions of these equations are obtained for a large duration taking small time steps. Here, the energy equations are carried out iteratively until the temperature difference between the open nodes approaches the preassigned error criteria. Thus the physical condition of "*M*" being one and the same is satisfied numerically. The solution obtained from the energy equations gives a new set of temperature distribution of the coupling fluid along the loop, MNOP, the hot stream temperature distribution in HEHE, and the cold stream temperature distribution in CEHE. Next, the solution of the momentum equation is carried out with the obtained coupling fluid temperature profile iteratively by using Newton–Raphson method. In the solution scheme, the iteration continues until C_{cf} difference between two successive iterations satisfies preassigned error criteria. The solution of the momentum equation gives the updated value of the C_{cf}. This completes the first time step calculation. The value of C_{cf} and the coupling fluid temperature distribution, θ_{cf}, obtained after the first time step calculation is used in the next time step. In this manner, the computation is carried out. The stability condition of the loop is judged from the signals of the temperature and the coupling fluid velocity obtained from the solution. Judging the nature of the temporal variation of the said parameters one can determine whether the loop is in stable, unstable, or neutrally stable condition for the given set of input and process variables. And, finally one can determine the stability envelope for the operation of the loop. For this one needs to find the solution for the loop behavior covering a wide range of operating parameters.

To check the validity of this numerical technique, initially solution is obtained for the steady-state case. For this, step excitation of the inlet temperature of hot stream ($\theta_{hi} = 1.0$) is considered and the finite element program is run for a sufficiently long time to get the solution of the coupled system. Results are compared with those obtained from analytical solution of steady-state equations (Rao [40]) and depicted in Figs. 3(*a*) and 3(*b*). Finite element solutions exhibit excellent agreement with the analytical results.

In the present simulation, the loop behavior depends on six nondimensional parameters namely, Ntu_h^*, Ntu_c^*, C_h^*, C_c^*, R_h^*, R_c^*, and Gr_L apart from the geometrical parameters of the loop. The geometry of the loop can be specified again in terms of two nondimensional parameters namely, $K_1(L_2/L_1)$ and $K_2(L_1/D)$. In the present study, $K_1 = 2$ and $K_2 = 20$. Characteristics of end heat exchangers are also fixed considering $Ntu_h^* = 5.0$; $Ntu_c^* = 2.0$. Moreover, C_c^*, R_h, and R_c are also kept constant. Solution of the coupled set of equations are obtained taking different combinations of C_h^* and Gr_L covering a wide range of these two parameters. The results are discussed in the following section.

Results and Discussion

Though the stability behavior of the loop is analyzed covering a wider range of Gr_L and C_h^* only some typical results are reported here to avoid repetition.

For $Gr_L = 1.2 \times 10^9$ and $C_h^* = 1.0 \times 10^4$ the response of cold heat exchanger exit temperature and the coupling fluid velocity for different initial perturbations are shown in Figs. 4(*a*)–4(*c*). In Fig. 4(*a*) results are reported for a 15% perturbation (i.e., the initial of the C_{cf}^* is 0.85 times of its steady-state value under the given condition) of the steady-state circulation rate. One can observe that the circulation rate starts from its specified value at $\tau = 0$, rises quickly and starts oscillating around its steady-state value. However, the amplitude of the oscillation decreases continuously and ultimately C_{cf}^* reaches its steady-state value at around $\tau = 0.015$. The cold stream exit temperature also shows the behavior similar to the circulation velocity. It exhibits oscillatory behavior where it oscillates around its steady-state value and finally reaches the steady-state along with the circulation velocity. This clearly depicts a stable behavior of the loop for the chosen input condition.

Results are reported in Figs. 4(*b*) and 4(*c*) for 25% and 35% perturbations, respectively, for the same input parameters. In both these cases circulation velocity and cold stream exit temperature

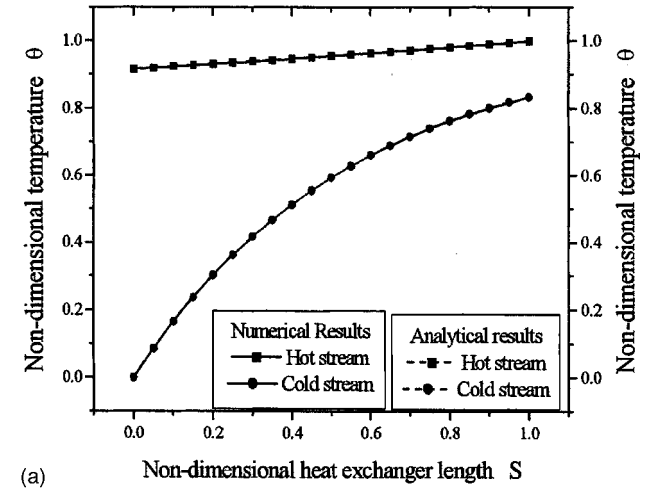

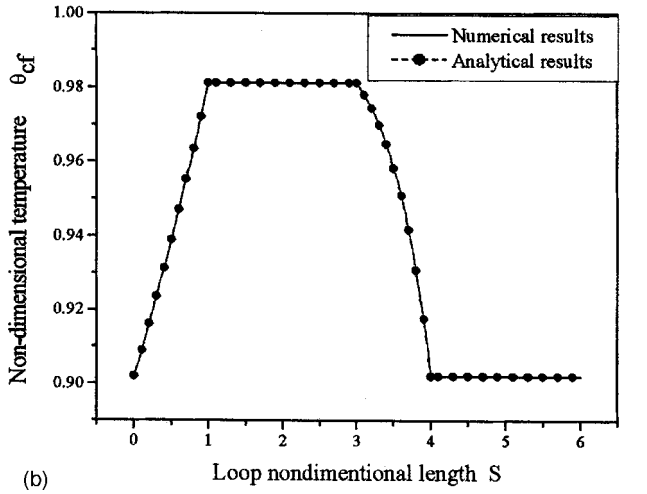

Fig. 3 Comparison between numerical and analytical results at steady state: (*a*) Hot and cold stream temperature profile, (*b*) coupling fluid temperature profile ($Ntu_h^*=5.0$, $Ntu_c^*=2.0$, $C_h^*=100000$, $C_c^*=1000$, $Gr_L=100000000$, $R_h=5000$, $R_c=1000$, $K_1=2.0$ and $K_2=20.0$)

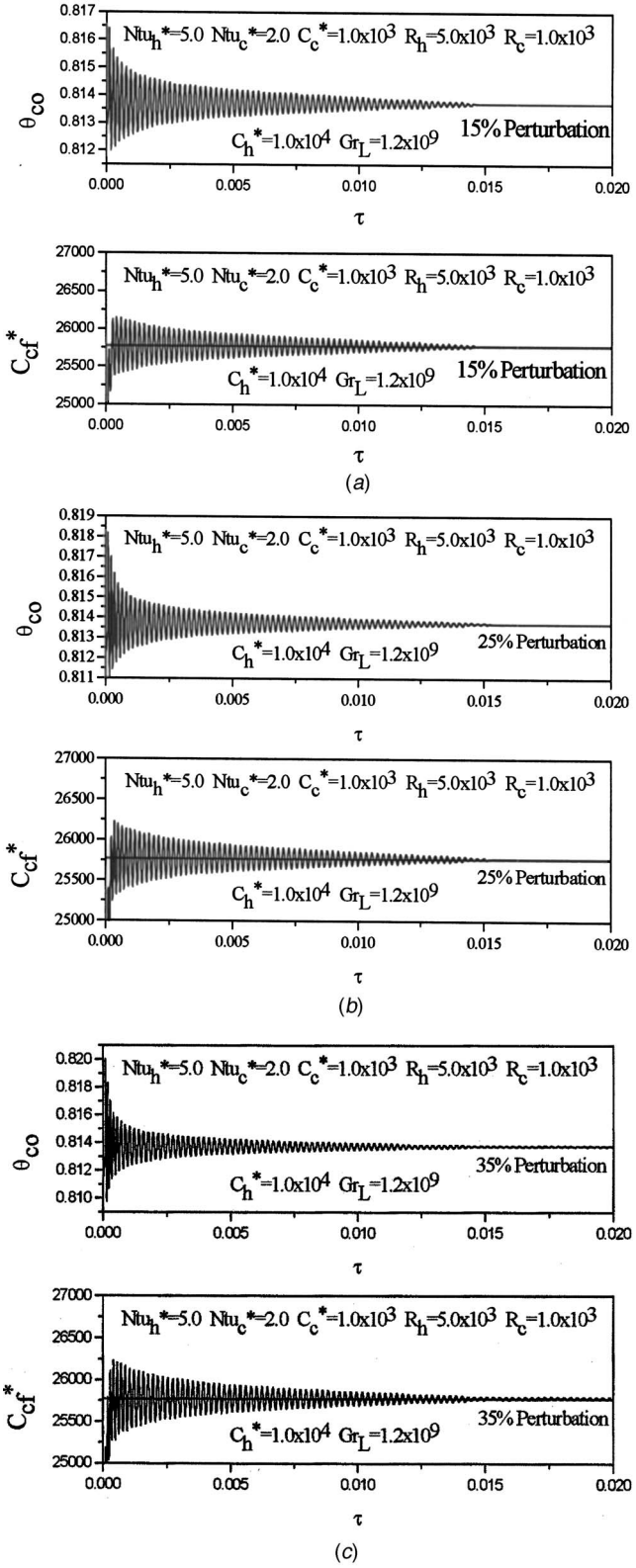

Fig. 4 Variation of cold stream outlet temperature and coupling fluid flow rate at stable equilibrium (*a*) 15% perturbation, (*b*) 25% perturbation, (*c*) 35% perturbation

reach their steady-state value through damped oscillations. However, the time to reach the steady state increases to the magnitude of perturbation. It may be noted that the condition of stability for the loop, though, depends on the specified geometry and operating parameters, it does not depend on the imposed perturbation.

It is further noted that the hot stream exit temperature and temperature at any point inside the loop also reach their respective steady-state values following a nature similar to those reported in Fig. 4. Figure 5 shows the typical solution trajectory for the exit temperatures of the two streams. One can clearly observe that the solution evolves to the steady state for the input variables selected.

Next, the loop response is considered for $C_h^*=1.0\times10^4$ and $Gr_L=1.24\times10^9$. The temporal variation of the cold stream exit temperature and the circulation velocity are shown in Fig. 6. Both these variables depict oscillatory behavior where the amplitude and frequency of the oscillation remain constant over the time.

However, both the responses have identical frequency and the average of the circulation velocity and the cold stream exit temperature exactly matches with their steady-state value. This is a clear indication of neutral stability where the local values of temperature and the circulation velocity oscillate around their steady-state. Figure 7 shows the variation of the stream exit temperatures of hot and cold end heat exchangers with time. Their perfect periodic natures with constant amplitude and frequency are obvious from Fig. 7. The phase difference between these two response curves is almost 90 deg. This explains the steady oscillatory behavior of the loop under a condition of neutral stability. The evolution of neutral stability could be understood from Fig. 8, which

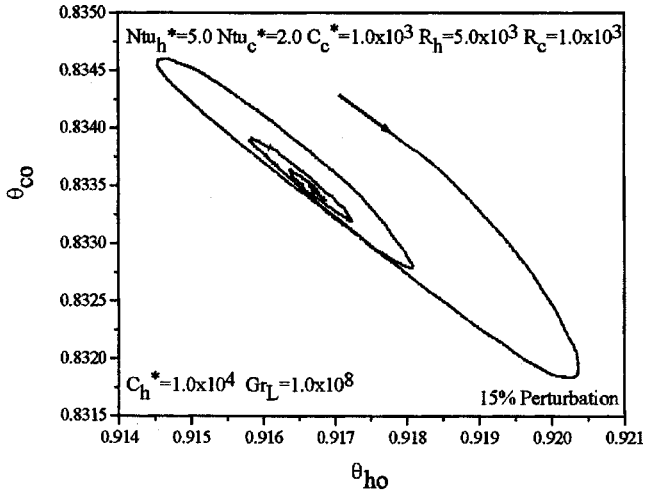

Fig. 5 State space plot of hot and cold stream outlet temperatures for stable condition

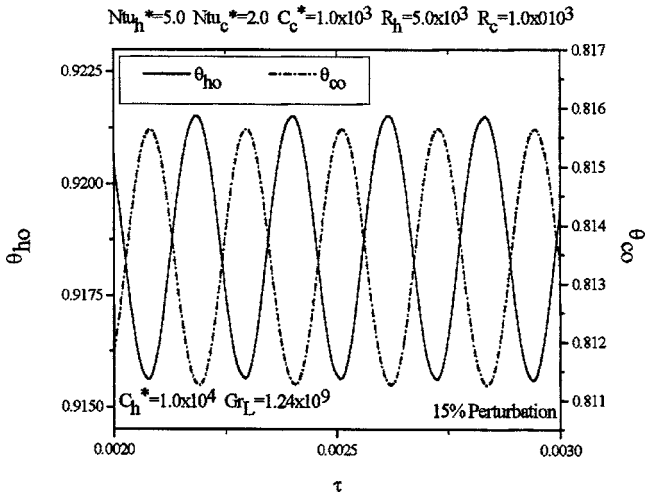

Fig. 7 Time series plot of hot and cold stream outlet temperatures for neutral stability

shows the plot of the hot and cold stream exit temperatures on a state space. For a better appraisal enlarged scales are used for this figure. One can observe that after a brief initial oscillation the attractor takes a highly elongated elliptical shape. This is because the two temperature curves are sinusoidal in nature and are almost out of phase. Hence, the attractor will be Lissajous figure of the observed shape.

Finally, the performance of the loop is investigated for $C_h^* = 1.0 \times 10^4$ and $Gr_L = 2.0 \times 10^9$. The response of the cold stream exit temperature and coupling fluid velocity are shown in Fig. 9. In both these cases the amplitude of the oscillating response grows continuously. This represents a situation of unstable equilibrium. Temperature anywhere in the loop also experiences an oscillatory behavior where the amplitude grows on with time as can be seen from Fig. 10. In Figs. 10(*a*)–10(*c*) temperature from a pair of points in the loop are depicted. For each of the pair one point is exactly opposite to the other; or in other words, the points are so selected that the distance between them is half the total length of the loop. In all these figures one can observe that the oscillations for the opposite points are out of phase. This is clearly discernable in Fig. 10(*c*) where the temperature of the coupling fluid at the midpoint of the heat exchangers is depicted.

This indicates that when the temperature of the C_{cf}^* is the lowest at the bottom of the riser it is the highest at the top of the downcomer. Moreover, from the results it is observed that when a "hot pocket" of a fluid enters the CEHE a "cold pocket" of fluid enters the HEHE. Buoyancy effect is the maximum at this instant. Similar observations were made by Welander [8] during the analysis of a NCL with a point heat source and point heat sink. Welander [8] drew one analogy between the motion of a pendulum and fluid flow for the loop he has studied. Further, he has commented that these unstable motions are due to the thermal anomalies in the fluid that passes through the loop. These anomalies get amplified through the variation in flow rate. A warm pocket of fluid, when passing through the upper part of the loop, creates a maximum mass flow rate and it creates a minimum flow rate when it passes through the lower part of the loop. Or in other words it passes quickest through heat sink than through the heat source. Though, in the present study the heat source and heat sink are of finite length, the oscillatory behavior of the fluid flow is not much different as are observed in the earlier investigations.

The relationship between the exit temperatures of hot and cold streams is mapped in Fig. 11. The spiral elliptic repeller clearly indicates that the frequency of the oscillatory temperatures increases indefinitely indicating an unstable behavior.

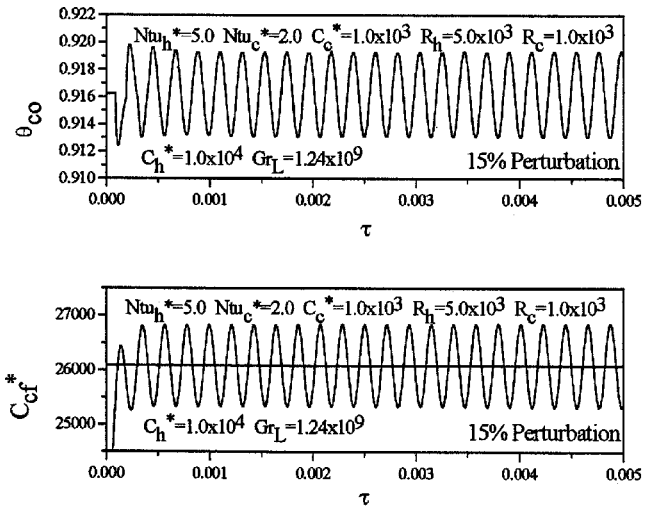

Fig. 6 Typical characteristics of the loop for neutral stability

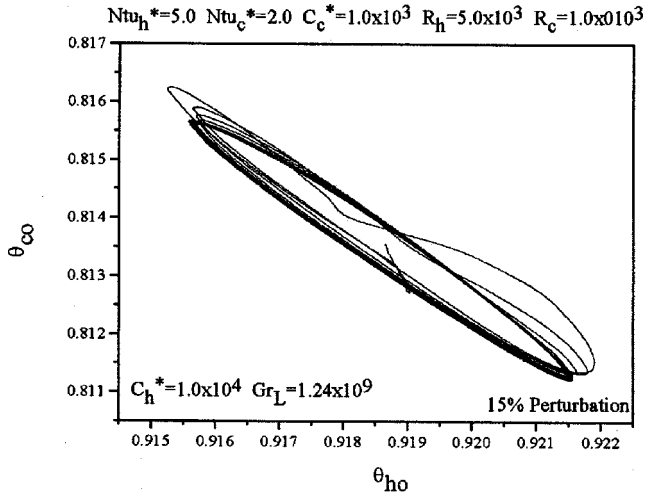

Fig. 8 State space plot of hot and cold stream outlet temperatures for neutral stability

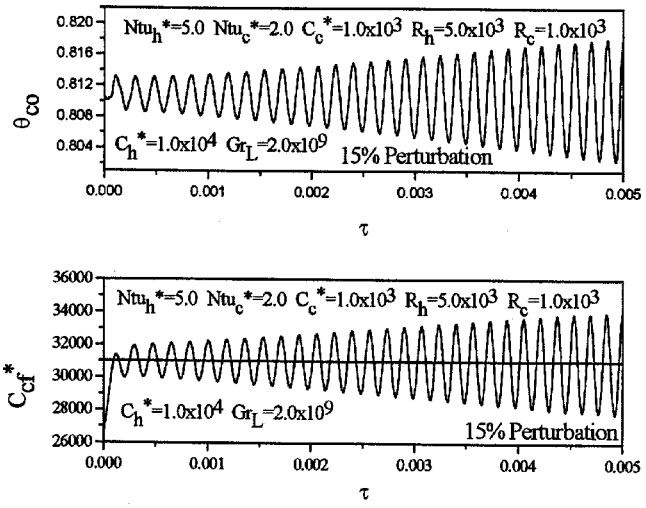

Fig. 9 Typical characteristics of the loop for unstable condition

The two-dimensional space bounded by a wide range of C_h^* and Gr_L is thoroughly scanned to determine the stability behavior of the natural circulation loop. Regions are identified for stable and unstable operation of the loop joining all the points of neutral stability as depicted in Fig. 12.

In the previous discussion we have taken three examples where the value of C_h^* is kept constant and the Gr_L values are varied in such a way that three different cases of stability namely, stable, neutrally stable, and unstable behavior of the loop can be demonstrated. One can take additional points on the same constant C_h^* line to study the growth of the flow oscillation in the loop. For this two additional Gr_L values are chosen and all these five operating points are depicted in Fig. 12 on the vertical line of $C_h^*=10000$. The variation of C_{cf}^* with different Gr_L are plotted in Fig. 13 for a comparison. At $Gr_L=1.0\times10^8$ [point "*A*" in Fig. 12] the circulation rate reaches the steady-state with a few oscillations only.

From Fig. 12 one can also verify that this operating point is in a highly stable region. As Gr_L is increased one approaches the boundary of the stability curve. The loop takes more time to reach the stable equilibrium as depicted in Fig. 13(*b*) [point "*B*" in Fig. 12]. The duration of this oscillation will increase and at the boundary of the stability envelope [point "*C*" of Fig. 12] loop circulation rate will oscillate continuously with fixed values of amplitude and frequency indicating neutrally stable condition [Fig. 13(*c*)]. Once the Gr_L is increased above its value corresponding to neutral stability, the loop operates in unstable region and the amplitude of the oscillation grows continuously.

However, the growth of amplitude is slower at low value of Gr_L [point "*D*" Fig. 12] and it increases as the Gr_L increased further (point "*E*"). These are depicted in Figs. 13(*d*) and 13(*e*), respectively. As the oscillation grows the solution indicates the circulation can occur even in a reverse direction. If Gr_L is increased further the series of phenomenon described in the earlier section will repeat in a reverse order. Growth of oscillation will gradually decay as the Gr_L approaches the opposite boundary of the stability envelope and the flow will become stable once the stability envelope is crossed.

It is understandable from the momentum equation that the oscillations in flow are merely due to the interplay between the frictional and buoyancy forces. Momentum equation shows that total buoyancy is also a function of Gr_L apart from the temperature gradient. On the other hand, frictional force is solely a function of flow rate. For a given C_h^* and Gr_L as discussed by Walender [8] an increase in flow rate above the steady-state value produces a corresponding increase in friction and a decrease in total buoyancy. The net effect is to retard the flow, thus tending to return the system to the original steady-state. A decrease in flow produces the opposite effect. According to this argument the system is self-correcting under any flow disturbance. This is true at lower values of Gr_L. However, as Gr_L increases the system be-

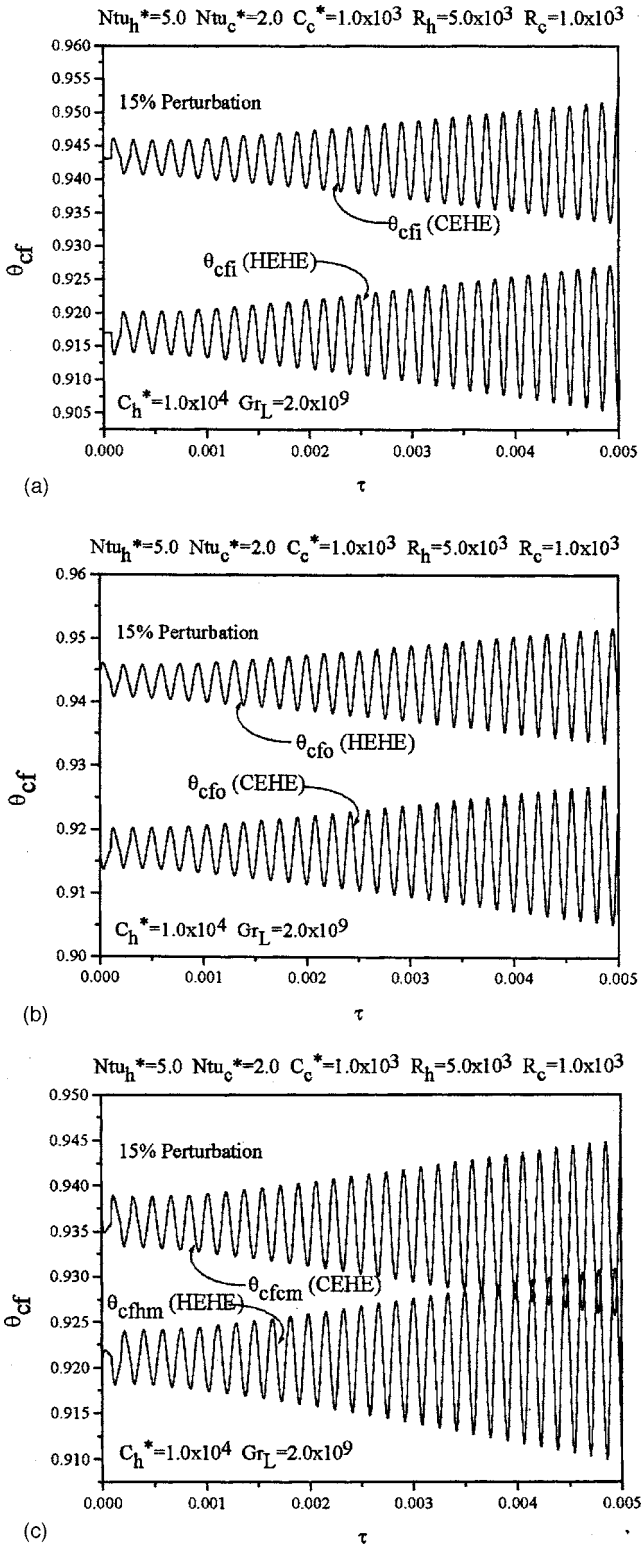

Fig. 10 Typical characteristics of the loop for unstable condition variation of coupling fluid temperature. (*a*) At the inlet of heat exchangers, (*b*) at the exit of heat exchangers, (*c*) at the midpoint of heat exchangers

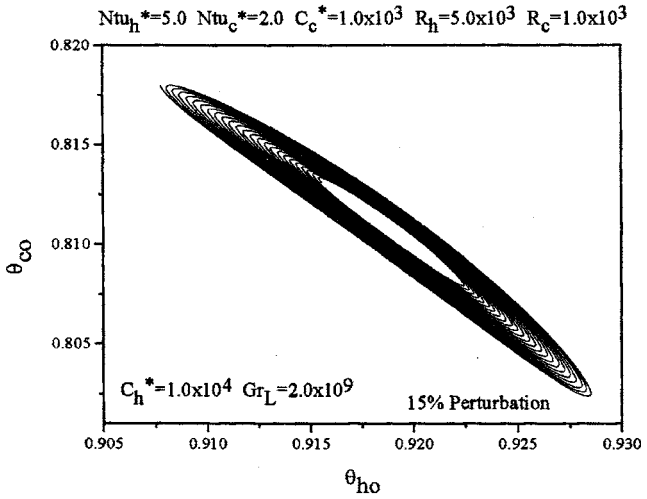

Fig. 11 State space plot of hot and cold stream outlet temperatures for unstable condition

comes unstable as described in the previous paragraph and the rate of amplification of these oscillations increases as Gr_L increases. However, it is observed that the rate of amplification increases up to a certain value of Gr_L thereafter eventually diminishes. The physical reasoning may be at this value of Gr_L where the instability is the highest, the interplay between frictional force and buoyancy force is at the highest degree (both will highly dominate over each other). However, further increase of Gr_L makes retardation in interplay between frictional and buoyancy forces since Gr_L starts to play a dominating role.

Though a one-dimensional approach is used to tackle the present problem, a two-dimensional and three-dimensional study may provide a better understanding of both the steady and transient behavior. In a one-dimensional approach, the governing equations are averaged over the cross section. They, therefore, require a priori specifications of friction and the heat transfer coefficients as is taken in the present problem. In the two-dimensional formulation (axial and radial directions) the variation of friction and heat transfer coefficients would be determined. Since the governing equations are averaged over the cross section, one-dimensional analysis may overestimate the flow rate (Misale et al. [41], Mertol et al. [42], and Su and Chen [43]). However, the qualitative trend of the stability behavior of the system will not be altered. On the other hand, three-dimensional analysis can predict stream-wise flow reversal, secondary motion and nonaxisymmetric velocity and temperature profiles which are unable to predict these phenomena by both one-dimensional and two-dimensional because of their simplifying assumptions (Lavine et al. [44]). However, the qualitative trend of the stability behavior of the system will not be altered but one can observe these peculiar characteristics during experimentation, which will be tackled well by three-dimensional analysis.

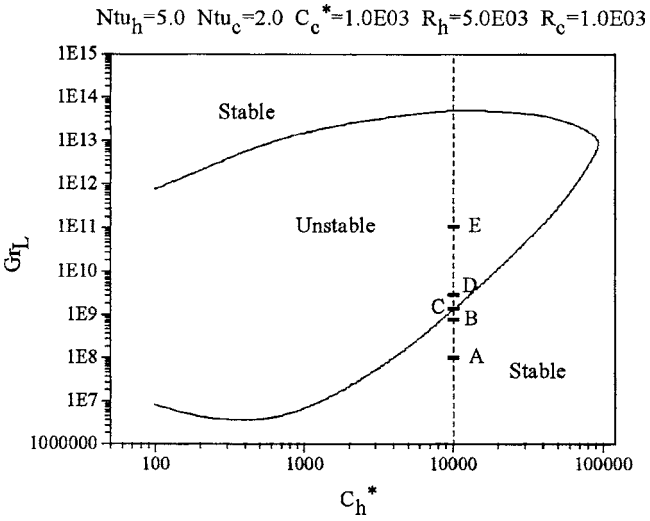

Fig. 12 Stability map

Conclusion

The stability analysis for the NCL with end heat exchangers is carried-out in the present investigation. The one-dimensional transient conservation equations of the loop fluid and the two fluid streams of hot end and cold end heat exchangers are solved simultaneously using a finite element program. Initially, a typical steady-state value of the loop circulation is selected. The local temperatures corresponding to this circulation rate are assigned as the initial temperature. However, a perturbed value of the above steady-state circulation rate is taken as the initial parameter. With these initial values the loop performance is studied for a long duration. Examining the nature of response the type of stability (stable, unstable, or neutral) is understood. Though the stability may depend on a number of parameters, variation of only two nondimensional parameters namely C_h^* and Gr_L is studied. It is observed that in the case of stable behavior the steady-state value does not change with the degree of perturbation, but the time needed to reach the steady state depends on it. In case of neutral stability, the frequency of oscillation for various loop parameters like temperature, circulation rate are identical. However, the temperatures of two diametrically opposite points in a loop have a phase difference of 90 deg. Further, in case of unstable equilibrium, the amplitude of oscillations increases continuously. The phase difference between temperatures of diametrically opposite points is also observed to be 90 deg. The stability behavior is scanned over a wide range of C_h^* and Gr_L values and the stability envelope is also prepared. All the secondary effects like axial conduction, viscous dissipation and conduction through the pipe wall are neglected in the present work as the thrust was on the study of stability behavior due to only natural circulation. As axial conduction tends to equalize the temperature difference, it may have a stabilizing effect. However, this effect becomes less significant for high circulation velocity (as the present case is). Nevertheless, consideration of axial conduction may constitute an interesting study. Further, it may be noted that in the present case the conservation equations are not linearized and considered in their full form for stability analysis.

Nomenclature

A_s = cross-sectional area, m^2
c = specific heat, kJ/kg-K
C = heat capacity rate, kW/K
C^* = nondimensional heat capacity rate, $(C/(\mu cD)_{cf})$
C_f = friction factor, dimensionless
$C^*_{\max,c}$ = larger heat capacity rate of the fluid in CEHE side, dimensionless
$C^*_{\max,h}$ = larger heat capacity rate of the fluid in HEHE side, dimensionless
$C^*_{\min,c}$ = smaller heat capacity rate of the fluid in CEHE side, dimensionless
$C^*_{\min,h}$ = smaller heat capacity rate of the fluid in HEHE side, dimensionless
CR^*_c = $C^*_{\min,c}/C^*_{\max,c}$ (cold fluid side), dimensionless
CR^*_h = $C^*_{\min,h}/C^*_{\max,h}$ (hot fluid side), dimensionless
D = loop diameter, m
g = gravitational acceleration, m/s^2

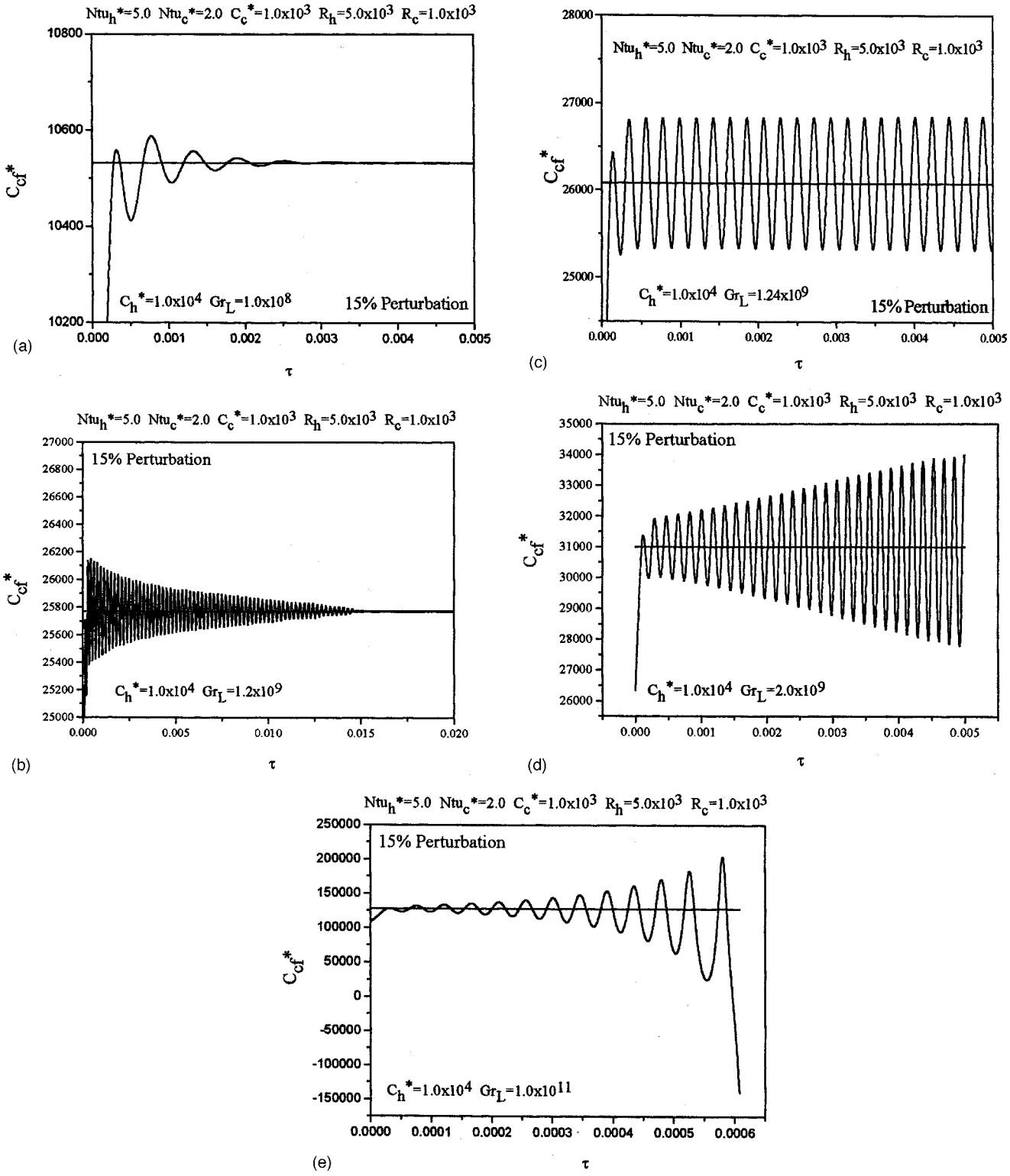

Fig. 13 Change of stability behavior with the increase of Gr_L, (*a*) for $C_h^*=1\times10^4$ $Gr_L=1.0\times10^8$, (*b*) for $C_h^*=1\times10^4$ $Gr_L=1.2\times10^9$, (*c*) for $C_h^*=1\times10^4$ $Gr_L=1.24\times10^9$, (*d*) for $C_h^*=1\times10^4$ $Gr_L=2.0\times10^9$, (*e*) for $C_h^*=1\times10^4$ $Gr_L=1.0\times10^{11}$

Gr_L = loop Grashof number, dimensionless, $(\rho_0^2 g\beta D^3(T_0-T_{ci})/\mu_{cf}^2)$
$\{K\}$ = global coefficient matrix
L_1 = horizontal length of the loop, m
L_2 = vertical length of the loop, m
$[M]$ = global mass matrix
Ntu_c = $(UA)_c/C_{\min,c}$ (CEHE), dimensionless
Ntu_h = $(UA)_h/C_{\min,h}$ (HEHE), dimensionless
Ntu_c^* = $(UA)_c^*/C_c^*$
Ntu_h^* = $(UA)_h^*/C_h^*$
P = pressure, kN/m^2
Re = Reynolds number, $(\rho uD/\mu)_{cf}$
s = space coordinate, m

S = nondimensional space coordinate, (s/L_1)
t = time, s
T = temperature, K
u = velocity, m/s
UA = product of over-all heat transfer coefficient and heat transfer area, kW/K
$(UA)^*$ = nondimensional product of over-all heat transfer coefficient and heat transfer area, $((UA)/(\mu cD)_{cf})$

Greek symbols

β = thermal expansion coefficient, K^{-1}
ε^* = effectiveness
θ = nondimensional temperature, $((T-T_{ci})/(T_0-T_{ci}))$
$\theta_j^e(\tau)$ = nodal temperatures of an element "e"
μ = viscosity, kg/m-s
ρ = density, kg/m^3
τ = nondimensional time, dimensionless, $(t[(\mu D/\rho A_s)_{cf}1/L_1])$
$\Psi_j^e(S)$ = Lagrange quadratic interpolation functions for three nodal points of an element "e"
ϕ = angle of inclination

Subscripts

c = cold stream
cf = coupling fluid
$cf1$ = steady state (downcomer)
$cf2$ = steady state (riser)
cfS = spatial variation of coupling fluid
$cfSS$ = steady-state coupling fluid
ci = cold stream inlet
co = cold stream outlet
cS = spatial variation of cold fluid
d = delay
hi = hot stream inlet
ho = hot stream outlet
hS = spatial variation of hot fluid
0 = reference

Superscript

$\bullet$ = nondimensional

References

[1] Schmidt, E., Eckert, E. R. G., and Grigull, U., 1939, "Air Material Command," AAF Trans. No. 527, Wright Field, Dayton, Ohio.
[2] Holman, J. P., and Boggs, J. H., 1960, "Heat trans of Freon 12 near the Critical State in a Natural Circulation Loop," ASME J. Heat Transfer, **82**, pp. 221–226.
[3] Van Putte, D. V., 1961, M. S. thesis, Prude University.
[4] Harden, D. G., 1963, Argonne Nat. Lab. Rep. ANL-6710.
[5] Cornelius, A. J., 1965, Argonne Nat. Lab. Rep. ANL-7032.
[6] Alstad, C. D., Isbin, H. S., Amundson, N. R., and Silvers, J. P., 1956, Argonne Nat. Lab. Rep. ANL-5409.
[7] Keller, J. B., 1966, "Periodic Oscillations in a Model of Thermal Convection," J. Fluid Mech., **26**, pp. 599–606.
[8] Welander, P., 1967, "On the Oscillatory Instability of a Differentially Heated Fluid Loop," J. Fluid Mech., **29**, pp. 17–30.
[9] Creveling, H. F., De Paz, J. F., Baladi, J. Y., and Schoenhals, R. J., 1975, "Stability Characteristics of a Single Phase Free Convection Loop," J. Fluid Mech., **67**, pp. 65–84.
[10] Greif, R., Zvirin, Y., and Metrol, A., 1979, "The Transient and Stability Behavior of a Natural Convection Loop," ASME J. Heat Transfer, **101**, pp. 684–688.
[11] Mertol, A., Greif, R., and Zvirin, Y., 1981, "The Transient, Steady State and Stability Behavior of a Thermosyphon with Throughflow," Int. J. Heat Mass Transfer, **24**, pp. 621–633.
[12] Damerell, P. S., and Schoenhals, R. J., 1979, "Flow in a Toroidal Thermosyphon with Angular Displacement of Heated and Cooled Sections," ASME J. Heat Transfer, **101**, pp. 672–676.
[13] Zvirin, Y., 1980, "The Effects of a Throughflow on the Steady State and Stability of a Natural Circulation Loop," *Proceedings of the 19th National Heat Transfer Conference*, Orlando, Florida.
[14] Sen, M., Ramos, E., and Trevino, C., 1985, "The Toroidal Thermosyphon with Known Heat Flux," Int. J. Heat Mass Transfer, **28**, pp. 219–233.
[15] Hart, J. E., 1985, "A Model of Flow in a Closed-Loop Thermosyphon Including the Soret Effect," ASME J. Heat Transfer, **107**, pp. 840–849.
[16] Hart, J. E., 1985, "Observations of Complex Oscillations in a Closed Thermosyphon," ASME J. Heat Transfer, **107**, pp. 833–839.
[17] Singer, J., Wang, Y. Z., and Bau, H. H., 1991, "Controlling a Chaotic System," Phys. Rev. Lett., **66**, pp. 1123–1125.
[18] Wang, Y., Singer, J., and Bau, H. H., 1992, "Controlling Chaos in a Thermal Convection Loop," J. Fluid Mech., **237**, pp. 479–498.
[19] Japikse, D., 1973, "Advances in Thermosyphon Technology," *Advances in Heat Transfer*, edited by Irvine, Jr., T. F., and Hartnett, J. P., Vol. **9**, pp. 1–111. Academic Press, New York.
[20] Sen, M., Pruzan, D. A., and Torrance, K. E., 1988, "Analytical and Experimental Study of Steady-State Convection in a Double-Loop Thermosyphon," Int. J. Heat Mass Transfer, **31**, pp. 709–722.
[21] Bernier, M. A., and Baliga, B. R., 1992, "A 1-D/2-D Model and Experimental Results for a Closed-Loop Thermosyphon with Vertical Heat Transfer Sections," Int. J. Heat Mass Transfer, **11**, pp. 2969–2982.
[22] Zvirin, Y., 1981, "A Review of Natural Circulation Loops in Pressurized Water Reactors and Other Systems," Nucl. Eng. Des., **67**, pp. 543–558.
[23] Mertol, A., and Greif, R., 1985, "A Review of Natural Circulation Loops," *Natural Convection: Fundamentals and Applications*, edited by Kakac, S., Aung, W., and Viskanta, R., Hemisphere, New York, pp. 1033–1071.
[24] Greif, R., 1988, "Natural Circulation Loops," ASME J. Heat Transfer, **110**, pp. 1243–1258.
[25] Torrance, K. E., 1979, "Open-Loop Thermosyphons with Geological Applications," J. Heat Transfer, **101**, 677–683.
[26] Bau, H. H., and Torrance, K. E., 1981, "Transient and Steady Behaviour of an Open, Symmetrically-Heated, Free Convection Loop," Int. J. Heat Mass Transfer, **24**, pp. 597–609.
[27] Bau, H. H., and Torrance, K. E., 1981, "On the Stability and Flow Reversal of an Asymmetrically Heated Open Convection Loop," J. Fluid Mech., **106**, pp. 417–433.
[28] Zvirin, Y., 1979, "The Effect of Dissipation on Free Convection Loops," Int. J. Heat Mass Transfer, **22**, pp. 1539–1546.
[29] Bau, H. H., and Torrance, K. E., 1983, "On the Effects of Viscous Dissipation and Pressure Work in Free Convection Loops," Int. J. Heat Mass Transfer, **26**, pp. 727–734.
[30] Vijayan, P. K., Mehta, S. K., and Date, A. W., 1991, "On the Steady-State Performance of Natural Circulation Loops," Int. J. Heat Mass Transfer, pp. 2219–2230.
[31] Chen, Z., Qian, S., Abrams, W. R., Malamud, D., and Bau, H. H., 2004, "Thermosiphon-Based PCR Reactor: Experiment and Modeling," Anal. Chem., **76**, pp. 3707–3715.
[32] Huang, B. J., and Zelaya, R., 1988, "Heat Transfer Behavior of a Rectangular Thermosyphon Loop," ASME J. Heat Transfer, **110**, pp. 487–493.
[33] Vijayan, P. K., 1999, "Experimental Observations on the General Trends of the Steady State and Stability Behavior of Single-Phase Natural Circulation Loops," Eurotherm Seminar No.63 on Single and Two-Phase Natural Circulation, DITEC-University of Genoa (Italy), 6–8 Sept.
[34] Nayak, A. K., Vijayan, P. K., Saha, D., and Venkat Raj, V., 1995, "Mathematical Modelling of the Stability Characteristics of a Natural Circulation Loop," Math. Comput. Modell., **22**, pp. 77–87.
[35] Fichera, A., and Pagano, A., 2003, "Modelling and Control of Rectangular Natural Circulation Loops," Int. J. Heat Mass Transfer, **46**, pp. 2425–2444.
[36] Rao, N. M., Mishra, M., Maiti, B., and Das, P. K., 2002, "Effect of End Heat Exchanger Parameters on the Performance of a Natural Circulation Loop," Int. Commun. Heat Mass Transfer, **29**, pp. 509–518.
[37] Rao, N. M., Maiti, B., and Das, P. K., 2004, "Pressure Variation in a Natural Circulation Loop with End Heat Exchangers," Int. J. Heat Mass Transfer **48**(7), pp. 1403–1412.
[38] Zvirin, Y., and Greif, R., 1979, "Transient Behaviour of Natural Circulation Loops: Two Vertical Branches with Point Heat Source and Sink," Int. J. Heat Mass Transfer, **22**, pp. 499–504.
[39] Mertol, A., Greif, R., and Zvirin, Y., 1981, "The Transient, Steady State and Stability Behavior of a Thermosyphon with Throughflow," Int. J. Heat Mass Transfer, **24**, pp. 621–633.
[40] Rao, N. M., 2002, "Investigations on Buoyancy Induced Circulation Loops," Ph.D., Thesis, Indian Institute of Technology, Kharagpur.
[41] Misale, M., Ruffino, P., and Frogheri, M., 2000, "The Influence of the Wall Thermal Capacity and Axial Conduction over a Single Phase Natural Circulation Loop: 2D Numerical Study," Heat Mass Transfer, **36**, pp. 533–539.
[42] Mertol, A., Greif, R., and Zvirin, Y., 1984, "Two-Dimensional Analysis of Transient Flow and Heat Transfer in a Natural Circulation Loop," Waerme-Stoffuebertrag., **18**, pp. 89–98.
[43] Su, Y., and Chen, Z., 1995, "2-D Numerical Study on a Rectangular Thermosyphon with Vertical or Horizontal Heat Transfer Sections," Int. J. Heat Mass Transfer, **38**, pp. 3313–3317.
[44] Lavine, A. S., Greif, R., and Humphrey, J. A. C., 1986, "Three Dimensional Analysis of Natural Convection in a Toroidal Loop: Effect of Tilt Angle," ASME J. Heat Transfer, **104**, pp. 508–514.

Optimized Heat Transfer for High Power Electronic Cooling Using Arrays of Microjets

Matteo Fabbri

Vijay K. Dhir
e-mail: vdhir@seas.ucla.edu

Mechanical and Aerospace Engineering Department,
Henry Samuely School of Engineering and Applied Science,
University of California, Los Angeles,
420 Westwood Plaza,
Los Angeles, CA 90095

Electronic cooling has become a subject of interest in recent years due to the rapidly decreasing size of microchips while increasing the amount of heat flux that they must dissipate. Conventional forced air cooling techniques cannot satisfy the cooling requirements and new methods have to be sought. Jet cooling has been used in other industrial fields and has demonstrated the capability of sustaining high heat transfer rates. In this work the heat transfer under arrays of microjets is investigated. Ten different arrays have been tested using deionized water and FC40 as test fluids. The jet diameters employed ranged between 69 and 250 μm *and the jet Reynolds number varied from 73 to 3813. A maximum surface heat flux of* 310 W/cm^2 *was achieved using water jets of* 173.6 μm *diameter and* 3 mm *spacing, impinging at* 12.5 m/s *on a circular* 19.3 mm *diameter copper surface. The impinging water temperature was* 23.1°C *and the surface temperature was* 73.9°C. *The heat transfer results, consistent with those reported in the literature, have been correlated using only three independent dimensionless parameters. With the use of the correlation developed, an optimal configuration of the main geometrical parameters can be established once the cooling requirements of the electronic component are specified.* [DOI: 10.1115/1.1924624]

Introduction

With time, the demand for high performance electronics has increased. More and more applications require the electronic components to be faster, smaller, able to handle a higher amount of power, and be more reliable than before. Small size and high power unfortunately lead to high heat fluxes that need to be removed from the components to avoid failure; speed and reliability improve as the surface temperature of the device decreases. To obtain an idea of how seriously the electronic world is looking for more effective cooling methods, one just has to note that even personal computers, which are not considered as power electronic applications, and whose speed is increasing constantly are reaching the point where traditional cooling techniques (i.e., air cooling) are not sufficient. Even greater are the problems in power electronics, where the limitations of the present cooling methods impose a constraint on the amount of power that a component can handle.

A promising technique, which has received particular attention, is spray cooling. Spray cooling can be implemented by means of liquid jets or liquid droplets. This method presents, while still providing very high heat flux removal capabilities, the possibility of minimizing the amount of liquid employed and pumping power needed in the cooling process. The pressure drop across the nozzle or orifice needed to form the spray or jets does not depend on the mechanism of heat transfer at the surface. In contrast, in channel cooling, when boiling occurs on the heat transfer surface, the pressure drop across the channel increases significantly. Thus, the ratio between power spent for the cooling process and the heat removed decreases faster for spray cooling than for channel cooling, when surface temperature is increased. Furthermore, spraying directly on the heat source eliminates the thermal resistance represented by the bonding layer used for attaching the heat source to the heat spreader. All the reasons mentioned above make the idea of using spray cooling for electronic applications very attractive. Obviously, not only is it necessary that the desired amount of heat be removed from the electronic component, but it must also be accomplished with the least amount of pumping power needed to implement the scheme.

Jet impingement cooling has been studied by many researchers and because of the high heat transfer rates that are achievable, it is used in a variety of applications from the sheet metal industry to cooling of laser and electronic equipment. The jet can be submerged, which means that it flows within the same fluid in the same state (i.e., gas into gas or liquid into liquid), or free surface, which means that the liquid jet is injected into a gaseous environment. Gaseous jets, that obviously have low heat transfer potential, and submerged liquid jets are not considered in this work. The focus of this study is only on free surface liquid jets.

Extensive studies have been performed in the past particularly on single-phase single jet configurations, and most of the experimental data available have been obtained for values of the jet Reynolds number (Re_{dn}) that fall in the turbulent regime, ($Re_{dn} > 2000$). An important conclusion from these studies is that the local rate of heat transfer decreases sharply as one moves radially outward from the stagnation region to the periphery [1]. Elison and Webb [2] experimentally investigated the heat transfer associated with a single water jet. Their major finding was that in the laminar regime ($Re_{dn} < 2000$), the Nusselt number (Nu) varied as $Re_{dn}^{0.8}$, whereas previous studies had shown that $Nu \propto Re_{dn}^{0.5}$. They attributed this enhancement to surface tension effects at the nozzle exit, which increased the actual jet diameter. A summary of the range of the main experimental parameters for this and other studies is presented in Table 1.

Most of the theoretical work has involved laminar jets, and a good summary of the results is presented in [1]. Multiple jets impinging on a heater surface can improve the spatial uniformity of the heat transfer coefficient on the surface. Jiji and Dagan [3] found that the surface temperature uniformity improved as the spacing between the jets decreased. The heat transfer rate was found to be independent of the ratio of the nozzle to heater distance (z) and the jets' diameter (d_n) in the range between 3 and 15. They correlated their data as,

Contributed by the Heat Transfer Division for publication in the JOURNAL OF HEAT TRANSFER. Manuscript received May 23, 2004. Final manuscript received November 23, 2004. Review conducted by: Jay M. Khodadadi.

Table 1 Important parameter ranges investigated by [2–5,7–9]

Ref.	Re	s/d_n	d_n (mm)	N_{jets}	Heater (mm)	Fluid
[2]	300 - 7000	0	0.246, 0.315, 0.584	1	n.a.	H_2O
[3]	2800 - 12600	5.08, 10.16	0.5,1.0	1, 4, 9	12.7x12.7	FC77, H_2O
[4]	5000 - 20000	2, 4, 6, 8	1, 2, 3	7, 9	n.a.	H_2O
[5]	500 - 20000	4.98 – 19.8	0.513, 1.02	4, 9	12.7x12.7	FC77, H_2O
[7]	7100 - 48000	13.8 - 330	n.a.	n.a.	n.a.	n.a.
[8]	3150 – 11300	n.a.	1, 1.59	4, 7	1.9	H_2O
[9]	410 - 4170	6.7 - 60	0.05, 0.1, 0.15	n.a.	19.3	H_2O

$$\mathrm{Nu}_L = \mathrm{Re}_{d_n}^{1/2}\mathrm{Pr}^{1/3}\, 3.84\left(0.08\frac{L}{d_n}N + 1\right) \tag{1}$$

where L is the heater length and N is the number of jets.

Pan and Webb [4] concluded that the stagnation Nu was independent of the interjet spacing, but it exhibited a dependence on the nozzle to plate spacing. The local heat transfer for the two different configurations studied (7 and 9 jets) had only minor differences, mainly in the radial flow region between the jets. They also observed a transition for the central jet from being confined and submerged at $z/d_n=2$ to a free surface jet as z/d_n was increased to 5. They correlated their data for the average heat transfer coefficient as

$$\overline{\mathrm{Nu}_{d_n}} = 0.225\,\mathrm{Re}_{d_n}^{2/3}\mathrm{Pr}^{1/3}\, e^{-0.095(s/d_n)} \tag{2}$$

Womac et al. [5] performed experiments with 2×2 and 3×3 jet arrays using water and FC-72. They found that varying z/d_n had negligible effect on the heat transfer, and that for a given flow rate, the heat transfer improved with an increase in jet velocity. They also pointed out that the reduction in the heat transfer that occurs with lowering the flow rate became more pronounced at very low flow rates. This was attributed to the bulk heating of the fluid (a condition that occurs when the thermal boundary layer reaches the free surface of the liquid film). Unfortunately, they did not provide any evidence to support their claim. The data were correlated by using an area weighted combination of correlations associated with the impingement and wall jet region following the same procedure as Womac et al. [6] had applied in a previous work on single jets. The final correlation was given as,

$$\mathrm{Nu}_L = \left[0.516\,\mathrm{Re}_{d_i}^{0.5}\left(\frac{L}{d_i}\right)A_r + 0.344\,\mathrm{Re}_{L^*}^{0.579}\left(\frac{L}{L^*}\right)(1-A_r)\right]\mathrm{Pr}^{0.4} \tag{3}$$

where $A_r=N(\pi d_i^2/4L^2)$, $V_i=(V_n^2+2gz)^{0.5}$, $d_i=(V_n d_n^2/V_i)^{0.5}$, L is the heater length, and L^* is an estimate of the average distance associated with radial flow in the wall jet regions of the heater and is given by

$$L^* = \frac{(\sqrt{2}+1)s - 2d_i}{4}.$$

Yonehara and Ito [7] carried out an analytical study of the heat transfer under a square array of impinging free surface liquid jets on an isothermal surface. The resulting correlation was given as,

$$\mathrm{Nu} = 2.38\,\mathrm{Re}_{dn}^{2/3}\,\mathrm{Pr}^{1/3}(s/d_n)^{(-4/3)} \tag{4}$$

They also performed experiments to validate their model and found good agreement between experimental and theoretical data for $\mathrm{Re}_{dn}/(s/d_n)^2 \geqslant 5$.

Another study involving arrays of jets was carried out by Oliphant et al. [8], in which the performance of sprays and arrays of liquid jets were compared to each other. However, no particular effort was made towards investigating or understanding the effect of the parameters which affect the heat transfer with liquid jet arrays. The jet diameters and the mass fluxes utilized to generate the jets used in their study can be considered large for electronic cooling applications.

Jiang [9] performed few experiments using circular arrays of free surface water jets having very small diameters. A unique feature of these experiments was that the mass fraction of air in the environment surrounding the jets was controlled. Experiments were conducted both at very low air partial pressures, 2–4 kPa, and also at partial pressures close to 101 kPa. The total system pressure was maintained at 101 kPa. The experiments revealed a surprising increase in the single-phase heat transfer coefficient as the air content was reduced. This was probably due to an increase in the evaporation rate from the liquid film on the heater. Unfortunately, only limited data were collected.

From the above literature survey, it can be concluded that in single-phase impingement cooling with multiple jets, the heat transfer improves when either the liquid mass flow rate, or the jet velocity of the liquid, or the number of jets is increased. The nozzle to heater distance has no significant effect on the heat transfer unless it is decreased to the point where the jets become submerged. The higher the number of jets the more uniform is the surface temperature. Also, the presence of noncondensibles can hinder the heat transfer rate considerably.

It also appears to be better to use a large number of smaller jets than a single large jet to cool a flat surface. Also, since the motivation behind this work is high power electronic cooling, the use of an array of small jets makes it possible to selectively spray the liquid at the locations where the heat is generated. Lastly, all the previous studies have employed flow rates of coolant which appear considerably high for cooling of a small microchip. This work focuses on the heat transfer under arrays of microjets and on finding an optimal configuration for the jet spacing, diameter, and coolant flowrate.

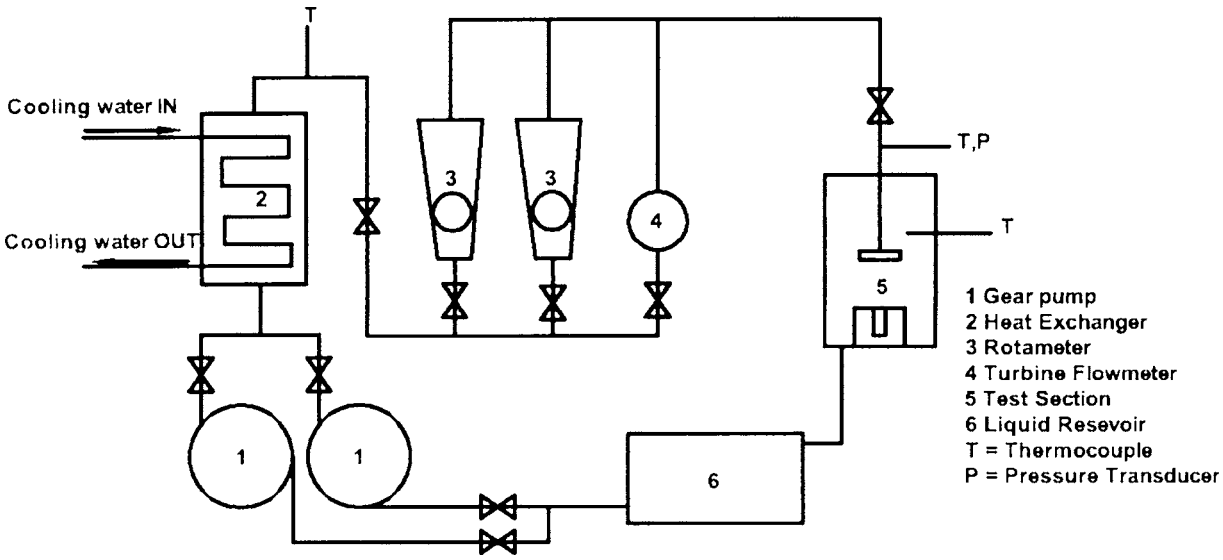

Fig. 1 Schematic of the experimental setup

Experiments

Experimental Apparatus. An experimental rig was designed and built to test ten different arrays of microjets. Figure 1 shows a schematic of the experimental setup. The coolant is circulated with two variable speed gear pumps, installed in parallel. Two rotameters and a turbine flowmeter were installed in parallel to measure the flow rate of the liquid being sprayed. The accuracy of these flowmeters is ±3%. Before entering the flowmeters, the coolant passed through a heat exchanger, where it was cooled down to the specified spray temperature. The liquid was then pushed through a 0.5 mm thick stainless steel orifice plate to form jets. The holes in the plate were laser drilled and were arranged in a circular pattern with a radial and circumferential pitch of 1 mm, 2 mm, and 3 mm. The number of jets corresponding to 1, 2, and 3 mm pitch spacing were 397, 127, and 61, respectively.

Unfortunately, the laser drilling process was not very accurate when dealing with such small dimensions. Visual inspection of the orifice plates under a microscope showed that the holes in the plate are slightly tapered and not exactly circular. Based on photographs of the orifice plates, taken using a camera attached to a microscope, the size of the holes were determined. These values are listed in Table 2. The measurement of the diameters on both sides of the plate confirms that the holes are tapered. The taper also varied from hole to hole.

Table 2 Orifice plate details

s mm	N_{total}	$N_{on\ heater}$	d_n exit μm	STD μm	d_n inlet μm	STD μm	t_{plate} mm
1	397	271	69.3	1.5	94.3	2.9	0.51
2	127	61	76.4	3.3	139.5	6.3	0.51
3	61	37	122.6	6.0	69.2	4.5	0.63
1	397	271	118.7	4.7	136.8	9.7	0.51
2	127	61	113.8	3.9	167.5	6.3	0.51
3	61	37	116.3	5.4	184.8	6.3	0.51
1	397	271	182.1	8.3	263.8	10.0	0.51
2	127	61	178.5	5.8	228	9.6	0.51
3	61	37	173.6	5.1	263	8.7	0.51
1	397	271	250	n.a.	n.a.	n.a.	0.51

The orifice plate was attached with screws to a stainless steel adapter, which was in turn connected to the flowmeters with a pipe. The pipe passed through a flange positioned on top of the heat transfer surface. The pipe could be moved in the vertical direction such that the distance between the orifice plate and the cooling surface could be adjusted to the desired value. The jet pressure was measured upstream of the stainless steel adapter using an Omega PX202-300AV absolute pressure transducer (0–2.07 MPa), which had been factory calibrated. It had an accuracy of 0.25% and a zero balance within 1% of full scale.

The jets impinged on the top surface of a 19.3 mm diameter copper cylinder, which represented the backside of an electronic microchip. The cylindrical surface was enclosed in a Teflon jacket that provided thermal insulation. The cylinder had a larger cylindrical base (76.2 mm in diameter and 16.5 mm in length), which contained six 750 W cartridge heaters. The power to the heaters was controlled with a variac. Four *K*-type thermocouples, soldered at different axial locations (5 mm apart starting from 1.8 mm below the top surface) along the central axis of the cylinder were used to compute the heat flux and to extrapolate the temperature of the heat transfer surface.

Figure 2 shows a schematic of the test chamber. The Teflon jacket–copper block assembly was mounted on a stainless steel plate. The impinged liquid was drained to a reservoir installed below the test section. Thermocouples to measure the liquid temperature were installed both upstream of the flow meters and downstream of the orifice plate. Another thermocouple was used to measure the ambient temperature. All the data were recorded using two IO-Tech 16-bit data acquisition boards. Deionized water and FC40 were the test fluids. FC40 was chosen because of its higher boiling point with respect to the widely used FC72 and FC77 in an attempt to limit the evaporation from the liquid film.

Numerical simulations of the copper block–Teflon jacket–stainless steel plate assembly using a commercial finite element package showed linear axial temperature profiles in the cylindrical part where the thermocouples were installed. As a measure of possible heat losses, the heat flux in the radial direction at any location was calculated to be always less than 1.5% of the heat flux in the axial direction when the latter is 2.5 W/cm^2. At higher heat fluxes the losses were predicted to be even smaller.

It is important to note that the outer one or two rings of jets, depending on the pitch used, did not directly hit the copper surface but instead impinged on the surrounding Teflon surface.

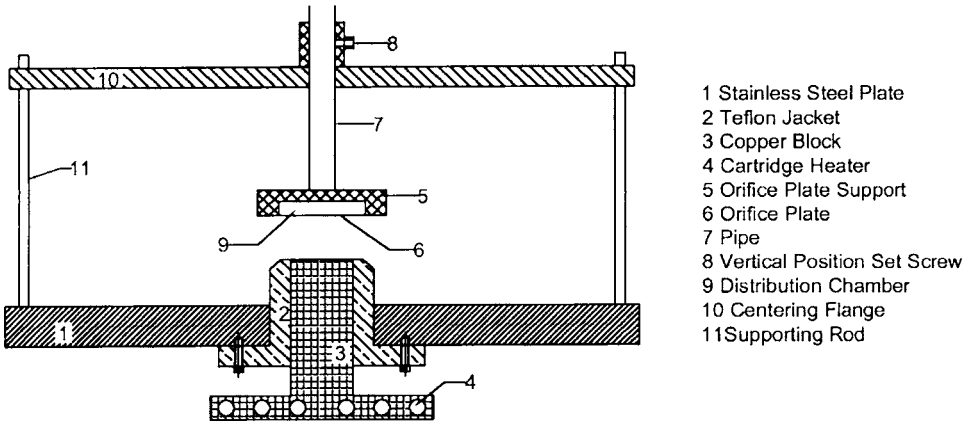

Fig. 2 Details of the test section

Thus, the actual number of jets impinging directly on the copper surface was 271, 61, and 37 for 1, 2, and 3 mm pitch, respectively.

Experimental Procedure. The thermocouples were calibrated prior to installation, by submerging them in an ice bath and in boiling water, and comparing the readings with those provided by a high accuracy mercury thermometer (±0.1°C). Prior to running the experiment the copper surface was polished using a 600 grit sandpaper and then a copper polishing solution, which made the surface very smooth and shiny. Thereafter, in order to guarantee the same surface condition throughout the duration of the experiment, the surface was oxidized in air for 5 h at 320°C. The contact angle was measured to be approximately 44° before and after the experiments.

After the pumps were started, and the liquid flow rate set to the desired value, the cartridge heaters were energized. Visual observation of the jets was perfomed to insure that the jets did not merge with one another, did not break into droplets prior to impinging on the surface, and that they were free surface jets and not submerged jets. Once all the parameters reached steady state, values were recorded for 100 s at a sampling rate of 1 Hz. The data acquisition system allowed real time monitoring of all parameters in both numerical and graphical form so that it was possible to assess when steady state had been reached. Thereafter, the power to the copper block was increased and a new set of data recorded. The experiment was stopped when either the surface temperature was above the boiling point or when the temperature at the base of the copper block rose to above 350°C, which could damage the Teflon jacket and the electrical wires.

Data Reduction. For each data set recorded, the heat flux at the heat transfer surface was calculated from the slope of the temperature profile obtained from the four thermocouples embedded in the copper block. The same temperature profile, which was mostly linear, also allowed the temperature at the heat transfer surface to be calculated (by extrapolation).

The average heat transfer coefficient, Nusselt number, and Reynolds number are defined as,

$$\overline{h} = \frac{q}{T_w - T_{\text{jets}}} \tag{5}$$

$$\overline{\text{Nu}} = \frac{\overline{h} d_n}{k_{\text{film}}} \tag{6}$$

$$\text{Re}_{d_n} = \frac{v_n d_n}{\nu_{\text{film}}} \tag{7}$$

where,

$$v_n = \frac{4\dot{V}}{N\pi d_n^2} \tag{8}$$

All the physical properties were evaluated at the mean film temperature, T_{film}. Repeatability of the data was explored by randomly repeating some of the cases already tested. The data sets fell within the 95% confidence band.

The maximum and minimum uncertainties on the main parameters, calculated according to the procedure described by Kline and McClintock [10], are listed in Table 3. The highest uncertainty in the heat flux (305%) occurred for an FC40 case where the heat flux was only 0.15 W/cm^2. This was caused by the small temperature difference between the four thermocouples installed in the copper block. Only a few other data points had an uncertainty above 30%. For a heat flux of 1.54 W/cm^2 the uncertainty was 29.7%. At a heat flux of 3.1 W/cm^2 the uncertainty was only 14.6% and at 6.6 W/cm^2 only 7.3%. The highest heat flux removed was 310 W/cm^2. The uncertainty on Re_{dn} is highest when d_n and $\dot{V}$ are the smallest and it decreases with increasing d_n and $\dot{V}$.

Results and Discussion

A comparison of the heat transfer data from the present work with the results obtained by Oliphant et al. [8] is shown in Fig. 3. It shows that the same heat transfer rate is obtained at much lower coolant flowrates when arrays of microjets are used instead of arrays containing a few large jets. The reduction in the flowrate is around one order of magnitude. If a regression line through Oliphant et al. [8] data is drawn to the range of flowrates covered in this study, it would lie below the present data sets indicating that for the same flowrate the microjet arrays provide higher heat transfer rates. In such case, the microjet arrays would experience a higher pressure drop than the arrays with larger diameter jets.

Table 3 Maximum and minimum experimental uncertainties

	% data pts	δq/q	δh/h	δNu/Nu	δRe/Re
Max	0.35%	305%	305%	306%	22.7%
Typical	77%	<10%	<10%	<10%	<22.7%
Min	9.9%	2.7%	2.9%	6.7%	7.2%

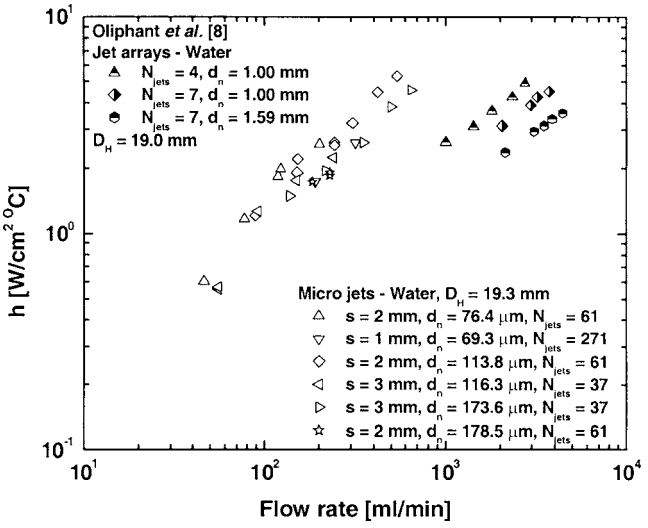

Fig. 3 Comparison between the heat transfer under arrays of microjets and the results by Oliphant et al. [8] using water

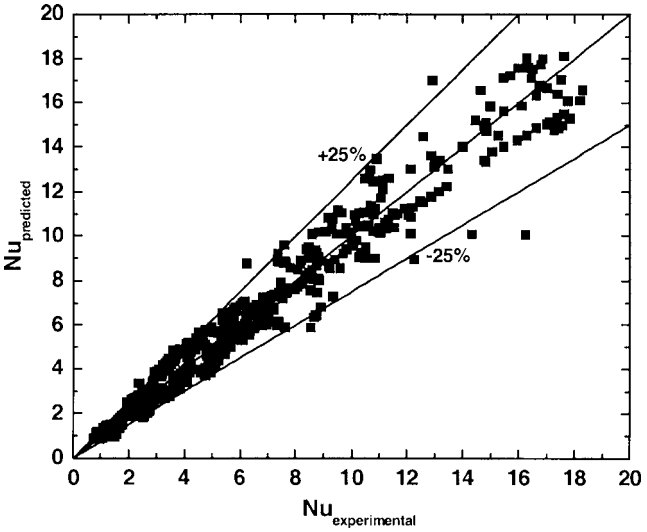

Fig. 4 Comparison of the experimental and predicted Nusselt number

Although cooling with impinging jets is quite a complicated phenomenon, where many variables affect the heat transfer rate, in this work only three dimensionless quantities are used to describe the time- and area-averaged heat transfer coefficients. They are the jet Reynolds number (Re_{dn}), the liquid Prandtl number (Pr), and the ratio of jet pitch and diameter at the nozzle exit (s/d_n). The distance from the nozzle exit to the heated surface was kept fixed at 10 mm and is not considered to be a parameter. All fluid properties are evaluated at the mean film temperature. In the experiments it was noticed that air bubbles existed in the liquid film covering the impinged surface, particularly when the surface temperature approached the saturation value. This phenomenon, resulting from air being trapped by the liquid jets, became more evident at higher liquid velocities and closely spaced jets. It is possible that this lead to some enhancement of the heat transfer from the surface to the liquid. Therefore, even though boiling usually is initiated at a wall temperature higher than the saturation value, only data obtained for $T_w < T_{\mathrm{sat}}$ are considered.

Pan and Webb's study [4] also included the results obtained for a nozzle to heater distance of 2 jet diameters, where the jets were changing from submerged to free surface jets. Using only the data for higher nozzle to heater distance (only free jets) Pan and Webb [4] reported a better fit to their experimental data. The data were correlated with the expression,

$$\overline{\mathrm{Nu}} = 0.129\,\mathrm{Re}_{d_n}^{0.71}\mathrm{Pr}^{0.4}\exp\left(-0.1\frac{s}{d_n}\right) \tag{9}$$

Different functions were tried to fit all the experimental data obtained but the best correlation was achieved with the following expression:

$$\mathrm{Nu} = 0.043\,\mathrm{Re}_{d_n}^{0.78}\,\mathrm{Pr}^{0.48}\exp\left(-0.069\frac{s}{d_n}\right) \tag{10}$$

A commercial software Datafit 7.1 by Oakdale Engineering was used to perform the least-squares fitting process. The goodness of the fit for the 571 experimental data points given by Eq. (10) is listed in Table 4. Figure 4 shows a comparison of prediction from Eq. (10) with the data. Almost all of the experimental data are predicted to within ±25%. The correlation developed is strictly valid for the following range of parameters: $43 \leqslant \mathrm{Re}_{d_n} \leqslant 3813$; $2.6 \leqslant \mathrm{Pr} \leqslant 84$; $4 \leqslant S/d_n \leqslant 26.2$.

Figure 5 gives a graph which shows the variation of the quantity $\mathrm{Nu}/0.043\,\mathrm{Pr}^{0.48}\exp(-0.069(s/d_n))$ as a function of Re_{dn}. From Eq. (10) and Fig. 5, it can be seen that Nu varies as $\mathrm{Re}_{dn}^{0.78}$, which is higher than the 2/3 power found by Pan and Webb [4] and the 0.5 power obtained by Jiji and Dagan [3]. However, Eq. (9) gives $\mathrm{Nu} \propto \mathrm{Re}^{0.71}$, which is close to the dependence found in the present study. It should however be noted that none of the previous studies fully investigated the supposedly laminar regime.

As has been reported by Webb and Ma [1], several researchers have found that Nu varies as $\mathrm{Re}_{dn}^{0.5}$ for a single free surface liquid jet in the laminar regime. Only Elison and Webb [2] found a stronger dependence of Nu on Re_{dn} ($\mathrm{Nu} \propto \mathrm{Re}_{dn}^{0.8}$), but they attributed this enhancement to surface tension effects at the nozzle exit, which caused the jet diameter to be bigger than the actual inner diameter of the nozzle. In the present study, surface tension caused the jets to merge together at low jet velocities. All of the

Table 4 Prediction error on the experimental data

Percentage of data points predicted by Eq. (10)	84.1	91.8	96.2
Standard Error (percentage)	20	25	30

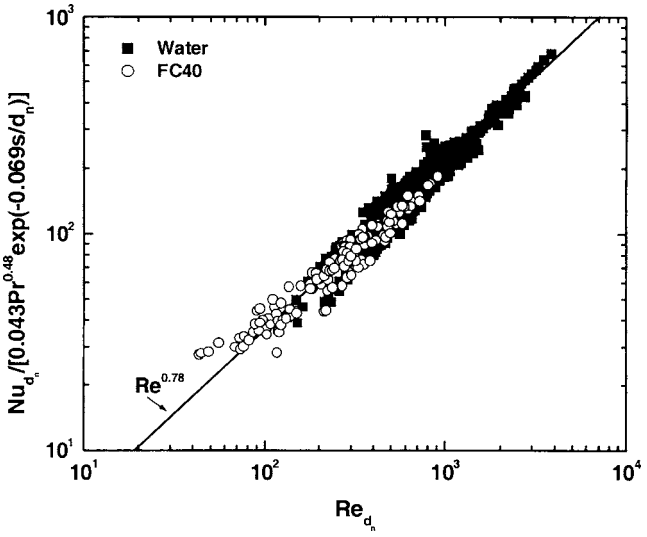

Fig. 5 Variation of Nu with Re_{dn} for varying Pr and s/d_n

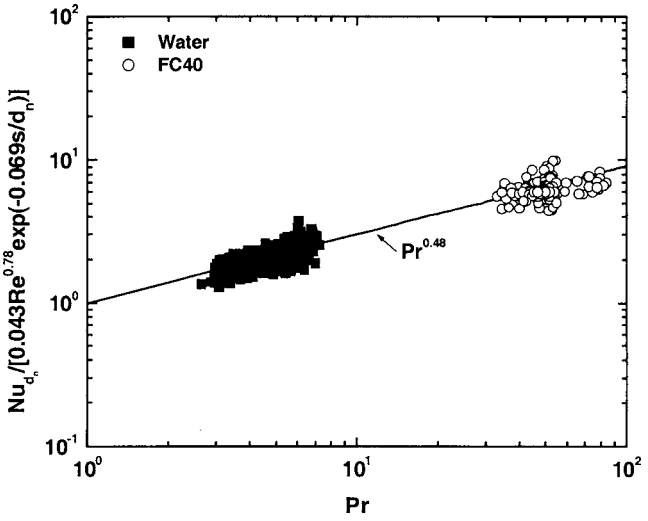

Fig. 6 Variation of Nu with Pr for varying Re_{dn} and s/d_n

data reported here are for velocities at which merger did not occur. Because the data for two liquids, with widely different surface tensions, show the same dependence on the Reynolds number, surface tension is not considered to be playing a role in causing a stronger dependence on Re_{dn}. Entrained air may be the reason for enhanced heat transfer.

In Fig. 6, the parameter $Nu/0.043\,Re_{d_n}^{0.78}\exp(-0.069(s/d_n))$ is plotted as a function of Pr. Consistent with correlation Eq. (10), Nusselt number is found to vary as $Pr^{0.48}$, which is slightly higher than that found by Womac et al. [5] ($Nu \propto Pr^{0.4}$). Figure 7 shows that Nu decreases exponentially with increasing s/d_n.

Figures 8(*a*)–8(*c*) show the Nusselt number obtained from Eqs. (9), (4), (3), and (10) as a function of Re_{dn} for same Pr, but for s/d_n of 26.1, 13.3, and 6.7, respectively. It is found that the predictions differ somewhat from each other. This difference could be due to the fact that in most cases the magnitude of at least one of the parameters lies outside the range of the correlations. A similar trend was found for higher values of the Prandtl number.

Figure 9 shows a comparison of predictions of various correlations as a function of s/d_n. It is found that for small s/d_n values, the experimental results of Pan and Webb [4] do not differ significantly from those predicted by extrapolating Eq. (10). For $5000 < Re < 20000$ the three lines representing the work of Pan and

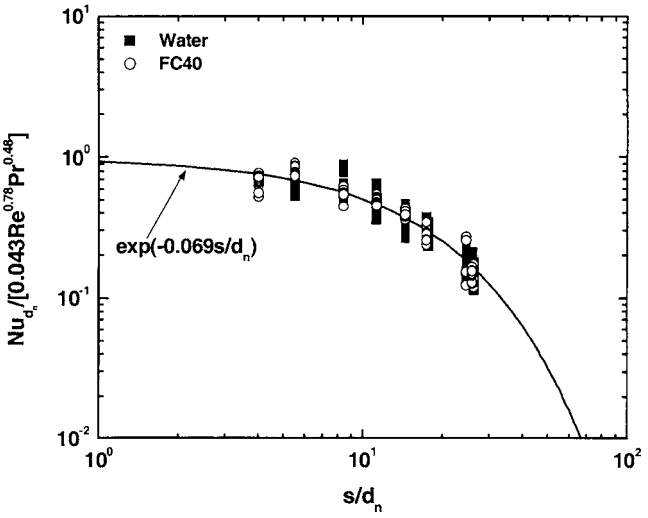

Fig. 7 Variation of Nu with s/d_n for varying Re_{dn} and Pr

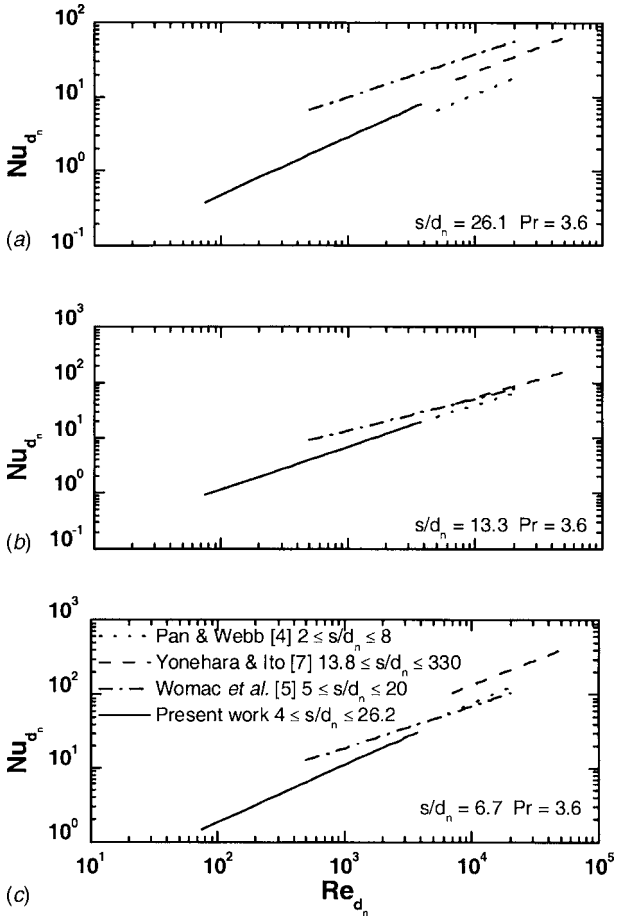

Fig. 8 Comparison of the Nusselt number predicted by various correlations for Pr=3.6 as a function of Re_{dn} (a) s/d_n=6.7, (b) s/d_n=13.3, and (c) s/d_n=26

Webb, Eq. (9), normalized using the quantity $Re_{d_n}^{0.78}\,Pr^{0.48}$ from Eq. (10), fall very close to each other and to the one representing the present work. At higher s/d_n the present work matches well with the work of Yonehara and Ito [7], Eq. (4). The data Yonehara

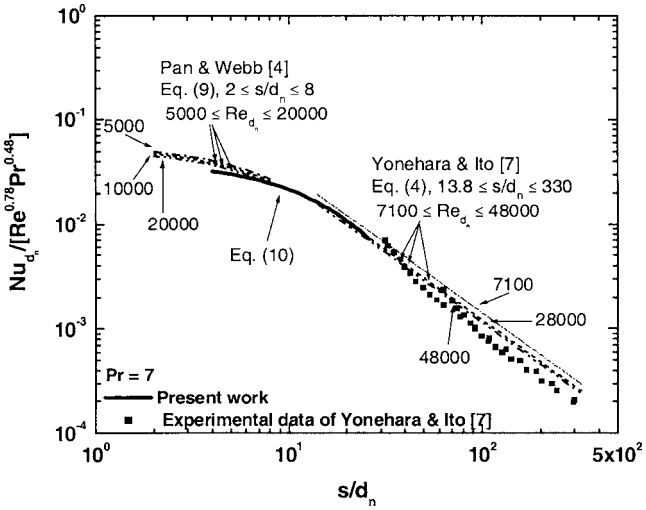

Fig. 9 Comparison of the effect of s/d_n on the Nusselt number in the present work and those of Pan and Webb [4] and Yonehara and Ito [7]

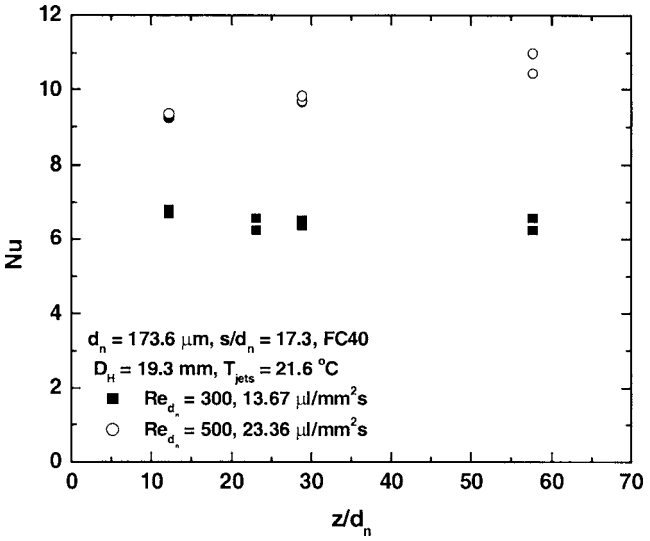

Fig. 10 Effect of orifice plate to heater distance on the heat transfer

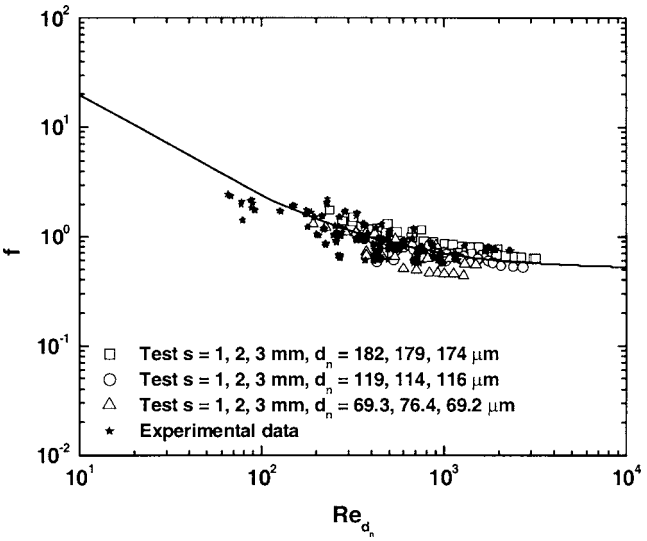

Fig. 11 Normalized pressure drop across the orifice plates

and Ito used to validate their theoretical work are also plotted. The data from the present work nicely fills in the gap in the previous data with respect to s/d_n ($8 \leqslant s/d_n \leqslant 13.8$).

It should be noted that in this work we have only determined the average heat transfer coefficient. Spatial variations are not considered. Since the extent of spatial variations in the heat transfer coefficient depend on the spacing between jets, it is difficult to discern *a priori* as to how much spatial variation in temperature will occur in a given application.

Effect of the Orifice Plate to Heater Distance. A series of experiments was carried out to investigate the effect of the nozzle to heater distance (z) on the heat transfer rate. With FC 40 as the test liquid, experiments were conducted at flowrates of 240 ml/min [13.67 μl/mm^2 s] and 410 ml/min [23.36 μl/mm^2 s]. Only a single configuration of jets was tested. It had a jet pitch of 3 mm and a jet diameter of 173.6 μm. The spray distance was parametrically varied from 10 mm to 2.1 mm, which corresponds to a range of z/d_n between 12.1 and 57.6.

Figure 10 shows the Nu as a function of the nondimensional nozzle to heater distance. It can be seen that there is little effect of the spray distance on the rate of heat transfer for z/d_n greater than 12.1. A small increase in Nusselt number is observed for Re =500 when z/d_n increases by almost a factor of 5. No effect is seen at Re=300. However, at large distance, away from the heater surface the jets may become hydrodynamically unstable and break up into droplets. The heater would then be impinged by monodispersed droplets and the heat removal process will change. This was not investigated in this work.

Optimal Jet Configuration. It is a matter of interest to know if there exists a particular combination of jet parameters that yields optimal performance. To find an optimum, a cost function must be defined and the constraints of the range of parameters must be taken into account. In the design phase of an electronic cooling concept, the requirements are usually the maximum power that must be removed from the component, the dimensions of such a device and the maximum junction temperature that allows the component to work reliably.

The heat exchanger, which ultimately transfers the heat removed from the electronic component to the environment, controls the coolant spraying temperature. Once $T_w - T_{\text{jets}}$ is fixed, the two quantities that can be minimized are the coolant flowrate and the power needed to pump the liquid. The choice of one over the other depends on the specific requirements of the application. For example, there might be constraints on the volume or on the energy consumption.

The pumping power required to push the liquid through the orifice plate can be calculated by multiplying the volumetric flowrate and the pressure drop, ΔP, across the orifice plate. This can be expressed as

$$Q_{\text{pumping}} = \dot{V}\Delta P \tag{11}$$

In this study, the pressure drop data were recorded during each experiment. Additional tests using water were also conducted to measure only the pressure drop across the orifice plates. Based on the data, the friction factor was calculated using the expression,

$$f = \frac{\Delta P}{1/2\rho v_n^2 (t/d_n)} = \frac{\Delta P}{1/2\rho\left(\dfrac{4\dot{V}}{N_{\text{jets}}\pi d_n^2}\right)^2 (t/d_n)} \tag{12}$$

The calculated friction factors are plotted in Fig. 11 as function of Re_{dn}. A least-squares fit of the data yields,

$$f = 0.507 + \frac{189.9}{\text{Re}_{d_n}} = 0.507 + \frac{189.9\mu N_{\text{jets}}\pi d_n}{4\rho\dot{V}} \tag{13}$$

where Re_{dn} is the jet Reynolds number calculated using fluid properties evaluated at the jet temperature. The jet diameter used to calculate Re_{dn} is based on the smallest orifice diameter.

It is common practice to use discharge coefficients to predict the pressure drop through orifices. Using this approach, the coefficients plotted against the Reynolds number could be generalized displaying trends similar to those shown in Fig. 11. However, the values for the coefficients would generally be lower than 1.0 over the entire range of Reynolds numbers. The optimization process that follows takes into consideration also orifice plates with different thickness to hole diameter ratio, number of jets and jet diameters different from those investigated in this study. The use of a friction factor as expressed in Eqs. (12) and (13) makes it easier to estimate the pressure drop across those plates without having to interpolate between several different coefficients. Ildechik [11] recommends predicting the pressure drop across orifice plates by adding the inlet contraction losses to the frictional losses through the holes. The expression used by Ildechik for the friction factor has the same functional dependence as Eq. (13). The difference is that Eq. (13) includes also the entrance losses. Unfortunately, the particular hole geometry of this set of plates does not allow us to generalize the use of Eq. (13). to orifice plate

Table 5 Number of jets impinging on a circular surface of 292.5 mm^2

s [mm]	0.5	1	2	3	4	5
N_{jets}	1141	271	61	37	19	7

with different hole geometries.

Once s, d_n, $Q_{removed}$, $T_w - T_{jets}$, and A_H are specified, Eq. (10) can be used to determine the flowrate necessary to remove the given power. This flowrate can be expressed as,

$$\dot{V} = \left[\frac{Q_{removed} \cdot d_n}{0.043\,\mathrm{Pr}^{0.48} \exp\left(-0.069\frac{s}{d_n}\right) k(T_w - T_{jets}) A_H} \right]^{1/0.78} \frac{N_{jets}\pi d_n \mu}{4\rho} \tag{14}$$

The pumping power can then be calculated by substituting $\dot{V}$ obtained from Eq. (14) into Eq. (11). The pumping power is finally only a function of d_n, $Q_{removed}/(T_w - T_{jets})$, s, and the fluid properties. The jets impinging on a given area is a discrete number. Table 5 lists the number of jets impinging on a circular surface of 19.3 mm diameter from a circular array with equal radial and circumferential pitch.

It is not possible to determine the minimum of $Q_{pumping}$ analytically [with respect to d_n, s, and $Q_{removed}/(T_w - T_{jets})$] due to the nonlinearity of the function and the discrete nature of N_{jets} (s can only change discretely). As such, $Q_{pumping}$ is determined by parametrically varying the independent parameters. For a given $Q_{removed}$, $T_w - T_{jets}$, T_{jets}, and fluid, a graph like the one shown in Fig. 12 can be easily obtained. The extrapolated results for s =0.5, 4, and 5 mm are plotted along with the 1, 2, and 3 mm values of s studied in the present work. The value of $Q_{pumping}$ for fixed pitch, as a function of d_n is obtained by following the procedure described above. The largest value of d_n is equal to $s/2$ (where the jets would start merging) and the smallest value of d_n is 25 μm (where the jets are so small that the chances of clogging of the holes of the orifice plate are considered to be too high). From Fig. 12 it is seen that optimum jet diameter increases with increase in pitch. In this particular case, the optimal configuration, yields a pumping power of $2.53 \cdot 10^{-2}$ W using a jet spacing of 2 mm and a jet diameter of 325 μm. If the results of this study are extrapolated to jet spacings larger than those tested in this study, the optimal configuration for the same case requires a jet spacing of 5 mm and jet diameter of 775 μm, consuming $1.16 \cdot 10^{-2}$ W.

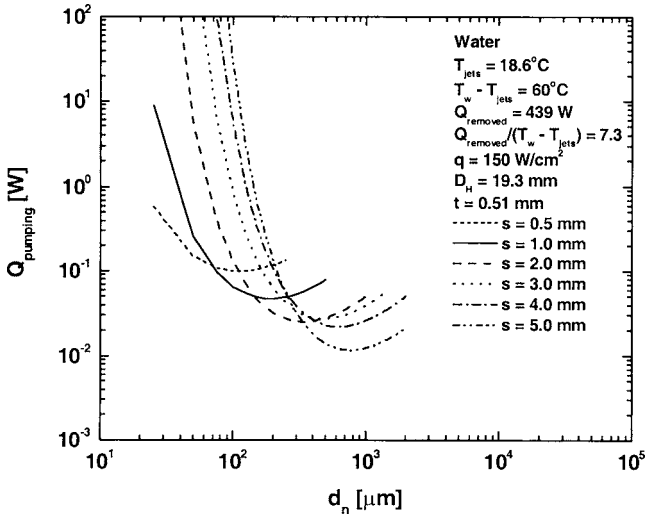

Fig. 12 $Q_{pumping}$ as a function of d_n for a specific $Q_{removed}/(T_w - T_{jets})$

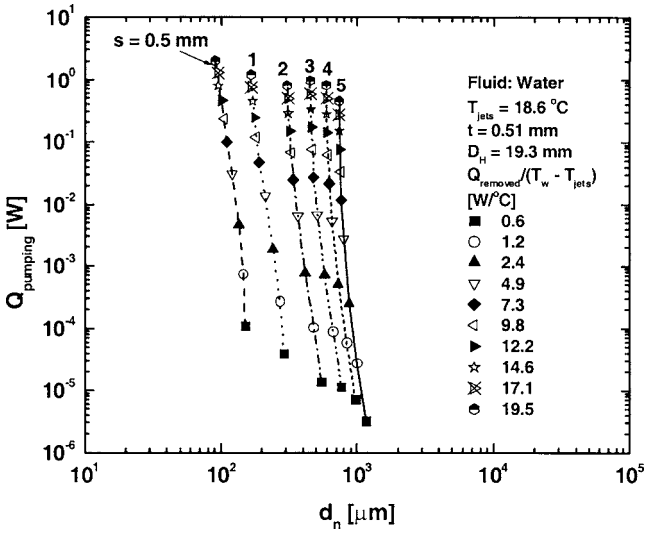

Fig. 13 Variation of the optimal $Q_{pumping}$ as a function of d_n for different $Q_{removed}/(T_w - T_{jets})$ and s

The above procedure can be repeated for different $Q_{removed}/(T_w - T_{jets})$ and the minimum value of each curve can be used to develop a graph like that shown in Fig. 13 that includes the effect of all the main parameters. It is seen from Fig. 13 that for a fixed s, the optimum pumping power increases with $Q_{removed}/(T_w - T_{jets})$, but the corresponding optimum jet diameter is weakly dependent on $Q_{removed}/(T_w - T_{jets})$. The pumping power for a fixed s increases with $Q_{removed}/(T_w - T_{jets})$ because a larger flowrate is needed for the cooling process.

There are also some constraints that must be satisfied. For the chosen combination of geometrical parameters, flowrate and coolant it must be possible to form jets, and that the jet velocity or the pressure drop must not attain unrealistic or impractical values.

If the flowrate is the parameter that must be minimized then the minimum value for Eq. (14) must be found. It is easy to find for the given values of $Q_{removed}/(T_w - T_{jets})$, A_H, and fluid properties the volumetric flowrate versus d_n for different values of s, as shown in Fig. 14.

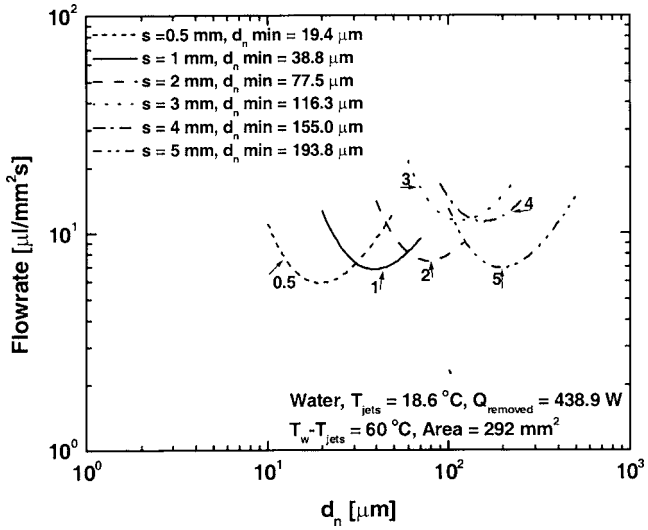

Fig. 14 Flowrate versus d_n for different s

Table 6 $Q_{removed}$, v_{jets}, ΔP for a flowrate of $2\cdot10^{-6}$ m^3/s of water. $T_w - T_{jets} = 60°C$, $T_{jets} = 18.6°C$, Area = 292 mm^2 (6.84 μl/mm^2 s), $t = 0.51$ mm

s [mm]									
		1		2			3		
d_n [μm]	$Q_{removed}$ [W]	v_{jets} [m/s]	ΔP [Pa]	$Q_{removed}$ [W]	v_{jets} [m/s]	ΔP [Pa]	$Q_{removed}$ [W]	v_{jets} [m/s]	ΔP [Pa]
50	**418.7**	3.76	76899	**337.1**	16.70	*894007*	**125.3**	27.53	*2236197*
100	**243.1**	*0.94*	3678	**390.2**	4.17	33600	**289.0**	6.88	79216
150	**148.7**	*0.42*	652	**300.3**	*1.86*	5170	**280.0**	3.06	11661

Alternatively, setting the first derivative of Eq. (14) with respect to d_n to zero, the value of d_n can be obtained as,

$$d_n = 3.876 \cdot 10^{-2} \text{ s} \tag{15}$$

The minimum flowrate is then obtained by substituting Eq. (5) into Eq. (14). This yields,

$$\dot{V} = \left[\frac{Q_{\text{removed}}}{\text{Pr}^{0.48}\, k(T_w - T_{\text{jets}})A_H} \right]^{1/0.78} \frac{0.365 N_{\text{jets}} \pi \mu s^{2.282}}{\rho} \tag{16}$$

The smallest feasible value of s will yield the minimum flowrate. After the minimization of Q_{pumping}, it must be checked that jet velocity and pressure drop have acceptable values.

As a final consideration, it is interesting to see which combination of jet diameter and jet pitch gives the highest heat removal rate for the same flowrate. Table 6 shows an example for a water flowrate of $2\cdot10^{-6}$ m^3/s impinging on an area of 292 mm^2 (6.84 μl/mm^2 s), with a jet temperature of 18.6°C, $T_w - T_{\text{jets}} = 60°C$, and an orifice plate thickness of 0.51 mm. The best performing configuration is the one having the largest number of the smallest diameter jets. When the jet number is decreased the best configuration has a $d_n = 100$ μm. At smaller values of d_n, the jets are too far apart, and the increase in v_{jet} cannot compensate for the effect of large jet spacing. At a higher d_n, the jet velocity is too low and the increased s/d_n does not make up for it.

The numbers in italics indicate parameters that are not acceptable. For those jet diameters and velocities below 2 m/s (using water), jets start to merge at the exit of the orifice plate. A pressure drop above 0.5 MPa is not acceptable for electronic applications. It should be noted that the pumping power given here does not include pump efficiency and the pressure losses in the piping forming the loop. For implementing the concept in a closed system a fan must also be used to dissipate heat to the environment. Such fan losses will also be in addition to the pumping power calculated here.

Summary

Single phase heat transfer under circular free surface microjet arrays using water and FC 40 as tests liquids has been experimentally studied. It was found that Nu improves with increasing Re_{dn}, and Pr, and decreasing s/d_n. The Nusselt number was found to have stronger dependence on the Reynolds number than that reported by previous researchers. However, the previous studies did not consider arrays with as many jets as those used in the present study, and also never used jet diameters smaller than 500 μm.

An empirical correlation containing only three dimensionless parameters has been developed. It was used in conjunction with the pressure drop data to find an optimal configuration which depends on the heat flux and the cooling requirements. For the 150 W/cm^2 sample case, the optimal configuration, yields a pumping power of $2.53\cdot10^{-2}$ W using a jet spacing of 2 mm and a jet diameter of 325 μm. If the results of this study are extrapolated to larger jet spacing, the optimal configuration for the same case will require a jet spacing of 5 mm and jet diameter of 775 μm, consuming $1.16\cdot10^{-2}$ W.

If the flowrate has to be minimized, it was found that $d_n = 3.876\cdot10^{-2}$ s. In employing this approach, one must always verify that the jet velocity and the pressure drop have acceptable values. If the flowrate is kept constant, the configuration that has the highest heat removal rate has a large number of small diameter jets. For example, 418 W could be removed using a jet spacing of 1 mm and a jet diameter of 50 μm.

Acknowledgments

This work received support from DARPA under the HERETIC program.

Nomenclature

A = area (m^2)
c_p = specific heat (J/kg K)
d = jet or droplet diameter (m)
D = diameter (m)
e = Napier's constant
h = heat transfer coefficient (W/m^2 K), $h = q/(T_w - T_{\text{liq}})$
h_{fg} = latent heat of vaporization (J/kg)
k = thermal conductivity (W/mK)
L = heater characteristic length (m)
L^* = length of the radial flow region (m)
N = number of jets
Nu = Nusselt number $\text{Nu} = hd_n/k$
ΔP = pressure drop across the nozzle or the orifice plate (Pa)
Pr = Prandtl number
q = heat flux (W/m^2)
Q = power (W)
Re = Reynolds number $\text{Re} = \rho v_{\text{jets}} d_n/v$
s = jet pitch: distance between the centers of two neghiboring jets (m)
STD = standard deviation
T = temperature (K)
t = orifice plate thickness (m)
v = velocity (m/s)
$\dot{V}$ = volumetric flowrate (m^3/s)
z = nozzle to heater distance (m)

Greek symbols

α = thermal diffusivity (m^2/s)

μ = dynamic viscosity (kg/ms)
ν = kinematic viscosity (m^2/s)
ρ = density (kg/m^3)
σ = surface tension (N/m)

Subscripts

H = heater
i = at the impinging point
jets = jets
n = at nozzle or orifice plate exit
plate = of the orifice plate
w = wall or surface

References

[1] Webb, B. W., and Ma, C. F., 1995, "Single-Phase Liquid Jet Impingement," Adv. Heat Transfer, **26**, pp. 105–217.
[2] Elison, B., and Webb, B. W., 1994, "Local Heat Transfer to Impinging Liquid Jets in the Initially Laminar, Transitional, and Turbulent Regimes," Int. J. Heat Mass Transfer, **37**(8), pp. 1207–1216.
[3] Jiji, L. J., and Dagan, Z., 1987, "Experimental Investigation of Single-Phase Multijet Impingement Cooling of an Array of Microelectronic Heat Sources," in Proceedings of the International Symposium on Cooling Technology for Electronic Equipment, W. Aung, ed., Hemisphere Publishing Corporation, Washington, D.C., pp. 333–351.
[4] Pan, Y., and Webb, B. W., 1995, "Heat Transfer Characteristics of Arrays of Free-Surface Liquid Jets," ASME J. Heat Transfer, **117**, pp. 878–883.
[5] Womac, D. J., Incropera, F. P., and Ramadhyani, S., 1994, "Correlating Equations for Impingement Cooling of Small Heat Sources with Multiple Circular Liquid Jets," ASME J. Heat Transfer, **116**, pp. 482–486.
[6] Womac, D. J., Ramadhyani, S., and Incropera, F. P., 1993, "Correlating Equations for Impingement Cooling of Small Heat Sources with Single Circular Liquid Jets," ASME J. Heat Transfer, **115**, pp. 106–115.
[7] Yonehara, N., and Ito, I., 1982, "Cooling Characteristics of Impinging Multiple Water Jets on a Horizontal Plane," Technol. Rep. Kyushu Univ., **24**, pp. 267–281.
[8] Oliphant, K., Webb, B. W., and McQuay, M. Q., 1998, "An Experimental Comparison of Liquid Jet Array and Spray Impingement Cooling in the Non-Boiling Regime," Exp. Therm. Fluid Sci., **18**, pp. 1–10.
[9] Jiang, S., 2002, "Heat Removal Using Microjet Arrays and Microdroplets in Open and Closed Systems for Electronic Cooling," Ph.D. dissertation, University of California, Los Angeles, Los Angeles, CA.
[10] Kline, S. J., and McClintock, F. A., 1953, "Describing Uncertainties in Single-Sample Experiments," Mech. Eng. (Am. Soc. Mech. Eng.), **75**, pp. 3–12.
[11] Ildechik, I. E., 1994, *Handbook of Hydraulic Resistance*, CRC Press, Boca Raton, FL.

Fluid Flow and Thermal Characteristics of a Microchannel Heat Sink Subject to an Impinging Air Jet

Seok Pil Jang
School of Aerospace and Mechanical Engineering,
Hankuk Aviation University,
Goyang, Gyeonggi-do, 412-791 Korea

Sung Jin Kim[1]
e-mail: sungjinkim@kaist.ac.kr
Department of Mechanical Engineering,
Korea Advanced Institute of Science and Technology,
Daejeon, 305-701, Korea

In the present study, fluid-flow and heat-transfer characteristics of a microchannel heat sink subject to an impinging jet are experimentally investigated. In order to evaluate the cooling performance of a microchannel heat sink subject to an impinging jet under the condition of fixed pumping power, the pressure drop across the heat sink and temperature distributions at its base are measured. Specifically, a microthermal sensor array is fabricated and used to accurately measure temperature distributions at the base of the heat sink. Based on these experimental results, a correlation for the pressure drop across a microchannel heat sink subject to an impinging jet and a correlation for its thermal resistance are suggested. In addition, it is shown that the cooling performance of an optimized microchannel heat sink subject to an impinging jet is enhanced by about 21% compared to that of the optimized microchannel heat sink with a parallel flow under the fixed-pumping-power condition. [DOI: 10.1115/1.1924628]

1 Introduction

As electronic equipment becomes smaller and more advanced, it necessitates higher circuit integration per unit area, which in turn contributes to a rapid increase of heat generation [1]. As a consequence, the working temperature of electronic components may exceed a desired temperature level, which increases the critical failure rate of the equipment in the absence of sufficient heat removal. Therefore, advanced electronic equipment with small size and high heat generation requires efficient and compact cooling devices to provide reliable system operation.

Many ideas for improving cooling technology of electronic equipment with high heat generation and compact size have been proposed, including a microchannel heat sink with a parallel flow and a manifold microchannel heat sink. The microchannel heat sink with a parallel flow was first introduced by Tuckerman and Pease [2,3] two decades ago. The microchannel heat sink was shown to have an advantage in that the heat transfer coefficient is much higher than that of a conventional heat sink because it is inversely proportional to the hydraulic diameter of the channel. However, Copeland et al. [4] indicated that a microchannel heat sink with a parallel flow has two disadvantages: one is a high pressure drop due to the combination of narrow channel width and high flow rate, and the other is a significant temperature difference within the heat sink. Therefore, as an alternative cooling method, they introduced a manifold microchannel heat sink for cooling electronic equipment with high heat generation, as shown in Fig. 1(*a*). They explained that the manifold microchannel heat sink has a smaller pressure drop than the microchannel heat sink with a parallel flow. Pak et al. [5] presented that the thermal resistance of the optimal manifold microchannel heat sink for pumping power ranging from 0.02 W to 1.2 W is approximately 35% lower than that of the microchannel heat sink with a parallel flow. Even though the manifold microchannel heat sink has higher cooling performance and lower pressure drop, it is difficult to apply to advanced electronic equipment with a compact size because the manifold itself is larger than the microchannel heat sink.

In this paper, we study heat transfer and fluid flow in a microchannel heat sink subject to an impinging air jet. This type of heat sink retains the high heat transfer coefficient associated with the typical microchannel heat sink and experiences a low pressure drop compared to the microchannel heat sink with a parallel flow. The thermal characteristics of this type of microchannel heat sink are experimentally investigated. In order to evaluate the cooling

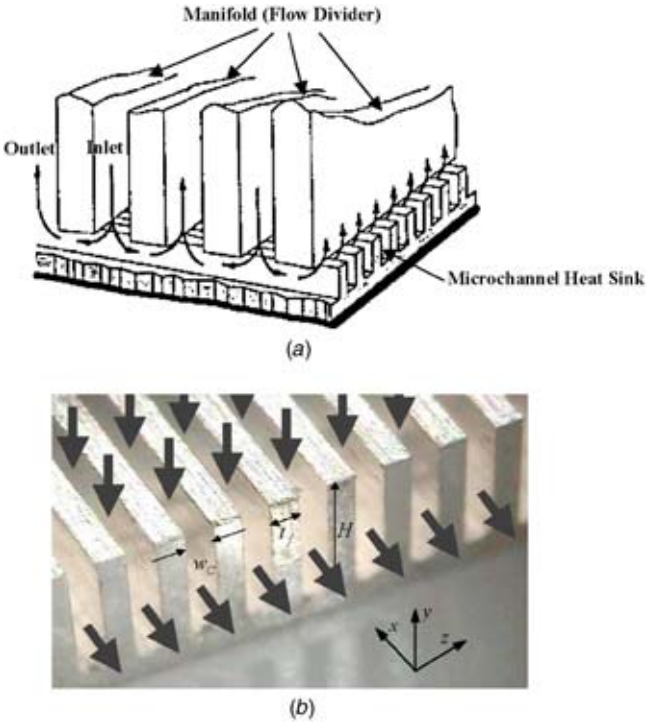

Fig. 1 Cooling technology for electronic equipment: (*a*) manifold microchannel heat sink [5]; (*b*) microchannel heat sink

[1]Author for correspondence.

Contributed by the Heat Transfer Division for publication in the JOURNAL OF HEAT TRANSFER. Manuscript received April 7, 2004. Final manuscript received December 26, 2004. Review conducted by: Karen Thole.

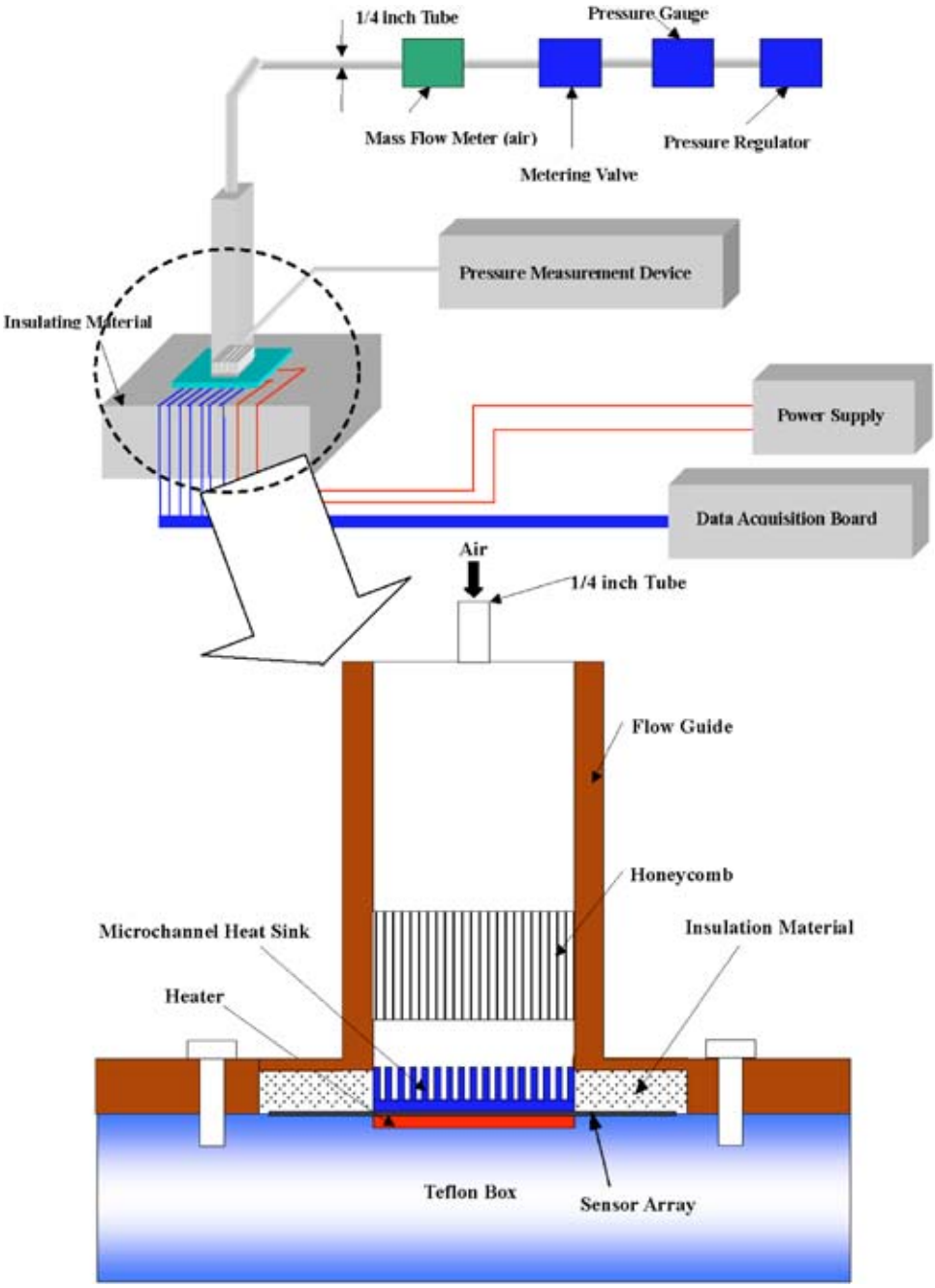

Fig. 2 Experimental apparatus

performance of a microchannel heat sink subject to an impinging air jet under the condition of fixed pumping power, the pressure drop across the heat sink and temperature distributions at its base are measured. Specifically, a microthermal sensor array developed by the authors is used to accurately measure temperature distributions at the base of the heat sink. Based on these experimental results, a correlation for the pressure drop across a microchannel heat sink subject to an impinging jet and a correlation for its thermal resistance are suggested. In addition, we show that the cooling performance of a microchannel heat sink subject to an impinging jet is superior to that of the microchannel heat sink with a parallel flow under the fixed-pumping-power condition.

2 Experimental Apparatus

The problem under consideration in this paper is an impinging air flow through a microchannel heat sink, which is laminar and steady. The fluid impinges on the microchannel heat sink along the y-axis and then leaves parallel to the x-axis, as shown in Fig. 1(b). For the experimental investigation, we fabricated microchannel heat sinks using micromechanical sawing processes. The microchannel heat sinks have a channel width of 200 μm, 400 μm, 600 μm, and 800 μm, a fin thickness of 200 μm, and a channel height of 0.6 mm, 1.0 mm, 1.4 mm, 1.8 mm, and 2.2 mm, respectively. The base of the microchannel heat sink is 10 mm $\times$ 10 mm. The number of microchannel heat sinks that are used in this experiment is 20.

The experimental apparatus is shown in Fig. 2. Air is used as a coolant. An MFC (mass flow controller) manufactured by Brooks, Inc. is used to control the mass flow rate of air. Its accuracy and repeatability are ±1% and ±0.15%, respectively. The full-scale range of the MFC is 100 SLM (standard liters per minute). To measure the pressure drop across the microchannel heat sink, a

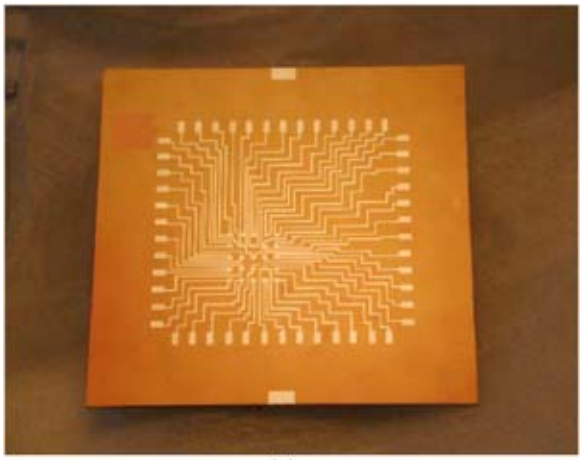

(a)

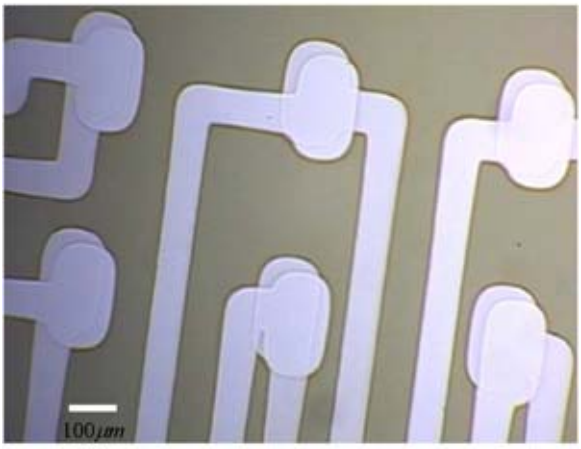

(b)

Fig. 3 Microthermal sensor array: (*a*) microfabricated microthermal sensor array; (*b*) junctions of a microthermal sensor array

DP 103 pressure transducer manufactured by Validyne, Inc. is used. Its full-scale range and accuracy are 3500 Pa and 0.25%, respectively. In order for the air flow to impinge uniformly on the microchannel heat sink, a honeycomb is placed in the rectangular duct through which air is delivered [6]. The honeycomb consists of rectangular channels with the size of 0.5 mm $\times$ 0.5 mm. The microchannel heat sink is placed on top of the microthermal sensor array. In order to reduce the thermal contact resistance between the microchannel heat sink and the microthermal sensor array, a thermally conductive epoxy manufactured by OMEGA, Inc. is used. The thermal conductivity of the epoxy is 16.6 W/mK. A heater with maximum heat generation of 30 W and a size of 1 cm $\times$ 1 cm is attached under the microthermal sensor array with the same epoxy. The sides of the microchannel heat sink are lined with insulation material. An insulating box made of Teflon® is mounted underneath the heater and the sensor array to minimize the heat loss through the insulating box. We have measured the temperatures of the insulating box in order to estimate the heat loss through the insulating box.

Microthermal Sensor Array. Various temperature measurement methods such as thermocouples and liquid crystals have been used to measure the surface temperature of conventional structures [7–11]. Of the two, many investigators have chosen thermocouples over liquid crystals in evaluating the thermal resistance of conventional heat sinks because the base of heat sinks where temperatures are measured is not typically exposed for

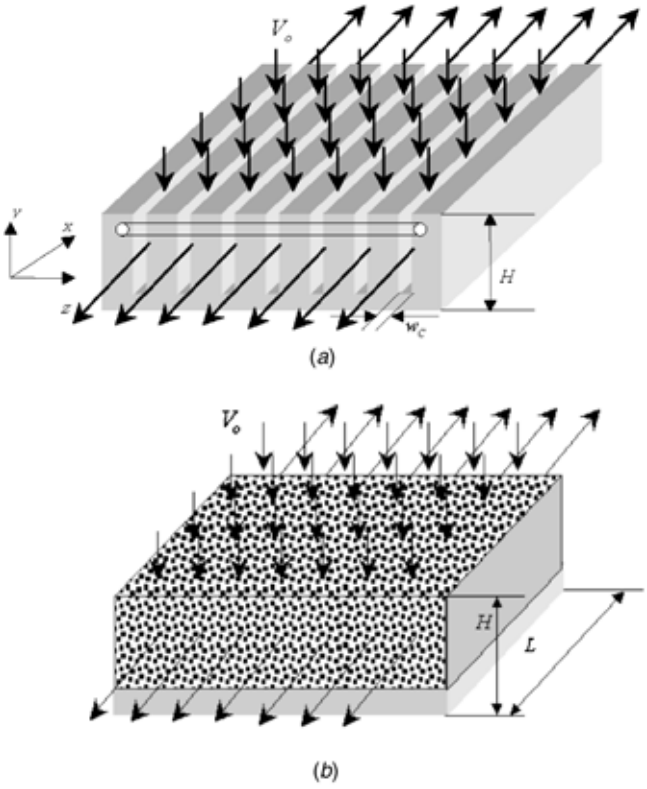

Fig. 4 Porous medium approach: (*a*) microchannel heat sink subject to an impinging jet; (*b*) equivalent porous medium

measurement. However, commercial thermocouples, which have a thickness of several hundred microns, have disadvantages for measuring temperature distributions at the surface of a microscale structure. It is impossible to attach a thermocouple to an exact location at the surface without modifying the surface geometry, let alone measure the surface temperatures at many locations. Therefore, this method for measuring the surface temperature distribution of a microscale structure is not appropriate [12].

In the present study, a microthermal sensor array is fabricated based on the idea presented by Jang et al. [12] for measuring temperature distributions of a microchannel heat sink subject to an impinging jet. The microthermal sensor array has 25 sensors in the area of 5 mm $\times$ 5 mm on a silicon wafer. The microthermal sensor array uses two materials, Alumel and Chromel, to cause the Seebeck effect. These materials are the same ones used to make a *K*-type thermocouple. A photograph of the microthermal sensor array manufactured for this work is shown in Fig. 3(*a*). The size of a junction of the microthermal sensor array is 116 μm $\times$ 233 μm as shown in Fig. 3(*b*). Temperature measurements from the microthermal sensor array agree with those obtained using a commercial *K*-type thermocouple to within 0.6%.

3 Results and Discussion

Fluid Flow Characteristics. In order to show the fluid-flow characteristics of the microchannel heat sink subject to an impinging jet, the pressure drop across the microchannel heat sink is measured. In addition, a correlation for the pressure drop is mathematically derived by using a porous-medium approach based on the idea proposed by Kim and Jang [13]. Results from this correlation are compared with experimental results.

As shown in Fig. 4, Kim and Jang [13] modeled the microchannel heat sink subject to an impinging jet as a porous medium. The representative elementary volume (REV) used for the volume-averaging is a slender cylinder aligned parallel to the *z*-direction.

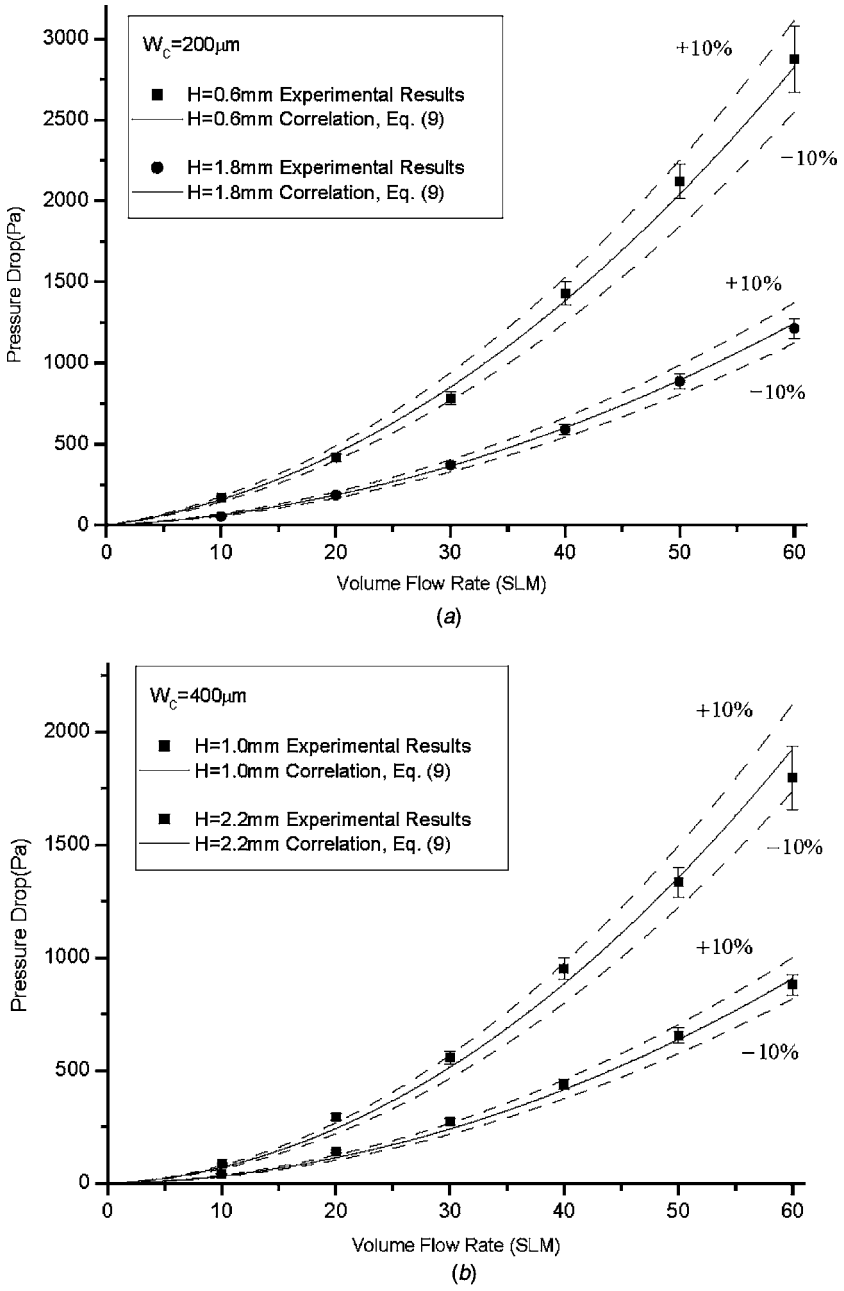

Fig. 5 Comparison between the pressure drop obtained from the correlation of Eq. (9) and that from experimental results: (*a*) w_C=200 μm; (*b*) w_C=400 μm; (*c*) w_C=600 μm; (*d*) w_C=800 μm

They obtained similarity solutions for the velocity profile and the pressure drop for a microchannel heat sink subject to an impinging jet and showed that the similarity solutions agreed closely with classical numerical results. Their solutions are restricted within the Darcy flow regime. In other words, their solutions can be used only when the inertia force can be neglected in a porous medium. Because we are interested in the flow regime in which the inertia force is dominant, the Brinkman-extended Darcy equation used by Kim and Jang [13] is modified by including the Forchheimer inertia term. The modified Darcy equations, which are the momentum equations averaged along the *z*-axis, are given as follows:

X-momentum equation

$$\langle u\rangle_f\frac{\partial\langle u\rangle_f}{\partial x}+\langle v\rangle_f\frac{\partial\langle u\rangle_f}{\partial y}=-\frac{1}{\rho}\frac{\partial\langle p\rangle_f}{\partial x}+\nu_f\left[\frac{\partial^2\langle u\rangle_f}{\partial x^2}+\frac{\partial^2\langle u\rangle_f}{\partial y^2}\right]-\frac{\varepsilon_x\nu_f}{K_x}\langle u\rangle_f-\frac{C_{E,x}\varepsilon_x^2}{K_x^{1/2}}|\langle \boldsymbol{V}\rangle|\langle u\rangle_f \quad (1)$$

Y-momentum equation

$$\langle u\rangle_f\frac{\partial\langle v\rangle_f}{\partial x}+\langle v\rangle_f\frac{\partial\langle v\rangle_f}{\partial y}=-\frac{1}{\rho}\frac{\partial\langle p\rangle_f}{\partial y}+\nu_f\left[\frac{\partial^2\langle v\rangle_f}{\partial x^2}+\frac{\partial^2\langle v\rangle_f}{\partial y^2}\right]-\frac{\varepsilon_y\nu_f}{K_y}\langle v\rangle_f-\frac{C_{E,y}\varepsilon_y^2}{K_y^{1/2}}|\langle \boldsymbol{V}\rangle|\langle v\rangle_f$$

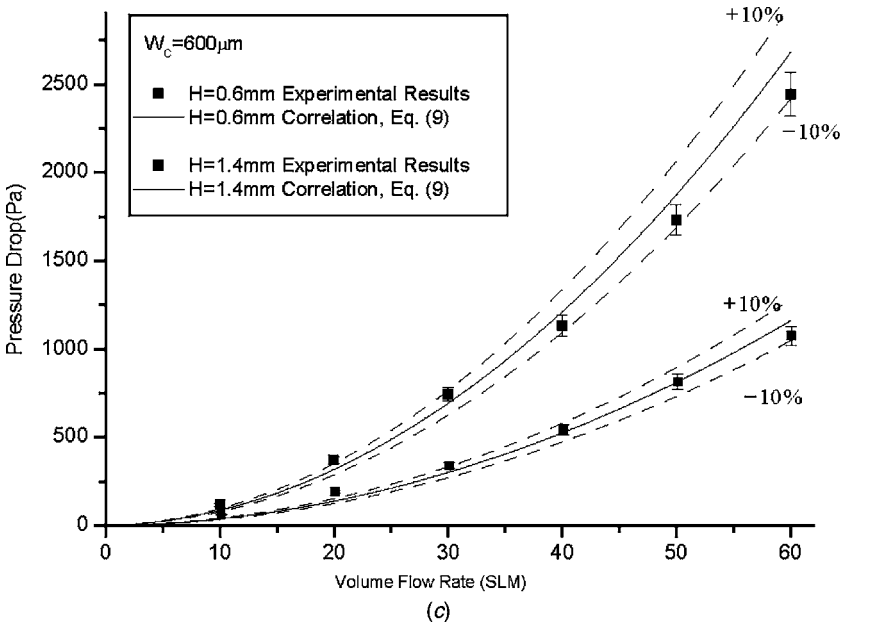

(*c*)

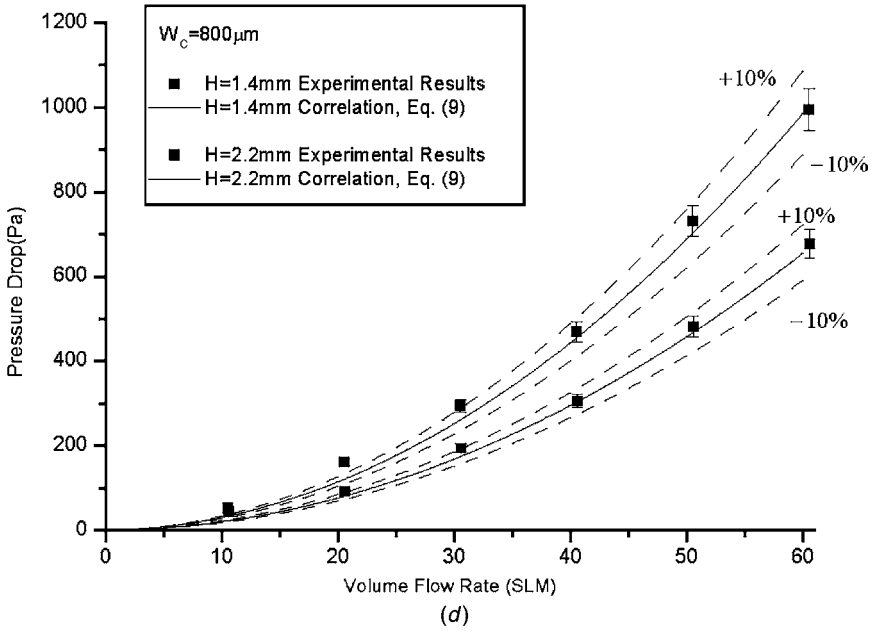

(*d*)

Fig. 5 (***Continued***).

$$\langle u\rangle_f = \langle v\rangle_f = 0 \text{ at } y = 0, \quad \langle v\rangle_f = V_0 \text{ at } y = H \tag{2}$$

where $\langle\ \rangle_f$ denotes a volume-averaged value over the fluid phase and p, ν_f, ε, K, C_E, V_0, and H are pressure, fluid dynamic viscosity, porosity, permeability, Ergun coefficient, impinging velocity at the inlet of the microchannel heat sink, and channel height, respectively.

Since

$$\varepsilon_x = \varepsilon_y = \varepsilon = \frac{w_c}{w} \tag{3}$$

it follows that

$$K_x = K_y = K = \frac{\varepsilon w_c^2}{12} \tag{4}$$

In order to derive a correlation for the pressure drop mathematically, the stream function of an impinging flow in a porous medium is assumed to be a fractional function, as in the case of inviscid flow near the stagnation point over a flat plate [13]. This is due to the fact that the boundary layer thickness is much smaller than the channel height. Based on this assumption, the velocities can be represented as

$$\langle u\rangle_f = Bx, \quad \langle v\rangle_f = -By \tag{5}$$

Substituting Eq. (5) into Eqs. (1) and (2), the pressure drop across a microchannel heat sink subject to an impinging jet can be obtained as follows:

$$\Delta p = \rho\left(\frac{V_0}{H}\right)^2\left(\frac{L^2}{8}\right)\left(1 + \frac{12}{\mathrm{Re}_{w_C}}\frac{H}{w_C} + \frac{C_{E,x}\varepsilon^2 L}{3K^{1/2}}\right) - \rho\left(\frac{V_0}{2}\right)^2\left(2 - \frac{24}{\mathrm{Re}_{w_C}}\frac{H}{w_C} - \frac{4C_{E,y}\varepsilon^2 H}{3K^{1/2}}\right) \tag{6}$$

The Ergun coefficient is determined using the general correlation presented by Jang [14] as

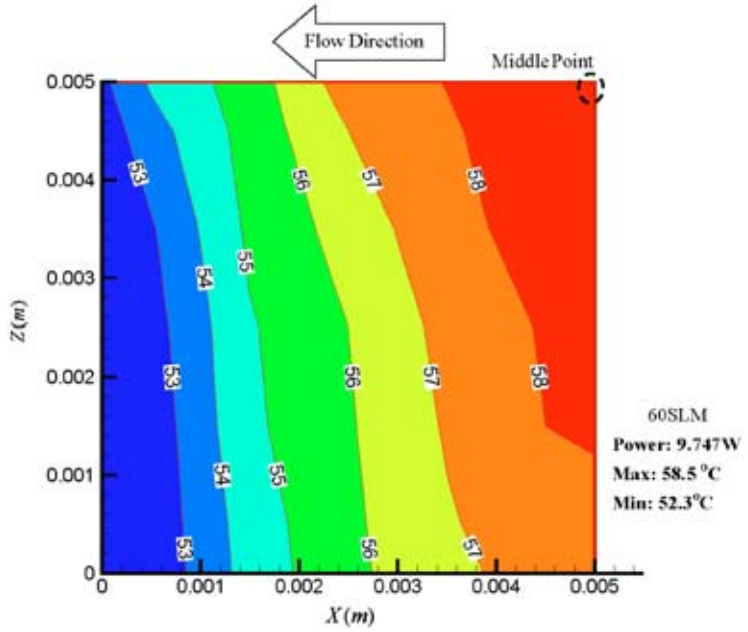

Fig. 6 Temperature distribution measured experimentally on the base of the microchannel heat sink subject to an impinging jet

$$C_{E,i} = 0.525\left[\left(\frac{P}{\sqrt{A_f}}\right)_i^3 (1-\varepsilon_i^{5/2})\right]^{0.4} - 0.32, \quad 0 < \mathrm{Re}_{d_P} < 500 \tag{7}$$

In order to check the validity of the proposed correlation for the pressure drop across the microchannel heat sink subject to an impinging jet, we should compare it to the experimentally measured pressure drop. However, the pressure drop obtained from experimental results includes the inlet effect. So, we should include the inlet effect into Eq. (6). The effect of the inlet on the pressure drop is considered using the following equation [15]:

$$\Delta p_{\mathrm{inlet}} = \frac{1}{2}\rho V_0^2\left[1-\left(\frac{A_0}{A_1}\right)^2\right] + K_{\mathrm{inlet}} \tag{8}$$

where A_1 and A_0 are cross-sectional areas immediately before and after the entrance of the microchannel heat sink, respectively. K_{inlet} denotes the loss coefficient, which can be neglected because the flow is laminar [15]. In addition, the effect of the outlet on the pressure drop can be neglected due to the very small ratio of the channel area to the outlet area. Consequently, the pressure drop including the inlet effect is given as

$$\Delta p = \rho\left(\frac{V_0}{H}\right)^2\left(\frac{L^2}{8}\right)\left(1+\frac{12}{\mathrm{Re}_{w_C}}\frac{H}{w_C}+\frac{C_{E,x}\varepsilon^2 L}{3K_x^{1/2}}\right) - \rho\left(\frac{V_0}{2}\right)^2 \times\left(2-\frac{24}{\mathrm{Re}_{w_C}}\frac{H}{w_C}-\frac{4C_{E,y}\varepsilon^2 H}{3K_y^{1/2}}\right)+\frac{1}{2}\rho V_0^2\left[1-\left(\frac{A_0}{A_1}\right)^2\right] \tag{9}$$

The results for the pressure drop calculated by Eq. (9) are compared with those obtained experimentally, as shown in Fig. 5. The proposed correlation for the pressured drop corresponds to the experimental results within about ±10%.

Thermal Characteristics. In order to show the thermal characteristics of the microchannel heat sink subject to an impinging jet, temperature distributions at its base are measured using the microthermal sensor array. The area where temperature is measured is a quarter of the base area of the microchannel heat sink because the temperature distribution is symmetric over the rest of the area. Figure 6 shows the temperature distributions measured experimentally over a quarter area of the base of the microchannel heat sink with a size of 1 cm × 1 cm when a volume flow rate of air is 60 SLM. A center point at the base of the heat sink has the maximum temperature, while the corner point has a minimum temperature because velocity along the *x*-axis in the microchannel heat sink is the lowest at the center point. In addition, the temperature difference along the *z*-axis, perpendicular to the channel direction, is less than 1 °C and that along the *x*-axis, the channel direction, is about 5 °C. This is due to the fact that the velocity is almost uniform along the *z*-axis and increases linearly in the streamwise direction (along the *x*-axis).

The cooling performance of the microchannel heat sink subject to an impinging jet can be evaluated in terms of the thermal resistance [16,17]. The thermal resistance can be defined as follows:

$$\theta = \frac{T_{\max} - T_{\mathrm{inlet}}}{q} \tag{10}$$

where θ, $T_{\max}$, T_{inlet}, and q are thermal resistance, maximum temperature, at the base of the microchannel heat sink, inlet temperature, and total amount of heat, respectively. The thermal resistance is expressed as the sum of the thermal resistance of the fin and that of the flow [18]:

$$\theta = \frac{T_{\max} - T_{b,\mathrm{out}}}{q} + \frac{T_{b,\mathrm{out}} - T_{\mathrm{inlet}}}{q} = \frac{T_{\max} - T_{b,\mathrm{out}}}{q} + \frac{1}{\dot{m}C_P} \tag{11}$$

The first term of Eq. (11) depends on geometry and the Reynolds number. Based on the experimental results, the first term is correlated as follows:

$$\frac{T_{\max} - T_{b,\mathrm{out}}}{q} = f(H, L, w_C, \varepsilon, \mathrm{Re}_{d_P}) = 0.028\frac{1}{k_f L}\left(\frac{w}{L}\right)^{0.332}(\mathrm{Re}_{d_P}\cdot \mathrm{Ar})^{-0.324} \tag{12}$$

where

$$w = w_C + t_f, \quad \mathrm{Ar} = \frac{H}{w_C}, \quad d_P = \frac{4Hw_C}{2H + w_C}. \tag{13}$$

In the above equations, Ar, d_P, L, n, t_f, w, and w_C denote aspect ratio, pore diameter, base length of the microchannel heat sink, number of channels, fin thickness, sum of the channel width and the fin thickness, and channel width, respectively. Substituting Eq.

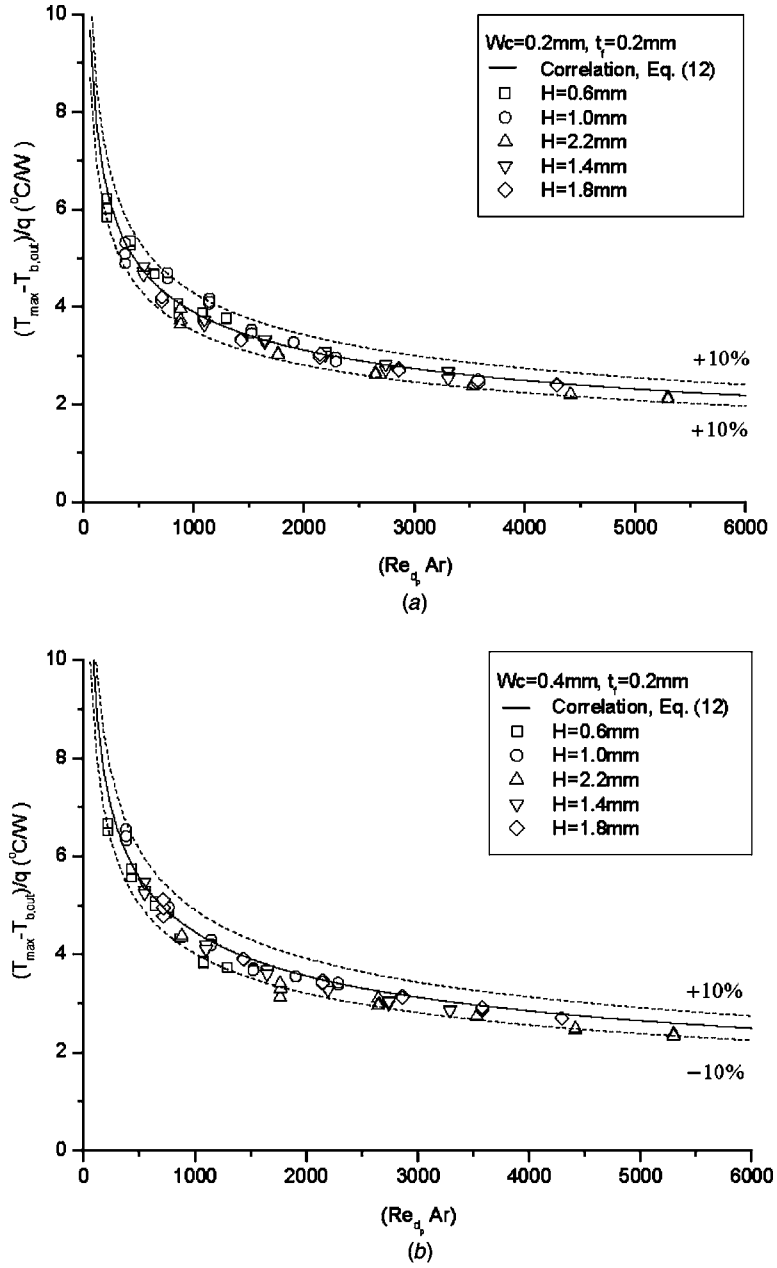

Fig. 7 Comparison between the thermal resistance obtained from the correlation of Eq. (12) and that from experimental results: (*a*) w_C=200 μm; (*b*) w_C=400 μm; (*c*) w_C=600 μm; (*d*) w_C=800 μm

(12) into Eq. (11), a correlation for the thermal resistance of the microchannel heat sink subject to an impinging jet is obtained as

$$\theta = \frac{1}{\dot{m}C_P} + 0.028\frac{1}{k_f L}\left(\frac{w}{L}\right)^{0.332}(\mathrm{Re}_{d_p}\cdot Ar)^{-0.324}$$

$$3 \leqslant Ar \leqslant 11, \quad 0 < \mathrm{Re}_{d_p} < 500 \tag{14}$$

It is worth mentioning that the functional dependence of the thermal resistance in Eq. (14) is consistent with the thermal characteristics of the microchannel heat sink. Under fixed heat dissipation and geometry, according to Eq. (14) the thermal resistance of the microchannel heat sink is decreased if the volume flow rate is increased, as expected. In addition, under fixed volume flow rate and heat dissipation, the thermal resistance is decreased if the number of channels is increased or aspect ratio is increased. In order to check the validity of the correlation for the thermal resistance of the microchannel heat sink subject to an impinging jet, Eq. (12) is compared with experimental results as shown in Fig. 7. The proposed correlation corresponds to experimental results within about ±10%.

Comparison of the Cooling Performance. Based on the experimental results, we show that the microchannel heat sink subject to an impinging jet minimizes the two inherent disadvantages of the microchannel heat sink with a parallel flow which have been previously commented on by Copeland et al. [4]. Table 1 shows that the pressure drop through the microchannel heat sink subject to an impinging jet is decreased by about 90.5% compared to the heat sink with a parallel flow under fixed volume flow rate and geometry. These results mean that the microchannel heat sink subject to an impinging jet has a larger volume flow rate with a relatively smaller pressure difference. This is due mainly to the fact that the hydraulic diameter at the inlet of the microchannel heat sink subject to an impinging jet is larger than that of the

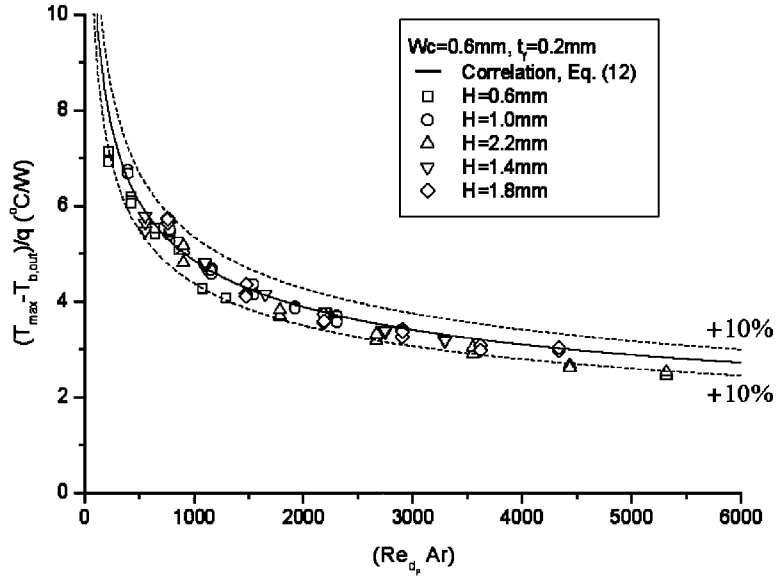

(*c*)

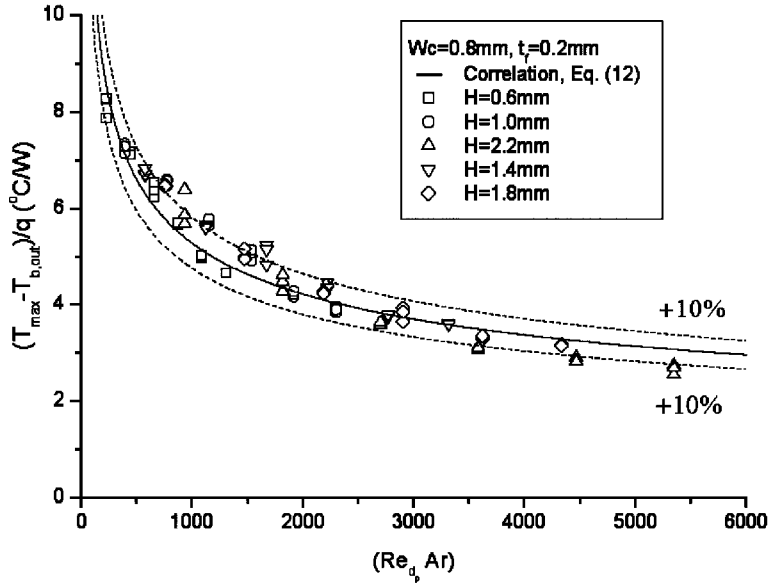

(*d*)

Fig. 7 (***Continued***).

microchannel heat sink with a parallel flow. The temperature difference across the base of the microchannel heat sink subject to an impinging jet is compared with that of the microchannel heat sink with a parallel flow as shown in Table 1. The results for the latter are obtained using the analytic solutions presented by Kim and Kim [19]. The temperature difference across the base of the microchannel heat sink subject to an impinging jet is 1.6 °C, while the temperature difference across the base of the microchannel heat sink with a parallel flow is 12.9 °C. Therefore, the temperature difference across the base of the former is only about 12.4% of that for the latter. This is because the length of the flow direction in the microchannel heat sink subject to an impinging jet is half that of the microchannel heat sink with a parallel flow, and the bulk-mean temperature of the fluid in the microchannel heat sink subject to an impinging jet is nearly constant.

To optimize the thermal performance of the microchannel heat sink subject to an impinging jet, its thermal resistance is minimized under the given constraints. So, in this paper, under the constraints of fixed pumping power and channel height, the optimum geometry of a microchannel heat sink subject to an impinging jet is obtained using the correlations developed in this study for the pressure drop and the thermal resistance, as shown in Table 2. In addition, the thermal resistance of the optimized microchannel heat sink subject to an impinging jet is compared to that of the optimized microchannel heat with a parallel flow presented by Kim and Kim [19]. Table 2 shows that the cooling performance of the optimized microchannel heat sink subject to an impinging jet is enhanced by about 21% compared to that of the optimized microchannel heat sink with a parallel flow when the pumping power is 0.08 W and the channel height is limited to 2.2 mm. Consequently, the microchannel heat sink subject to an impinging jet is shown to be superior to the microchannel heat sink with a parallel flow as a cooling device for advanced electronic equipment with high heat generation and compact size.

Table 1 Comparison for the pressure drop and the temperature difference between the microchannel heat sinks subject to an impinging jet and a parallel flow

	Microchannel heat sink with a parallel flow (Numerical Results by Kim and Kim [19])	Microchannel heat sink subject to an impinging jet (Experimental Results)
Geometry	Channel Height=1.4 mm Channel Width=200 mm Fin Thickness=200 mm	Channel Height =1.4 mm Channel Width=200 mm Fin Thickness=200 mm
Pressure Drop Q =30 SLM	4345.8 Pa	409.8 Pa
Temperature Difference Q =20SLM, Heat Source = 4.84W/cm^2	12.9°C	1.6°C

4 Conclusion

In this paper, we study heat transfer and fluid flow in a microchannel heat sink subject to an impinging air jet. This type of heat sink retains the high heat transfer coefficient associated with the typical microchannel heat sink and experiences a low pressure drop compared to the microchannel heat sink with a parallel flow. The thermal characteristics of a microchannel heat sink subject to an impinging jet are experimentally investigated. In order to evaluate the cooling performance of a microchannel heat sink subject to an impinging jet, the pressure drop across the microchannel heat sink and temperature distributions at its base are measured. Specifically, a microthermal sensor array developed by the authors is used to accurately measure temperature distributions at the base of the heat sink. Based on these experimental results, we suggest correlations for the pressure drop across a microchannel heat sink subject to an impinging jet as well as its thermal resistance. The correlations for the pressure drop, the thermal resistance are compared with experimental results, and both are shown to match with experimental results to within ±10%. In addition, we show that the microchannel heat sink subject to an impinging jet minimizes the two inherent disadvantages of the microchannel heat sink with a parallel flow which have been previously noted by Copeland et al. [4]. Finally, it is shown that the cooling performance of an optimized microchannel heat sink subject to an impinging jet is enhanced by about 21% compared to that of the optimized microchannel heat sink with a parallel flow when the pumping power is 0.08 W and the channel height is limited to 2.2 mm.

Acknowledgments

This work was supported by the Center for Electronic Packaging Materials of Korea Science and Engineering Foundation.

Nomenclature

A_f = average cross-sectional area of fluid phase within an REV (Representative Elementary Volume) (m^2)
Ar = aspect ratio
C_E = Ergun coefficient
C_P = specific heat [J/kg K]
H = height of a microchannel heat sink (m)
k_f = thermal conductivity of a coolant (W/m^2 K)

Table 2 Comparison between the thermal resistance of the optimized microchannel heat sink subject to an impinging jet and that of the optimized microchannel heat sink with a parallel flow

	Microchannel Heat Sink Subject to an Impinging Jet	Microchannel Heat Sink With a Parallel Flow [19]
Pumping Power	0.08 W	0.08 W
Channel Width	94.2 μm	277.1 μm
Fin Thickness	242.3 μm	32.1 μm
Channel Height	2.2 mm	2.2 mm
Pressure Drop	219 Pa	355 Pa
Total Thermal Resistance	4.786°C/W	6.045°C/W

K = permeability (m^2), defined in Eq. (4)
K_{inlet} = loss coefficient at the inlet
L = length of the base of a microchannel heat sink (m)
$\dot{m}$ = mass flow rate (kg/s)
n = number of channels
p = pressure (Pa)
P = average wetted perimeter in an REV
Re = Reynolds number
t_f = fin thickness (m)
T = temperature (°C)
u = volume averaged velocity in the x-direction (m/s)
v = volume averaged velocity in the y-direction (m/s)
V_0 = inlet velocity (m/s)
w = width of the base of a microchannel heat sink (m)
w_C = channel width (m)
t_f = fin thickness (m)

Greek symbols

β = fluid phase
ε = porosity, defined in Eq. (3)
ν = dynamic viscosity (m^2/s)
θ = thermal resistance (°C/W), defined in Eq. (10)
ρ = density (kg/m^3)

Subscript/superscripts

b = bulk mean
fin = fin
flow = flow
inlet = inlet
max = maximum

Special symbol

$\langle\ \rangle$ = volume-averaged value

References

[1] Chu, R. C., 1986, "Heat Transfer in Electronic Systems," in Proceedings of the 8th International Conference on Heat Transfer, New York, pp. 293–305.
[2] Tuckerman, D. B., and Pease, R. F. W., 1981, "High-Performance Heat Sinking for VLSI," IEEE Electron Device Lett., **2**, pp. 126–129.
[3] Tuckerman, D. B., and Pease, R. F. W., 1982, "Ultrahigh Thermal Conductance Microstructure for Integrated Circuits," *IEEE Proc. 32nd Electronics Conference*, pp. 145–149.
[4] Copeland, D., Behnia, M., and Nakayama, W., 1997, "Manifold Microchannel Heat Sinks: Isothermal Analysis," IEEE Trans. Compon., Packag. Manuf. Technol., Part A, **20**, pp. 96–102.
[5] Pak, B. C., Chun, W. C., Baek, B. J., and Copeland, D., 1997, "Forced Air Cooling by Using Manifold Microchannel Heat Sinks," Adv. Electron. Circuit Packag., **2**, pp. 1837–1842.
[6] Kim, S. Y., Kang, B. H., and Kim, J. H., 2001, "Forced Convection From Aluminum Foam Materials in an Asymmetrically Heated Channel," Int. J. Heat Mass Transfer, **44**, pp. 1451–1454.
[7] Kim, S. J., and Jang, S. P., 2001, "Experimental and Numerical Analysis of Heat Transfer Phenomena in a Sensor Tube of a Mass Flow Controller," Int. J. Heat Mass Transfer, **44**, pp. 1711–1724.
[8] Kondo, Y., Behnia, M., Nakayama, W., and Matsushima, H., 1998, "Optimization of Finned Heat Sinks for Impingement Cooling of Electronic Packages," ASME J. Electron. Packag., **120**, pp. 259–266.
[9] Choi, S. B., Barron, R. F., and Warrington, R. O., 1991, "Fluid Flow and Heat Transfer in Microtubes," ASME Micromechanical Sensors, Actuators and Systems, **32**, pp. 123–134.
[10] Rahman, M. M., 2000, "Measurements of Heat Transfer in Microchannel Heat Sinks," Int. Commun. Heat Mass Transfer, **27**, pp. 497–506.
[11] Harms, T. M., Kazmierczak, F. M., and Gerner, F. M., 1999, "Developing Convective Heat Transfer in Deep Rectangular Microchannels," Int. J. Heat Fluid Flow, **20**, pp. 149–157.
[12] Jang, S. P., Kim, S. J., and Paik, K. W., 2003, "Experimental Investigation of Thermal Characteristics for a Microchannel Heat Sink Subject to an Impinging Jet, Using a Micro-Thermal Sensor Array," Sens. Actuators, A, **105**, pp. 211–224.
[13] Kim, S. J., and Jang, S. P., 2002, "Effects of the Darcy Number, the Prandtl Number and the Reynolds Number on Local Thermal Non-Equilibrium," Int. J. Heat Mass Transfer, **45**, pp. 3885–3896.
[14] Jang, S. P., "Experimental and Numerical Study on Heat Transfer Enhancement Using a Microchannel Heat Sink Subject to an Impinging Jet," Doctoral thesis in KAIST, 2004.
[15] Blevins, R. D., 1992, *Applied Fluid Dynamics Handbook*, Krieger, Malabar.
[16] Lau, K. S., Mahajan, L. R., 1989, "Effects of Tip Clearance and Fin Density on the Performance of Heat Sinks for VLSI Packages," IEEE Trans. Compon., Hybrids, Manuf. Technol., **12**, pp. 757–765.
[17] Hilbert, C., Sommerfeldt, S., Gupta, O., Herrell, D. J., 1990, "High Performance Air Cooled Heat Sinks for Integrated Circuits," IEEE Trans. Compon., Hybrids, Manuf. Technol., **13**, pp. 1022–1031.
[18] Knight, R. W., Hall, D. J., Gooding, S. J., and Jaeger, R. C., 1992, "Heat Sink Optimization With Application to Microchannels," IEEE Trans. Compon., Hybrids, Manuf. Technol., **15**, pp. 823–842.
[19] Kim, S. J., and Kim, D., 1999, "Forced Convection in Microstructure for Electronic Equipment Cooling," ASME J. Heat Transfer, **121**, pp. 635–645.

Journal of Heat Transfer

Technical Briefs

Effects of Backfill on Heat Transfer From a Buried Pipe

C. C. Ngo
Graduate Research Assistant
Student Member ASME

F. C. Lai
Associate Professor
Member ASME

School of Aerospace and Mechanical Engineering,
University of Oklahoma, Norman, OK 73019

Natural convection from a buried pipe with a layer of backfill is numerically examined in this study. The objective of the present study is to investigate how a step change in the permeability of the backfill would affect the flow patterns and heat transfer results. Numerical calculations have covered a wide range of the governing parameters (i.e., $10 \leqslant \mathrm{Ra}_1 \leqslant 500$ *and* $0.1 \leqslant K_1/K_2 \leqslant 10$*) for various backfill thicknesses* ($0.5 \leqslant t/r_i \leqslant 2$). *The results suggest that a more permeable backfill can minimize the heat loss and confine the flow to a region close to the pipe.*
[DOI: 10.1115/1.1924631]

Introduction

Natural convection from a buried pipe has been a subject of great interest for many decades because of its important applications in engineering, which include the underground pipelines for gas and oil, power cables, and the disposal of nuclear wastes. For these applications, the surface temperature of pipe or canister is usually higher than that of surroundings due to artificial (reduction of viscosity by heating for oil transportation) or natural (ohm heating for transmission cables and decay heating for nuclear wastes) causes. As a result, a buoyancy-induced flow is initiated. Previous studies have considered various configurations and models of porous media [1–5]. For example, Bau [1] has obtained analytical solutions for heat convection from a pipe buried in a semi-infinite porous medium using the perturbation method. Farouk and Shayer [2] as well as Christopher and Wang [3] have obtained numerical results using Darcy and non-Darcy formulations, respectively. Experimental results have been reported by Fernandez and Schrock [4] and Fand et al. [5]. An excellent review of this subject has been presented by Nield and Bejan [6]. However, all the studies mentioned above have considered only a homogeneous porous medium despite that heterogeneous or layered porous media are encountered more frequently in engineering applications. For buried pipes, the soil structure near the buried site is usually modified from its original state in the excavation process. A similar situation is found in the mining process for a nuclear waste repository. In addition to the changes brought about by the excavation/mining process, it is customary to add backfill to the buried pipes and waste canisters. As a result, the soil or bed rock that hosts the pipes and waste canisters are never homogeneous, but heterogeneous instead.

Unfortunately, there are only very limited reports in the literature that deal with heat convection from a buried pipe in a heterogeneous porous medium [7]. Previous studies that most closely resemble the problem at hand are those reported by Muralidhar et al. [8] and Ngo and Lai [9] in which a layered porous annulus was considered. For the problem considered here, the properties of the excavation disturbed zone and backfill around the buried pipe would be different from those of the soil far away from the pipe. Among the properties involved, permeability is the most important one because of its direct influence on the convective flow. Therefore, it is the objective of the present study to examine the effects of permeability variation in the porous medium on the heat transfer results. To this end, numerical calculations cover a wide range of the governing parameters (i.e., $10 \leqslant \mathrm{Ra}_1 \leqslant 500$ and $0.1 \leqslant K_1/K_2 \leqslant 10$) for various backfill thicknesses ($0.5 \leqslant t/r_i \leqslant 2$).

Formulation and Numerical Method

The geometry considered is a horizontal pipe with a radius of r_i buried in a saturated porous medium at a depth of d beneath the top surface (Fig. 1). As a first attempt, the top surface is assumed impermeable and maintained at a constant temperature T_c while the buried pipe is maintained at a higher temperature T_h. The excavation disturbed zone and backfill immediate around the buried pipe is assumed to form a layer of thickness t and which has a distinct permeability from the soil outside of this region (far field). Although this is an idealization of actual excavation, it does reflect the fact that the permeability of the soil near the pipe is sharply different from that far away from it. Since the physical domain is symmetric, only one half of the domain ($-w \leqslant x \leqslant 0$ and $-w \leqslant y \leqslant d$) is considered for computations.

The governing equations based on Darcy's law are given by

$$\frac{\partial u_i}{\partial x} + \frac{\partial v_i}{\partial y} = 0, \tag{1}$$

$$u_i = -\frac{K_i}{\mu}\frac{\partial p_i}{\partial x}, \tag{2}$$

$$v_i = -\frac{K_i}{\mu}\left[\frac{\partial p_i}{\partial y} + \rho g\right], \tag{3}$$

Contributed by the Heat Transfer Division for publication in the JOURNAL OF HEAT TRANSFER. Manuscript received February 12, 2004. Final manuscript received October 21, 2004. Review conducted by: N. K. Anand.

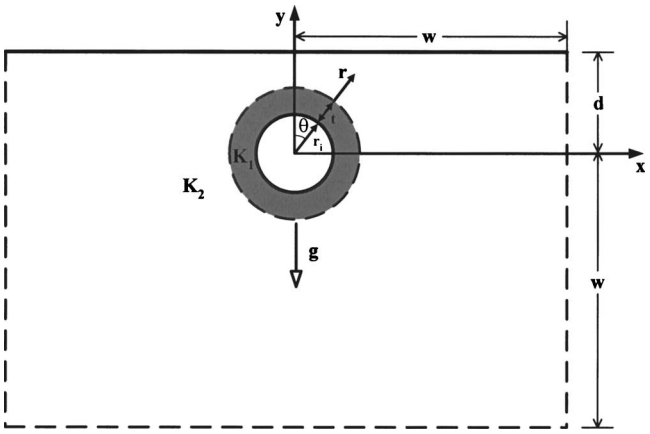

Fig. 1 A horizontal pipe embedded in a semi-infinite porous medium

$$u_i\frac{\partial T_i}{\partial x}+v_i\frac{\partial T_i}{\partial y}=\alpha_i\left[\frac{\partial^2 T_i}{\partial x^2}+\frac{\partial^2 T_i}{\partial y^2}\right], \tag{4}$$

where the subscript i (=1,2) denotes the inner and outer regions of the porous medium, respectively. The boundary conditions are given by

$$\text{At } r=r_i,\quad \pi\leqslant\theta\leqslant 2\pi,\quad T_1=T_h,\quad u_{r1}=0. \tag{5a}$$

$$\text{At } y=d,\quad -w\leqslant x\leqslant 0,\quad T_2=T_c,\quad v_2=0. \tag{5b}$$

$$\text{At } x=-w,\quad -w\leqslant y\leqslant d,\quad \frac{\partial T_2}{\partial x}=0,\quad v_2=0. \tag{5c}$$

$$\text{At } y=-w,\quad -w\leqslant x\leqslant 0,\quad \frac{\partial T_2}{\partial y}=0,\quad u_2=0. \tag{5d}$$

$$\text{At } x=0,\quad \pm r_i\leqslant y<\pm(r_i+t),\quad \frac{\partial T_1}{\partial x}=0,\quad u_1=0.$$

$$(r_i+t)<y\leqslant d,\quad \frac{\partial T_2}{\partial x}=0,\quad u_2=0.$$

$$-(r_i+t)<y\leqslant -w,\quad \frac{\partial T_2}{\partial x}=0,\quad u_2=0. \tag{5e}$$

Boundary conditions (5*c*) and (5*d*) state that heat and fluid flow far away from the pipe are negligibly small if the domain considered is sufficiently large.

In addition to the boundary conditions, appropriate conditions need to be specified at the interface between the two porous regions. The interface conditions applied in the present study are the continuity of pressure, temperature, radial flow, and heat flux:

$$p_1=p_2, \tag{6a}$$

$$T_1=T_2, \tag{6b}$$

$$u_{r1}=u_{r2}, \tag{6c}$$

$$k_1\frac{\partial T_1}{\partial r}=k_2\frac{\partial T_2}{\partial r}. \tag{6d}$$

The justification of these interface conditions has been given by McKibbin and O'Sullivan [10] as well as by Rana et al. [11]. In a separate study [12], it has been shown that the application of these interface conditions does produce a better agreement with experimental results.

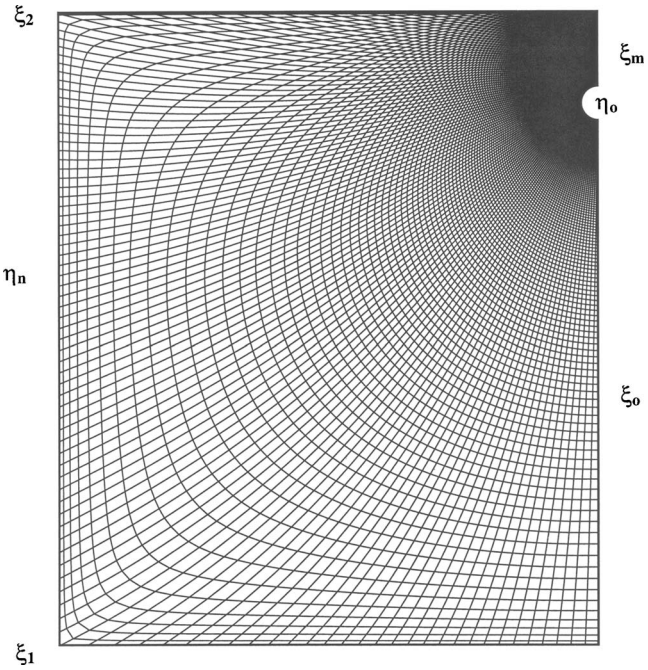

Fig. 2 Computational mesh for the present study

In this study, an elliptic grid-generating system has been chosen to produce the mesh for computations [13]. This approach is preferred over other coordinate transformation schemes for its ease of handling complex geometry. In addition, it has been successfully employed in the previous studies [7,14] involving a similar geometry. The computational mesh obtained for the present study is shown in Fig. 2.

After invoking the Boussinesq approximation,

$$\rho\approx\rho_c[1-\beta(T-T_c)], \tag{7}$$

one obtains the dimensionless governing equations in the transformed domain as follows:

$$\nabla^2_{\xi\eta}\Psi_i=-\frac{Ra_i}{J}\left[\frac{\partial\Theta_i}{\partial\xi}\frac{\partial Y}{\partial\eta}-\frac{\partial\Theta_i}{\partial\eta}\frac{\partial Y}{\partial\xi}\right], \tag{8}$$

$$\nabla^2_{\xi\eta}\Theta_i=\frac{1}{J}\left[\frac{\partial\Theta_i}{\partial\xi}\frac{\partial\psi_i}{\partial\eta}-\frac{\partial\Theta_i}{\partial\eta}\frac{\partial\psi_i}{\partial\xi}\right], \tag{9}$$

where

$$\nabla^2_{\xi\eta}=\frac{\alpha}{J^2}\frac{\partial^2}{\partial\xi^2}-\frac{2\beta}{J^2}\frac{\partial^2}{\partial\xi\partial\eta}+\frac{\gamma}{J^2}\frac{\partial^2}{\partial\eta^2}+P\frac{\partial}{\partial\xi}+Q\frac{\partial}{\partial\eta}, \tag{10}$$

is the Laplacian operator in the transformed domain.

Similarly, the dimensionless boundary conditions are given by

$$\text{At } \eta=\eta_0,\quad \xi_0\leqslant\xi\leqslant\xi_m,\quad \Theta_1=1,\quad \Psi_1=0. \tag{11a}$$

$$\text{At } \eta=\eta_n,\quad \xi_0\leqslant\xi\leqslant\xi_1,\quad \frac{\partial\Theta_2}{\partial\eta}\frac{\partial X}{\partial\xi}-\frac{\partial\Theta_2}{\partial\xi}\frac{\partial X}{\partial\eta}=0,\quad \frac{\partial\Psi_2}{\partial\eta}\frac{\partial X}{\partial\xi}-\frac{\partial\Psi_2}{\partial\xi}\frac{\partial X}{\partial\eta}=0.$$

$$\xi_1\leqslant\xi\leqslant\xi_2,\quad \frac{\partial\Theta_2}{\partial\xi}\frac{\partial Y}{\partial\eta}-\frac{\partial\Theta_2}{\partial\eta}\frac{\partial Y}{\partial\xi}=0,\quad \frac{\partial\Psi_2}{\partial\xi}\frac{\partial Y}{\partial\eta}-\frac{\partial\Psi_2}{\partial\eta}\frac{\partial Y}{\partial\xi}=0.$$

$$\xi_2\leqslant\xi\leqslant\xi_m,\quad \Theta_2=0,\quad \Psi_2=0. \tag{11b}$$

At $\xi=\xi_0$ and $\xi=\xi_m$.

$$\eta_0 \leq \eta < \eta_{\text{int}}, \quad \frac{\partial \Theta_1}{\partial \xi}\frac{\partial Y}{\partial \eta} - \frac{\partial \Theta_1}{\partial \eta}\frac{\partial Y}{\partial \xi} = 0, \quad \Psi_1 = 0, \quad (11c)$$

$$\eta_{\text{int}} < \eta \leq \eta_n, \quad \frac{\partial \Theta_2}{\partial \xi}\frac{\partial Y}{\partial \eta} - \frac{\partial \Theta_2}{\partial \eta}\frac{\partial Y}{\partial \xi} = 0, \quad \Psi_2 = 0, \quad (11d)$$

where the subscript "int" refers to the location of the interface. The transformed dimensionless interface conditions are:

$$\sin\theta\left[\frac{\partial \Psi_1}{\partial \xi}\frac{\partial Y}{\partial \eta} - \frac{\partial \Psi_1}{\partial \eta}\frac{\partial Y}{\partial \xi}\right] + \cos\theta\left[-\frac{\partial \Psi_1}{\partial \xi}\frac{\partial X}{\partial \eta} + \frac{\partial \Psi_1}{\partial \eta}\frac{\partial X}{\partial \xi}\right] = \frac{\alpha_2}{\alpha_1}\frac{K_1}{K_2}\left\{\sin\theta\left[\frac{\partial \Psi_2}{\partial \xi}\frac{\partial Y}{\partial \eta} - \frac{\partial \Psi_2}{\partial \eta}\frac{\partial Y}{\partial \xi}\right] + \cos\theta\left[-\frac{\partial \Psi_2}{\partial \xi}\frac{\partial X}{\partial \eta} + \frac{\partial \Psi_2}{\partial \eta}\frac{\partial X}{\partial \xi}\right]\right\}, \quad (12a)$$

$$\Theta_1 = \Theta_2, \quad (12b)$$

$$\cos\theta\left[\frac{\partial \Psi_1}{\partial \xi}\frac{\partial Y}{\partial \eta} - \frac{\partial \Psi_1}{\partial \eta}\frac{\partial Y}{\partial \xi}\right] - \sin\theta\left[-\frac{\partial \Psi_1}{\partial \xi}\frac{\partial X}{\partial \eta} + \frac{\partial \Psi_1}{\partial \eta}\frac{\partial X}{\partial \xi}\right] = \frac{\alpha_2}{\alpha_1}\left\{\cos\theta\left[\frac{\partial \Psi_2}{\partial \xi}\frac{\partial Y}{\partial \eta} - \frac{\partial \Psi_2}{\partial \eta}\frac{\partial Y}{\partial \xi}\right] - \sin\theta\left[-\frac{\partial \Psi_2}{\partial \xi}\frac{\partial X}{\partial \eta} + \frac{\partial \Psi_2}{\partial \eta}\frac{\partial X}{\partial \xi}\right]\right\}, \quad (12c)$$

$$\sin\theta\left[\frac{\partial \Theta_1}{\partial \xi}\frac{\partial Y}{\partial \eta} - \frac{\partial \Theta_1}{\partial \eta}\frac{\partial Y}{\partial \xi}\right] + \cos\theta\left[-\frac{\partial \Theta_1}{\partial \xi}\frac{\partial X}{\partial \eta} + \frac{\partial \Theta_1}{\partial \eta}\frac{\partial X}{\partial \xi}\right] = \frac{\alpha_2}{\alpha_1}\left\{\sin\theta\left[\frac{\partial \Theta_2}{\partial \xi}\frac{\partial Y}{\partial \eta} - \frac{\partial \Theta_2}{\partial \eta}\frac{\partial Y}{\partial \xi}\right] + \cos\theta\left[-\frac{\partial \Theta_2}{\partial \xi}\frac{\partial X}{\partial \eta} + \frac{\partial \Theta_2}{\partial \eta}\frac{\partial X}{\partial \xi}\right]\right\}. \quad (12d)$$

The governing equations along with the boundary conditions are solved by the finite difference method [15,16]. The interface conditions are implemented using imaginary nodal points as described by Rana et al. [11]. For the present study, the dimensionless buried depth is fixed at five ($d/r_i=5$) and the thermal diffusivity ratio is set to unity ($\alpha_1/\alpha_2=1$). Since the porous medium is assumed to saturate with the same fluid, the thermal diffusivity ratio is equal to the thermal conductivity ratio ($\alpha_1/\alpha_2=k_1/k_2$). Numerous trial runs have been conducted to ensure that the heat transfer results obtained from the present study are independent of the physical domain and grid size. It has been found that a dimensionless width (w/r_i) of 30 is sufficient to model the domain as a semi-infinite medium. To determine a proper grid size for use in the computation, a grid independence test has been conducted from a mesh of originally 61×81 with a subsequent refinement in the grid size (e.g., 101×141, 121×161, and 141×181). It has been found that a uniform grid of 121×161 in the transformed computational domain is the best choice for all calculations in terms of the computational efficiency and accuracy. This decision was supported by the result that a further refinement in the grid size does not produce any significant improvement in the heat transfer results (with $\Delta\text{Nu}<1\%$) or flow prediction (with $\Delta\Psi_{\max}<0.8\%$). As an additional check on the accuracy of the numerical results, an overall energy balance has been performed. A majority of the results obtained are satisfied within 1%; only a few cases are less than 3%.

To validate the numerical code, it has been tested against those reported in the literature for natural convection in a layered porous annulus with a slight modification of the code. The results obtained are in good agreement with those reported by Pan and Lai [12].

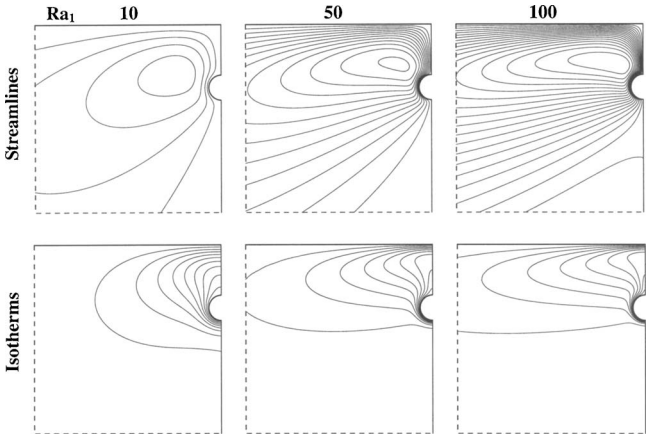

Fig. 3 Flow and temperature fields for a pipe buried in a homogeneous porous medium ($\Delta\Psi=1$ and $\Delta\Theta=0.1$)

Results and Discussion

For natural convection from a pipe buried in a homogeneous porous medium (Fig. 3), heated fluid rises along the pipe surface to the top boundary and then discharges to the left boundary. The flow field is replenished by cold fluid entering from the lower boundaries. Due to the action of thermal buoyancy, there exists a large recirculating cell. The strength of this recirculating cell increases with the Rayleigh number. Corresponding to this flow motion, a thermal plume is observed to develop from the top surface of the buried pipe, especially at high Rayleigh numbers. To better observe the flow structure and temperature field at the vicinity of the buried pipe, only partial results are presented in the figure ($-15\leq X\leq 0$, $-10\leq Y\leq 5$).

When the excavation disturbed zone or backfill is considered, the resulting flow and temperature fields (Figs. 4–7) are very different from those of the homogeneous one. For $K_1/K_2=10$, it is observed that the heat transfer mode is mainly by heat conduction at low Rayleigh numbers (e.g., $\text{Ra}_1=10$), which is evident from the isotherms displayed in Fig. 5. As the Rayleigh number (thermal buoyancy) increases, convective flow is first initiated from the

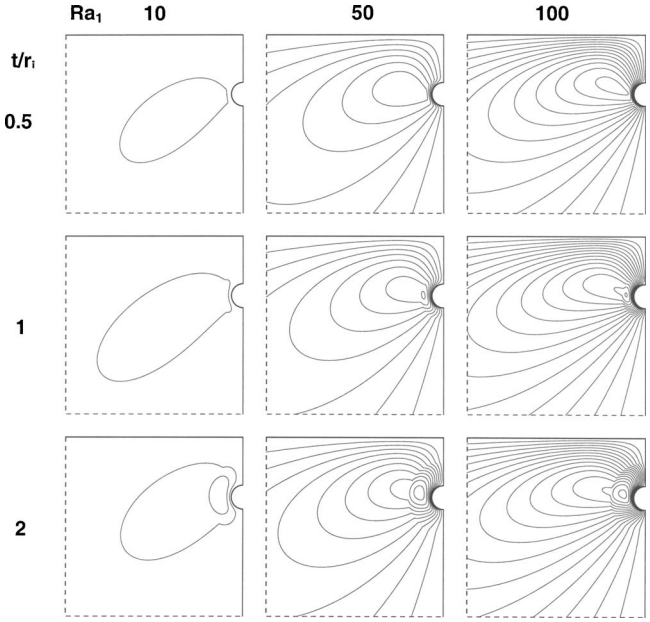

Fig. 4 Flow fields for a buried pipe with a backfill of $K_1/K_2=10$ ($\Delta\Psi=0.5$)

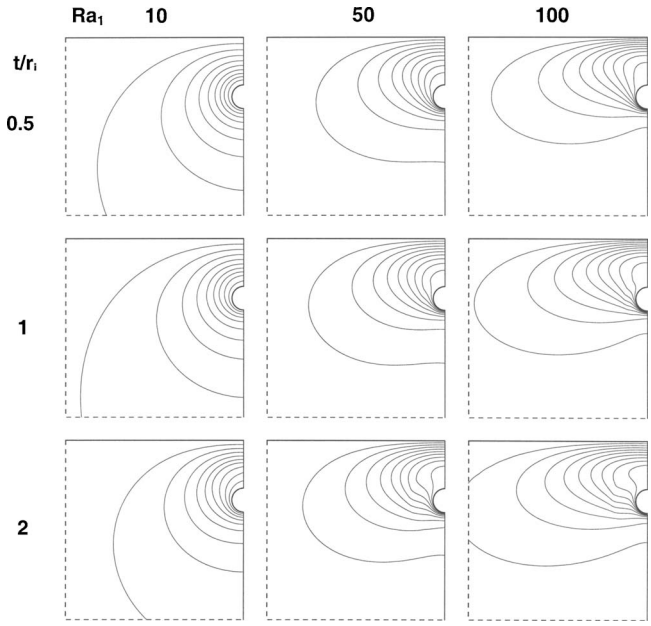

Fig. 5 Temperature fields for a buried pipe with a backfill of $K_1/K_2=10$ ($\Delta\Theta=0.1$)

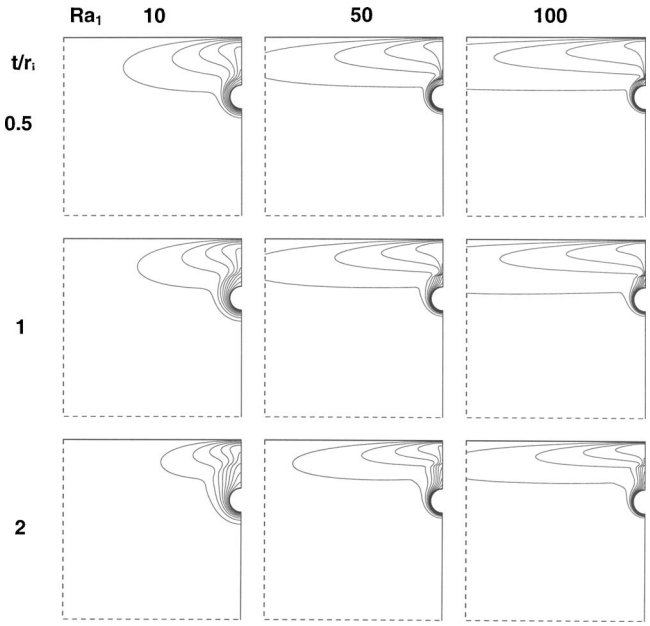

Fig. 7 Temperature fields for a buried pipe with a backfill of $K_1/K_2=0.1$ ($\Delta\Theta=0.1$)

inner layer (i.e., the more permeable layer) and then gradually penetrates the outer region (Fig. 4). Due to the added flow resistance in the outer region, the flow fields for $K_1/K_2=10$ are weaker than those of the homogeneous case. As a result, the eye of the convective cell is confined mostly in the inner layer. For a fixed Rayleigh number, the strength of the convective cell increases with the inner layer thickness (t/r_i). A thicker inner layer provides more room for the convective cell to develop.

On the other hand, for $K_1/K_2=0.1$, the outer region is more permeable than the inner layer, and consequently convection is promoted. It can be observed from Fig. 6 that convection is initiated even at a low Rayleigh number and the strength of the convective cell is notably strong when compared with that of the homogeneous case. It is interesting to note that the eye of the convective cell in this case always locates at the outer region. From the isotherms shown in Fig. 7, it is ascertained that heat transfer is always by convection for $K_1/K_2<1$. For a fixed Rayleigh number, the temperature gradient across the inner layer decreases with an increase in the inner layer thickness. The strength of the convective flow in the outer layer is weakened accordingly.

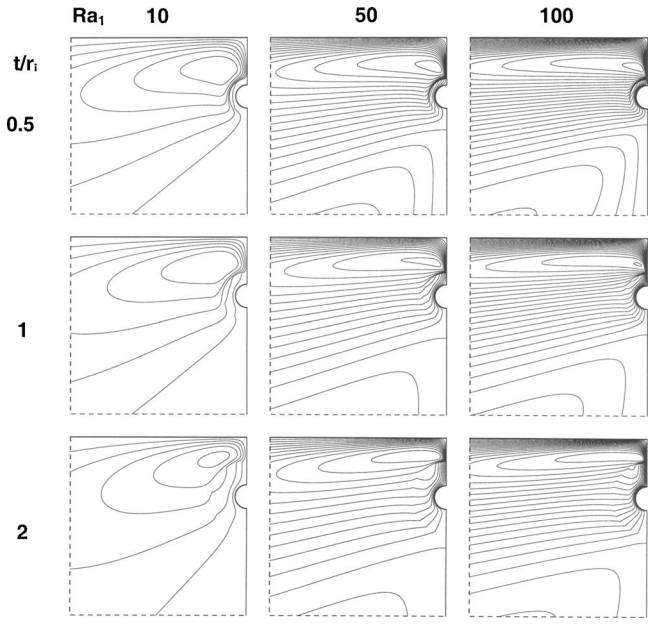

Fig. 6 Flow fields for a buried pipe with a backfill of $K_1/K_2=0.1$ ($\Delta\Psi=2$)

For the present study, heat transfer results are evaluated in terms of the Nusselt number at the top surface,

$$\mathrm{Nu} = -\int_{-w/r_i}^{0} \left.\frac{\partial\Theta}{\partial Y}\right|_{Y=d/r_i} dX, \tag{13}$$

which also represents the total heat flux through the top surface. For a homogeneous porous medium, the heat transfer results can be correlated by the following equation:

$$\mathrm{Nu} = \mathrm{Ra}^{1/2}. \tag{14}$$

The Nusselt numbers obtained for the present study are shown in Fig. 8 as a function of the Rayleigh number. It is observed that the Nusselt number for a buried pipe with a backfill of $K_1/K_2<1$ is always larger than that of a homogeneous one while it is always smaller for a buried pipe with a backfill of $K_1/K_2>1$. Also observed is that the slope of the Nusselt-versus-Rayleigh number curve (i.e., the power-law dependence of the Nusselt number with Rayleigh number) is less than $\frac{1}{2}$ for $K_1/K_2<1$ and greater than $\frac{1}{2}$ for $K_1/K_2>1$. It should be mentioned that for $K_1/K_2<1$, no converged solution has been obtained for high Rayleigh numbers ($\mathrm{Ra}_1\geqslant 500$) due to the nature of a highly convective flow field. It is interesting to note that the trend observed here is similar to that for a layered porous annulus [9] despite that the configurations for these two cases are very different.

Conclusions

The present study has considered a very fundamental problem in heat transfer. Although the problem has received extensive attention in the past, the present study addresses some critical aspects of the problem, particularly related to its applications to energy utilization and environmental protection. Based on the results obtained, one can conclude that, for the transportation of crude oil, it is desirable to have a layer of backfill or excavation

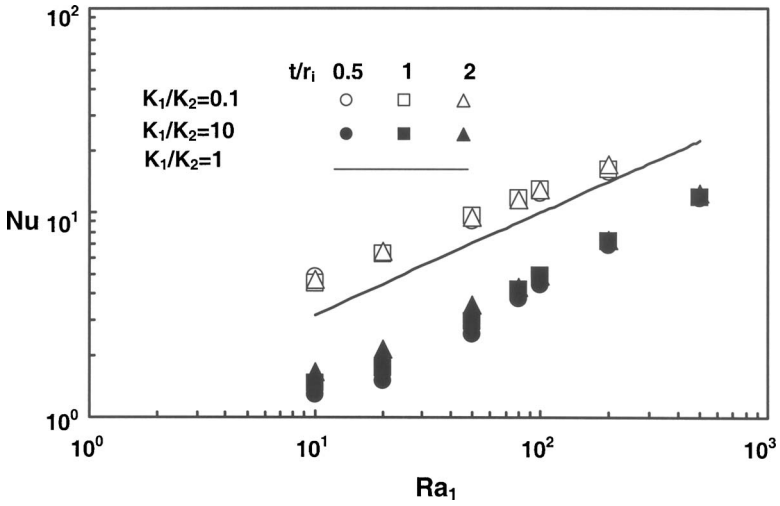

Fig. 8 Heat transfer results for natural convection from a buried pipe with and without backfill

disturbed zone that is more permeable than the hosting soil ($K_1/K_2>1$) so that the heat loss can be minimized. In fact, this is also the most desirable condition for the purpose of environmental protection since the contamination will be confined mostly in the disturbed zone or the backfill layer in the event that a leak should develop from a pipeline or a nuclear waste canister. On the other hand, for the application in electric power transmission, a backfill with $K_1/K_2<1$ may be used if overheating of transmission lines or power cables is to be avoided. Although the present study has addressed the primary effect of permeability variation on heat transfer from a buried pipe, the secondary effects of other thermophysical properties (such as the thermal conductivity and thermal capacity) are not included and await further investigation.

Nomenclature

c_p = specific heat (kJ/kg K)
d = buried depth (m)
g = gravitational acceleration (m/s^2)
h = heat transfer coefficient (W/m^2 K)
K = permeability (m^2)
k = thermal conductivity (W/m K)
Nu = Nusselt number, hr_i/k
P = grid control function
p = pressure (N/m^2)
Q = grid control function
r_i = radius of buried pipe (m)
Ra_i = Rayleigh number, $K_i g\beta(T_h-T_c)r_i/\alpha\nu$
T = temperature (K)
t = thickness of the sublayer (m)
u, v = velocity in the x- and y-direction (m/s)
x, y = Cartesian coordinates (m)
w = width of the physical domain (m)
α = thermal diffusivity, $k/\rho c_p$ (m^2/s)
β = coefficient of thermal expansion (l/K)
μ = dynamic viscosity (kg/m s)
ν = kinematic viscosity (m^2/s)
Θ = dimensionless temperature $(T-T_c)/(T_h-T_c)$
θ = angular coordinate
ρ = density (kg/m^3)
ξ, η = body-fitted coordinates
Ψ = stream function

References

[1] Bau, H. H., 1984, "Convective Heat Losses from a Pipe Buried in a Semi-Infinite Porous Medium," Int. J. Heat Mass Transfer, **27**, pp. 2047–2056.
[2] Farouk, B., and Shayer, H., 1988, "Natural Convection around a Heated Cylinder in a Saturated Porous Medium," ASME J. Heat Transfer, **110**, pp. 642–648.
[3] Christopher, D. M., and Wang, B.-X., 1993, "Non-Darcy Natural Convection around a Horizontal Cylinder Buried Near the Surface of a Fluid-Saturated Porous Medium," Int. J. Heat Mass Transfer, **36**, pp. 3663–3669.
[4] Fernandez, R. T., and Schrock, V. E., 1982, "Natural Convection from Cylinders Buried in a Liquid-Saturated Porous Medium," in Proceedings of the International Heat Transfer Conference, Munich, **2**, pp. 335–340.
[5] Fand, R. M., Steinberger, T. E., and Cheng, P., 1986, "Natural Convection Heat Transfer from a Horizontal Cylinder Embedded in a Porous Medium," Int. J. Heat Mass Transfer, **29**, pp. 119–133.
[6] Nield, D. A., and Bejan, A., 1999, *Convection in Porous Media*, 2nd ed., Springer-Verlag, New York.
[7] Hsiao, S.-W., Cheng, P., and Chen, C.-K., 1992, "Non-Uniform Porosity and Thermal Dispersion Effects on Natural Convection about a Heated Horizontal Cylinder in an Enclosed Porous Medium," Int. J. Heat Mass Transfer, **35**, pp. 3407–3418.
[8] Muralidhar, K., Baunchalk, R. A., and Kulacki, F. A., 1986, "Natural Convection in a Horizontal Porous Annulus with a Step Distribution in Permeability," ASME J. Heat Transfer, **108**, pp. 889–893.
[9] Ngo, C. C., and Lai, F. C., 2000, "Effective Permeability for Natural Convection in a Layered Porous Annulus," J. Thermophys. Heat Transfer, **14**, pp. 363–367.
[10] McKibbin, R., and O'Sullivan, M. J., 1981, "Heat Transfer in a Layered Porous Medium Heated from Below," J. Fluid Mech., **111**, pp. 141–173.
[11] Rana, R., Horne, R. N., and Cheng, P., 1979, "Natural Convection in a Multilayered Geothermal Reservoir," ASME J. Heat Transfer, **101**, pp. 411–416.
[12] Pan, C. P., and Lai, F. C., 1996, "Re-examination of Natural Convection in a Horizontal Layered Porous Annulus," ASME J. Heat Transfer, **118**, pp. 990–992.
[13] Thompson, J. F., Warsi, Z. U. A., and Mastin, C. W., 1982, "Boundary-Fitted Coordinates Systems for Numerical Solution of Partial Differential Equations-A Review," J. Comput. Phys., **47**, pp. 1–108.
[14] Himasekhar, K., and Bau, H. H., 1988, "Thermal Convection around a Heat Source Embedded in a Box Containing a Saturated Porous Medium," ASME J. Heat Transfer, **110**, pp. 649–654.
[15] Yost, B. A., 1984, "The Analysis of Fluid Flow/Solidification Problems in Arbitrarily Shaped Domains," Ph.D. dissertation, University of Delaware, Newark, DE.
[16] Patankar, S. V., 1980, *Numerical Heat Transfer and Fluid Flow*, Hemisphere, New York.

Fluid Flow Around and Heat Transfer From an Infinite Circular Cylinder

W. A. Khan

J. R. Culham

M. M. Yovanovich

Microelectronics Heat Transfer Laboratory,
Department of Mechanical Engineering,
University of Waterloo,
Waterloo, Ontario, Canada N2L 3G1

In this study, an integral approach of the boundary layer analysis is employed to investigate fluid flow around and heat transfer from an infinite circular cylinder. The Von Karman–Pohlhausen method is used to solve momentum integral equation and the energy integral equation is solved for both isothermal and isoflux boundary conditions. A fourth-order velocity profile in the hydrodynamic boundary layer and a third-order temperature profile in the thermal boundary layer are used to solve both integral equations. Closed form expressions are obtained for the drag and the average heat transfer coefficients which can be used for a wide range of Reynolds and Prandtl numbers. The results for both drag and heat transfer coefficients are in good agreement with experimental/numerical data for a circular cylinder.
[DOI: 10.1115/1.1924629]

Introduction

The equations describing fluid flow and heat transfer in forced convection are complicated by being nonlinear. These nonlinearities arise from the inertial and convective terms in the momentum and energy equations, respectively. From a mathematical point of view, the presence of the pressure gradient term in the momentum equation for forced convection further complicates the problem. The energy equation depends on the velocity through the convective terms and, as a result, is coupled with the momentum equation.

Because of these mathematical difficulties, the theoretical investigations about fluid flow around and heat transfer from circular cylinders have mainly centered upon asymptotic solutions. These solutions are well documented in the open literature and are valid for very large ($>2\times10^5$) and small (<1) Reynolds numbers. However, no theoretical investigation could be found that can be used to determine drag coefficients and average heat transfer from cylinders for low to moderate Reynolds numbers ($1-2\times10^5$) as well as for large Prandtl numbers ($\geqslant0.71$). For this range of Reynolds numbers and for selected fluids, there has been heavy reliance on both experiments and numerical methods. These approaches are not only expensive and time consuming but their results are applicable over a fixed range of conditions.

Unfortunately, many situations arise where solutions are required for low to moderate Reynolds numbers and for fluids having $\mathrm{Pr}>0.71$. Such solutions are of particular interest to thermal engineers involved with cylinders and fluids other than air or water. In this study a circular cylinder is considered in cross flow to investigate the fluid flow and heat transfer from a cylinder for a wide range of Reynolds and Prandtl numbers.

A review of existing literature reveals that most of the studies related to a single isolated cylinder are experimental or numerical. They are applicable over a fixed range of conditions. Furthermore, no analytical study gives a closed form solution for the fluid flow and heat transfer from a circular cylinder for a wide range of Reynolds and Prandtl numbers. At most, they provide a solution at the front stagnation point or a solution of boundary layer equations for very low Reynolds numbers. In this study, a closed form solution is obtained for the drag coefficients and Nusselt number, which can be used for a wide range of parameters. For this purpose, the Von Karman–Pohlhausen method is used, which was first introduced by Pohlhausen [1] at the suggestion of Von Karman [2] and then modified by Walz [3] and Holstein and Bohlen [4]. Schlichting [5] has explained and applied this method to the general problem of a two-dimensional boundary layer with pressure gradient. He obtained general solutions for the velocity profiles and the thermal boundary layers and compared them with the exact solution of a flat plate at zero incidence.

Analysis

Consider a uniform flow of a Newtonian fluid past a fixed circular cylinder of diameter D, with vanishing circulation around it, as shown in Fig. 1. The approaching velocity of the fluid is U_{app} and the ambient temperature is assumed to be T_a. The surface temperature of the wall is $T_w(>T_a)$ in the case of the isothermal cylinder and the heat flux is q for the isoflux boundary condition. The flow is assumed to be laminar, steady, and two-dimensional. The potential flow velocity just outside the boundary layer is denoted by $U(s)$. Using order-of-magnitude analysis, the reduced equations of continuity, momentum and energy in the curvilinear system of coordinates (Fig. 1) for an incompressible fluid can be written as:

Continuity:

$$\frac{\partial u}{\partial s}+\frac{\partial v}{\partial \eta}=0 \tag{1}$$

s-Momentum:

$$u\frac{\partial u}{\partial s}+v\frac{\partial u}{\partial \eta}=-\frac{1}{\rho}\frac{dP}{ds}+\nu\frac{\partial^2 u}{\partial \eta^2} \tag{2}$$

η-Momentum:

$$\frac{dP}{d\eta}=0 \tag{3}$$

Bernoulli equation:

$$-\frac{1}{\rho}\frac{dP}{ds}=U(s)\frac{dU(s)}{ds} \tag{4}$$

Energy:

$$u\frac{\partial T}{\partial s}+v\frac{\partial T}{\partial \eta}=\alpha\frac{\partial^2 T}{\partial \eta^2} \tag{5}$$

Hydrodynamic Boundary Conditions. At the cylinder surface, i.e., at $\eta=0$

$$u=0 \text{ and } \frac{\partial^2 u}{\partial \eta^2}=\frac{1}{\mu}\frac{\partial P}{\partial s} \tag{6}$$

At the edge of the boundary layer, i.e., at $\eta=\delta(s)$

$$u=U(s), \quad \frac{\partial u}{\partial \eta}=0 \text{ and } \frac{\partial^2 u}{\partial \eta^2}=0 \tag{7}$$

Contributed by the Heat Transfer Division for publication in the JOURNAL OF HEAT TRANSFER. Manuscript received May 25, 2004. Final manuscript received October 25, 2004. Review conducted by: N. K. Anand.

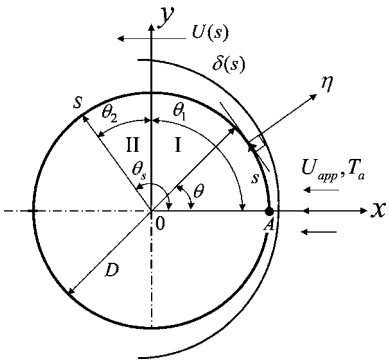

Fig. 1 Flow over a circular cylinder

Thermal Boundary Conditions. The boundary conditions for the uniform wall temperature (UWT) and uniform wall flux (UWF) are:

$$\eta = 0, \quad \begin{cases} T = T_w & \text{for UWT} \\ \dfrac{\partial T}{\partial \eta} = -\dfrac{q}{k_f} & \text{for UWF} \end{cases} \tag{8}$$

$$\eta = \delta_T, \quad T = T_a \text{ and } \frac{\partial T}{\partial \eta} = 0 \tag{9}$$

Velocity Distribution. Assuming a thin boundary layer around the cylinder, the velocity distribution in the boundary layer can be approximated by a fourth order polynomial as suggested by Pohlhausen [1]:

$$\frac{u}{U(s)} = (2\eta_H - 2\eta_H^3 + \eta_H^4) + \frac{\lambda}{6}(\eta_H - 3\eta_H^2 + 3\eta_H^3 - \eta_H^4) \tag{10}$$

where $0 \leqslant \eta_H = \eta/\delta(s) \leqslant 1$ and λ is the pressure gradient parameter, given by

$$\lambda = \frac{\delta^2}{\nu}\frac{dU(s)}{ds} \tag{11}$$

With the help of velocity profiles, Schlichting [5] showed that the parameter λ is restricted to the range $-12 \leqslant \lambda \leqslant 12$.

Temperature Distribution. Assuming a thin thermal boundary layer around the cylinder, the temperature distribution in the thermal boundary layer can be approximated by a third order polynomial

$$\frac{T - T_a}{T_w - T_a} = 1 - \frac{3}{2}\eta_T + \frac{1}{2}\eta_T^3 \tag{12}$$

for the isothermal boundary condition and

$$T - T_a = \frac{2q\delta_T}{3k_f}\left(1 - \frac{3}{2}\eta_T + \frac{1}{2}\eta_T^3\right) \tag{13}$$

for the isoflux boundary condition.

Boundary Layer Parameters. In dimensionless form, the momentum integral equation can be written as

$$\frac{U\delta_2}{\nu}\frac{d\delta_2}{ds} + \left(2 + \frac{\delta_1}{\delta_2}\right)\frac{\delta_2^2}{\nu}\frac{dU}{ds} = \frac{\delta_2}{U}\left.\frac{\partial u}{\partial \eta}\right|_{\eta=0} \tag{14}$$

where δ_1 and δ_2 are the displacement and momentum boundary layer thicknesses.

By solving the momentum integral equation, Khan [6] obtained the local dimensionless boundary layer and momentum thicknesses:

$$\frac{\delta}{D} = \frac{0.5}{\sqrt{\mathrm{Re}_D}}\sqrt{\frac{\lambda}{\cos\theta}} \tag{15}$$

$$\frac{\delta_2}{D} = \frac{0.3428}{\sqrt{\mathrm{Re}_D}}\sqrt{\frac{1}{\sin^6\theta}\int_0^\theta \sin^5\zeta d\zeta} \tag{16}$$

where Re_D is the Reynolds number, defined as

$$\mathrm{Re}_D = \frac{U_{\mathrm{app}}D}{\nu} \tag{17}$$

and λ is the pressure gradient parameter, whose values are obtained corresponding to each position along the cylinder surface. These values were fitted by the least squares method and given by Khan [6]. Using analytical definition of the point of separation, Khan [6] obtained the angle of separation as $\theta_s = 107.71$ deg, that depends on the velocity distribution inside the boundary layer. This angle of separation is in close agreement with Schöenauer [7] (=104.5 deg), Schlichting [5] (109.5 deg), Žukauskas and Žiugžda [8] (105 deg) and Churchill [9] (108.8 deg).

Fluid Flow. The first parameter of interest is fluid friction which manifests itself in the form of the drag force F_D, where F_D is the sum of the skin friction drag D_f and pressure drag D_p. Skin friction drag is due to viscous shear forces produced at the cylinder surface, predominantly in those regions where the boundary layer is attached. In dimensionless form, it can be written as

$$C_f = \frac{\tau_w}{\frac{1}{2}\rho U_{\mathrm{app}}^2} = \frac{4}{3}\frac{\lambda + 12}{\sqrt{\mathrm{Re}_D}}\sin\theta\sqrt{\frac{\cos\theta}{\lambda}} \tag{18}$$

The friction drag coefficient can be defined as

$$C_{Df} = \int_0^\pi C_f \sin\theta d\theta = \int_0^{\theta_s} C_f \sin\theta d\theta + \int_{\theta_s}^\pi C_f \sin\theta d\theta \tag{19}$$

Since the shear stress on the cylinder surface after boundary layer separation is negligible, the second integral will be zero and the friction drag coefficient can be written as

$$C_{Df} = \int_0^{\theta_s} C_f \sin\theta d\theta = \frac{5.786}{\sqrt{\mathrm{Re}_D}} \tag{20}$$

Pressure drag is due to the unbalanced pressures which exist between the relatively high pressures on the upstream surfaces and the lower pressures on the downstream surfaces. In dimensionless form, it can be written as

$$C_{Dp} = \int_0^\pi C_p \cos\theta d\theta \tag{21}$$

where C_p is the pressure coefficient and can be defined as

$$C_p = \frac{\Delta P}{\frac{1}{2}\rho U_{\mathrm{app}}^2} \tag{22}$$

The pressure difference ΔP can be obtained by integrating θ-momentum equation with respect to θ. In dimensionless form, it can be written as

$$\frac{\Delta P}{\frac{1}{2}\rho U_{\mathrm{app}}^2} = 2(1 - \cos\theta) + \frac{8}{\mathrm{Re}_D}(1 - \cos\theta) \tag{23}$$

So, the pressure drag coefficient for the cylinder up to the separation point will be

$$C_{Dp} = \int_0^{\theta_s} C_p \cos\theta d\theta = 1.152 + \frac{1.26}{\mathrm{Re}_D} \tag{24}$$

The total drag coefficient C_D can be written as the sum of both drag coefficients

$$C_D = \frac{5.786}{\sqrt{\mathrm{Re}_D}} + 1.152 + \frac{1.26}{\mathrm{Re}_D} \tag{25}$$

which was also obtained by Khan et al. [10] as a limiting case of an elliptical cylinder.

Heat Transfer. The second parameter of interest in this study is the dimensionless average heat transfer coefficient, Nu_D for large Prandtl numbers ($\geqslant 0.71$). This parameter is determined by integrating Eq. (5) from the cylinder surface to the thermal boundary layer edge. Assuming the presence of a thin thermal boundary layer δ_T along the cylinder surface, the energy integral equation for the isothermal boundary condition can be written as

$$\frac{d}{ds}\int_0^{\delta_T} (T - T_a) u d\eta = -\alpha \left.\frac{\partial T}{\partial \eta}\right|_{\eta=0} \tag{26}$$

Using velocity and temperature profiles Eqs. (10) and (12), and assuming $\zeta = \delta_T/\delta < 1$, Eq. (26) can be simplified to

$$\delta_T \frac{d}{ds}[U(s)\delta_T \zeta(\lambda + 12)] = 90\alpha \tag{27}$$

This equation can be rewritten separately for the two regions (Fig. 1), i.e.

$$\delta_T \frac{d}{ds}[U(s)\delta_T \zeta(\lambda_1 + 12)] = 90\alpha \tag{28}$$

for region I, and

$$\delta_T \frac{d}{ds}[U(s)\delta_T \zeta(\lambda_2 + 12)] = 90\alpha \tag{29}$$

for region II. Integrating Eqs. (28) and (29), in the respective regions, with respect to s, one can obtain local thermal boundary layer thicknesses

$$\left(\frac{\delta_T(\theta)}{D}\right) \cdot \mathrm{Re}_D^{1/2}\,\mathrm{Pr}^{1/3} = \begin{cases} \sqrt[3]{\dfrac{45 f_1(\theta)}{2(\lambda_1 + 12)^2 \sin^2\theta}} \sqrt{\dfrac{\lambda_1}{\cos\theta}} & \text{for region I} \\ \sqrt[3]{\dfrac{45 f_3(\theta)}{2\sin^2\theta}} \sqrt{\dfrac{\lambda_2}{\cos\theta}} & \text{for region II} \end{cases} \tag{30}$$

where the functions $f_1(\theta)$ and $f_3(\theta)$ are given by

$$f_1(\theta) = \int_0^{\theta} \sin\theta(\lambda_1 + 12) d\theta \tag{31}$$

and

$$f_3(\theta) = \frac{f_1(\theta)}{\lambda_1 + 12} + \frac{f_2(\theta)}{\lambda_2 + 12} \tag{32}$$

with

$$f_2(\theta) = \int_{\theta_1}^{\theta_s} \sin\theta(\lambda_2 + 12) d\theta \tag{33}$$

The local heat transfer coefficients, for the isothermal boundary condition, in both the regions can be written as

$$h_1(\theta) = \frac{3k_f}{2\delta_{T_1}} \text{ and } h_2(\theta) = \frac{3k_f}{2\delta_{T_2}} \tag{34}$$

Thus the dimensionless local heat transfer coefficients, for both the regions, can be written as

$$\frac{\mathrm{Nu}_D(\theta)|_{\text{isothermal}}}{\mathrm{Re}_D^{1/2}\,\mathrm{Pr}^{1/3}} = \begin{cases} \dfrac{3}{2}\sqrt[3]{\dfrac{2(\lambda_1 + 12)^2 \sin^2\theta}{45 f_1(\theta)}} \sqrt{\dfrac{\cos\theta}{\lambda_1}} & \text{for region I} \\ \dfrac{3}{2}\sqrt[3]{\dfrac{2\sin^2\theta}{45 f_3(\theta)}} \sqrt{\dfrac{\cos\theta}{\lambda_2}} & \text{for region II} \end{cases} \tag{35}$$

The average heat transfer coefficient is defined as

$$h = \frac{1}{\pi}\int_0^{\pi} h(\theta) d\theta = \frac{1}{\pi}\left\{\int_0^{\theta_s} h(\theta) d\theta + \int_{\theta_s}^{\pi} h(\theta) d\theta\right\} \tag{36}$$

The integral analysis is unable to predict heat transfer values from separation point to the rear stagnation point. However, experiments (Žukauskas and Žiugžda [8], Fand and Keswani [11], and Nakamura and Igarashi [12] among others) show that, the heat transfer from the rear portion of the cylinder increases with Reynolds numbers. From a collection of all known data, Van der Hegge Zijnen [13] demonstrated that the heat transferred from the rear portion of the cylinder can be determined from $\mathrm{Nu}_D = 0.001\,\mathrm{Re}_D$ that shows the weak dependence of average heat transfer from the rear portion of the cylinder on Reynolds numbers. In order to include the share of heat transfer from the rear portion of the cylinder, the local heat transfer coefficients are integrated upto the separation point and averaged over the whole surface, that is

$$h = \frac{1}{\pi}\int_0^{\theta_s} h(\theta) d\theta = \frac{1}{\pi}\left\{\int_0^{\theta_1} h_1(\theta) d\theta + \int_{\theta_1}^{\theta_s} h_2(\theta) d\theta\right\} \tag{37}$$

Using Eqs. (30)–(34), Eq. (37) can be solved for the average heat transfer coefficient which gives the average Nusselt number for an isothermal cylinder as

$$\mathrm{Nu}_D|_{\text{isothermal}} = 0.593\,\mathrm{Re}_D^{1/2}\,\mathrm{Pr}^{1/3} \tag{38}$$

For the isoflux boundary condition, the energy integral equation can be written as

$$\frac{d}{ds}\int_0^{\delta_T} (T - T_a) u d\eta = \frac{q}{\rho c_p} \tag{39}$$

Assuming constant heat flux and thermophysical properties, Eq. (39) can be simplified to

$$\frac{d}{ds}[U(s)\delta_T^2 \zeta(\lambda + 12)] = 90\frac{\nu}{\mathrm{Pr}} \tag{40}$$

Rewriting Eq. (40) for the two regions in the same way as Eq. (27), one can obtain local thermal boundary layer thicknesses δ_{T_1} and δ_{T_2} under isoflux boundary condition. The local surface temperatures for the two regions can then be obtained from temperature distribution

$$\Delta T_1(\theta) = \frac{2q\delta_{T_1}}{3k_f} \tag{41}$$

and

$$\Delta T_2(\theta) = \frac{2q\delta_{T_2}}{3k_f} \tag{42}$$

The local heat transfer coefficient can now be obtained from its definition as

$$h_1(\theta) = \frac{q}{\Delta T_1(\theta)} \quad \text{and} \quad h_2(\theta) = \frac{q}{\Delta T_2(\theta)} \tag{43}$$

which give the local Nusselt numbers for the cross flow over a cylinder with constant flux

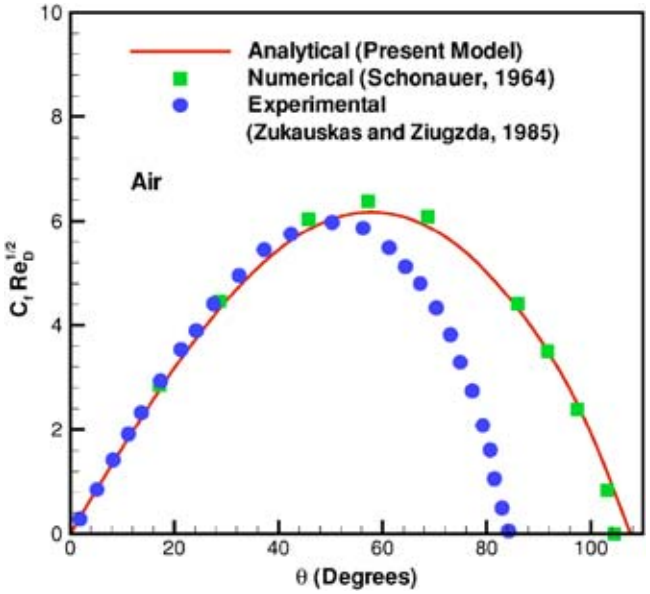

Fig. 2 Distribution of shear stress on a circular cylinder in air

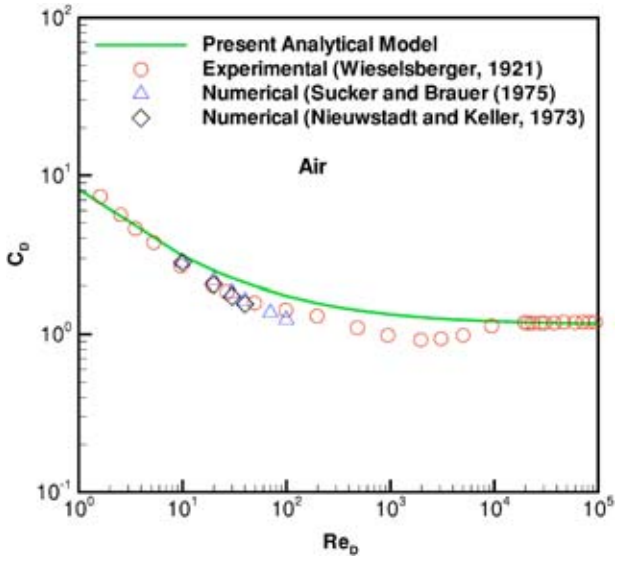

Fig. 3 Drag coefficient as a function of Re_D for a circular cylinder

$$\frac{Nu_D(\theta)|_{isoflux}}{Re_D^{1/2}\,Pr^{1/3}} = \begin{cases} \frac{3}{2}\sqrt[3]{\frac{4(\lambda_1+12)\sin\theta}{45 f_4(\theta)}}\sqrt{\frac{\cos\theta}{\lambda_1}} & \text{for region I} \\ \frac{3}{2}\sqrt[3]{\frac{4\sin\theta}{45 f_6(\theta)}}\sqrt{\frac{\cos\theta}{\lambda_2}} & \text{for region II} \end{cases} \tag{44}$$

Following the same procedure for the average heat transfer coefficient as mentioned above, one can obtain the average Nusselt number for an isoflux cylinder as

$$Nu_D|_{isoflux} = 0.632\,Re_D^{1/2}\,Pr^{1/3} \tag{45}$$

This Nusselt number is 6% greater than the average Nusselt number for an isothermal cylinder. Combining the results for both thermal boundary conditions, we have

$$\frac{Nu_D}{Re_D^{1/2}\,Pr^{1/3}} = \begin{cases} 0.593 & \text{for UWT} \\ 0.632 & \text{for UWF} \end{cases} \tag{46}$$

The same values were obtained by Khan [10] as a limiting case of an elliptical cylinder.

Results and Discussion

Flow Characteristics. The dimensionless local shear stress, $C_f\sqrt{Re_D}$, is plotted in Fig. 2. It can be seen that C_f is zero at the stagnation point and reaches a maximum at $\theta \approx 58$ deg. The increase in shear stress is caused by the deformation of the velocity profiles in the boundary layer, a higher velocity gradient at the wall and a thicker boundary layer. In the region of decreasing C_f preceeding the separation point, the pressure gradient decreases further and finally C_f falls to zero at $\theta = 107.7°$, where boundary-layer separation occurs. Beyond this point, C_f remains close to zero up to the rear stagnation point. These results are compared with the experimental results of Žukauskas and Žiugžda [8] and the numerical data of Schönauer [7]. Schönauer [7] data is in good agreement for the entire range, whereas, Žukauskas and Žiugžda [8] results are in good agreement for the front part of the cylinder only. This is probably due to high Reynolds numbers used in experiments.

The variation of the total drag coefficient C_D with Re_D is illustrated in Fig. 3 for an infinite cylinder in air. The present results are compared with the experimental results of Wieselsberger [14] as well as numerical data of Sucker and Brauer [15] and Niuwstadt and Keller [16]. The present results are in good agreement except at $Re_D = 2 \times 10^3$, where a downward deviation (23.75%) in the experimental results was noticed. No physical explanation could be found in the literature for this deviation.

Heat Transfer Characteristics. The comparison of local Nusselt numbers for the isothermal and isoflux boundary conditions is presented in Fig. 4. The isoflux boundary condition gives a higher heat transfer coefficient over the larger part of the circumference. On the front part of the cylinder (up to $\theta \approx 30$ deg), there is no appreciable effect of boundary condition. Empirical correlation of Kreith [17] as well as experimental data of Nakamura and Igarashi [12], van Meel [18] and Giedt [19] are also plotted to compare the analytical distribution of local heat transfer coefficients for isothermal boundary condition. The integral analysis of the boundary layer gives higher local heat transfer coefficients (around 15%)

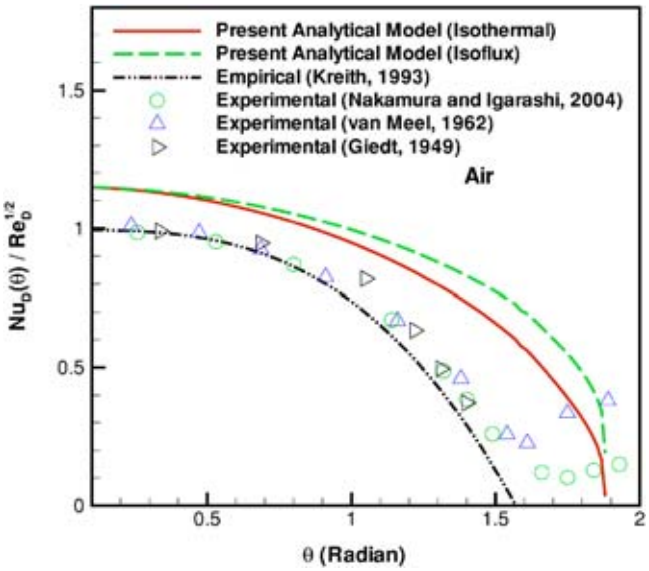

Fig. 4 Local Nusselt numbers for different boundary conditions

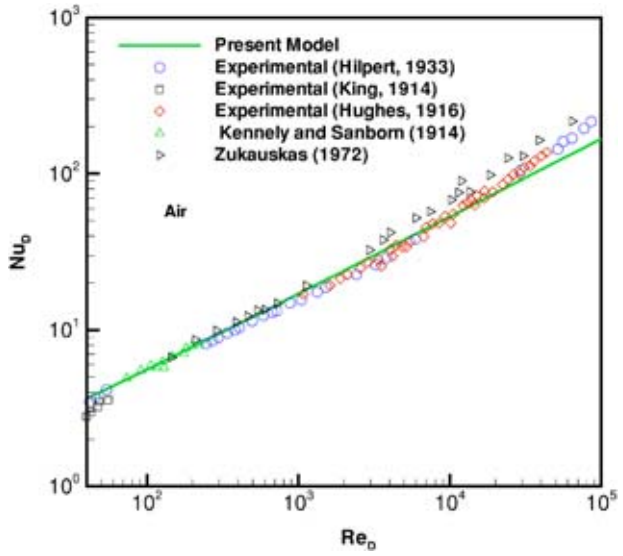

Fig. 5 Variation of average Nusselt number with Reynolds number for isothermal boundary condition

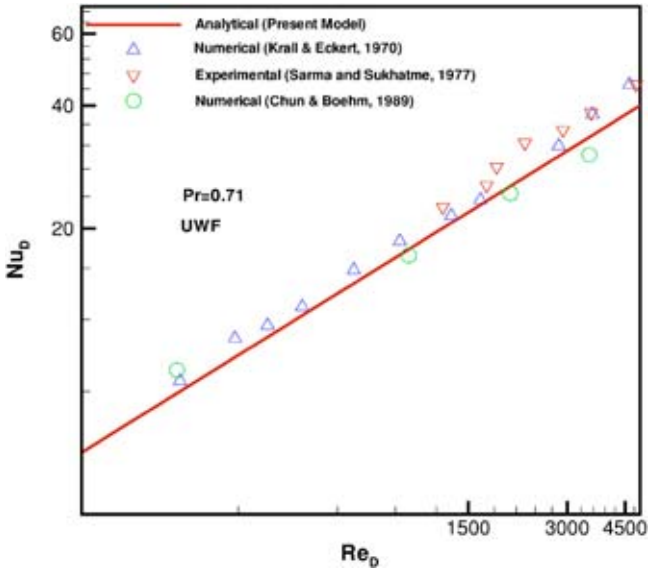

Fig. 6 Variation of average Nusselt number with Reynolds number for isoflux boundary condition

over the entire circumference of the cylinder. This discrepancy is probably due to the assumed velocity and temperature profiles in the boundary layer.

The results of heat transfer from a single isothermal cylinder are shown in Fig. 5, where they are compared with the experimental data of Hilpert [20], King [21], Hughes [22], Kennely and Sanborn [23], and Žukauskas [24]. Good agreement is observed in the entire laminar flow range except in the subcritical range. The discrepancy increases as the Reynolds number increases. This discrepancy is probably due to the effect of free-stream turbulence or vortex shedding in actual experiments. It was demonstrated by Kestin [25], Smith and Kuethe [26], Dyban and Epick [27], and Kestin and Wood [28] that the heat transfer coefficient increases with turbulence intensity and that this effect is more intense when the Reynolds number is higher. In the present analysis these effects are not included, so the discrepancy can be observed clearly in Fig. 5 for higher Reynolds numbers. Average Nusselt numbers for the isoflux boundary condition are compared in Fig. 6 with the experimental/numerical results. The average Nu_D values are found to be in a good agreement with both numerical results of Krall and Eckert [29] and Chun and Boehm [30]. However, the experimental results of Sarma and Sukhatme [31] are found to be higher ($\approx 8\%$).

Summary

An integral approach is employed to investigate the fluid flow and heat transfer from an isolated circular cylinder. Closed form solutions are developed for both the drag and heat transfer coefficients in terms of Reynolds and Prandtl numbers. The correlations of heat transfer are developed for both isothermal and isoflux boundary conditions. It is shown that the present results are in good agreement with the experimental results for the full laminar range of Reynolds numbers in the absence of free stream turbulence and blockage effects.

Acknowledgments

The authors gratefully acknowledge the financial support of Natural Sciences and Engineering Research Council of Canada and the Center for Microelectronics Assembly and Packaging.

Nomenclature

C_D = total drag coefficient
C_{Df} = friction drag coefficient
C_{Dp} = pressure drag coefficient
C_f = skin friction coefficient $\equiv 2\tau_w/\rho U_{\mathrm{app}}^2$
C_p = pressure coefficient $\equiv 2\Delta P/\rho U_{\mathrm{app}}^2$
c_p = specific heat of the fluid (J/kg K)
D = cylinder diameter (m)
k = thermal conductivity (W/m K)
h = average heat transfer coefficient ($\mathrm{W/m^2\,K}$)
Nu_D = average Nusselt number based on the diameter of the cylinder $\equiv hD/k_f$
Pr = Prandtl number $\equiv \nu/\alpha$
P = pressure ($\mathrm{N/m^2}$)
q = heat flux ($\mathrm{W/m^2}$)
Re_D = Reynolds number based on the diameter of the cylinder $\equiv DU_{\mathrm{app}}/\nu$
s = distance along the curved surface of the circular cylinder measured from the forward stagnation point (m)
T = temperature (C)
U_{app} = approach velocity (m/s)
$U(s)$ = potential flow velocity just outside the boundary layer $\equiv 2U_{\mathrm{app}} \sin\theta$ (m/s)
u = s-component of velocity in the boundary layer (m/s)
v = η-component of velocity in the boundary layer (m/s)

Greek Symbols

α = thermal diffusivity ($\mathrm{m^2/s}$)
δ = hydrodynamic boundary-layer thickness (m)
δ_1 = displacement thickness (m)
δ_2 = momentum thickness (m)
δ_T = thermal boundary layer thickness (m)
η = distance normal to and measured from the surface of the circular cylinder (m)
λ = pressure gradient parameter
μ = absolute viscosity of the fluid ($\mathrm{N\,s/m^2}$)
ν = kinematic viscosity of the fluid ($\mathrm{m^2/s}$)
ρ = density of the fluid ($\mathrm{kg/m^3}$)
τ = shear stress ($\mathrm{N/m^2}$)
θ = angle measured from front stagnation point (rad)

ζ = ratio of thermal and hydrodynamic boundary layers $\equiv \delta_T/\delta$

Subscripts

a = ambient
f = fluid or friction
H = hydrodynamic
p = pressure
s = separation
T = thermal or temperature
w = wall

References

[1] Pohlhausen, K., 1921, "Zur Näherungsweise Integration der Differential Gleichung der Laminaren Reibungschicht," Z. Angew. Math. Mech., **1**, pp. 252–268.
[2] Von Karman, T., 1921, "Über Laminar Und Turbulente Reibung," Z. Angew. Math. Mech., **1**, pp. 233–252.
[3] Walz, A., 1941, "Ein neuer Ansatz für das Greschwindligkeitsprofil der laminaren Reibungsschicht," Lilienthal-Bericht, **141**, p. 8.
[4] Holstein, H., and Bohlen, T., 1950, "Ein einfaches Verfahren zur Berechnung Laminaren Reibungsschichten," die dem Nahenungsansatz von K. Pohlhausen genugen, Lilenthal Bericht, **510**, p. 5.
[5] Schlichting, H., 1979, *Boundary Layer Theory*, 7th ed., McGraw–Hill, New York.
[6] Khan, W. A., 2004, "Modeling of Fluid Flow and Heat Transfer for Optimization of Pin-Fin Heat Sinks," Ph.D. thesis, Department of Mechanical Engineering, University of Waterloo, Canada.
[7] Schönauer, W., 1964, "Ein Differenzenverfahren zur Lösung der Grenzschichtgleichung für stationäre, laminare, inkompressible Strömung," Ing.-Arch., **33**, p. 173.
[8] Žukauskas, A., and Žiugžda, J., 1985, *Heat Transfer of a Cylinder in Crossflow*, Hemisphere, New York.
[9] Churchill, S. W., 1988, *Viscous Flows: The Practical Use of Theory*, Butterworths Series in Chemical Engineering, USA, pp. 317–358.
[10] Khan, W. A., Culham, J. R., and Yovanovich, M. M., 2005, "Fluid Flow and Heat Transfer from Elliptical Cylinders," J. Thermophys. Heat Transfer, **19**(2), pp. 178-185; also presented at AIAA 37th Thermophysics Conference, Portland, OR, June 29–July 1, 2004.
[11] Fand, R. M., and Keswani, K. K., 1972, "A Continuous Correlation Equation for Heat Transfer From Cylinders to Air in Crossflow for Reynolds Numbers From 10^{-2} to 2×10^5," Int. J. Heat Mass Transfer, **15**, pp. 559–562.
[12] Nakamura, H., and Igarashi, T., 2004, "Variation of Nusselt Number with Flow Regimes Behind a Circular Cylinder for Reynolds Numbers from 70 30000," Int. J. Heat Mass Transfer, **47**, pp. 5169–5173.
[13] Van der Hegge Zijnen, B. G., 1956, "Modified Correlation Formulae for Heat Transfer by Natural and Forced Convection from Horizontal Cylinders," Appl. Sci. Res., Sect. A, **6**, No. 2–3, pp. 129–140.
[14] Wieselsberger, C., 1921, "New Data on The Laws of Fluid Resistance," NACA TN No. 84.
[15] Sucker, D., and Brauer, H., 1995, "Investigation of the Flow Around Transverse Cylinders," Thermo and Fluid Dynamics, **8**, pp. 149–158.
[16] Nieuwstadt, F., and Keller, H. B., 1973, "Viscous Flow Past Circular Cylinders," Comput. Fluids, **1**, pp. 59.
[17] Kreith, F., and Bohn, M. S., 1993, *Principles of Heat Transfer*, 5th ed., West Publishing Company, New York, pp. 469–485.
[18] van Meel, D. A., 1962, "A Method for the Determination of Local Convective Heat Transfer from a Cylinder Placed Normal to an Air Stream," Int. J. Heat Mass Transfer, **5**, pp. 715–722.
[19] Giedt, W. H., 1949, "Investigation of Variation of Point Unit Heat-Transfer Coefficient Around a Cylinder Normal to an Air Stream," Trans. ASME, **71**, pp. 375–381.
[20] Hilpert, R., 1933, "Experimental Study of Heat Dissipation of Heated Wire and Pipe in Air Current," Forschungsarbeiten auf dem Gebiete des Ingenieurwesens - Ausgabe A, **4**(5), pp. 215–224.
[21] King, L. V., 1914, "The Convection of Heat from Small Cylinders in a Stream of Fluid: Determination of the Convection Constants of Small Platinum Wires with Applications to Hot-Wire Anemometry," Philos. Trans. R. Soc. London, Ser. A, **214**, pp. 373–433.
[22] Hughes, J. A., 1916, "The Cooling of Cylinders in a Stream of Air," Philos. Mag., **31**, pp. 118–130.
[23] Kennely, A. E., and Sanborn, H. S., 1914, "The Influence of Atmospheric Pressure Upon the Forced Thermal Convection from Small Electrically Heated Platinum Wires," Proceedings of the American Philosophical Society, Vol. 53, pp. 55–77.
[24] Žukauskas, A., 1972, *Advances in Heat Transfer*, Academic Press, New York, pp. 93–160.
[25] Kestin, J., 1966, "The Effect of Free Stream Turbulence on Heat Transfer Rates," *Advances in Heat Transfer*, Academic Press, New York, Vol. 3, pp. 1–32.
[26] Smith, M. C., and Kuethe, A. M., 1966, "Effects of Turbulence on Laminar Skin Friction and Heat Transfer," Phys. Fluids, **9**, pp. 2337–2344. *Advances in Heat Transfer*, Academic Press, New York, Vol. 3, pp. 1–32.
[27] Dyban, E. P., and Epick, E. Ya., 1970, "Some Heat Transfer Features in the Air Flows of Intensified Turbulence," in Proceedings of 4th Heat Transfer Conference, F. C. 5.7, Part 2, Paris-Versailles.
[28] Kestin, J., and Wood, R. T., 1971, "The Influence of Turbulence on Mass Transfer from Cylinders," *Advances in Heat Transfer*, Academic Press, New York, Vol. 3, pp. 1–32.
[29] Krall, K. M., and Eckert, E. R. G., 1970, "Heat Transfer to a Transverse Circular Cylinder at Low Reynolds Number Including Refraction Effects," Heat Transfer-Sov. Res., **3**, pp. 225–232.
[30] Chun, W., and Boehm, R. F., 1989, "Calculation of Forced Flow and Heat Transfer Around a Cylinder in Cross Flow," Numer. Heat Transfer, Part A, **15**(1), pp. 101–122.
[31] Sarma, T. S., and Sukhatme, S. P., 1977, "Local Heat Transfer from a Horizontal Cylinder to Air in Cross Flow: Influence of Free Convection and Free Stream Turbulence," Int. J. Heat Mass Transfer, **20**, pp. 51–56.

Study on the Imaginary Temperature of Open Boundary Wall in Cylindrical Medium by Partition Allocation Method

H. Qi

L. M. Ruan
e-mail: ruanlm@hit.edu.cn

L. H. Liu

School of Energy Science and Engineering,
Harbin Institute of Technology, Harbin,
People's Republic of China, 150001

By the partition allocation method, the radiative heat transfer in a cylindrical medium is approximated, in which every subdomain is overlapped with each other and isolated by an imaginary black wall at certain temperatures. The flux equivalent temperature (FET) from the incident radiative flux on the imaginary interface is proposed as the imaginary temperature of open boundary. Compared with the conventional method of the local medium temperature (LMT) as the imaginary temperature, the FET method is more suitable. The effects of the overlap optical thickness and the aspect ratio on the accuracy of partition allocation method were also investigated. [DOI: 10.1115/1.1924572]

Keywords: Open boundary, Radiative transfer, Partition allocation method, Overlap region

1 Introduction

Numerical solutions of the radiative transfer equation (RTE) in an absorbing, emitting, and scattering medium demand considerable effort in most practical systems filled with participating media. Theoretically speaking, the volume effect of the radiative transfer requires the calculation of the local volumetric radiation dissipation rate as an integral overall space. In the engineering applications of the pulverized coal-fired furnace, the free jet flow with very large aspect ratio, and so forth, it is necessary to refine the meshes to obtain an acceptable accuracy. In such cases, two facts have to be considered: namely the large built-in computer storage capacity and time consuming. With this idea, the domain decomposition methods were proposed to solve the RTE wholly or locally, in which the treatment of temperature and radiative properties of imaginary separating interfaces in every subdomain may be one of the key techniques.

In the last two decades, Yang et al. [1] and Coelho et al. [2] have focused on taking the open boundary of computational domain as black wall with local medium temperature (LMT) in numerical simulation of RTE. Zheng et al. [3] studied the combined laminar forced convection and thermal radiation in a helical pipe using the LMT method. More recently, Liu [4] and Ruan et al. [5] used the LMT method to investigate the local interesting zone of a three-dimensional (3D) boiler furnace and two-dimensional (2D) rectangle furnace, respectively. Nonetheless, the assumption of the black wall is not consistent with the physical conditions of the open boundary. In some 2D or more complex dimensional conditions, the assumption will result in errors that could not be neglected. More research has been done to solve local interesting domains with imaginary black walls, while less attention has been paid to the whole domain solution with the exception of a spatial multiblock procedure proposed by Chai [6]. In our previous paper [7], a new partition allocation method was proposed to solve the whole domain without error analysis. In the present study, the issues of one-dimensional (1D) and 2D temperature distributions in cylindrical medium are discussed and the feasibility, together with the applicability of the FET method, is analyzed.

Contributed by the Heat Transfer Division for publication in the JOURNAL OF HEAT TRANSFER. Manuscript received May 12, 2003; revision received March 3, 2005. Review conducted by: Gang Chen.

2 Numerical Model

Different numerical methods have been developed to solve the problem of radiative heat transfer in participant media [8–13], more specifically, the Monte Carlo (MC) method, the zonal method, the discrete ordinates method, the spherical harmonics method, diffusion approximation, the radiation element method by ray emission model (REM^2), and the ray tracing method. Because of its strong flexibility, the MC method is applied to solve the RTE in the absorbing, emitting, and anisotropically scattering cylindrical media in present study. The radiative exchange factor RD_{ij} is employed in the cylindrical MC simulation, which is defined as a fraction of emissive power of element i that is absorbed by element j. For numerical heat transfer calculation, the enclosure is separated into M finite surface elements and N finite volume elements. The heat flow absorbed by element i can be expressed as follows:

$$Q_{i,a} = \sum_{j=1}^{M} RD_{ji} Q_j + \sum_{k=1}^{N} RD_{ki} Q_k, \tag{1}$$

where $Q_j = F_j \varepsilon_j E_b(T_j)$ means the emissive energy of surface element j, and $Q_k = 4\kappa_{a,k} V_k E_b(T_k)$ is the emissive energy of volume element k. The details of the MC simulation is described in Ref. [14] and the uncertainty analysis of our MC model is discussed in Ref. [7]. In this study $NUM = 5 \times 10^6$ (bundles emitted from every element) is selected.

3 Results and Discussion

The physical model as shown in Fig. 1 simulates the ideal jet flame. The cylindrical medium is bounded by a black cylinder surface at $T = 300$ K with black walls on the left and right side, respectively. The axial length is $h_z = 6.0$ m and the radius length is $R = 0.5$ m. The radiative properties of the medium are homogeneous with albedo $\omega = 0.5$, the linearly scattering phase function $\Phi(\theta) = 1 + \cos\theta$ is adopted. The temperature distribution in the medium is known and the whole cylinder is divided into three subzones.

3.1 The 1D Temperature Distribution. The temperature distribution in the medium is assumed as: $T(z) = 2000 - 200z$ K. The temperature of left surface and the right surface is 2000 and 300 K, respectively. The radiative flux distribution of the boundary along the z axis is taken as the simulating results. The flux distribution without partition treatment is defined as standard result with meshes $N_z \times N_r = 600 \times 1$, where N_z and N_r refer to the number of meshes in the radial and axial directions. When simulating by the partition allocation method, the element mesh size in every subdomain remains the same as the standard meshes. Two methods are used to calculate the equivalent temperature of the imaginary black wall in every subdomain: (1) the local mean medium temperature (LMT) method and (2) the flux equivalent temperature (FET) method.

To have a clear understanding of FET, we suggest that the calculation of the equivalent temperature at boundary of every subdomain is derived from the incident radiative energy $Q = \Sigma_{i=1}^{M} Q_i$ on the imaginary surface, where Q_i is the incident energy by imagi-

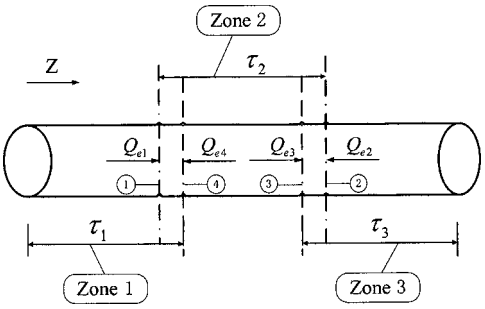

Fig. 1 The geometric model of partition allocation treatment by overlap regions

nary surface element i in the adjacent subdomain. The equivalent temperature is expressed in the following formula: $T=(Q/\sigma\pi R^2)^{1/4}$. The details of FET method are available in Ref. [7].

Firstly, the case without overlap regions ($\delta\tau=0.0$) by the LMT and FET methods is simulated and the relative error δq profile is shown in Fig. 2 and Fig. 3, respectively, $\delta\tau=\kappa_e L$ is the optical thickness of overlap region, where L is the length of overlap region and κ_e means the extinction coefficient. δq is defined as $\delta q=|q_c-q_s/q_s|\times 100\%$, where q_c is the calculated wall flux by partition allocation method, q_s means the standard result. The maximum and average relative error are denoted as $\delta q_{\max}$ and δq_{avg}. As shown in Fig. 2, the $\delta q_{\max}$ that occurs at the separating interface is more than 350% by the LMT method, which is too big to be neglected. By the FET method $\delta q_{\max}$ is much smaller (only

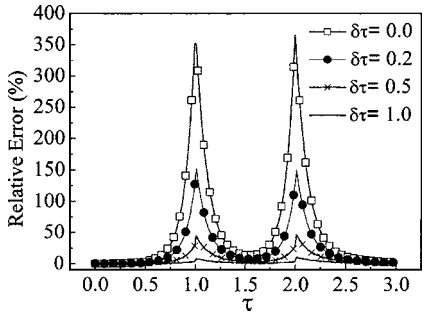

Fig. 2 The relative errors distribution with different overlap optical thickness using the LTM method

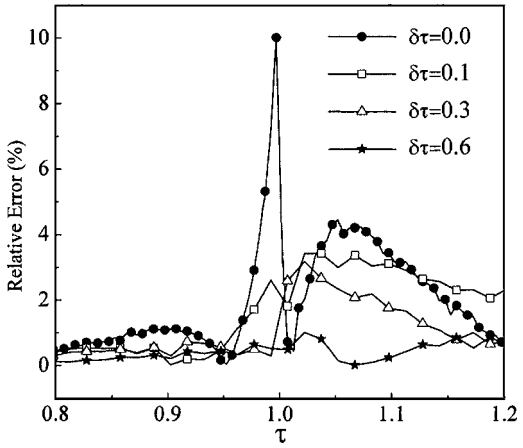

Fig. 3 The radiative flux distribution of the boundary along the *z* axis using the FET method and the LMT method (2D temperature distribution) $\delta\tau=0.2$ $L=0.4$ m

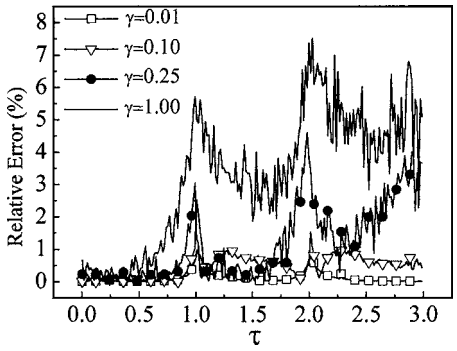

Fig. 4 The relationship between τ and relative error for a 1D problem using the FET method

about 10%) as shown in Fig. 3 ($\delta_\tau=0.0$), however, for getting more accurate results, the partition treatment with overlap regions is necessary as well.

Secondly, three cases with different $\delta\tau$ ($\delta\tau=0.2$, $\delta\tau=0.5$, $\delta\tau=1.0$) are selected to analyze the performance of partition method by the LMT method with $\kappa_e=0.5\ \mathrm{m}^{-1}$. As noted in Fig. 2, $\delta q_{\max}$ are about 160%, 50%, and 10%. Apparently if the criterion is defined as $\delta q_{\max}\leqslant 10\%$ and $\delta q_{avg}\leqslant 5\%$, it needs $\delta\tau\geqslant 1.0$ to obtain acceptable results by the LMT method. The reason is that the radiative energy transfers by exponential attenuation, when $\delta\tau\geqslant 1.0$, the influence of the imaginary wall radiation could be neglected.

Finally, as the $\delta q_{\max}$ appears in the overlap region, the following error analysis focuses on the overlap region in high temperature zone by the FET method. Two parameters influencing the accuracy of the results are studied: one is the $\delta\tau$, the other is the aspect radio $\gamma=R/(h_{zi})$ (where h_{zi} means the z-axis length of subzone i). Figure 3 demonstrates that when $\delta\tau=0.1$, $\delta q_{\max}$ is less than 5%, with the increase of $\delta\tau$, the relative errors decrease. It indicates that the FET method is more accurate and less memory required than LMT method. Figure 4 shows that when $\gamma_{\max}<1$, the $\delta q_{avg}\leqslant 5\%$. With the decrease of γ, the δq decreases as well. The reason is that with the decrease of the aspect ratio, the equivalent temperature of the imaginary black wall decreases, which reduces the influence of the volume effect of radiative transfer in the adjacent domain.

3.2 The 2D Temperature Distribution. The wall flux profile

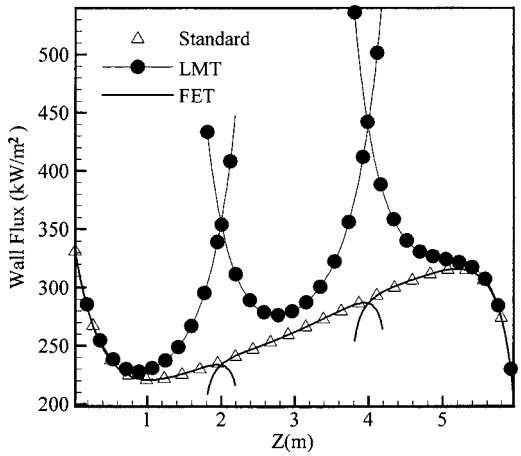

Fig. 5 The relationship between γ and relative error for a 1D problem using the FET method

by the LMT and FET methods in 2D temperature distribution absorbing and scattering medium is simulated. The temperature distribution is supposed to be

$$T(z,r) = 1700 + 50 \cdot z + 50 \times [1 - (r/R)^2], \quad 0 \leqslant z \leqslant 6.0 \text{ m}. \tag{2}$$

The left surface of the cylinder is black wall with 1700 K and the other parameters are the same as the 1D problem discussed above. The standard result is calculated with meshes $N_z \times N_r = 600 \times 20$. When taking the LMT as the imaginary temperature, the following formula is used:

$$T_e = \sqrt[4]{\left(\sum_{i=1}^{N_r} \sigma T_i^4 \cdot F_i\right) \Big/ (\sigma F)}, \tag{3}$$

where T_e is the equivalent temperature of the imaginary black wall, $F = \Sigma_{i=1}^{n} F_i$ is the total area of the cylindrical cross surface, T_i is calculated by Eq. (1) on the basis of $r = \sqrt{(r_{i-1}^2 + r_i^2)/2}$.

The wall flux are presented in Fig. 5 with $\delta\tau = 0.2$. Compared with the standard result, the deviation caused by the LMT method is serious, especially in the overlap regions. In this case, the FET method is more accurate. Therefore, for the 2D problem, the FET method is more suitable, while the LMT method will lead to serious errors. It should be mentioned that the calculation by the FET method is performed for different $\delta\tau$ and γ. The conclusion is almost the same as in the case of 1D.

Our MC code runs on AMD2500+. The total CPU time of standard result is 21.39×10^3 s with $NUM = 5 \times 10^6$ for condition of $h_z = 6.0$ m, $\kappa_e = 0.5$ m^{-1}, $N_z \times N_r = 600 \times 1$ by the FET method. With the same NUM for every subzone ($h_z = 1.9$ m, $N_z \times N_r = 190 \times 1$, $\kappa_e = 0.5$ m^{-1}), the time is 6.14×10^3 s (the total time is about $6.14 \times 10^3 \times 3$ s). Because the CPU time of MC depends mainly on the numbers of bundles, the time saving is not obvious. Additionally, many numerical methods such as the finite element method, the zone method, and the finite volume method need to calculate the exchange arrays or factors of point to point, or surface element to surface element, or surface element to volume element, or volume element to volume element step by step, the time saving will be significant when using our partition allocation method. Besides the time saving, memory storage is saved accordingly. For example, the dimensions of the array RD_{ij} with meshes $N_z \times N_r = 600 \times 20$ might be $600 \times 20 \times 600 \times 20$, but for each subzone, as in the case of zone 1, it might be $220 \times 20 \times 220 \times 20$. Consequently, the partition treatment by overlap regions can save memory and CPU time efficiently.

This study for the 2D problem might offer some insight into taking the open boundary of the computational domain as a black wall with different equivalent temperatures at each different element. It might be more accurate but might be not suitable to practical applications for the complexity. In the present paper, we assume that the temperature of the media is known in advance, if not, the energy conservation equation should be solved to obtain the temperature distribution and the equivalent temperature should be calculated at every iterative step, which will be the future study.

4 Conclusion

In this paper, the partitioned treatment simulation of radiative heat transfer in participating cylindrical media is investigated, in which every subdomain is overlapped each other and isolated by an imaginary black wall at a given equivalent temperature. By the FET assumption, the temperature of every interface is calculated on the basis of the incident radiative heat flux and the radiative transfer equation is solved independently in each isolated subdomain, which could reduce memory requirements, execution times, and solve completely the problem of interesting zones. The simulation shows that the FET method could predict the radiative flux distributions more accurately than the LMT method. For the specific cases of simulating the jet flame, the conclusions can be summarized as follows:

(1) When the optical thickness of the overlap region is larger than 1.0, the error resulted from the partitioned treatment could be neglected for a 1D cylindrical problem by the LMT method, while the optical thickness is larger than only 0.1 by the FET method.
(2) For a 2D problem, when the optical thickness of the overlap region is larger than 0.2, a reasonable result could be obtained by FET assumption. By LMT assumption the errors could not be neglected.
(3) The accuracy of the partitioned treatment by FET assumption is mainly influenced by the optical thickness of the overlap region and the aspect ratio. To satisfy $\delta q_{avg} \leqslant 5\%$, the aspect ratio of every subdomain should be less than 1.0.

Acknowledgment

The support of this work by the National Natural Science Foundation of China (Grant No. 50276014) is gratefully acknowledged.

References

[1] Yang, G., and Ebadian, M. A., 1991, "Combined Conductive-radiative Heat Transfer in a Duct Applying the Modified Differential Approximation Radiation Model," in *Fundamentals of Radiation Heat Transfer*, Proceedings of the ASME Jsme Thermal Engineering Joint Conference, **160**, pp. 45–53.
[2] Coelho, P. J., Goncalves, J. M., and Carvalho, M. G., 1998, "Modeling of Radiative Heat Transfer in Enclosures with Obstacles," Int. J. Heat Mass Transfer, **41**, pp. 745–756.
[3] Zheng, B., Lin, C. X., and Ebadian, M. A., 2000, "Combined Laminar Forced Convection and Thermal Radiation in a Helical Pipe," Int. J. Heat Mass Transfer, **43**, pp. 1067–1078.
[4] Liu, L. H., 2003, "Domain Isolation Concept for Solution of Radiative Transfer in Large-Scale Semitransparent Media," J. Quant. Spectrosc. Radiat. Transf., **78**, pp. 373–379.
[5] Ruan, L. M., Liu, L. H., and Tan, H. P., 2004, "The study on Approximating the Open Boundary of Two-dimension Medium as One Black Wall," Heat Mass Transfer, **40**, pp. 319–324.
[6] Chai, J. C., and Moder, J. P., 1997, "Spatial-multi-block Procedure for Radiation Heat Transfer," Numer. Heat Transfer, Part B, **31**, pp. 277–293.
[7] Ruan, L. M., Qi, H., Liu, L. H., and Tan, H. P., 2004, "The Radiative Transfer in Cylindrical Medium and Partition Allocation Method by Overlap Regions," J. Quant. Spectrosc. Radiat. Transf., **86**, pp. 343–352.
[8] Maruyama, S., and Aihara, T., 1997, "Radiation Heat Transfer of Arbitrary Three-dimensional Absorbing, Emitting, and Scattering Media, and Specular and Diffuse Surfaces," ASME J. Heat Transfer, **119**, pp. 129–136.
[9] Modest, M. F., 1993, *Radiative Heat Transfer*, McGraw-Hill, New York.
[10] Siegel, R., and Howell, J. R., 1992, *Thermal Radiation Heat Transfer*, 3rd ed., Taylor & Francis, New York.
[11] Coelho, P. J., and Carvalho, M. G., 1997, "A Conservative Formulation of the Discrete Transfer Method," ASME J. Heat Transfer, **119**, pp. 118–128.
[12] Ruan, L. M., and Tan, H. P., 2002, "Solution of Radiative Heat Transfer in Three-dimensional Inhomogeneous Scattering Media," ASME J. Heat Transfer, **124**, pp. 985–988.
[13] Yi, H. L., and Tan, H. P., 2004, "Scattering Characteristics Effect on Combined Heat Transfer Through an Anisotropic Nongray Media," J. Quant. Spectrosc. Radiat. Transf., **85**, pp. 285–310.
[14] Ruan, L. M., Tan, H. P., and Yan, Y. Y., 2002, "A Monte-Carlo (MC) Method Applied to the Medium with Non-gray Absorbing-emitting-anisotropic Scattering Particles and Gray Approximation," Numer. Heat Transfer, Part A, **42**, pp. 253–268.